RUHR-UNIVERSITÄT BOCHUM

SFB 837
Interaction Modeling in
Mechanized Tunneling

Florian Christ

Experimental investigations on
the hydro-mechanical behaviour of clay shales
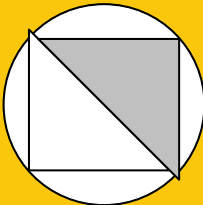for tunnelling relevant boundary conditions

Bochum 2025

Heft 83

Hydro-mechanical behaviour of clay shales

Florian Christ

83

Experimental investigations on the hydro-mechanical behaviour of clay shales for tunnelling relevant boundary conditions

Dissertation

as a requirement for the degree of

Doktor-Ingenieur (Dr.-Ing.)

at the Faculty of

Civil and Environmental Engineering

Ruhr-Universität Bochum

by

Florian Christ

Reviewers

Prof. Dr.-Ing. habil. Torsten Wichtmann

Prof. Dr.-Ing. Arash Alimardani Lavasan

Prof. Dr. Snehasis Tripathy

Bochum, 2025

Preface of the editor

Tunnelling in swellable soils or rocks like clay shales may trigger swelling processes, due to the excavation-induced unloading and the transport of water or vapor to the swellable geomaterials. The transport of water from distant aquifers along the tunnel axis may occur in the so-called excavation damaged zone (EDZ), showing an increased permeability due to the formation or opening of cracks and dilative shear bands induced by the excavation. The diffusion of vapor in the direction perpendicular to the tunnel axis due to a hydraulic gradient is another source of additional humidity potentially evoking swelling processes. These processes may lead to the development of swelling pressures under constant-volume conditions and to swelling strains if free swelling is possible. The development of both swelling pressures and strains is expected under mixed boundary conditions allowing a certain amount of deformation.

For tunnel construction in swellable geomaterials mainly two different strategies can be followed. The first one uses a massive stiff lining capable of carrying large swelling pressures. The second involves a deformable tunnel support system, allowing some swelling deformations to occur and thus reducing the swelling pressures acting on it. Up to now tunnel construction in swellable soils or rocks has been mainly performed using conventional methods, since they can be more easily adapted to the local soil or rock conditions. However, mechanised tunnelling is an attractive alternative, since it regularly allows more economical and time-efficient tunnel construction. For an application in swellable geomaterials, a deformable tunnel support system can be realized by deformable lining segments and / or a deformable grout. Extensive research on such deformable tunnel support systems was done in the framework of the collaborate research centre SFB 837 „Interaction modelling in mechanised tunnelling" funded by the German Research Council (DFG). Thereby, the sub-project A5 investigated the hydro-mechanical behaviour of swellable clay shales, with a special focus on the development of swelling pressures and strains due to hydration under tunnel-relevant boundary conditions. The doctoral thesis of Florian Christ is dedicated to the experimental study performed within that research project.

The experimental program included tests on the development of swelling pressure under constant-volume conditions, swelling strains in free swelling tests, as well as special tests with mixed boundary conditions as they are typical for a deformable tunnel support system. For the latter, Florian Christ has developed new and innovative swelling test devices which allow the application of controlled volumetric deformations (unloading) to the samples during the swelling process. The extreme boundary conditions (constant-

volume and free swelling) can also be studied with the new devices. Another novel device developed by Florian Christ allowed investigations on the anisotropy of the swelling strains by three-dimensional measurements on cubic samples. The tested Opalinus clay shale from the reference project "Sanierungstunnel Belchen" in northern Switzerland is relevant not only for tunnelling projects, but also for underground nuclear waste repositories planned in the same rock formations. The clay shale was tested in the highly anisotropic intact as well as the reconstituted state.

Florian Christ has performed a detailed parametric study on reconstituted, powder-compacted samples, including a variation of the grain size distribution of the powder, initial density, initial saturation and fabric. In the tests with mixed boundary conditions, the number, magnitude and sequence of the unloading steps was varied. Afterwards the observations and established relationships were confirmed by selected tests on the very sensitive intact material, which was tested perpendicular and parallel to the bedding plane orientation. Important outcomes of the experimental program are 1) a pronounced effect of the grain size distribution curve of the powder on the swelling behaviour of powder-compacted samples, 2) a significant change of the fabric of reconstituted samples during constant-volume swelling tests which affects the further free swelling potential, 3) the pronounced anisotropy of the swelling of the intact samples depending on the volumetric boundary conditions, and 4) the path-independence of the equilibrium swelling pressures and strains in the tests with controlled volumetric deformations.

In his thesis Florian Christ has collected a unique set of experimental data on swelling phenomena in clay shales which will be very useful for the future development of respective numerical models. The thesis provides plausible explanations of the macro-mechanical observations based on experimental investigations or theoretical considerations on the microstructure. The developed design charts, giving the equilibrium swelling pressure in dependence of the allowed deformations, are helpful for the planning of a deformable tunnel support system in swellable soils or rocks.

Bochum, March 2025   Torsten Wichtmann

Acknowledgment

This thesis represents a large part of my work as a research assistant at the Chair of Foundation Engineering, Soil and Rock Mechanics at the Ruhr-Universität Bochum and, since 2019, at the Chair of Soil Mechanics, Foundation Engineering and Environmental Geotechnics at Ruhr-Universität Bochum. The research conducted in this dissertation was part of Subproject A5 of the Collaborative Research Centre (SFB) 837 "Interaction Modeling in Mechanized Tunneling" at Ruhr-Universität Bochum.

Over nearly a decade, starting with my time as a student assistant, I had the privilege of working at the chair before finally completing my dissertation. This period was not only highly instructive but also incredibly rewarding, and it is an experience I will always cherish. I am deeply grateful to everyone who accompanied me throughout this journey, and I would like to take the opportunity to thank the following individuals and groups.

I would like to express my sincere gratitude to Dr.-Ing. König, who took my interest in geotechnics to a new level during my Bachelor's thesis, sparking my academic journey in this field. I am also profoundly grateful to Professor Schanz, whose guidance opened the doors to my academic career, and to Professor Wichtmann, who provided full support and allowed me the freedom to explore and complete my research. My heartfelt thanks go to Professor Lavasan, who, as the project manager of Subproject A5 in SFB 837, has been a constant source of insightful discussions and advice throughout the course of my work. It was an honor to have Professor Tripathy agree to be an additional reviewer of my thesis, and I deeply appreciate his time and effort in this regard.

I would also like to extend my gratitude to Dr.-Ing. Baille and Dr.-Ing. Lieske, who provided valuable insights into the field of clays and significantly expanded my understanding of the subject.

Furthermore, I would like to acknowledge my colleagues, who were always there to listen to my ideas, provide feedback, and offer stimulating conversations during coffee and lunch breaks. These breaks were not only a source of great inspiration but also a true source of enjoyment. Their support, positive attitude, and willingness to engage in lively discussions have made this experience all the more enjoyable and enriching.

Special thanks are due to those who directly supported me in the laboratory. I am grateful to Mr. Skubisch and Mr. Müller, the laboratory staff, whose support and expertise were crucial in the success of the experiments. I also appreciate the work of Mrs. Kallerhoff and Mrs. Diehl, who assisted as student assistants in carrying out various experiments within

Abstract

In the context of tunnelling in swellable soils, it is of great importance to consider the potential for swelling processes to exert additional loads on the tunnel lining. These can be reduced by the yielding principle, i.e., controlled deformations of the tunnel support system. For a long time, conventional tunnelling was the predominant method in this regard, as it can be individually adapted to the conditions encountered. However, in many instances, mechanised tunnelling is more time- and cost-efficient. Consequently, the yielding principle, utilising deformation-tolerant lining segments, has been integrated into mechanised tunnelling over recent years. Nevertheless, the majority of studies examining the swelling pressure-swelling strain relationship have centred on conventional tunnelling.

The objective of the present study was to investigate the hydro-mechanical behaviour of clays and claystones under boundary conditions relevant to tunnelling, with a particular focus on mechanised tunnelling. An extensive test programme with complementary hydro-mechanical tests was developed. The main focus was on the investigation of the influence of flexible tunnel support systems on the swelling pressure development of the surrounding subsoil. New swelling pressure cells for tunnelling relevant boundary conditions were developed for this purpose, which allow different volumetric boundary conditions and saturation modes. In addition to the limiting boundary conditions of free and constant volume swelling, it was possible to carry out strain-controlled swelling tests with these devices, which are intended to represent the case of a flexible tunnel support system.

The material analysed was Opalinus clay shale (OPA), a well-known geological formation of the Southern German and the Swiss Jura. The samples were obtained from the construction site of the Sanierungstunnel Belchen, which served as a reference project, and was analysed in both its original state and as a reconstituted material. The use of reconstituted OPA permitted a more time-efficient and reproducible analysis of fundamental mechanisms. Subsequently, the findings were validated on intact OPA. The experimental investigations included permeability tests, the water retention behaviour, swelling pressure tests, swelling strain tests and strain-controlled swelling pressure tests. Different boundary conditions were varied in the swelling pressure and swelling strain tests in order to provide insight into specific aspects of the material behaviour. The investigations were supplemented by microstructure analyses, which facilitated the discussion of some of the observed phenomena. Ultimately, based on the results of the strain-controlled swelling pressure tests, it was possible to derive design charts for the purpose of dimensioning future refurbishment measures or the flexible tunnel support system to be used.

Contents

1. Introduction

1.1. Background

The infrastructure network is experiencing an increase in demand over the past decades, which can be attributed to a number of factors, including the continuous growth in traffic volumes. The latest forecasts indicate that traffic in Germany will increase in all areas by 2051, whereas heavy goods vehicles will continue to represent the predominant mode of transportation in the freight sector, with an anticipated increase of up to 54 % on the roads (BMDV, 2023). Nevertheless, it is anticipated that freight transportation by rail will increase by approximately one-third, while that by waterways is expected to remain relatively stagnant. Similarly, passenger transport is anticipated to expand by 13 %. In order to adapt the existing infrastructure to the ever-increasing demand for mobility, the importance of tunnel construction has grown considerably in recent years. The relocation of infrastructure underground enhances quality of life in densely populated urban areas. Nevertheless, the construction of tunnels enables the overcoming of geographical obstacles, such as mountain ranges, in sparsely populated regions. This results in the reduction of both time and financial expenditure through the establishment of a direct connection, which presents opportunities for regional growth. Furthermore, the concept of underground cities and underground farming will become increasingly relevant in the future as a consequence of environmental pollution and climate change. It is also noteworthy that the radioactive waste repositories in Switzerland are to be constructed in swelling clay shale, with the galleries planned to be excavated with tunnelling machines.

Tunnelling in swelling soils or rocks (including clay shales, which can be categorised as both stiff soils and weak rocks) poses a significant challenge. In addition to anhydrite-containing rocks, which are not considered here, clay-rich rocks are of major importance in this respect. If these contain clay minerals from the smectite group, which are 2:1 layer minerals with an isomorphic induced negative charge, the influx of water initiates a swelling process (Mitchell and Soga, 2005). The swelling process, depending on the volumetric boundary conditions, manifests itself as swelling pressure (volume constrained

1

conditions), or as swelling strain (volume unconstrained conditions). In the majority of applications, a combination of the two occurs, with the process being controlled by either strain or stress (transient volumetric boundary conditions). The occurrence of swelling is based on two underlying mechanisms: innercrystalline swelling, i.e., the hydration of interlayer cations which equalise the negative charge of the smectite particles, and osmotic swelling, i.e., the formation of a diffusive double layer with ions of the pore water on the surface of the negatively charged clay particles and their repulsion. In the context of tunnel construction, osmotic swelling is of greater importance (Madsen and Müller-Vonmoos, 1989). Innercrystalline swelling is typically already completed, as it generates swelling pressures of a magnitude that cannot be suppressed by the overburden pressure. Osmotic swelling, however, occurs when the clay-rich soil is unloaded by the tunnel excavation and can therefore absorb further water. A potential source of the incoming water can be, among other things, distant water-bearing soil layers, which serve an advective flux along the tunnel structure into previously naturally sealed soil layers, or also an diffusive flux in radial direction towards the tunnel, which results from the unloading-induced dilatancy of the surrounding soil with an accompanying reduction in the degree of saturation. Another highly relevant property of clay shales is the pronounced anisotropy of the material due to its burial diagenesis. This becomes evident in the hydraulic, mechanical, thermal and coupled behaviour (Minardi et al., 2016; Bossart et al., 2017b; Gens et al., 2017; Favero et al., 2018; Wild and Amann, 2018).

Conventional methods are typically employed for tunnelling in swellable soils for a long time, as they allow for greater flexibility in adapting to the challenges that arise during construction. Two principal methods may be employed to regulate the additional swelling pressures acting on the tunnel lining. The first is the resistance principle, which entails the reinforcement of the lining through the incorporation of robust materials and the second is the evasion principle, which utilises compression elements. The greatest swelling pressure, and therefore the greatest additional load on the tunnel structure, occurs with a rigid support system. Flexible tunnel support systems, on the other hand, reduce the additional loads from the swelling pressure by allowing volumetric deformations. Compressible zones to avoid the transfer of the swelling pressure to the tunnel support system have proven effective in conventional tunnelling. Nevertheless, mechanised tunnelling offers a number of advantages over conventional methods, including the capacity for a higher advance rate, as well as the potential for a reduced disruptive impact on existing structures, such as buildings on the surface. In recent years, significant progress has been made in the production of deformation-tolerant segments, meaning that this concept can now also be applied to mechanised tunnelling (Radončić et al., 2009; Mezger et al., 2018; Vu et al.,

2020).

A current practical example of mechanised tunnelling in swellable soils is the Sanierungstunnel Belchen in the north of Switzerland. This tunnel has been cut through a total of 640 m of Opalinus clay (OPA), a swellable clay shale. As the tunnel was to be constructed using a tunnel boring machine and there was insufficient experience with deformable segmental linings, a rigid lining with a 35 cm thick outer lining and an additional inner cast-in-place lining with a thickness of 65 cm was chosen in the tunnel sections that were considered to be at risk. This meant enormous additional costs and construction effort. The installation of the additional inner reinforcement is shown in Fig. 1.1. However, a monitoring section was chosen and extensively instrumented. In-situ long term monitoring was set up in the relevant tunnel sections with OPA with various installed sensors between the rock mass and the tunnel lining. In addition, several samples were drilled in-situ, which are investigated in this study (Ziegler and Loew, 2017, 2018). These measures were implemented with the objective of enabling a detailed investigation into the hydro-mechanical behaviour of the surrounding OPA under conditions relevant to mechanised tunnelling.

The fact that OPA is the selected host rock for radioactive waste repositories in Switzerland adds more attention to this topic. For this reason, years of research have already been carried out at OPA to investigate all aspects of the material behaviour of the host rock during the storage of radioactive waste (Bossart and Milnes, 2018). However, the galleries in these repositories are to be constructed using mechanised tunnelling. For this reason,

Figure 1.1.: Installation of the additional inner cast-in-place lining of the Sanierungstunnel Belchen with a thickness of 65 cm (Marti Gruppe, 2017).

the Sanierungstunnel Belchen project and the knowledge gained from it offers significant added value for the repository issue as well.

An additional topic of significant interest is the analysis of reconstituted clay shales. In addition to the experimental advantages of working with this material, such as a considerably shorter experiment duration or better reproducibility thanks to more homogeneous samples, there are also practical applications for this type of material. During tunnelling in clay shales, a so-called excavation damaged zone (EDZ) is created around the tunnel boring machine, in which the previously intact material is present in a disturbed and destructured state. The reconstituted material thus serves as a counterpart to the fully intact material, and together they define the relevant range of conditions in which the material can be present in the EDZ. Furthermore, the behaviour of disturbed clay shales is gaining relevance, as excavated clay shales mixed with bentonite can be used as buffer and backfill material in the context of radioactive disposal (Souza and Pejon, 2020; Zeng et al., 2021, 2023).

1.2. Objectives

The objective of this work is to examine the impact of volumetric deformations on the swelling pressure development of clay shales, with a particular focus on boundary conditions relevant to mechanised tunnelling. The classical tests on the swelling potential of a soil cover the extreme cases of constant volume swelling (rigid tunnel lining) and free swelling (no tunnel lining). These boundary conditions are of high relevance as they define the limit states. In the context of flexible tunnel support systems, a test device was developed as part of this research, which is capable of conducting strain-controlled swelling pressure tests in addition to the aforementioned two limiting boundary conditions. As the focus of the device is on tunnelling relevant boundary conditions, it offers the possibility to saturate the sample via water (advectiv flux along the tunnel) as well as via the vapour phase (diffusive flux in radial direction towards the tunnel).

Reconstituted samples were used to better understand the basic mechanisms based on a homogeneous starting material, as intact OPA has a pronounced anisotropy and many inhomogeneities. Furthermore, knowledge of the intrinsic properties of a material is important from an engineering perspective as it provides a framework for assessing the in-situ condition of a structured soil. Concepts developed in this way on reconstituted OPA can subsequently be validated using the intact material. Another advantage of utilising reconstituted samples is the reduction in time required for analysis. As will be seen in

the course of the work, experiments on intact OPA take considerably longer before they reach maximum or equilibrium values compared to experiments on reconstituted OPA. The practical relevance of destructured OPA has already been mentioned in the previous section.

Based on the challenges of mechanised tunnelling in swelling clay shales, the main objectives of the present work are as follows:

- Investigation of the influence of the particle size distribution of ground OPA on the hydro-mechanical behaviour of reconstituted samples.

- Holistic analysis of the hydro-mechanical behaviour of a clay shale under various boundary conditions with relevance to mechanised tunnelling.

- Assessment of the relevance of the initial microstructure of reconstituted samples on the swelling behaviour.

- Derivation of a simplified design concept for the influence of flexible tunnel support systems on the forces acting on the tunnel structure.

1.3. Layout of the thesis

This thesis is organised in six chapters. This introductory chapter sets out the motivation for the work, defines its objectives and outline.

Chapter 2 provides an overview of the current and relevant literature on the topic of this thesis. It begins with a brief summary of clays, their mineralogy and hydration behaviour. Selected fundamentals of unsaturated soil mechanics are presented before the focus is placed on sample preparation and methodology for investigating swelling behaviour in the existing literature. Analytical swelling laws are also presented. The literature study is concluded with a brief overview of mechanised tunnelling in order to highlight relevant boundary conditions.

Chapter 3 provides a short overview of the reference project, the Sanierungstunnel Belchen. The material investigated in the current study originates from its construction site and the superordinate project (subproject A5 of the Collaborative Research Centre 837: Interaction Modeling in Mechanized Tunneling) is generally oriented towards the findings and measured data obtained at this real tunnelling project.

Chapter 4 presents the materials analysed in this work, the sample preparation and the experimental methods used. The boundary conditions of the experiments are clearly defined and newly developed as well as established equipment and methods are presented in detail.

Chapter 5 presents and discusses the most important results obtained in the course of this work. It is divided into four sections with a focus on microstructural investigations, mechanical, hydro-mechanical and thermal behaviour. The section on microstructure investigations analyses the materials on the basis of pore size distributions and microscope images. Based on the microstructure of the materials, the results in the following sections can be discussed. The section on the mechanical behaviour is for the sake of completeness and summarises the results of simple tests to determine the stiffness and shear strength of reconstituted OPA. On this basis, parameter sets for numerical investigations can be calibrated in further studies. Mechanical parameters of intact OPA can already be found sufficiently in the literature and are briefly summarised here. In the hydro-mechanical tests, the focus is on swelling pressure tests at constant volume conditions, swelling strain tests without volumetric constraints and combined strain-controlled swelling pressure tests. Aspects such as the saturation mode or the initial microstructure are also considered. Finally, the section on thermal conductivity provides an insight into the thermal behaviour of OPA, which is to be followed up by planned further studies.

Chapter 6 finally summarises the study. The most important conclusions drawn from this work are presented and suggestions for further potential studies are given.

2. State of the art

This chapter provides an overview of the fundamental knowledge regarding clays and their mineralogy, with a particular focus on illite, illite/smectite, kaolinite and chlorite, as these are components of the material under study. Additionally, it examines the water adsorption properties of clays, with a specific emphasis on the relevant swelling mechanisms for tunnelling applications. Finally, it addresses the microstructure of clays. These are the fundamental elements for the assessment of the observed phenomena. Additionally, the laboratory configurations for the determination of swelling pressure and the analytical methodologies for the modelling of swelling pressure are presented. An overview is provided of the previous laboratory testing of Opalinus Clay shale (OPA). Finally, a brief insight into the technique of mechanised tunnelling is given.

2.1. Clays and clay behaviour

There are a number of different approaches that can be taken in order to provide a definition of the term 'clay'. The official joint definition by the Association Internationale pour l'Étude des Argiles (AIPEA), originating in Europe, and the Clay Minerals Society (CMS), originating in the United States, is the following:

"The term 'clay' refers to a naturally occurring material composed primarily of fine-grained minerals, which is generally plastic at appropriate water contents and will harden when dried or fired. Although clay usually contains phyllosilicates, it may contain other materials that impart plasticity and harden when dried or fired. Associated phases in clay may include materials that do not impart plasticity and organic matter."

Guggenheim and Martin (1995)

Consequently, the mineralogical aspects, the natural origin and the plastic behaviour are combined. In the field of civil engineering, two additional definitions are widely employed.

One definition is based on particle size and limits clays to fine-grained soils with a particle size smaller than 2 μm (Bergaya et al., 2006; DIN EN ISO 14688-1:2020-11, 2020). The other definition is centered on the plasticity of the material. In accordance with DIN EN ISO 17892-12 (2020), clays are characterised by a liquid limit exceeding 30 %, and are situated within the Casagrande plasticity chart above the A-line.

2.1.1. Clay mineralogy

Clays are phyllosilicates and consist of two different sheets, namely tetrahedral and octahedral sheets. Different clays are characterised by the structure of the sheets which form a layer, how the layers are held together and furthermore the cations in the tetrahedrons and octahedrons. Two-sheet layers are also referred to as 1:1 layers and comprise a tetrahedral and an octahedral sheet (TO), whereas three-sheet layers are designated as 2:1 layers and consist of an octahedral layer sandwiched between two tetrahedral layers (TOT). A tetrahedral sheet is composed of multiple tetrahedron basic units (see Fig. 2.1a), which are typically a Si^{4+}, Al^{3+} or Fe^{3+} cation coordinated by four oxygen atoms. The octahedrons, which constitute the basic units of the octahedral sheets (see Fig. 2.1b), typically contain an Al^{3+}, Fe^{3+}, Mg^{2+} or Fe^{2+} cation coordinated by six oxygen atoms. Nevertheless, other cations were also observed, though at a lower frequency (Bergaya et al., 2006). Tetrahedral sheets are linked by sharing three corners of basal oxygen atoms (Fig. 2.1c), whereas in octahedral sheets, octahedrons are linked by sharing edges (Fig. 2.1d). This results in both sides of an octahedral sheet being identical, whereas one side of a tetrahedral sheet is composed of the tetrahedrons' tops and the other by their bases. An octahedral sheet is designated as trioctahedral when all positions within the sheet are occupied. This is typically the case when the cation within the octahedron is divalent. In the case of a trivalent cation, approximately one-third of the layer remains unoccupied, resulting in a dioctahedral sheet. The grey octahedrons depicted in Fig. 2.1d are indicative of the trioctahedral form. A TO or TOT layer is held together by the sharing of an oxygen atom. In the case of the tetrahedral sheet, this is the top oxygen atom of a tetrahedron. It can therefore be stated that the tetrahedral layer is always oriented in such a way that its tips face the octahedral layer. The oxygen atoms of the octahedrons that do not form a bond with a tetrahedron bind an H^+ proton, resulting in the formation of Hydroxyl (Mitchell and Soga, 2005).

The net negative charge exhibited by clay layers can be attributed to isomorphous substitution. This indicates that ions are replaced by ions of a different type, with the same or differing valence, without altering the crystal structure. An exception to this is the
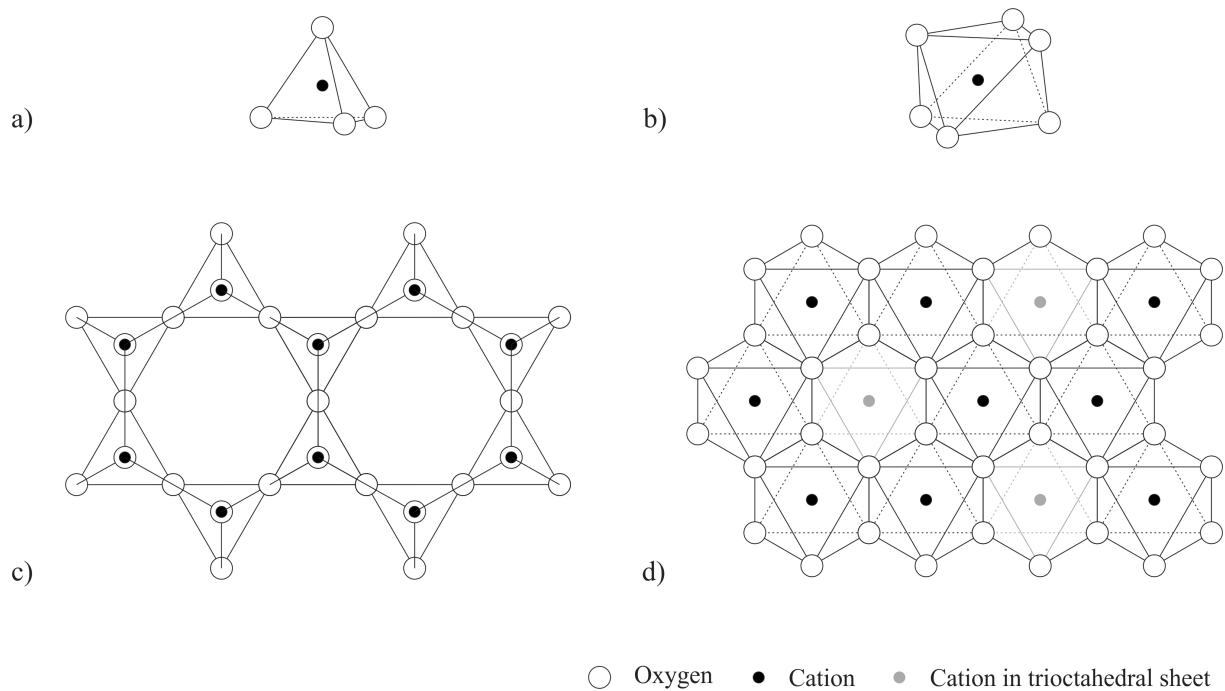
Figure 2.1.: Scheme of a) tetrahedral and b) octahedral basic units and top view of c) tetrahedral and d) octahedral sheet structures. Grey octahedrons are only present in the trioctahedral form of sheets, modified after Bergaya et al. (2006).

kaolin, for which the source of the net negative charge is still under debate (Grim, 1968; Wang and Siu, 2006a,b). In general, the charge deficit in 2:1 layers is more pronounced than in 1:1 layers. Cations are retained in close proximity to the surfaces and edges of the layer, as well as between the layers, in order to achieve electrical neutrality. The majority of these cations can be replaced by cations of a different type, and their quantity can be determined through cation exchange capacity (CEC). The CEC can be determined experimentally, which is described more in detail later. It is evident that the cation exchange capacity (CEC) of 1:1 layer minerals with a low negative net charge is considerably lower in comparison to 2:1 layer minerals with a larger negative net charge. In general, the CEC serves as an indicator for the activity of a clay and can be directly correlated to different soil mechanical parameters, such as plasticity values.

The nature of the bonding between layers can be of different types, which has a direct impact on the physical and chemical behaviour of the clay. In general, clays with a similar bonding type exhibit similar properties. Consequently, clays can be classified according to this type of bonding, as illustrated in Fig. 2.2. The bonding between layers can be attributed to a number of factors, including van der Waals forces, hydrogen bonds, the

presence of potassium, a single sheet layer, or the involvement of interlayer cations. The strongest bonds are observed in the case of a single sheet layer between two 2:1 layers (chlorite) and potassium, due to the fact that potassium is able to fit within the interstitial spaces between the tetrahedron bases (Fig. 2.1c). Nevertheless, adsorbed ions between layers with a moderate charge density may undergo hydration, which can result in layer expansion and potential separation (e.g., smectites) (Mitchell and Soga, 2005). The clay minerals present in the material under study will be presented in greater detail in the following sections, arranged in order of the frequency of their occurrence.

Figure 2.2.: Cross section of 1:1 and 2:1 layers with the corresponding clay groups resulting from different types of layer bonding, modified after Mitchell and Soga (2005). Grey cations in the octahedral sheets are only present in the trioctahedral form.

2.1.1.1. Illite

Illite is a mica-like clay mineral that is widely distributed in marine sediments, shales and mudstones. It is composed of 2:1 layers with a dioctahedral sheet. As a consequence of the replacement of one-quarter of the Si^{4+} positions by Al^{3+}, the negative net charge is increased. This is counterbalanced by the presence of potassium between the layers. The

radius of potassium ions is 1.33 Å, which allows them to fit precisely within the holes between tetrahedron bases, which have a radius of 1.32 Å (Mitchell and Soga, 2005). The formula for a unit cell is given by Eq. 2.1.

$$(OH)_4 K_2 (Si_6 Al_2) Al_4 O_{20} \tag{2.1}$$

The structure of illite is analogous to that of mica; however, it is markedly smaller in size and comprises a lower potassium content with a higher water content. Consequently, it is also frequently designated as hydrous mica. Nevertheless, due to the strong bonding by the non-exchangeable potassium, illite is essentially non-swelling. The basal spacing, defined as the distance between the lower edges of stacked layers is fixed at 10 Å. The most frequently observed CEC values are within the range of 10 to 40 meq/100 g.

2.1.1.2. Illite/Smectite - Mixed layer

The comparable crystal structures of the layers in clay minerals frequently result in the interstratification of diverse layer types. The most common mixed-layer clay is illite/smectite, which is formed by the interstratification of non-expandable illite and expandable smectite layers. It is typically observed that smectite undergoes transformation to illite/smectite as a by-product of the transformation to illite (Altaner and Ylagan, 1997; Drits et al., 1997). However, retrograde illite to illite/smectite transformation has also been documented (Zhao et al., 1999; Nieto et al., 2005).

Smectites are 2:1 layer clay minerals with a prototype TOT structure. The electrically neutral unit cell formula is as follows:

$$(OH)_4 Si_8 Al_4 O_{20} \cdot n H_2 O \tag{2.2}$$

The net negative charge is a consequence of the replacement of Al^{3+} in the dioctahedral sheet by Mg^{2+}, Zn^{2+}, Li^{1+} or other cations, as well as the substitution of up to 15 % Si^{4+} by Al^{3+} in the tetrahedral sheet. The net negative charge is relatively low and is compensated for by cations situated between the layers, which are typically sodium or calcium. The interlayer cations, in combination with van der Waals forces, serve to bind the stacked layers. The interlayer cations represent a potential weak point between the layers, and they have the capacity to hydrate, which can result in an increase in the interlayer distance. Consequently, the basal spacing ranges from 9.6 Å to complete separation. The CEC typically ranges from 80 to 150 meq/100 g (Mitchell and Soga, 2005). Montmorillonite represents the most prevalent mineral within the smectite group, while bentonite is a

clay with a significant smectite composition. Bentonites are well-known in the field of geotechnical engineering for sealing purposes, as they have a high swelling potential. In the most extreme case, the individual layers separate from each other, resulting in a suspension (bentonite slurry) that can be used as a supporting fluid in mechanised tunnelling or diaphragm wall construction.

The most widely used model, the polar 2:1 layer model, postulates that in illite/smectite mixed-layer clays, a TOT can exhibit a smectite charge on one side and an illitic charge on the other, resulting in the interstratification of illite and smectite. Further models exist and are under discussion (Altaner and Ylagan, 1997). Ultimately, this indicates that an illite/smectite mixed-layer clay can undergo hydration, expansion and swelling as a result of the interstratified smectite.

2.1.1.3. Kaolinite

Kaolinite is a 1:1 layer clay mineral comprising a dioctahedral layer. The interlayer bonding is attributed to van der Waals forces and hydrogen bonds. This bonding is sufficiently robust to prevent interlayer swelling in the presence of water. The composition of kaolinite is given by the following equation:

$$(OH)_8Si_4Al_4O_{10} \tag{2.3}$$
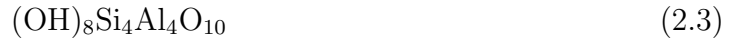
The CEC values of kaolinite range from 3 to 15 meq/100 g, indicating that the particles possess a slight net negative charge (Mitchell and Soga, 2005). However, the origin of this negative net charge remains a topic of debate, as previously discussed in Section 2.1.1. The basal spacing is 7.2 Å. Kaolinite does not swell and is a widely used material in the ceramics industry.

2.1.1.4. Chlorite

Chlorite is a clay group comprising negatively charged 2:1 layers, which are bonded by a single positively charged octahedral sheet via hydrogen bonds. The classification of these minerals is based on the di- or trioctahedral appearance of the octahedral sheet in the 2:1 layer and the single octahedral sheet in the interlayer. Most common are trioctahedral chlorites, where all octahedral sheets are trioctahedral. Nevertheless, also dioctahedral - all octahedral sheets are dioctahedral - di-trioctahedral - dioctahedral 2:1 layer and trioctahedral interlayer sheet - and tri-dioctahedral - trioctahedral 2:1 layer and dioctahedral

interlayer sheet - exist (Bergaya et al., 2006). The general formula of chlorites is as follows:

$$(\text{Mg,Fe})_3(\text{Si,Al})_4\text{O}_{10}(\text{OH})_2 \cdot (\text{Mg,Fe})_3(\text{OH})_6 \tag{2.4}$$

The basal spacing of chlorites is 14 Å and the CEC is in the range of 10 to 40 meq/100 g. Chlorite does not undergo any swelling processes since the interlayer spaces are unable to adsorb water. It is a rock-forming mineral, occurring in sedimentary rocks as a common constituent.

2.1.2. Water adsorption of clays

In their study, Mitchell and Soga (2005) built upon the findings of Low (1961) to identify four key mechanisms underlying the water adsorption process in clay minerals. These mechanisms can be attributed to electrostatic attraction (dipole-dipole or ion-dipole) and osmosis.

As illustrated in Fig. 2.2, the surfaces of clay layers are composed of either oxygen or hydroxyl. Water molecules are bipolar, meaning they are electrically neutral yet possess an unequal distribution of charge. They are capable of forming hydrogen bonds with either oxygen or hydroxyl groups, being attracted by the hydroxyl groups of octahedral sheets with negative corners and the oxygen groups of tetrahedral sheets with positive corners. These are dipole-dipole bonds. Ion-dipole bonds are formed between exchangeable cations at the negatively charged clay surfaces and water molecules. As a result of additional dipole-dipole interactions between water molecules, these molecules form hydration shells with multiple layers. This mechanism is of particular significance when the water content is low. In both cases, namely dipole-dipole and ion-dipole bonds, the involved water is coordinated and thus exhibits reduced mobility compared to free water.

The remaining two mechanisms can be directly associated with clay swelling on the macroscale in an engineering context. They are described in greater detail in the following sections, Section 2.1.2.1 and Section 2.1.2.2. Chemical swelling processes also frequently occur in the context of mechanised tunnelling in clay rocks containing anhydrite (e.g. Gipskeuper). This chemical process is associated with the transformation of anhydrite to gypsum, which can lead to considerable swelling strains and pressures. According to Rauh et al. (2006), the reaction can be described as follows:

$$\text{CaSO}_4 + 2\text{H}_2\text{O} \rightarrow \text{CaSO}_4 \cdot 2\text{H}_2\text{O} \tag{2.5}$$
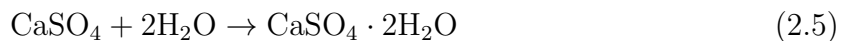
Nevertheless, anhydrite swelling is not within the scope of the present study, which is concerned with the swelling of clays, which will now be examined in greater detail.

2.1.2.1. Innercrystalline Swelling

The phenomenon of innercrystalline swelling can be defined as the hydration of interlayer cations, which in turn results in an increase in the interlayer spacing. This process can only occur when the attractive forces between mineral layers are exceeded. According to Mitchell and Soga (2005), attractive forces may be classified as hydrogen bonds in 1:1 layer silicates or van der Waals forces and ionic bonds in 2:1 layer silicates. Van der Waals forces are relatively weak non-covalent interactions between atoms or molecules. The interaction energy of these forces decreases with approximately the sixth power of the distance between the interacting particles. These forces are comparatively weak in comparison to atomic bonding and ionic bonding. Furthermore, hydrogen bonds are also too strong for interlayer hydration, which is why hydration of 1:1 layer silicates only occurs on the outer surfaces. It can thus be concluded that innercrystalline swelling is a relevant phenomenon for 2:1 layer silicates with comparatively weak bondings, namely smectites and vermiculites. The focus here will be set on innercrystalline swelling of smectites, which, as interstratified with illite, are the minerals responsible for the observed swelling of the investigated material.

The process of innercrystalline swelling of smectites is characterised by a stepwise increase in the number of interlayer water molecules, reaching a maximum of three planes (Fig. 2.3). The layer-to-layer distance d_{001}, defined as the distance between the lower edges of superimposed clay mineral layers, is around 9.6 to 10.7 Å in the dehydrated, 11.8 to 12.9 Å in the mono-hydrated, 14.5 to 15.8 Å in the bi-hydrated and 18.0 to 19.5 Å in the tri-hydrated state (Ferrage, 2016). The calculation of the corresponding swelling pressure for different hydration steps can be achieved through the utilisation of water adsorption isotherms. The swelling pressures resulting from innercrystalline swelling can exceed 100 MPa. It can be stated that overburden pressures of such a high magnitude to prevent this process do not occur in engineering practice. Therefore, the process is already complete at relevant depths and does not significantly impact tunnelling. In contrast, the distances over which the forces of innercrystalline swelling act on the micro-scale are extremely small (< 1nm) (Madsen and Müller-Vonmoos, 1989). This mechanism is of higher significance in the context of buffer systems, such as relatively dry compacted bentonite blocks, which are commonly used in the context of radioactive waste repositories.

As previously stated in Section 2.1.2, dipolar water molecules exhibit a coordinated behaviour when bonded to cations and negatively charged clay surfaces. This phenomenon also occurs in the context of innercrystalline swelling within the interlayer space. In this instance, the negative charges of the water molecules are oriented towards the interlayer

cations, while the positive charges are oriented towards the surface of the clay layers. The chemical and physical properties of this water differ from those of free bulk water. This phenomenon is most evident in the bi-hydrated state. The degree of orientation is observed to decrease with increasing distance from the surface. Dazas et al. (2014) demonstrated this through a combined X-ray diffraction and molecular simulation study. The atomic density profiles revealed the presence of two distinct water molecule planes that were observed to be in contact with the opposing surfaces, along with a third layer comprising poorly organised water molecules. In his review of the literature on the organisation of interlayer water, Ferrage (2016) identified the combination of experimental methods (X-ray diffraction) and molecular simulations (molecular dynamics or Monte Carlo) as the current state of the art.
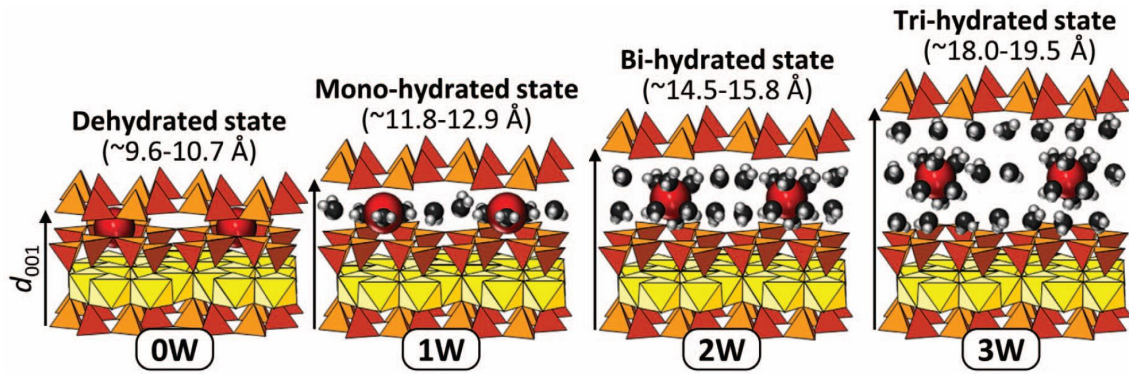
Figure 2.3.: Scheme of the stepwise hydration of interlayer cations in the process of inner-crystalline swelling (Ferrage, 2016).

2.1.2.2. Osmotic Swelling

According to Madsen and Müller-Vonmoos (1989), osmotic swelling represents the primary mechanism responsible for the swelling of clays in the context of tunnel construction. In an undisturbed state, the repulsive forces of this mechanism and the overburden pressure are in equilibrium. In comparison to the innercrystalline swelling, the osmotic swelling is less strong (up to 2 MPa swelling pressure), yet it acts over a much larger distance. In extreme cases this can result for sodium montmorillonites in the complete separation of layers. This phenomenon is utilised for supporting fluids in diaphragm wall construction or mechanised tunnelling. It does not occur for calcium montmorillonites, as the calcium cations are more strongly adsorbed (Caenn et al., 2017). Consequently, osmotic swelling

occurs when clayey sedimentary rocks are unloaded due to a tunnel excavation, thereby allowing for the adsorption of additional water.

As previously stated, clay particles possess a negative electrical charge. In order to neutralise this negative charge, positive ions are attracted to the clay surfaces. Consequently, the concentration of cations near the surface is greatly increased, resulting in a negative potential that decreases with increasing distance from the clay surface to the pore water (see Fig. 2.4). The amount of anions shows an inverse relationship. The negatively charged clay surface and the surrounding cloud of cations together form a so-called diffuse double layer. Two overlapping diffuse double layers exert a repulsive force on each other due to their negative potentials, resulting in the phenomenon of osmotic swelling (Madsen and Müller-Vonmoos, 1989; Civan, 2007).
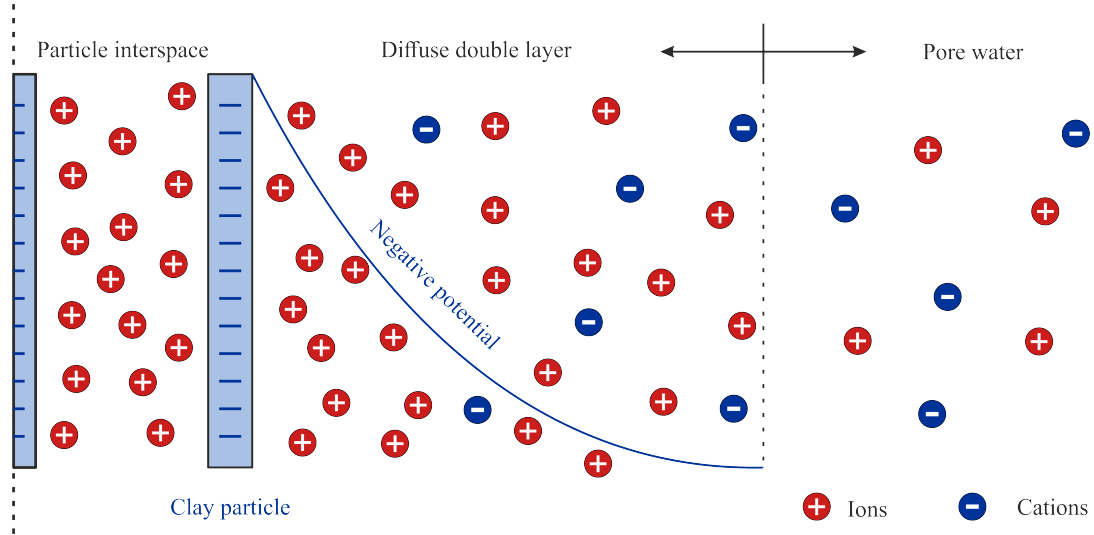
Figure 2.4.: Negatively charged clay particle, ion distribution and diffuse double layer, modified after Madsen and Müller-Vonmoos (1989).

Bolt (1956) proposed the diffuse double layer theory to calculate the swelling pressure in compacted bentonites. The theory considers the initial dry density and operates within an electrostatic framework. Thereby, the focus is set on the osmotic and not the inner-crystalline part of swelling. Sridharan and Jayadeva (1982) derived a distinct form that is more readily applicable to engineering purposes. Consequently, the swelling pressure is given by:

$$p = 2n_0 kT (\cosh u - 1) \tag{2.6}$$

where n_0 is the molar concentration of ions in the pore fluid, k is Boltzmann's constant, T is the absolute temperature and u is the nondimensional midplane potential. This again is

a function of soil parameters, water electrolyte properties and distance between the clay particles.

Tripathy et al. (2004) introduced another modification in dependence of the weighted average valency ν of exchangeable cations present in the considered clay.

For $\nu = 1.14$ to 1.5:

$$p = 2n_0 kT[\cosh(-7.277 \log_{10} Kd - 2.91) - 1] \tag{2.7}$$

For $\nu = 1.66$ to 1.73:

$$p = 2n_0 kT[\cosh(-10.427 \log_{10} Kd - 7.72) - 1] \tag{2.8}$$

For $\nu = 1.97$:

$$p = 2n_0 kT[\cosh(-9.190 \log_{10} Kd - 3.26) - 1] \tag{2.9}$$

where Kd is a nondimensional distance function.

As demonstrated by Schanz and Tripathy (2009), this approach yields favourable outcomes for compacted bentonites with a dry density of up to 1.55 g/cm^3 in comparison to the results of the experimental investigation. This can be explained by the fact that at higher densities, the role of adsorptive forces due to surface and ion hydration in the swelling process is more significant. Nevertheless, additional models have been proposed, based on semi-empirical considerations (e.g., Low and Margheim, 1979), thermodynamic principles (e.g., Kahr et al., 1990), and further double layer considerations (e.g., Komine and Ogata, 1996).

2.1.2.3. Influence of pore-water chemistry

In addition to effects on the mechanical behaviour of clays, such as a reduction in residual shear strength (Di Maio, 1996) or purely hydraulic effects, such as a reduction in hydraulic conductivity (Jo et al., 2001), the pore-water chemistry also exerts a significant influence on the hydro-mechanical behaviour, namely the swelling capacity of a clay (Studds et al., 1998; Rao and Thyagaraj, 2007; Siddiqua et al., 2011; Ye et al., 2015). Given the involvement of electrostatic processes, osmotic swelling is susceptible to increased ion concentrations in the pore fluid. An increase in ion concentration results in a reduction in the thickness of the diffuse double layer, due to a decrease in the osmotic gradient, which in turn leads to a reduction in swelling. These effects are primarily reversible following re-exposure to pure water, provided that the cations introduced into the clay are identical

to the interlayer cations present. This suggests that, for instance, the addition of a NaCl solution to a saturated Na-bentonite results in a reduction in volume, which is reversible when the solution is changed back to pure water (Di Maio, 1996). Conversely, influences that can be attributed to cation exchange may prove irreversible. However, this would have implications for not only the physico-chemical adsorption but also the soil structure. As demonstrated by Laird (2006), cation exchange plays a role in stabilising particles and promoting flocculation. Cation exchange may occur if the ions present in the external fluid differ from those within the clay, and if certain thermodynamic conditions are met. Given that cation exchange requires a high liquid-to-solid ratio and external energy, it is not a significant factor in mechanised tunnelling in clay shales. However, in the context of radioactive waste repositories, the presence of salts in the host rock, such as clay shales or salt rocks, can result in the infiltration of the installed bentonite buffer, thereby reducing its sealing capability (Rao and Thyagaraj, 2007; Herbert et al., 2008).

As outlined by Sridharan and Gurtug (2004), the swelling process can be divided into three distinct phases, namely initial, primary and secondary swelling. This is illustrated in Fig. 2.5. The initial and primary swelling can be related to the dissipation rate of matric suction, whereas the slower secondary swelling is controlled by the diffusion of salts (Rao et al., 2006). The rate of secondary swelling is observed to decrease as the concentration of salt increases. The rates of primary (C_{ps}) and secondary swelling (C_{ss}) are expressed in a manner analogous to that used for compression coefficients:

$$C_{ps} = \frac{\Delta H_p / H_0}{\Delta \lg t_p} \tag{2.10}$$

$$C_{ss} = \frac{\Delta H_s / H_0}{\Delta \lg t_s} \tag{2.11}$$

where ΔH_p and ΔH_s are the sample height increments of the primary and secondary swelling, H_0 is the initial height and t_p and t_s are the time intervals of primary and secondary swelling.

Nevertheless, it is also possible to affect the process of innercrystalline swelling through the introduction of chemical influences in the form of organic pollutants. One such example is diammoniumdodecane, which is a waste product of the cosmetic industry. The intercalation (incorporation of molecules) and displacement of interlayer cations result in the clay surface becoming hydrophobic, which in turn leads to a reduction in the layer-to-layer distance. The resulting effects are an increase in hydraulic conductivity by a factor of three and a transition from highly active (Activity index $I_A > 1.25$; the activity index is the plastic limit I_p divided by the mass percentage of finer < 0.02 mm) to inactive
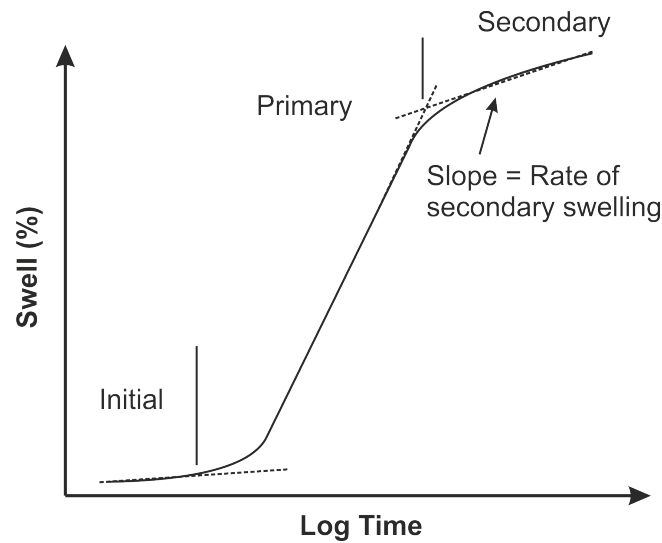
Figure 2.5.: Schematic diagram showing the three distinct phases of swelling, modified after Sridharan and Gurtug (2004).

($I_A < 0.75$) in the Atterberg limits (Hasenpatt et al., 1989). Nevertheless, this is less frequently observed.

2.1.3. Microstructure of clays

The microstructure of a soil, and in particular that of a clay, exerts a considerable influence on the material behaviour. The term 'microstructure' is used to describe the combination of fabric and bonding of a soil. In this context, 'fabric' refers to the pure spatial arrangement of particles, while 'bonding' denotes the physico-chemistry related to interparticle forces (Burland, 1990).

Prior to examining the genesis, properties, and consequences of soil structure, it is essential to establish several fundamental concepts. Accordingly, Fig. 2.6 provides a comprehensive overview of the various levels and terminology associated with the microstructure of clays. As previously outlined in Section 2.1.1, a clay layer is comprised of tetrahedral and octahedral sheets. The particles are held together by interlayer cations (or other elements, such as potassium and magnesium, as illustrated in Fig. 2.2). The layer-to-layer distance, defined as the distance between the lower edges of superimposed clay mineral layers, and the interlayer distance, which represents the distance between layers within a particle, are two key measures utilised in the analysis of clay mineralogy. An aggregate is formed by the stacking of several particles. In an assembly of aggregates, the intra-aggregate and

inter-aggregate space, or more specifically the intra-aggregate and inter-aggregate pores, constitute the primary components of the pore size distribution (PSD). The PSD can be divided into discrete segments, each of which corresponds to a specific range of porosity.

Some literature specifies an upper limit for micropores, for example 100 nm (Schanz and Al-Badran, 2014), and refers to the larger pores as macropores. Nevertheless, a precise definition of the pore diameter is not an absolute necessity, given that the two pore types are associated with distinct voids within the material. In general, micropores are defined as intra-aggregate pores, whereas macropores are defined as inter-aggregate pores (Romero and Simms, 2008; Acikel et al., 2018). Further subdivisions into ultramicropores and mesopores exist (Pineda et al., 2014), but are not considered here as they do not contribute to the present study's objectives. The two pore types can be readily identified and differentiated in a PSD of compacted clay, as they manifest as two distinct peaks.
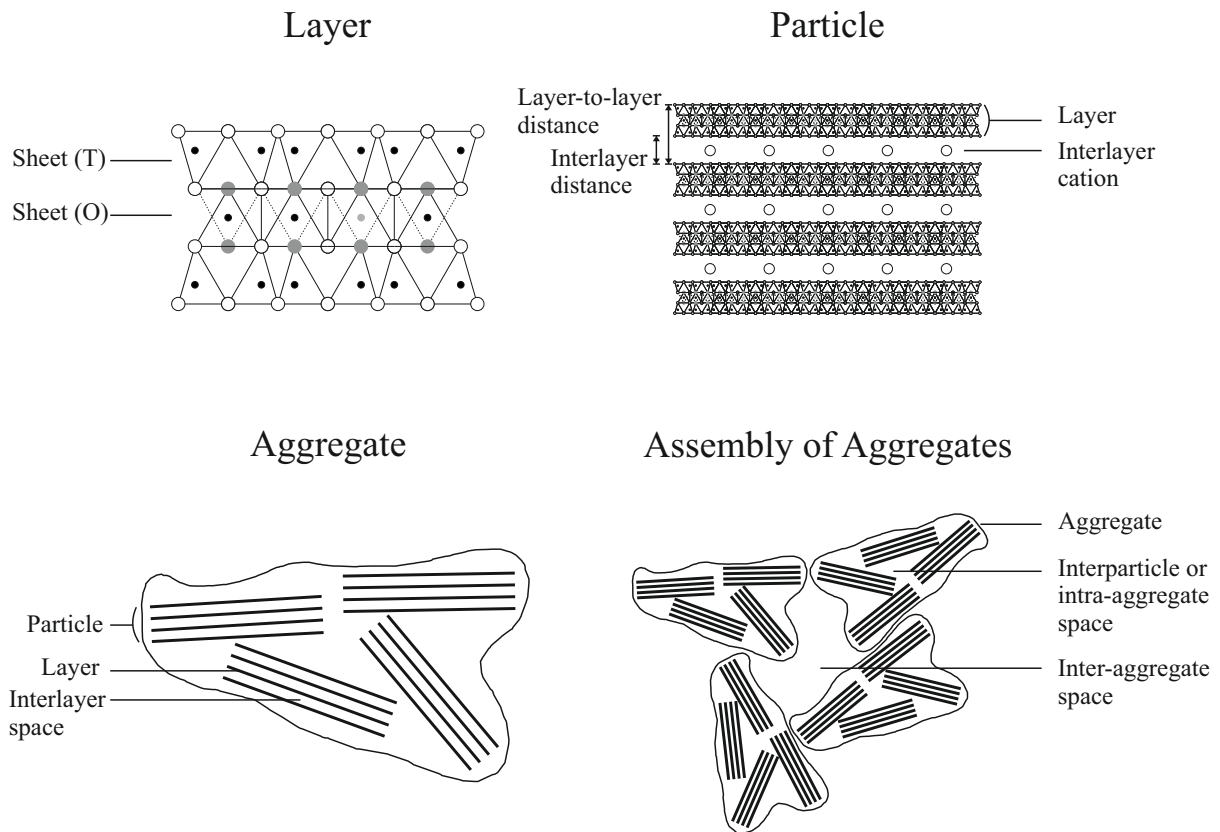

Figure 2.6.: Different levels and terms of the microstructure of clays, modified after Bergaya et al. (2006) and Baille (2014).

2.1.3.1. Fabric of compacted clays

It was already observed early on by Lambe (1958), that the microstructure of compacted fine-grained soils is related to the water content during compaction with respect to the Proctor water content, in addition to other factors such as compaction type and soil composition. When the water content is below the optimum level (on the dry side of the Proctor curve), the microstructure is observed to be in a flocculated state. Conversely, when the water content is above the optimum level (on the wet side of the Proctor curve), the microstructure is seen to be in a dispersed state. The flocculated state gives rise to a bimodal PSD, with peaks in micro- and macroporosity, which are associated with intra-aggregate and inter-aggregate pores, respectively. In contrast, the dispersed state exhibits a monomodal PSD with a peak in microporosity, resulting from the relatively high moisture content and merging of aggregates. This indicates that compacted clay powders typically exhibit a bimodal pore size distribution, as they are typically compacted with a water content that is lower than the optimal value (dry side). The wetting of fine-grained soils with an initially flocculated state results in a reduction in the diameter of the dominant pore fraction of macropores, while maintaining a bimodal PSD. This reduction is associated with the swelling of particles (an increase in interlayer distance) into the intra-aggregate space. The influence of the wetting process on the micropores is small (Alonso et al., 2013b).

At the next higher level of microstructure, dispersed or aggregated structures can again be distinguished according to their contact surfaces. The contacts can be either on the edges or on the faces of the minerals and can be edge-to-edge or edge-to-face. This is illustrated in Fig. 2.7. However, Cetin et al. (2007) observed that edge-to-edge contacts dominate in the very dry state, change to edge-to-face contacts with slowly increasing water content and result in face-to-face contacts (deflocculated) near the optimum water content.

When working with compacted clay powder which was previously ground from intact clay shale, the original microstructure is destroyed. A new fabric is produced by compacting, while the bonding is destroyed and remains so.

2.1.3.2. Structure of clay shales

The formation of the microstructure of clay shales is influenced by a number of additional factors that are not as significant in the case of compacted clays. The most evident factor is time. For example, the Callovian-Oxfordian (COx) and OPA formations are es-
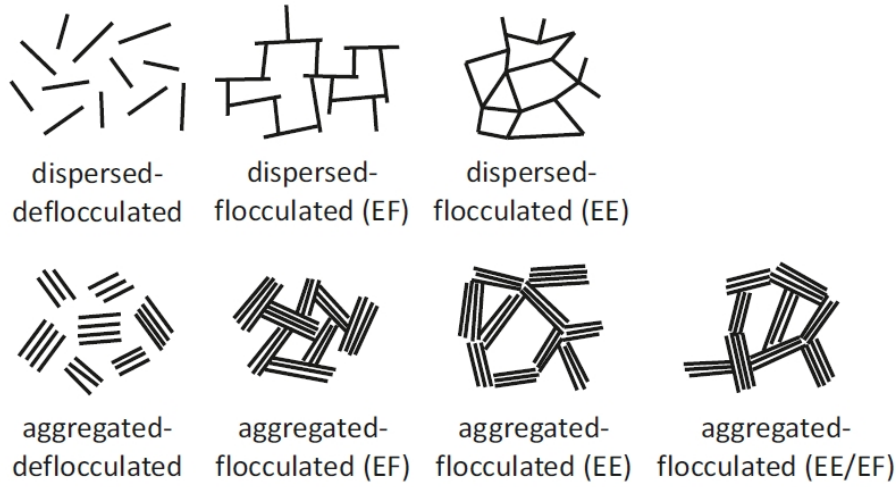
Figure 2.7.: Contact modes of dispersed and aggregated structures from Baille (2014).

timated to be approximately 164 and 174 million years old, respectively. Consequently, the importance of bonding increases.

According to Benett et al. (1991), the formation of the microstructure of clay shales can be attributed to three groups of processes: physico-chemical, bio-organic and burial-diagenesis. Physico-chemical processes are those which bring particles together in aggregates, hold, break and reorient them. The corresponding mechanisms are electrostatic interaction and chemical bonding, thermally driven movement of particles and interactions at the contact surfaces between different materials and phases. Bioorganic processes are the direct effects of living organisms and the indirect effects of organic materials that they may produce. Related processes include mechanical alterations of the fabric as a result of the activities of organisms, particle binding through polymer bridging, and changes in the microenvironment due to metabolic activities of organisms which can result in breakage of the aforementioned polymer bridging and formation of pyrite. Burial diagenesis processes are alterations of the fabric that occur subsequent to the deposition of the material. Main mechanisms are the mass gravity stresses within the deposit including creep and deformations besides consolidation and compaction, and diagenesis-cementation like mineral alteration, cementation, leaching and clay gas interactions.

Clay shales typically exhibit pronounced anisotropy, which is attributed to burial diagenesis and significantly influences the mechanical, hydraulic, and thermal properties of the material (Minardi et al., 2016; Bossart et al., 2017b; Gens et al., 2017; Favero et al., 2018; Wild and Amann, 2018). It is therefore crucial to consider the orientation of the bedding planes in both experimental investigations and numerical simulations. A sec-

ond feature of clay shales of high relevance is their notable inhomogeneity. As observed by Seiphoori et al. (2017), scanning electron microscopy (SEM) micrographs of Opalinus clay revealed the presence of numerous calcareous microfossils and non-clay particles dispersed throughout the shale matrix. The observed microfossils are predominantly calcareous foraminiferan shells. The non-clay particles are iron pyrite, which are characterised by prominent framboidal crystals and occur either individually or as aggregates. These microscale inhomogeneities can result in significant discrepancies in the outcomes of laboratory tests conducted on samples obtained merely a few centimetres apart. Furthermore, Kneuker and Furche (2021) demonstrated that the lithological variability of Opalinus clay is greater in the direction perpendicular to the bedding plane orientation than parallel. At the meso- and macro-scales, the presence of quartz lenses, fossils and fissure zones contributes to the observed inhomogeneity of the material (Orellana et al., 2022).

The PSDs of clay shales typically exhibit a monomodal distribution, with the majority of pores lying in the microporosity range. This is attributed to the highly dense clay matrix, as evidenced by previous studies (Mohajerani et al., 2011; Seiphoori et al., 2016). It should be noted that peaks in macroporosity can also occur as an exception to the rule. Such phenomena are attributable to microfissures, which may be caused by a number of factors, including drying-induced shrinkage or unloading (Pineda et al., 2014). The experimental determination of the PSD, which is presented in Section 4.3.2.2, is particularly prone to error in the case of clay shales, given that the pore space is, according to Keller et al. (2013), poorly connected.

2.2. Soil suction

The term soil suction is defined in Wilson (2020) as the suction required to remove water from a soil. This is largely made up of the matric potential, which is the force that holds water in soil pores by capillary action, and the solute potential, which is the osmotic effect of dissolved salts. The concept has its origins in soil sciences, with its earliest formulations dating back to the work of Buckingham (1907). However, it has since then gained significant traction in the field of geotechnical engineering, particularly with the advent of unsaturated soil mechanics in the 1980s. Soil suction is a quantifiable state variable that serves as the foundation for the assessment of gradients driving water flow in soils and other fine-grained materials, as well as the characterisation of soil-water retention behaviour.

2.2.1. Suction components

In accordance with the aforementioned definition, the total soil suction (ψ_{tot}) is comprised of two distinct components, namely matric suction (ψ_m) and osmotic suction (ψ_o):

$$\psi_{tot} = \psi_m + \psi_o \qquad (2.12)$$

As outlined in Lu and Likos (2004), matric suction represents the component of total suction associated with the interactions between the soil water and the soil matrix. The ratio of the partial pressure of water vapour to the vapour pressure of water is defined as the relative humidity. The curved surface of soil water within pores is a consequence of the capillary effect, which is known as the contractile skin. In contrast, the same water has a flat surface when it is stored in a large container. Additionally, the partial pressure of water vapour above a curved surface of soil water is less than that above a flat surface of soil water. These two facts result in a reduction in the relative humidity of the soil. Moreover, the relative humidity is observed to decrease with a reduction in the radius of the curved soil water, with this radius being inversely proportional to the difference between the air and water pressure (Fredlund and Rahardjo, 1993). Thus, the matric suction can also be expressed as follows:

$$\psi_m = u_a - u_w \qquad (2.13)$$

where u_a is the pore-air pressure and u_w is the pore-water pressure.

The concept of osmotic suction encompasses the general presence of dissolved salts in soil water. The water vapour pressure above the surface of a saline solution is less than the vapour pressure above the surface of pure water. The osmotic suction can be derived from the ratio of these two quantities. Accordingly, the relative humidity is observed to decrease in conjunction with an increase in the salt content of the soil water. This concept is illustrated by the definition provided by Aitchison (1965), which states that the osmotic suction is equal to the negative pressure to which a pool of pure water must be subjected in order to be in equilibrium with a pool containing water of the soil water composition through a semi-permeable membrane.

2.2.2. Soil-water retention behaviour

A soil-water characteristic curve (SWCC) is determined experimentally and indicates the relationship between the amount of water retained by a soil and the applied suction.

The amount of water is typically expressed as the volumetric water content or degree of saturation.

A schematic SWCC is outlined in Baille (2014) and illustrated in Fig. 2.8. The degree of saturation is plotted on the vertical axis versus the logarithmic suction represented on the horizontal axis. Point A represents the beginning of the initial drying curve with $S_r = 1$. The range between points A and B indicates a state of complete saturation. Only from point B air begins to intrude into the soil, which is why the corresponding suction ψ_{AEV} is referred to as the air-entry value (AEV). However, another widely used definition of the AEV is also the suction that separates the saturated zone from the desaturation zone, but is determined by the intersection of a tangent at the inflection point of the SWCC and the horizontal at $S_r = 1$ (Wijaya et al., 2015; Pasha et al., 2016). The desaturation zone, in which the water phase is continuous, extends until point C. At point C, with the corresponding suction ψ_{res}, the residual zone begins, in which the air phase is assumed to become continuous and the water phase discontinuous. Point D represents the suction at which $S_r = 0$. A further wetting of the soil will lead to the grey main wetting curve. As a consequence of entrapped air that occurs during the initial drying process, it is not possible to reach point A again. It is therefore the grey main drying path that will prove decisive for future considerations. The area between the main wetting and main drying curve is a consequence of hysteresis effects.
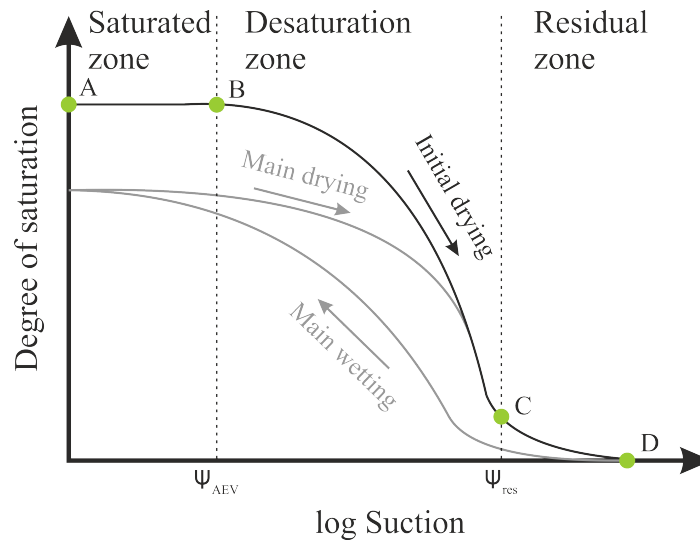

Figure 2.8.: Schematic SWCC modified after Baille (2014).

In order to determine SWCCs, usually a minimum of two methods are combined to cover the entire suction range: the axis translation technique (ATT), which is employed for

suctions up to 1.5 MPa and the vapour equilibrium technique (VET), which is used for suctions above 3 MPa. The osmotic method (OM) is another widely-used method that overlaps the suction ranges of both techniques (100 kPa to 10 MPa) and can therefore be considered a valuable addition (Kassiff and Shalom, 1971; Delage et al., 1998).

For the ATT, the soil samples are placed directly on a porous ceramic plate within a pressure plate apparatus. The ceramic plate is saturated with water and connected to a burette. This means that the pore water within the sample is in direct contact with the water within the ceramic plate and the burette. A water pressure u_w can be applied to the sample from below via the height of the water column in the burette. In the pressure plate apparatus, a regulated air pressure u_a is applied via an external compressed air system. The suction acting on the sample is a result of the difference between the air pressure and water pressure, and is therefore a matric suction as shown in Eq. 2.13. The maximum suction that can be applied in the ATT is contingent upon the pore size of the porous ceramic plate, thereby defining the maximum air pressure that can be applied without air entering the ceramic plate.

In the osmotic method, the soil sample is separated from a solution of polyethylene glycol (PEG) by means of a cellulosic, semipermeable membrane. The macromolecules present in the PEG solution tend to undergo hydration, thereby exerting a negative water pressure since they can not penetrate the membrane. Consequently, the water from the soil sample is attracted (Fleureau et al., 1993). The magnitude of the negative pressure can be regulated by modifying the concentration of PEG in the solution. Assuming that the osmotic suction of a salt solution is solely a function of the molecules present in the solution and thus linear, the simplified van't Hoff equation can be used to calculate the resulting suction (Steuter, 1981):

$$\pi = RTc \tag{2.14}$$

where π is the osmotic suction, R the universal gas constant, T the absolute temperature and c the mass ratio polymer/solution.

Nevertheless, assuming that this direct correlation is not correct due to different hydrodynamic, thermodynamic and other effects, modifications exist that take into account the non-linearity between the concentration of the PEG solution and the resulting suction. These highly precise approaches are exceedingly inconvenient as virial coefficients have to be determined experimentally, so that most recently a simplified approach has been introduced in Lieske et al. (2020):

$$\pi = RTc^* \left(\frac{1}{M_n} + \Gamma \cdot c^* \right) \tag{2.15}$$

where c^* is the mass ratio polymer/water, M_n the number average molar mass (the average mass of polymer chains in a sample) and Γ an empirical coefficient.

Delage et al. (1998) were among the first to transfer the VET from soil science to geotechnical engineering. In this process, the originally used sulphuric acid in soil sciences was replaced with salt solutions for safety reasons. In the VET, soil samples are placed in closed desiccators above different oversaturated salt solutions. The salt solution serves to regulate the relative humidity within the desiccator, thereby exerting a suction on the soil samples. The imposition of different relative humidities is achieved through the utilisation of diverse salt solutions. The resulting suction of a certain combination of temperature and relative humidity can be calculated using the Kelvin equation:

$$\psi_{tot} = -\frac{RT}{v_{w0}w_v}ln\left(\frac{u_v}{u_{v0}}\right) \tag{2.16}$$

where R is the universal gas constant, T is the absolute temperature, v_{w0} is the specific volume of water, w_v is the molecular mass of water vapour, u_v is the partial pressure of pore-water vapour and u_{v0} is the saturation pressure of water vapour above pure free water at the same temperature. $\frac{u_v}{u_{v0}}$ equals and thus can be replaced by the relative humidity RH.

A variety of analytical equations may be employed to model experimentally determined SWCCs. The most well-known models are the models proposed by van Genuchten (1980) and Fredlund and Xing (1994), as presented in Eq. 2.17 and Eq. 2.18, respectively. Both models have been shown to yield satisfactory results when fitted with experimental data. According to general experience, the range between 0.5 and 40 MPa can be adequately covered.

van Genuchten (1980):

$$\theta = \theta_r + \frac{\theta_s - \theta_r}{[1 + (\alpha\psi)^n]^m} \tag{2.17}$$

Fredlund and Xing (1994):

$$\theta = \theta_s \left[\frac{1}{\ln[e + (\psi/a)^n]}\right]^m C(\psi) \tag{2.18}$$

where θ is the volumetric water content, θ_r the residual volumetric water content, θ_s the saturated volumetric water content, m, n, a, α are soil/ fitting parameters and ψ is the total suction. $C(\psi)$ is a correction function defined as

$$C(\psi) = \frac{\ln(1 + \psi/\psi_r)}{\ln[1 + (1,000,000/\psi_r)]} \tag{2.19}$$

where ψ_r is the suction corresponding to the residual water content θ_r.

2.3. Swelling tests and modelling

The aforementioned swelling mechanisms of clay at the micro level manifest themselves at the macro level in two different ways, depending on the volumetric boundary conditions: swelling pressure at volume constrained conditions or swelling strain for unconstrained conditions. The swelling strain and the swelling pressure of a clay are summarised in the literature as swelling potential or swelling capacity. Nevertheless, while experimental studies conducted in laboratory settings predominantly focus on examining those extreme boundary conditions, in practical geotechnical applications, coupled processes often play a more significant role. This suggests that, at a given stress level, limited volumetric deformations may occur. It is therefore of interest to establish a direct correlation between swelling pressure and swelling strain. This correlation can be expressed through the use of swelling laws. In order to ascertain the swelling pressure and swelling strain, as well as their interaction in a laboratory setting, a number of different methods exist, which are presented in the following sections.

2.3.1. Sample preparation of artifically compacted and field samples

It is important to distinguish between the determination of soil swelling properties on artificially produced reconstituted samples and on intact samples obtained from the field with minimal disturbance. While reconstituted samples in the literature are predominantly compacted bentonites, which are employed as sealing elements in contexts such as disused salt mines or radioactive waste repositories, and are therefore to be tested for suitability, samples from the field are tested with the objective of estimating the additional loads acting on underground structures such as tunnels. Compacted samples can usually be produced directly in the ring of the experimental apparatus using a hydraulic jack or any other press. Thus, they are more flexible in production and can be produced with precisely defined initial boundary conditions as often as desired.

The utilisation of intact field samples introduces novel possibilities and constraints pertaining to the laboratory assessment of swelling properties, which must be taken into account when designing appropriate experiments. In general, the same tests that are conducted on artificially produced samples can also be carried out on field samples. It is recommended that tests requiring only a single sample be conducted, as it is challenging to obtain multiple field samples with identical initial conditions. In materials that have been deposited, a number of naturally occurring variations can be observed, including

changes in the void ratio, water content and mineralogical composition. However, more pronounced inhomogeneities, such as quartz lenses, biological residues, pyrite or fossils may also be present. In the case of anisotropic materials, such as heavily overconsolidated marine sediments (e.g., clay shales), the direction of sampling is also of significant importance. The material properties can be studied perpendicular, parallel or oblique with respect to the bedding plane direction, provided that the appropriate angle is employed during the sampling process. The orientation of the sample has an impact on the mechanical, hydraulic and thermal behaviour of the material, as well as all possible coupled combinations of these. To investigate the anisotropy of the swelling strain on a single sample, cubic samples can be obtained directly from the drill cores with a band or rock saw. The direction of the bedding planes is taken into account in order to ensure that the final sample comprises four surfaces parallel to the bedding planes and two surfaces perpendicular to them.

The preparation of samples from the field for test devices with stiff sample rings represents a more challenging process, typically involving the extraction of specimens from drill cores, which must be precisely fitted within the ring of the device. In technical recommendations, this is frequently described as a 'snugly fit'. The International Society for Rock Mechanics (ISRM) proposes in Madsen (1999) a press and a trimm ring. This method is applicable to stiff clays, but not to clay shales or clay rocks. In the case of clay shales such as OPA, as studied in this work, the procedure proposed by the Deutsche Gesellschaft für Erd- und Grundbau (DGGT) is more appropriate. In DGGT (1986), the utilisation of a lathe is advised to obtain the exact diameter from the drill cores for a perfect fit into the ring. This allows for the preparation of a longer cylindrical sample with a precise diameter, which can then be cut into several samples of the required height using a band saw or rock saw. In general, all preparation works must be carried out with air flushing or other anti-swelling admixtures in order to prevent the initiation of the swelling process.

2.3.2. Laboratory set-ups for determining swelling properties

In their study, Sridharan et al. (1986) outline three fundamental techniques for measuring the maximum swelling pressure of soils using conventional oedometer cells. These are: 1. 'From the Conventional Consolidation Test', 2. 'Method of Equilibrium Void Ratios for Different Consolidation Loads' and 3. 'Constant Volume Method'. The schematic curves of the three aforementioned methods in the stress-strain plane are illustrated in Fig. 2.9. The initial state for all three methods is indicated with a red star.

In the case of method 1, 'From the Conventional Consolidation Test', a common oedo-metric consolidation test set up can be used. The sample is placed in the oedometer ring with specific initial conditions (dry density, water content) and subjected to a minimum necessary dead weight load. Subsequently, the sample is saturated with water, thereby initiating a swelling process, until an equilibrium heave is reached. From this equilibrium state, the sample is subjected to incremental loading. At each load step, the consolidation of the sample is observed, with the subsequent load step being applied once the sample has reached equilibrium. In Fig. 2.9, curve 1 illustrates the progression of a test involving a total of seven load steps following the initial swelling. The corresponding swelling pressure (σ_1) is the interpolated value where the initial height of the sample is obtained again, and thus the strain is zero. The test provides supplementary data on the consolidation behaviour of the material and can be conducted with a single sample, thus making it suitable for in-situ samples from the field. Moreover, a correlation between swelling pressure and swelling strain can be derived from the data, thereby providing a foundation for a potential swelling law. The determined swelling pressure is higher than that obtained by methods 2 and 3. This test setup is also suitable for determining the maximum swelling strain of a soil. The maximum swelling strain is the strain of the material in the first test step, i.e. the saturation of the material under the lowest necessary load.

Method 2 entails the examination of at least three distinct samples separately. Each sample is installed in the oedometer device under identical initial conditions and subsequently subjected to a different load. Once consolidation of the samples has been completed, the addition of water initiates a swelling process until an equilibrium strain is reached. A trend line is then added to the equilibrium values of the individual tests in order to be able to obtain the swelling pressure. The swelling pressure is again equivalent to the interpolated value of the stress at which the strain equals zero. The determined swelling pressure with this method is rather low. Given that at least three samples with identical initial conditions are required to perform this method, it is not suitable for testing undisturbed in-situ samples. This method is particularly unsuitable for soils with frequently occurring inhomogeneities, such as heavily overconsolidated marine sediments.

In method 3, a single sample is placed within the oedometer apparatus and water is introduced directly. The swelling strain is regulated by adding loads, with the objective of maintaining the resulting strain at a value close to zero. This process is repeated throughout the duration of the experiment, resulting in the numerous peaks observed in curve 3a in Fig. 2.9. As can be observed, compression occurs in close proximity to the equilibrium state. The interpolated pressure value at which the strain is zero for the final load step

represents the final swelling pressure. It is essential to conduct continuous monitoring and to implement regular manual intervention throughout the process. However, in comparison to the other methods, it is relatively fast to perform and necessitates only a single sample.

In recent years, the use of specially manufactured constant volume swelling pressure cells has become increasingly prominent in the determination of the maximum swelling pressure of swellable soils, which is referred to here as method 3b in Fig. 2.9. The uniform increase in swelling strain which can be observed is a consequence of the self-deformation of the apparatus and load cell as a result of the increasing swelling pressure. The use of constant volume swelling pressure cells is more convenient and results in a high degree of reproducibility. In the literature, different authors have presented experimental set-ups that focus on different details, which are adapted to particular applications, for example highly dense bentonites and thus high swelling pressures (Khan, 2012), temperature cycles (Sau, 2021), high salt concentrations of the used fluids (Komine et al., 2009) or a combination of them (Chen et al., 2019). Thereby, individual aspects, such as the temperature control in Chen et al. (2019) and Sau (2021), are implemented in different ways. The former entails regulating the temperature changes of the sample by placing the entire cell within a tank filled with silicone oil and controlling the temperature of the silicone oil with a thermostat and heating rod. In the second, temperature control is achieved through the use of an electrical heating element, which is situated in close proximity to the sample within the sample ring. Constant volume swelling pressure cells are highly individual devices, typically designed and constructed for a specific application.

In order to establish a correlation between the swelling pressure and strain and to derive a swelling law, Huder and Amberg (1970) proposed an additional test procedure in oedometer cells. The original study was conducted with Opalinus clay and Gipskeuper, both from the Belchen Tunnel in northern Switzerland. A schematic representation of the test is provided in Fig. 2.10. For this purpose, beginning from point P_0, the sample is first subjected to a defined load σ_a (Path I), subsequently unloaded (II) to a minimum load σ_c and loaded again (III) up to σ_a. This procedure is intended to partially compensate for the influence of extracting the sample from a great depth and to ascertain the material behaviour without introducing water during loading and unloading. Afterwards, the sample is saturated, resulting in a heave (IV). Once equilibrium has been reached, the sample is stepwise unloaded (V) up to σ_c. The point $\sigma_{z,q0}$ is the intersection between the extrapolated curves III and V and represents the pressure necessary to eliminate swelling. This procedure illustrates the influence of the preloading steps (I, II and III) on the final
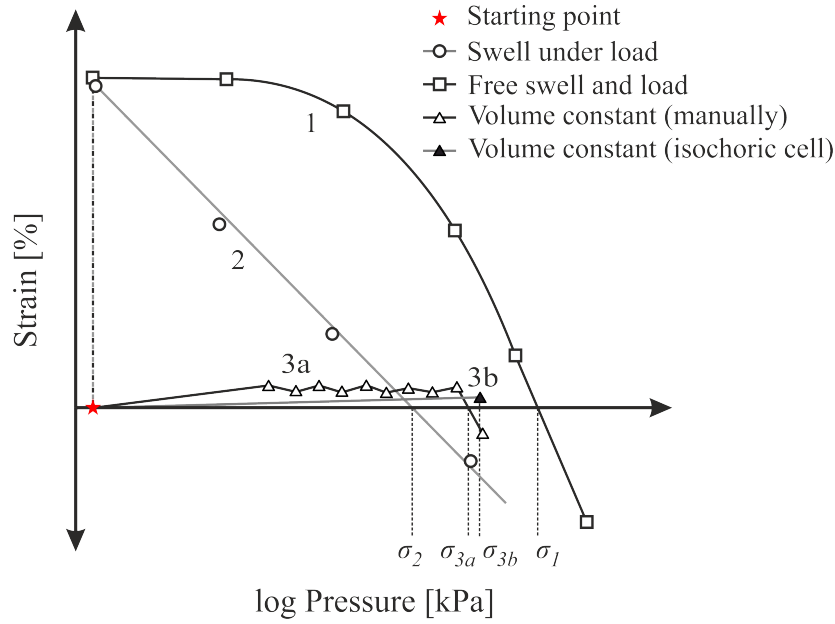
Figure 2.9.: Schematic curves of different tests for swelling pressure determination, modified after Sridharan et al. (1986).

swelling pressure. In the absence of these steps, the determined swelling pressure from loading subsequent to free swelling would be σ_0. The ISRM likewise proposes a comparable procedure. However, in this instance the sample is subjected to a single loading phase prior to saturation. This means that there is no additional unloading and reloading. Subsequently, the sample is saturated and the applied load is stepwise reduced.

An alternative and more specialised device is presented in Pimentel (1996) which is capable of determining the swelling pressure to swelling strain relationship of a soil with a similar procedure but in a more convenient way. The device has been employed over time and has undergone modifications in accordance with the experience gained in Vergara et al. (2014) and Vergara (2019). The device facilitates conducting stress or strain controlled swelling tests. It consists of a rigid frame and a sample ring, which holds the sample between two porous stones and is placed in a container that can be filled with water for the saturation process. Constant volume conditions or controlled deformations are ensured by a spindle at the top of the cell. The pressure is measured with a load cell situated at the bottom plate, while deformations are measured in its original form at the top of the spindle with a dial gauge and in its modified form with two dial gauges between the loading plate and the bottom of the container with the sample, thus eliminating the potential self-deformation of the device from the measured strain. The device permits the examination of stress-strain paths comprising constant volume swelling, followed by
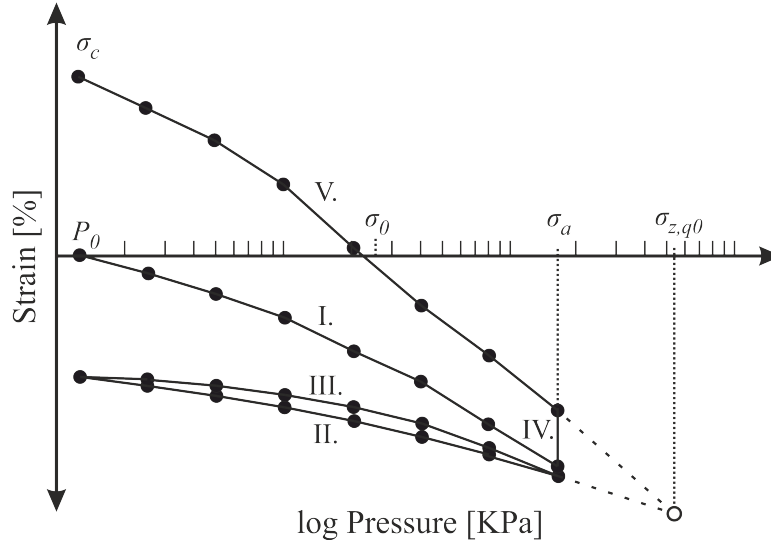
Figure 2.10.: Schematic curve of a Huder & Amberg swelling pressure test, modified after Gattermann (1998).

a stepwise unloading. In contrast to other comparable test procedures proposed in Huder and Amberg (1970) and Madsen (1999), the recommended procedure does not provide a pre-loading. A more detailed comparison of the aforementioned test types, including the one from the current study, can be found in Chapter 4.3.4.4.

In order to determine the swelling strain of intact field samples, it is also feasible to examine cubic samples. This approach offers the advantage that the anisotropy during swelling can be examined directly on a single sample, while simplifying the sample preparation as no stiff ring is required. The swelling strain can be measured simultaneously in three directions on these cubic samples, for example with linear variable differential transformers (LVDTs), provided that the displacements in the other three directions are fixed. Experimental set-ups of this nature are commonly employed in rock mechanics and can be found in the literature for example in Wild et al. (2017), Crisci et al. (2018) or Vergara (2019). As Pimentel (2015) notes, ensuring that the sample does not disintegrate during saturation represents a significant challenge. To avoid this issue, the rate of saturation must be strictly controlled.

However, the latest recommendation from the ISRM in Madsen (1999) suggests an alternative experimental setup, replacing the testing of a cubic sampleby that on a cylindrical sample. The vertical deformation is measured with a dial gauge, while the radial deformation is measured with a stainless steel band. Pimentel (2015) observed that this approach presents challenges in accurately measuring deformations. Measured deformations in both

directions should be in the same order of accuracy, which is not the case with the combined use of a dial gauge and a stainless steel band. Schematics of the experimental set-ups recommended by the ISRM for determining the swelling pressure, swelling strain, and swelling pressure as a function of strain can be seen in Fig. 2.11.

1) stainless-steel ring, 2) porous metal plates, 3) stainless-steeel loading plate, 4) container, 5) dial gauges, 6) load measuring device, 7) rigid frame, 8) loading piston, 9) stainless-steel plate, 10) container, 11) dial gauge, 12) glass plate, 13) stainless-steel band, 14) sample, 15) stainless-steel ring, 16) porous metal plates, 17) stainless-steel loading plate, 18) container, 19) dial gauge, 20) loading frame

Figure 2.11.: Proposed methods by the ISRM in Madsen (1999) for determining the axial swelling stress (a), the swelling strain (b) and axial swelling stress as a function of axial swelling strain (c).

2.3.3. Analytical swelling laws

A number of analytical approaches have been developed in the literature with the objective of describing the relationship between swelling-induced stresses and strains. The first swelling law in this regard was formulated by Grob (1972) on the basis of the previously conducted experiments by Huder and Amberg (1970). It was originally derived for marl, clay shales and anhydrite-bearing rocks. Some authors, such as Kirschke (1995), Pimentel (2007) or Butscher et al. (2018), have expressed doubt as to the validity of the swelling law for the latter, citing ambiguity in the underlying data as a reason for this scepticism. However, given that clay shales are considered in this study, this specific criticism will not be addressed further here.

The swelling law proposed by Grob (1972) is a semi-logarithmic swelling function, which consequently results in a linear relation between the swelling strain and the logarithmic

pressure. This is illustrated in Fig. 2.12a and can be formulated as:

$$\varepsilon = -k \left(\log \frac{\sigma}{\sigma_0} \right) \tag{2.20}$$

where ε is the swelling strain, k a material parameter describing the slope of the strain-log pressure line, σ the swelling pressure and σ_0 the maximum swelling pressure at constant volume conditions, i.e., $\varepsilon = 0$.

Kiehl (1990) incorporated the temporal aspect of swelling processes and extended the formulation to the three-dimensional space, a topic that will not be addressed here. Reduced again to the one-dimensional case, this results in the swelling law with additional consideration of the time t in Fig. 2.12b as stated in von Wolffersdorff and Heidkamp (2005). Consequently, σ_c is a minimum stress below which no further increase in swelling occurs. The strain for $t = \infty$ corresponds analogously to Eq. 2.20 to:

$$\varepsilon_{z\infty,max}^q = -k \left(\log \frac{\sigma_{z,\infty}}{\sigma_{z,0}} \right) \tag{2.21}$$

where $\varepsilon_{z\infty,max}^q$ is the equilibrium swelling strain at $t = \infty$ for the particular load of $\sigma_{z,\infty}$.

By introducing the specific time $\hat{t}$ as a time unit independent of the layer thickness of the swelling material, the influence of the time in this swelling law was addressed. This approach enables the determination of the swelling strain at any given time through the application of the following equation:

$$\varepsilon_z^q(\hat{t}) = -k \cdot \ln \frac{\sigma_{z,\infty}}{\sigma_{z,0}} \left[1 - \exp\left(-\frac{\hat{t}}{\eta_q} \right) \right] \tag{2.22}$$

where η_q is a reference time from laboratory heave tests.

In order to calculate the specific time $\hat{t}$, which takes into account the influence of the thickness of a swellable layer, a power approach is proposed for one-dimensional modelling:

$$\hat{t} = t \cdot \left(\frac{d_M}{d_P} \right)^n \tag{2.23}$$

where d_M is the thickness of the studied sample in the laboratory, d_P the thickness of the swellable layer to be considered in the field and n captures the usually unknown water permeability in-situ by controlling the transfer of the time from the laboratory test to the in-situ case.

The temporal development of the swelling process is strongly dependent on the permeability, which cannot be reliably predicted in the field due to the presence of inhomogeneities

and fissures, among others. In order to circumvent this issue, the standardised dimension-less water content ω has been proposed as a substitute (Gattermann, 1998; Wittke, 2003; Wittke et al., 2004). In this concept, the authors conducted a comprehensive investigation into the prediction of swelling processes in tunnelling, with a particular focus on their practical applications in engineering. The swelling law, which considers the dimensionless water content ω, is illustrated in Fig. 2.12c and can be formulated as follows:

$$\varepsilon_z = k(\omega) \cdot \left(\log \frac{\sigma_z}{\sigma_{z,0}(\omega)} \right) \tag{2.24}$$

where $k(\omega)$ and $\sigma_{z,0}(\omega)$ are again the material parameter describing the slope of the strain-log pressure line and the maximum swelling pressure at constant volume conditions, but both in dependence of ω.

Thereby, ω is defined as:

$$\omega = \frac{w - w_0}{w_{sat} - w_0} \tag{2.25}$$

with the actual water content w, the water content at $\sigma_z = 0$ as w_0 and the water content in the fully saturated state w_{sat}. Thus, ω is ranging from 0 to 1, which means dry to saturated.

Laboratory tests demonstrated a linear correlation between water content and swelling pressure, resulting in the following equation for the swelling pressure depending on the water content considering ω:

$$\sigma_z = \omega \cdot \sigma_z(w_{sat}) \tag{2.26}$$

In general, swelling laws based on Grob's formulation demonstrate a high degree of correlation with the swelling pressures of clay shales in laboratory tests (Wittke et al., 2004). Nevertheless, Dobrowolsky (2008) introduced further considerations regarding a swelling law for the volume change behaviour of fine-grained soils due to moisture changes. The swelling law is illustrated in Fig. 2.12d and includes both swelling (SW) and shrinkage (SW) paths. The curve intersects the x-axis at a value σ_{max}^{SW}, which describes the maximum swelling pressure of the sample as a function of the void ratio and the degree of saturation. Desaturation and an associated reduction in swelling pressure can always occur and are reversible, i.e. the exact previous state can be achieved again after another saturation and associated swelling. This refers to the SN path. This demonstrates that shrinkage $\Delta\varepsilon^{SN}$ can only occur after the corresponding swelling pressure $\Delta\sigma^{SN}$ has been dissipated.

The volume change behaviour can be described with the following equations for spatial stress conditions:

$$I_\varepsilon^{SW} = I_{\sigma,max}^{SW}(e_0, S_{r,0}, S_{r,\infty}) \cdot f_1(I_\sigma) \qquad , \ I_{\sigma c} \leq I_\sigma \leq I_{\sigma,max}^{SW} \qquad (2.27)$$

$$I_\varepsilon^{SW} = 0 \qquad\qquad\qquad , \ I_\sigma > I_{\sigma,max}^{SW} \qquad (2.28)$$

where I_ε^{SW} is the swelling strain, $I_{\sigma,max}^{SW}$ is the maximum swelling pressure at constant volume conditions as a function of the initial void ratio e_0, initial degree of saturation $S_{r,0}$ and degree of saturation $S_{r,\infty}$, and I_σ is the current stress state.

A seperable partial differential equation including the atmospheric pressure p_a is given by:

$$I_{\sigma,max}^{SW} = p_a \cdot f_2(S_{r,0}) \cdot f_3(e_0) \cdot f_4(S_{r,\infty}) \qquad (2.29)$$

Overall, it can be noted that as the complexity of the swelling laws increases, more details can be taken into account, but the ease of use decreases as a result.

Constitutive models have been developed to simulate the hydro-mechanical behaviour of partially saturated soils, including the swelling processes. As numerical simulations are not within the scope of this study, they are not discussed in detail here. Noteworthy examples are the formulations according to Anagnostou (1993) or the work of Alonso et al. (1990) enhanced by Gens et al. (1995). Alonso et al. (1990) introduced the Modified Cam-Clay based Barcelona Basic Model (BBM), which is designed to reproduce the characteristics of the soil mechanical behaviour of unsaturated and slightly or moderately expansive soils, including sands, silts and low plasticity clays. These characteristics include an increase in shear strength and stiffness with an increase in suction; the volumetric response of unsaturated soils to changes in stress and suction, including a differentiation in elastic and plastic components; and the possibility of a volumetric expansion or collapse of the soil due to a decrease in suction (wetting of the soil). In Gens et al. (1995) the BBM is enhanced by incorporating the influence of temperature on unsaturated soils to the thermo-elasto-plastic Barcelona Basic Model (BBM-TEP). Therein, findings from Hueckel and Borsetto (1990) are adopted. The model is designed to reproduce two additional effects, which are a reduction of the yield surface for increasing temperatures (softening) and, vice versa, an enlargement of the yield surface with increasing suction (hardening). This numerical framework is most known for its application in the THM-analysis of clay barriers that are used to isolate high-level radioactive waste in the FEBEX mock-up test (Sánchez et al., 2012).
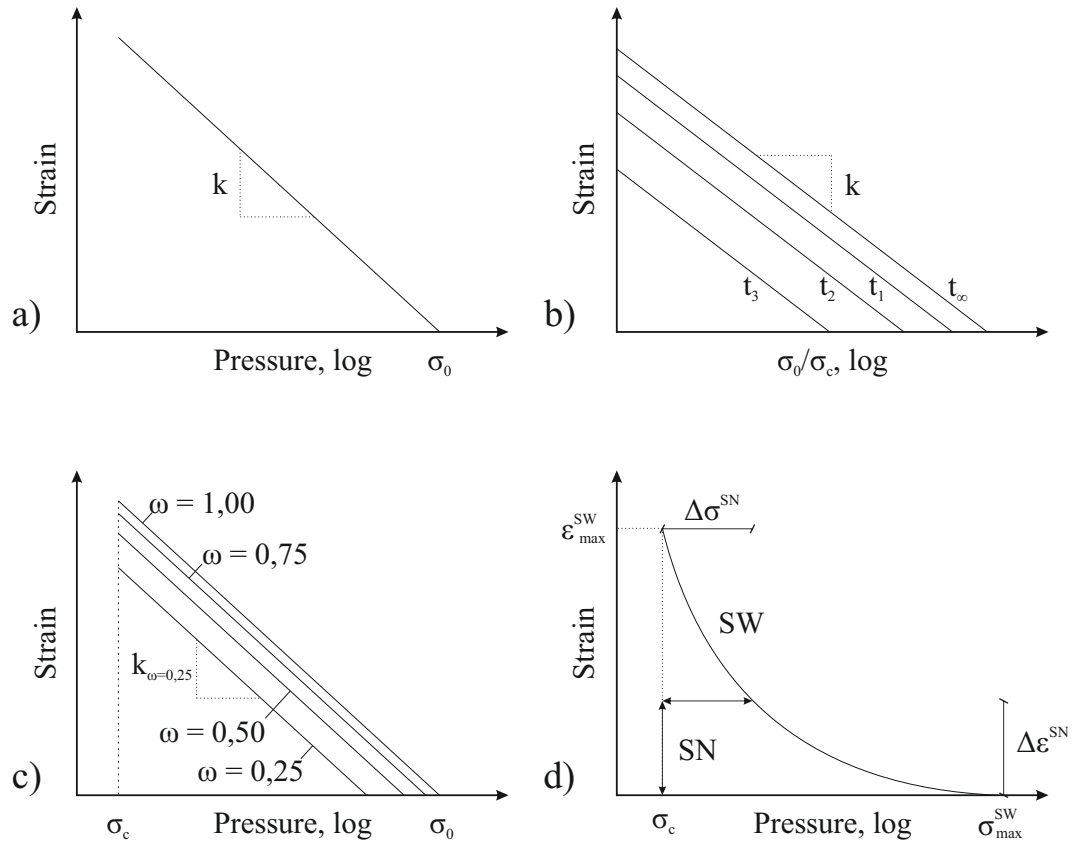
Figure 2.12.: a) Swelling law according to Grob (1972), considering b) time (Kiehl, 1990; von Wolffersdorff and Heidkamp, 2005), c) unsaturated states (Wittke et al., 2004) and d) a further approach by Dobrowolsky (2008) focusing on swelling and shrinkage of fine grained soils.

2.4. Laboratory testing on Opalinus clay shale

Extensive investigations have been carried out on Opalinus Clay, which has been selected as the host rock for the disposal of radioactive waste in Switzerland. Over the past 25 years, a multitude of studies have been conducted to gain a deeper understanding of the geology, mineralogy, rock chemistry, porewater chemistry, petrophysical, hydraulic and rock mechanical parameters associated with this material (Bossart and Thury, 2008; Bossart and Milnes, 2018). An essential element of this was in the hydro-mechanical field the experimental analysis of the swelling capacity of OPA. A brief summary of laboratory tests in this context is presented in Table 2.1. The initial work in this field was conducted by Huder and Amberg (1970), who developed a novel experimental protocol for the determination of the swelling pressure of clay shales in oedometer cells (as introduced in Section

2.3.2). In order to partially compensate for the influence of the sample being taken from a considerable depth, loading, unloading and reloading steps were conducted prior to the saturation of the sample. Once equilibrium heave was achieved, the sample was unloaded in a stepwise manner. The point of intersection between the extrapolated unloading curve following saturation and the reloading curve represents the pressure required to prevent swelling, and is therefore defined as the swelling pressure. Grob (1972) employed the same protocol and Bock (2001) a similar protocol without the unloading and reloading steps as proposed by the ISRM in Madsen (1999). For all other swelling pressure tests, isochoric cells with attached load cells were used. The values of the swelling pressure generally fall within a range from 0.5 to 5.5 MPa. The pronounced anisotropy in the hydro-mechanical behaviour is evident in these tests. The swelling pressure parallel to the bedding plane is consistently lower than that perpendicular to it. It is not possible to identify a clear trend with respect to the swelling pressure over the sampling depth or the amount of clay content. This demonstrates the inhomogeneity and variability of the material. The utilisation of vapour, deionised or synthetic pore water for saturation has an impact on the experimental outcomes. In all tests involving water saturation, synthetic pore water was employed.

The results of the swelling strain tests exhibit a comparable pattern. The strains in the direction perpendicular to the bedding are consistently greater than those in the direction parallel to it. This observation has been made in three-dimensional tests on cubic samples (Wild et al., 2017) and in one-dimensional tests with uniaxial strain conditions (Bock, 2001; Zhang et al., 2010). Compacted powder produced from drilling cores from Mont Terri was investigated in Nitsch et al. (2023) for initial dry densities of approximately 1.9 g/cm^3. Grob (1972) used the procedure proposed by Huder and Amberg (1970) to derive a stress-strain correlation. This correlation could not be derived in the other studies using isochoric cells for volume-constant swelling tests. Sridharan et al. (1986) demonstrated that the two procedures yield disparate results of the maximum swelling pressure due to the divergent evolution of microstructure. Furthermore, the stress-strain correlation will be different when unloading subsequent to an initial volume-constant swelling, given that the volumetric swelling is initiated at differing initial microstructures. Considering the procedure outlined by Huder and Amberg (1970), the material undergoes deformation beginning with its initial microstructure following the sample extraction in a relatively dry state. On the other hand, the application of isochoric conditions while saturation, with following stepwise unloading, enables the acquisition of the swelling-strain correlation subsequent to a volume-constant swelling pressure test. Thus, the sample is saturated and particles are rearranged when the unloading procedure is initiated. The second case is of

greater relevance for mechanised tunnelling, given that the subsoil is typically completely saturated and swollen in the undisturbed state prior to the construction of the tunnel. In mechanised tunnelling, the ground is then permanently supported by the tunnel shield, shield tail and grouting, preventing it from free swelling. In order to accurately reflect reality, the test setup described in Section 4.3.4.3 was developed in this work.

Table 2.1.: Summarised hydro-mechanical tests on OPA from the literature.

	Depth [m]	Clay content [%]	Swelling pressure [MPa]		Swelling strain [%]	
			Perp.	Parallel	Perp.	Parallel
Intact						
Huder and Amberg (1970)	30	-	0.5	-	-	-
Grob (1972)	-	-	0.8-2	-	-	-
Bock (2001)	ca. 300	-	1.2	0.6	7	1
Péron et al. (2009)	ca. 300	-	0.5-0.56*		-	-
Zhang et al. (2010)	ca. 300	58-76	5.5**	-	8	2
Giger et al. (2014)	-	40-75	1.39	-	10.75	-
Favero et al. (2016)	300	-	3.7	-	-	-
	890	-	0.65	-	-	-
Wild et al. (2017)	ca. 300	50-80	-	-	1.0**	0.2**
Crisci et al. (2019)	22.6	61	0.9	0.7	-	-
	38.2	46	0.9	0.22	-	-
Powder						
Nitsch et al. (2023)	ca. 300	56	0.6-1	-	9-11	-

* = direction not specified, ** = vapour saturation (RH = 95 %)

2.5. A brief insight into tunnel construction with a focus on swellable rocks

The creation of cavities in the underground has played an important role since the advent of civilisations. The earliest known tunnels date from between 500 and 700 BC and were constructed for the purpose of water supply, such as the Eupalinos Tunnel on Samos, Greece (Zambas, 2017). In recent years, the construction of tunnels has become an indispensable component of sustainable infrastructure in modern societies, as existing infrastructure must adapt to accommodate the continually increasing demand for mobility. In this context, the construction of tunnels is a particularly reasonable solution to overcome a variety of topographic, geological and hydrogeological obstacles, including rivers and mountains. Furthermore, urban areas with high population density have the potential to relocate their infrastructure into the underground space. The construction of direct underground connections has the potential to result in significant time and cost savings, while also presenting opportunities for regional growth.

Drill and blast methods, subsequently mucking and installing a support system represent the conventional tunnelling technique. For centuries, this method was regarded as the primary approach for the construction of railway tunnels and transalpine crossings. The concept of automating the tunnelling process was first proposed at the end of the 18th century. However, it was not until 1966 that the first tunnel was successfully driven with the use of a modern full-face cutting machine (Garbotz, 1975).

The forthcoming section provides an overview of the hydro-mechanical processes that occur during tunnel driving and are responsible for initiating the swelling process in swellable rocks. This is followed by an introduction to the damage caused to tunnel structures due to swelling, along with concepts for load transfer. Finally, an insight into the processes of mechanised tunnelling is presented.

2.5.1. Origin of water and hydro-mechanical processes in tunnelling

The development of the swelling pressure during tunnelling is contingent upon the hydro-mechanical processes that accompany it. In its natural state, dry rock exhibits low porosity and permeability, which effectively functions as an aquitard, impeding the migration of fluids between the rock and the surrounding saturated soil layers (aquifer). Moreover, the osmotic swelling at this point is in equilibrium with the considerable stresses resulting from the overlying soil layers. It is only when the stress state undergoes a change that

these processes may begin anew. Therefore, it can be concluded that the swellable clay rock is relatively dry in its initial equilibrium state.

The water which enters the equilibrium state can be categorised after Amstad and Kovári (2001) according to Table 2.2 into mountain water, process water and meteoric water. In this context, mountain water is defined as the water that is already present in the surrounding rock, such as pore or fissure water, and which moves towards the tunnel as a result of the disturbance of the state of equilibrium. Process water is the water that is supplied to the tunnel structure for construction purposes or during the operational phase, such as cooling or cleaning water. Meteoric water is defined as precipitation-derived water that can enter the system through the tunnel portal or shafts, in both liquid and gaseous phases.

Table 2.2.: Possible origins of water triggering swelling processes in the framework of tunnelling in swellable rocks, modified after Amstad and Kovári (2001).

	Mountain water	Process water	Meteoric water
Initial state	- Natural water content of the rock - Natural water circulation in the rock		
Construction phase & Operation phase	- Water from the rock - Water from distant, water-bearing rock strata. Inflow via the structure. - Water from leaking exploratory boreholes	- Cooling and drilling water - Cleaning water - Water for dust control	- Inflow of meteoric water - Transport of meteoric water in the tunnel air - Road water

It is standard practice to collect and recirculate service water during the construction phase of a tunnel in order to prevent any swelling processes being initiated by it. However, it is also possible for unintentional and artificial water inflow to occur during tunnelling. This may result from a leak in the drainage pipes or the cutting of water-bearing boreholes (Anagnostou, 1991). The impact of meteoric water on swelling processes in the vicinity of the tunnel is also a subject of contention. For example, Henke (1976) demonstrated that

the direct influx of water into test tunnels, in contrast to atmospheric humidity, resulted in an uplift that exceeded a tenfold increase.

Anagnostou (1995) posited that the phenomenon of floor heave is not contingent upon the relative humidity of the air within the tunnel. Moreover, he asserted that the movement of the tunnel crown and side is negligible for relative humidities below 90 %. Alonso et al. (2013a) reached a comparable conclusion in their examination of anhydrite expansion in the Lilla tunnel in Spain. Their findings indicated that the quantity of water required for the observed expansion cannot be solely supplied by evaporation from the air. In general, the present study concentrates on the hydro-mechanical processes occurring over an extended period during the operational phase of the tunnel structure. Consequently, the focus is on the inflow of mountain water.

During the process of mechanised tunnelling, a redistribution of stress and an unloading-induced dilation of the surrounding rock are observed. The area of disturbance in the near field of the tunnel, as illustrated in Fig. 2.13, is designated the Excavation Damaged Zone (EDZ) (Emsley et al., 1997; Bossart et al., 2004; Tsang et al., 2005). The EDZ induces an advective water flux from the saturated layers along the tunnel due to the high water pressure or gravity (**A** in Fig. 2.13), as well as a diffusive flux in the radial direction towards the tunnel upon unloading-induced dilation and thus an increase in suction (**B** in Fig. 2.13).

Basically, the flow path of groundwater in rocks occurs along various discontinuities, including the bedding planes that are characteristic of sedimentary rocks, as well as fractures and joints (Butscher et al., 2016). As a consequence of the unloading and dilation of the rock material caused by tunnelling, these discontinuities open up. This results in the initiation of a hydraulic flow due to a gradient in water pressure within these farctures (**A** in Fig. 2.13). Thereby, within the EDZ, water is transported into the swellable clay rock in the nearfield of the tunnel. As a consequence of the alteration in the stress state resulting from the excavation process, the material has once again developed the potential for (osmotic) swelling. The influx of water and the expansion of the rock are two opposing processes. The swelling of the rock closes the preferential flow paths and reduces the hydraulic permeability, thereby slowing down the rate of water transport.

At the same time, the void ratio of the clay rock in the EDZ is observed to increase as a consequence of unloading-induced dilation. Given that the quantity of water remains unaltered and the volume increases, the saturation within the EDZ is reduced. A saturation gradient is thus established. Consequently, water diffuses from the more saturated intact

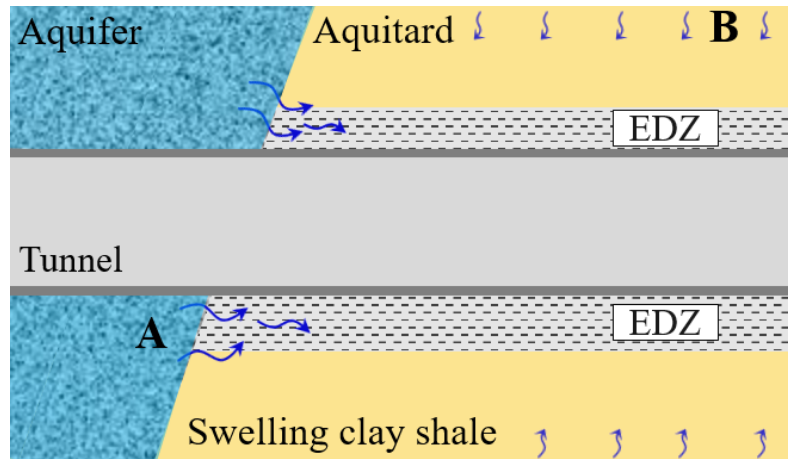swellable rock in a radial direction towards the tunnel. This is indicated by the symbol **B** in Fig. 2.13.

Figure 2.13.: Potential mechanisms of water flux of mountain water.

2.5.2. Swelling-induced damage patterns in tunnelling structures

The swelling processes and their effects on the tunnel structure during the construction and subsequent operational phases can be classified into three categories, as outlined by Kovári et al. (1987):

- Floor heave: Uplifts develop in the non-constructed tunnel floor.

- Swelling pressure on the invert arch: If the tunnel floor is fully constructed, swelling pressure builds up in the invert arch. If the support system cannot withstand the resulting pressure, it may be damaged and the load-bearing capacity will be impaired.

- Lifting of the structure: If the tunnel floor is fully constructed and the structure is rigid enough not to be damaged by swelling pressure, an uplift of the complete structure is possible. This again impairs the serviceability and can induce longitudinal damages into the tunnel structure.

The concentration of the swelling process in the tunnel floor can be attributed to the hydraulic gradient around the tunnel. As a consequence, water tends to accumulate in the tunnel floor, thereby initiating the swelling process in this specific area. In the crown and sidewall of the tunnel, water inflow tends to result in weathering of the rock. In the event of a completely sealed support system, particularly in mechanised tunnelling, with

a strong inflow of water, a more uniform distribution of the water around the tunnel and thus the associated swelling processes is also a possibility.

Amstad and Kovári (2001) have assembled and assessed the knowledge gained from construction projects in swelling clay rocks. The data corroborated the findings that damage in conventional tunnelling is concentrated in the tunnel floor, particularly in the frequently utilised horseshoe cross-sections. Such observations have been made in the construction of the Rickentunnel and the Grenchenberg Tunnel, both located in Switzerland. In these instances, the swelling process occurred at depths reaching up to 1.5 times the diameter of the tunnel. Additionally, damage to the side walls of the tunnel can be attributed to heaves in the tunnel floor. When these occur relative to the tunnel lining, they lead to shear joints on both sides of the invert. No practically relevant heaves were detected in round cross-sections. This phenomenon can be attributed to a potentially lower swelling potential of the rock or a lack of water inflow. However, it can also be attributed to the statically more advantageous case of a circular cross-section.

The first two tubes of the Belchentunnel in Switzerland were constructed beginning in 1963 using conventional techniques in sections of swelling clay rocks and anhydrite-rich rocks. In the section with clay rocks, a pronounced invert heave was observed prior to the installation of the invert arch, which reached almost 60 cm. Subsequently, during the operational phase, damage was observed exclusively in sections of the tunnel containing anhydrite-rich rocks (Amstad and Kovári, 2001). In Chiaverio et al. (2017), damage patterns observed during the construction phase (Fig. 2.14a) and later in the operational phase (Fig. 2.14b) are presented. The image of the construction phase a) illustrates the fractured concrete mass of the tunnel floor and the deformed invert arch at the sidewall. The image of the operational phase b) illustrates the phenomenon of spalling in the concrete of the inner lining.

2.5.3. Concepts for tunnelling support systems in swelling rocks

For an extended period, conventional tunnelling was the predominant method employed for tunnelling in swelling rocks. This approach was favoured due to its flexibility in controlling the swelling loads, and clay rocks typically exhibit a medium to long stand-up time, which renders the support of the tunnel face unnecessary. In general, two main principles exist for resisting and controlling the additional loads on the tunnel lining. These are, according to Kovári et al. (1987), the resistance principle and the yielding principle. The actual realised concepts of the aforementioned support systems are categorised and
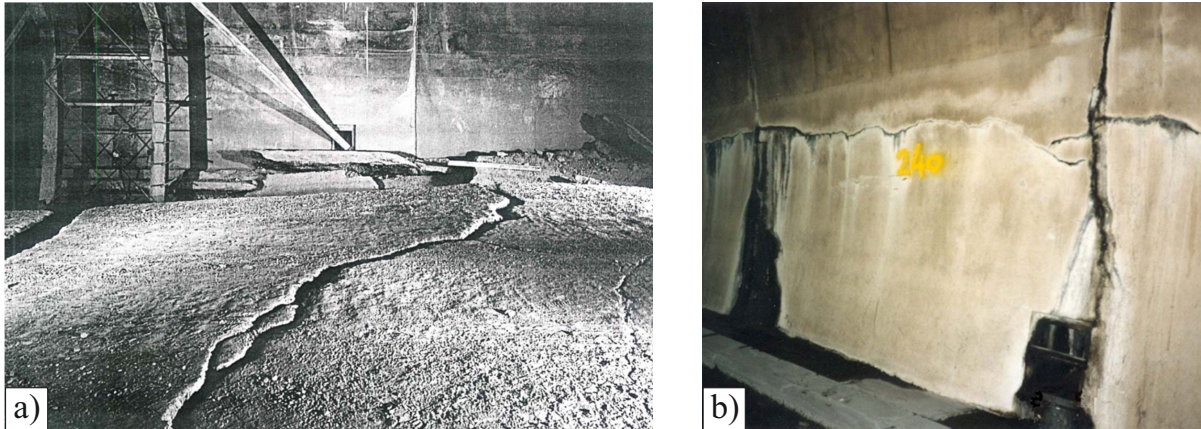
Figure 2.14.: Damage patterns from the Belchentunnel in Switzerland a) during the construction phase in the 1960s and b) the operation phase in the early 1990s as documented in Chiaverio et al. (2017).

summarised in Fig. 2.15. Sometimes, free swelling without pressure build-up is referenced as a third principle; however, this is not discussed further here. The resistance principle employs a rigid tunnel support system comprising a heavy tunnel lining or supplementary support, such as rock anchors, to resist the pressure exerted by the rock mass and prevent deformation. As a consequence of the rigidity of the lining, the maximum swelling pressure builds up within the swelling rock and exerts a force on the lining. It is thus crucial to ensure that the lining is adequately dimensioned to guarantee the load-bearing capacity of the structure. Translational displacements of the whole structure can also occur and thus become a relevant issue. Exemplary concepts are indicated as R1, R2, R3 and R4 in Fig. 2.15. R1 is a concept that is primarily applicable to mechanised tunnelling, whereas R2, R3 and R4 can be associated with conventional tunnelling. In this context, the R1 approach effectively combines the statically favourable load-bearing effect of the circular profile with efficient mechanised tunnel driving. The Sannierungstunnel Belchen (STB), which is the subject of the present study, was also constructed in accordance with this concept. Concepts based on the yielding principle are presented as Y1, Y2 and Y3 in Fig. 2.15. In general, these concepts take advantage of the fact that the swelling pressure of clays and clay rocks is reduced when the material undergoes volumetric expansion. Therefore, controlled compression of the tunnel support system is allowed. This compression can be achieved through the utilisation of diverse elements, including foam panels and support ribs (Amstad and Kovári, 2001). Other measures, such as a split shotcrete lining or sliding anchors, are also feasible, as are steel supports with sliding connections. The

latter represents an established method from the mining industry, which was successfully employed in the construction of the Gotthard Basistunnel, Teilabschnitt Sedrun (Kovári and Ehrbar, 2008). As illustrated in Fig. 2.15, it is evident that the cross-sections in the yielding principle are not circular, thereby precluding the use of mechanised tunnelling for their construction. The installation of special compression elements or systems on short, particularly exposed sections of the tunnel is more readily achievable through conventional tunnelling, as this approach allows for greater flexibility. Furthermore, it is not economically viable to interrupt mechanised tunnelling to modify the tunnel boring machine (TBM) in such instances, given the emphasis on efficiency in tunnelling operations.

Figure 2.15.: Principles for tunnel support systems in swelling rocks modified after Amstad and Kovári (2001). Realised projects in the corresponding categories are, for example: R1 Adlertunnel, Switzerland; R2 Hesslach II, Germany; R3 Loppertunnel, Switzerland; R4 Pfändertunnel, Austria; Y1/Y2 Freudensteintunnel, Germany; Y3 Tunnel T8 of A16, Switzerland.

In recent years, there have been significant developments in the materials used for segments as well as in the techniques employed in their production. Compressible annular gap grouts and deformable tunnel lining segments are already employed in tunnelling practice and are undergoing further development (Radončić et al., 2009; Mezger et al., 2018; Vu

et al., 2020). The plastic compression of these elements enables the controlled deformation of the swelling ground and the regulation of the loads acting on the load-bearing part of the tunnel lining. Consequently, the risk of damage can be mitigated by tolerating the localised swelling pressure at the tunnel lining level. This enables the utilisation of mechanised tunnelling in swelling rocks. One advantage of this approach is the ability to specifically control the development of the EDZ by precisely setting the tunnelling parameters in a TBM.

2.5.4. Process of mechanised tunnelling

In comparison to conventional tunnelling techniques, mechanised tunnelling provides a higher level of automation, consequently resulting in a more rapid construction process. The high cost of a tunnel boring machine (TBM) requires a robust assurance of the efficacy of the tunnelling process, taking into account the specific characteristics of the subsoil. It is of the utmost importance to guarantee a favourable return on the initial investment throughout the project's duration in comparison to conventional tunnelling. Accordingly, a variety of TBMs are available, each optimised for distinct ground conditions. Recommendations for the use of TBM types depending on the particular subsoil are given in DAUB (2020). They are divided in full-face machine types and partial-face machine types as indicated in Table 2.3. Thereby, with respect to DIN 18312:2019-09 (2019) excavation classes are defined as follows: without support (VS1), with support that must be installed in coordination with the construction method in such a way that loosening and loading is not interrupted (VS2), and with support for which the loosening and loading must be interrupted for installation (VS3). At this point, it is important to point out the inconsistent terminology in international and German-speaking countries regarding TBMs. In the international context, TBM is an overarching term for all mechanised tunnelling techniques. In Germany, however, it is defined as a machine used in hard rocks with a full face cutterhead, which is for example a Gripper TBM in Table 2.3. A gripper TBM is typically utilised in hard rock with a medium to long stand-up time (Maidl et al., 2013). In this work, the international terminology is used.

In general, the tunnel face may be unsupported, supported mechanically, with compressed air to prevent water inflow, with a support slurry (slurry shield) or with the conditioned excavated earth mass (earth pressure balance (EPB) shield). The excavation is carried out over the full tunnel face, utilising a circular cutterhead equipped with cutting tools adapted to the soil encountered, or partial tunnel face, employing hydraulic excavators or boom-type roadheaders (Maidl et al., 2013). A further classification is made with

regard to the operational mode of a TBM. An open mode may be employed for the excavation of stable tunnel faces and in the presence of a limited water inflow, whereby the excavation chamber is maintained at atmospheric pressure. The closed mode is employed for tunnelling in loose rocks or granular soils, both above and below the groundwater level. In this operational mode, the excavation chamber is maintained at a certain pressure level, and the tunnel face is supported by a slurry or a conditioned earth mass. In varying subsoils, a transition mode may also be employed when the tunnel is temporarily driven through stable rocks below the groundwater level. In this instance, the supporting medium of the corresponding closed mode is partially lowered, and the excavation chamber is pressurised with compressed air to prevent the inflow of water. In general, a low level of the support medium is advantageous for the tunnelling process, as it reduces wear on the excavation tools.

Table 2.3.: Classification of TBMs according to DAUB (2020).

Name	Operation mode			Excavation class
	Open	Closed	Transition	(DIN 18312:2019)
Full-face machines				
Gripper TBM	x	-	-	VS1
Single shield	x	-	-	VS1
Double shield	x	-	-	VS1
Slurry shield	x	x	-	VS2
Earth pressure balance shield	x	x	x	VS3
Variable density shield	x	x	x	VS2/3
Hybrid shield	x	x	x	VS2/3
Extension TBM	x	-	x	VS1
Partial-face machines				
Excavator shield	x	(x)		VS1
Roadheader shield	x	(x)		VS1

An exemplary TBM, in this case a single shield, is shown in Fig. 2.16. Single-shield TBMs have been successfully employed for the construction of tunnels in swellable clay rocks in recent years. Furthermore, a single-shield TBM was utilised in the reference project, the Sanierungstunnel Belchen (STB), which forms the basis of this study. In the process

of tunnelling, the soil in front of the TBM is excavated with the appropriate excavation tool at the cutting head (1). Subsequently, the excavated rock mass is conveyed with the bucket (2) from the face through the muck ring (3) in the TBM. The excavated material is transported out of the tunnel with a machine belt (5) or a screw conveyor, and the TBM is advanced by thrust cylinders (6) that push against the installed lining segments or in case of the gripper TBM by regripping. The shield (4), temporarily serves to protect the cavity against the ground pressure until the final tunnel lining (9) is installed.
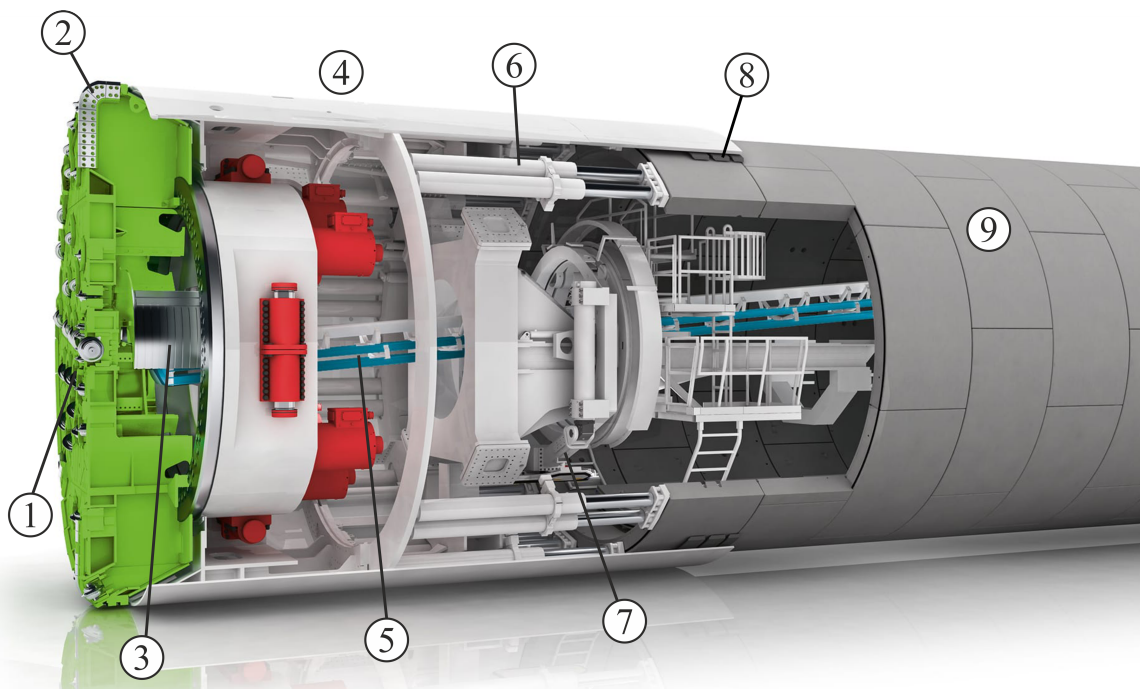
Figure 2.16.: Structure of a single shield TBM from Herrenknecht AG (2023). (1) is the cutting head, (2) the bucket, (3) the muck ring, (4) the shield, (5) the machine belt, (6) the thrust cylinders, (7) the erector, (8) the backfilling and (9) the tunnel lining.

Excluding the rare case of swelling rocks, segmental linings constructed from precast reinforced concrete, comprising either steel bars, mesh or fibres as reinforcement, represent the current standard for tunnel support systems in mechanised tunnelling and have superseded steel or cast iron segments. As previously stated, compressible segments composed of, for instance, porous concrete can be employed to control additional swelling pressures while tunnelling in swellable clay rocks. A closed annular ring is formed by the combination of five to eight segments, with seven segments being the most common number. The final segment, the keystone, serves to close the ring and is typically of a smaller size than the other segments (Maidl et al., 2012). The lining is installed with the use of an

erector (7) under the protection of the TBM's shield. This process creates an annular gap between the excavated surface of the ground and the tunnel lining due to the presence of the shield. This gap is subsequently filled with the annular gap grout (8) during the tunnel driving process.

3. Introduction to the case study

The Belchen tunnels form part of the A2 motorway in Switzerland, providing a connection between Basel and Lucerne via the main chain of the Jura Mountains in the north. The existing two tunnel tubes of the Belchen tunnel (Bestehendes Tunnelsystem Belchen, BTB) were constructed in the 1960s and subsequently damaged as a result of the swelling of the surrounding anhydrite-rich marl (Gipskeuper) and OPA (Grob, 1976; Amstad and Kovári, 2001; Steiner et al., 2011; Steiner, 2020). A number of repair measures were undertaken during this period, most recently between 2002 and 2003, with the objective of extending the operational lifespan by a further 20 years. The construction of a third tunnel tube to the west of the BTB, with the objective of relieving traffic congestion in the event of further remediation works (Sanierungstunnel Belchen, STB), commenced in 2016 and was finally completed and opened to the public in 2022. Subsequently, the initial phase of the renovation and reinforcement of the first tunnel tube in the direction of Basel was initiated.

The STB serves as the reference project for this study. From the outset of its construction, the Department of Earth Sciences at ETH Zurich was involved to provide comprehensive data acquisition for the purpose of studying the behaviour of the OPA rock mass during TBM tunnelling and subsequently in the operational phase. The project's objectives were to investigate structural geology, hydrogeology, rock mass stress and deformations, and the hydro-mechanical behaviour of OPA for tunnelling-relevant boundary conditions. This entailed considering in-situ conditions and an interaction with the tunnel support (Ziegler and Loew, 2017). The present study is concerned with the latter objective, namely the hydro-mechanical laboratory testing of OPA for tunnelling-relevant boundary conditions. Consequently, OPA drilling cores from the STB construction site were employed.

The STB was driven with a single-shield TBM of 75 m length and a 10 m long shield. The length of the tunnel tube is 3.2 km, with a diameter of approximately 14 m. The support system comprises a 35 cm thick outer lining with seven segments per ring, a drainage membrane and an inner cast-in-place lining of 65 cm thickness (Ziegler et al., 2022a). The location of the STB and a cross-section of the Chambersberg syncline with the STB are

shown in Fig. 3.1. OPA is crossed on two occasions over the length of the tunnel, from tunnel meter (TM) 3180 to 3300 and from TM 2200 to 2720. The primary objective of the research programme is to investigate the latter segment (Fig. 3.1b). The thickness of the OPA formation and dip direction of its bedding planes are inconsistent in this area due to folding and thrusting.
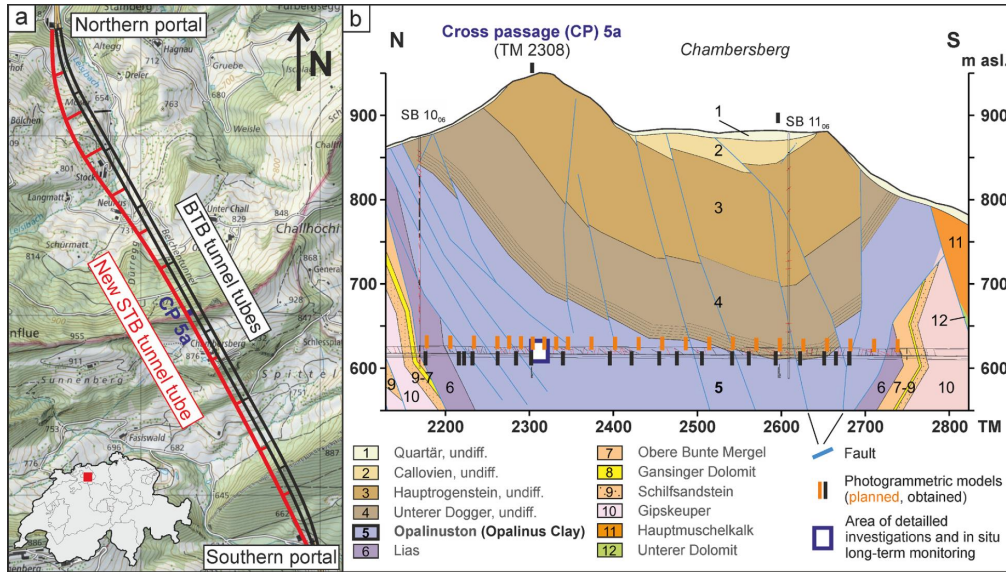
Figure 3.1.: a) Location overview and b) geological cross-section of the STB (Ziegler et al., 2022a).

The area of detailed investigations and the in-situ monitoring is located in TM 2315 to 2317. Those investigations include the installation of:

- Sliding micrometer boreholes: Three radial boreholes with extensiometers to measure the deformation in the surrounding rock mass (see Fig. 3.2a).

- Total pressure cells (TPCs): Seven cells around the tunnel to measure the total pressure acting on the lining.

- TDR packer: Packer installed in the invert with TDR sensors in two depths (close to the interface between gap grout and rock formation, as well as at greater depth) to measure the development of the water content.

- Pore pressure sensors: Installed in the same boreholes as the TDRs, directly at the gap grout/rock formation interface and at the end of the borehole deep in the rock formation.

Of great importance for the current study is cross passage (CP) 5a at TM 2308 (see Fig. 3.2b). CP 5a has a length of 28 m and connects the STB with the western tube of the BTB. The overburden is 330 m. Four boreholes with lengths ranging from 14.70 m to 17.50 m were drilled in June 2017 from CP 5a with the objective of obtaining samples for laboratory analysis. The cores were obtained using a triple-tube core barrel system and subsequently vacuum-sealed in PVC liners. Two boreholes were drilled in a direction parallel to the expected bedding planes (CP-1 and CP-2), while two others were drilled in a direction perpendicular to these planes (CP-3 and CP-4). Moreover, the boreholes were aligned in a manner that enabled them to penetrate fault zones. The obtained core samples were found to meet the aforementioned specifications. They were drilled within $10°$ of the planned bedding orientation and penetrated fault zones ranging in thickness from 0.1 to 0.5 m. The drilled cores exhibited approximately two to five fractures per metre (Ziegler and Loew, 2018). Cores were subsequently analysed and documented in Soares (2017), photographs are shown in the Appendix 1 and 2. The details of the drilled boreholes are summarised in Table 3.1.
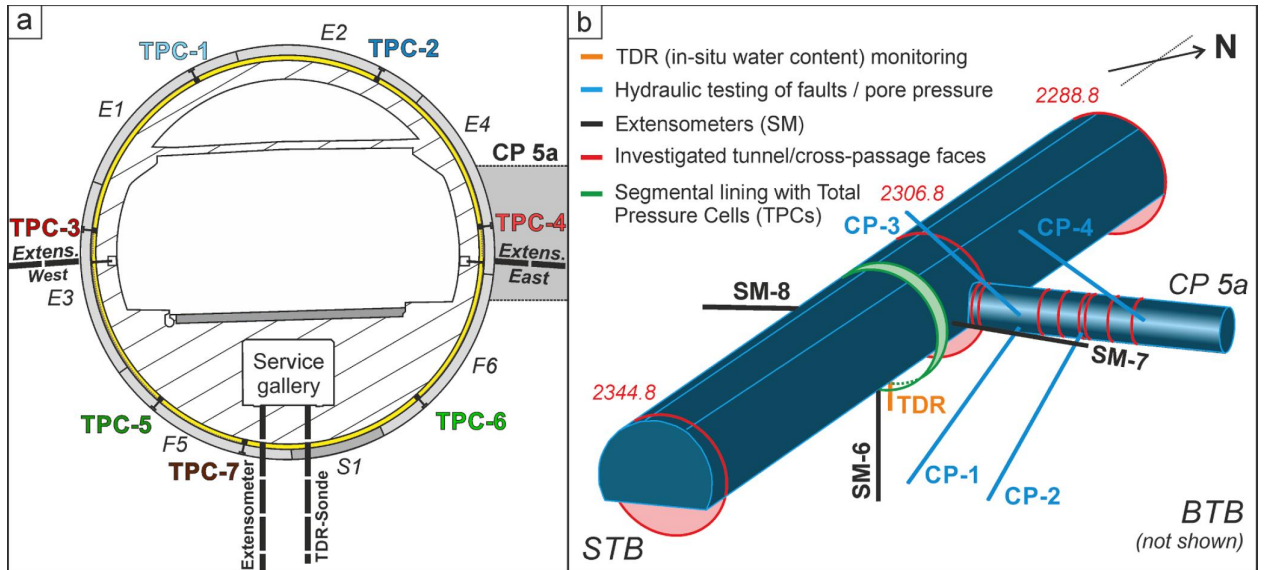
Figure 3.2.: a) Cross-section of the STB and b) 3D-sketch of cross passage 5a with installed in-situ monitoring (Ziegler et al., 2022a).

The yearly reports pertaining to the entirety of the project are published in Ziegler and Loew (2017), Ziegler and Loew (2018), Renz et al. (2019), Ziegler et al. (2020), Ziegler et al. (2021) and Ziegler et al. (2022a).

Table 3.1.: General overview of drilling cores used in this study.

Borehole	Orientation	Length	Comment
CP-1	parallel	16.75 m	
CP-2	parallel	17.25 m	
CP-3	perpendicular	17.50 m	hydraulic pulse test after core extraction
CP-4	perpendicular	14.70 m	hydraulic pulse test after core extraction

4. Materials and methods

The current chapter presents the material analysed in this thesis and the methods employed. Subsequent to the mineralogical and geotechnical classification, the sample preparation is described in detail. Thereafter, the methods and equipment used are presented. Both available equipment and new equipment developed as part of this study are employed. The latter is presented in more detail.

4.1. Opalinus clay

OPA is a sedimentary rock formation that is most likely originated during the early Aalenian to late Toarcian period (Bundesamt für Landestopografie swisstopo, 2023), which corresponds to an age of approximately 174 million years. The formation is located in northern Switzerland, within the Jura Mountains, extending to the Swabian Jura (Schwäbische Alb) in southern Germany. Leioceras opalinum is the eponymous guide fossil for the formation. The OPA studied in this work originates from a crosspassage (CP 5a) at the Sanierungstunnel Belchen (STB), as presented in Chapter 3. In general, three distinct facies are identified in the Jura Mountains: the shaly facies, the sandy facies and the carbonate-rich facies. Thereby, the STB is driven through the shaly facies. In terms of mineralogical composition, OPA has a clay content of 40-80 %, which is highest in the shaly facies (NAGRA, 2002). In descending order of abundance, the other minerals present are calcite, quartz, siderite, pyrite and organic matter. The clay content is primarily constituted of illite/smectite mixed-layer clay minerals and kaolin. The comprehensive mineralogical composition of the material under examination will be presented in the following chapter. OPA can be classified as both stiff clay and weak rock, as it exhibits properties of both material groups (Schuster et al., 2023). It is therefore the subject of research in both soil mechanics and engineering geology. This ultimately led to a collaboration with the Chair of Engineering Geology at ETH Zurich on this project. However, it should be noted that OPA exhibits a high overconsolidation ratio (OCR). The preconsolidation pressure of OPA from the shaly facies at a comparable depth to that of the material examined in

this study was determined to be between 20 and 25 MPa (Horseman et al., 2005), while the actual in-situ stress was estimated to be 4.5 to 6 MPa (Martin and Lanyon, 2003), resulting in an OCR between 3.3 and 5.5.

One particularly interesting aspect of the STB is that the tunnel is excavated through the same facies of OPA as that in which the Mont Terri Underground Rock Laboratory (URL) is located. Furthermore, the depth of the STB (320 m) and the URL (shaly facies at 280-320 m) exhibit a comparable range, indicating that findings from the STB project can be transferred to the URL and vice versa. The URL is an underground research laboratory situated to the north of Saint-Ursanne in the Jura canton. The facility is operated by the Swiss Federal Office of Topography (swisstopo) and is used to conduct experiments in the surrounding OPA under in-situ conditions, with the objective of acquiring knowledge about the thermal, hydraulic, mechanical, chemical and biological behaviour of OPA (Bossart et al., 2017a). This is of significant interest, as OPA has been identified as a potential host rock for radioactive repositories in Switzerland. The proof of suitability has been provided in the meantime. In Germany, OPA is likewise among the potential formations proposed by the Bundesgesellschaft für Endlagerung (BGE) for the purpose of radioactive repository construction. Nevertheless, the work is still in progress.

The fact that the URL and STB share the same facies of OPA and offer similar geological boundary conditions, facilitate a comparison between the comprehensive investigations on the THM behaviour of OPA in the context of radioactive waste disposal and the experimental outcomes presented in this study.

4.1.1. Mineralogy

The clay mineralogical analysis of the used OPA in this study was conducted at ETH Zurich via X-ray diffraction (XRD) using the Rietveld refinement method (Ziegler et al., 2022b). For this purpose, subsamples of 5 g were taken for the XRD analysis during the preparation of the samples for the swelling pressure tests. The material was subjected to milling with 7 ml of ethanol in a Retsch McCrome XRD mill, and subsequently oven-dried at 65°C. The material was then subjected to sieving with a 200 μm sieve and subsequently placed on the sample holder for further XRD analysis. Furthermore, the grain size fraction $<2\,\mu$m was separated by hydro-sieving and analysed in order to determine the quantity of illite present in the illite/smectite mixed layer phase. The results of the XRD analysis are presented in Table 4.1. The average proportion of clay minerals in the analysed material is 64.4 %, with a range of 58.5 % to 68.8 % across the individual subsamples. The

distribution of the individual components in the non-clay fraction is consistent across all subsamples. The average proportion of quartz is 18.0 %, beside 6.4 % of calcite, 4.1 % of siderite, 1.9 % of K-feldspar, 1.4 % of anatase, 1.4 % of pyrite, 1.3 % of dolomite and 1.1 % of Na-plagioclase. It is noteworthy that siderite exhibits considerable fluctuations, with a range of 1.8 to 13.0 %. Additionally, traces of gypsum were identified, though these were all below 0.4 %. The proportions of the individual clay minerals present were found to range between 22.8 and 31.4 % for muscovite/illite mixed layers, 17.4 and 20.3 % for kaolinite, 11.1 and 16.0 % for illite/smectite mixed layers and 4.0 to 5.3 % for chlorite. A differentiation of the illite and smectite in the associated mixed layer minerals reveals an illite content of between 64 and 75 %. A comparison of the OPA in this study with the compiled data in NAGRA (2002) reveals a similar composition of carbonates, quartz and clay minerals to that observed in the so-called shaly facies at other sites, including Riniken, Schafisheim, Benken, Waiach and the Mont Terri URL. A direct comparison with the best estimates of the mineralogy of the shaly facies in the Mont Terri URL, as presented in Bossart and Thury (2008), reveals a higher content of illite/smectite mixed layer minerals of 12.8 to 11 % and quartz of 17.8 to 13.7 %, but lower content of calcite of 6.4 to 13 % and chlorite 4.9 to 10.0 %. As outlined in Section 2.1.1, the illite/smectite mixed layers are of particular significance with regard to the swelling potential of OPA. The proportion of these minerals is slightly higher in the analysed material than in the shaly facies of Mont Terri, which suggests that the swelling potential may be slightly higher. Nevertheless, the observed discrepancy is minimal.

Sample no.	1	2	3	4	5	6	7	8	9	10	11
Borehole	CP1	CP1	CP1	CP1	CP1	CP2	CP2	CP3	CP3	CP3	CP3
Depth [m]	2.5-3.25	2.5-3.25	6.25-7.0	6.25-7.0	6.25-7.0	2.8-3.55	16.0-16.75	0.3-1.35	0.3-1.35	0.3-1.35	5.35-5.95
Kaolinite	20.1	20.2	20.3	20.0	20.0	17.4	19.9	19.8	19.3	19.6	19.7
Muscovite/Illite	28.5	31.3	31.0	31.4	26.9	22.8	26.7	24.5	25.4	26.9	23.4
Illite/Smectite	14.9	11.7	11.6	11.7	14.7	13.5	12.3	16.0	12.1	11.5	11.1
Chlorite	5.3	4.0	4.9	4.7	5.0	4.8	4.7	5.1	4.5	4.5	4.6
Quartz	16.9	17.1	17.0	17.2	15.6	15.9	19.2	16.9	20.4	21.2	20.3
Na-Plagioclase	1.2	1.0	1.0	1.0	1.1	0.9	1.2	1.2	1.2	1.2	1.2
K-Feldspar	2.0	1.9	1.8	1.8	1.7	1.8	2.1	2.0	2.0	2.2	2.1
Dolomite	1.4	1.3	1.1	1.1	1.0	1.5	1.4	1.4	1.4	1.5	1.1
Calcite	5.8	6.0	5.8	5.5	5.1	5.7	7.1	6.4	7.0	6.8	8.7
Siderite	1.8	1.6	4.2	4.0	7.0	13.0	1.9	3.4	2.1	2.2	3.8
Gypsum	0.3	<0.3	<0.3	0.3	0.3	0.3	<0.3	<0.3	0.4	0.3	<0.3
Pyrite	<0.4	2.6	<0.4	<0.4	<0.4	1.0	1.8	1.6	2.9	0.7	2.8
Anatase	1.6	1.3	1.2	1.4	1.5	1.5	1.5	1.6	1.3	1.4	1.3

Table 4.1.: XRD quantitative analyses of OPA investigated in this study. All values in %.

4.1.2. Geotechnical classification

A geotechnical classification of the material was conducted prior to the sophisticated hydro-mechanical testing. The same powder was employed for this purpose as was used for all other tests in this study, with the exception of the experimental investigation in Section 5.3.3 on the influence of grain size distribution on the hydro-mechanical behaviour. Further details regarding the preparation of the powder can be found in Section 4.2.2.1. As the powder for the entire study was not prepared in a single step, the determination of the grain size distribution (GSD) was repeated on individual batches to ascertain reproducibility and guarantee a consistent starting material. The grain size analysis was conducted using the sedimentation method, in accordance with DIN EN ISO 17892-4:2017-04 (2017). The GSDs of three batches are presented in Fig. 4.1. The GSDs of the powder obtained from different methods (mortar grinder and jaw crusher) already demonstrate a very good agreement. However, the GSDs derived from the same method (jaw crusher) exhibit even greater consistency across different batches. These results are almost identical, thereby allowing the assumption of a uniform starting material.
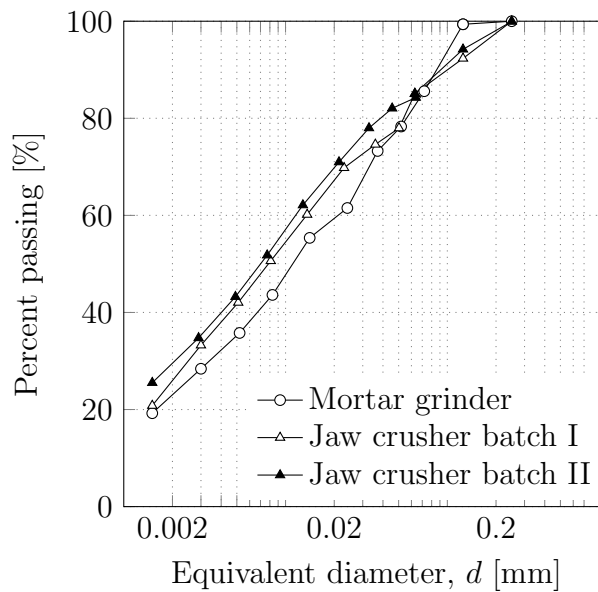

Figure 4.1.: Grain size distributions of OPA powder of various preparation methods and batches.

The grain density was determined according to DIN EN ISO 17892-3:2016-07 (2016) with the pycnometer method (capillary pycnometer) on three subsamples. The calculated mean value was 2.681 g/cm^3. Naegeli (2018) employed helium pycnometry at ETH Zurich as

part of the cooperation in this project on the same material and determined an average grain density of $\rho_s = 2.695$ g/cm^3 on 32 subsamples. In the following, the latter value is employed for the evaluation of all subsequent tests, as it has been demonstrated that helium pycnometry is the more accurate method (Columbu et al., 2021).

The plasticity values were determined according to DIN EN ISO 17892-12 (2020), and are presented in the plasticity chart in Fig. 4.2. The material under consideration is situated above the A-line and can be classified as a clay with intermediate plasticity. A comparison of the plasticity values from this study with those from other studies reveals a high degree of agreement. The activity is defined in accordance with Skempton (1953) as the plasticity index divided by the clay fraction (d <0.002 mm). The calculated values of 0.62 to 0.82, resulting from the different GSDs, fall within the range of kaolinite and illite clay minerals, which are also the primary clay components present in the tested material. They are by definition inactive to normal clays.

As previously outlined in Section 2.1.1, the CEC is employed to quantify the amount of exchangeable cations that neutralise the negative net charge of 2:1 layer minerals. Different methods for the determination exist, however, in this study the Cu-Triethylenetetramine method according to Meier and Kahr (1999) was employed. The calculated CEC value of 11.61 meq/100 g is in excellent agreement with the literature. Jaeggi et al. (2014) compiled data and concluded that a range of 9.4 to 13.4 meq/100 g for the shaly facies of OPA is reasonable. A summary of all determined values is provided in Table 4.2.

Table 4.2.: Geotechnical classification of the tested OPA.

OPA		
Grain density, ρ_s	[g/cm^3]	2.695
Liquid limit, w_l	[%]	42.5
Plastic limit, w_p	[%]	24.4
Plasticity index, I_p	[%]	18.2
Activity	[-]	0.62 - 0.82
Cation exchange capacity	[meq/100 g]	11.61
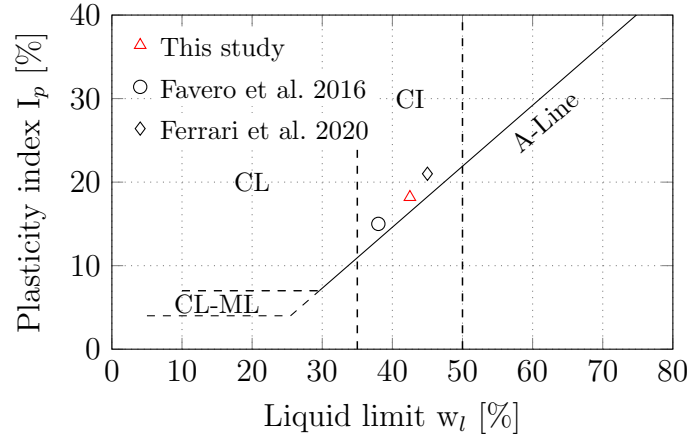
Figure 4.2.: Plasticity chart with the OPA investigated in this study.

4.2. Sample preparation

This study focuses on two main types of samples: intact samples, which are directly extracted from drill cores, and reconstituted samples, which are composed of milled and subsequently statically compacted OPA powder. The preparation of the corresponding samples is described in greater detail in the following subsections.

4.2.1. Preparation of intact OPA samples

Intact samples were prepared with consideration of their bedding plane orientation in four distinct geometries, as outlined in Table 4.3. Samples parallel to the bedding plane direction were obtained from drilling cores CP1 and CP2, whereas samples perpendicular to the bedding plane direction were obtained from CP3 and CP4. Photographs of the complete drill cores from Soares (2017) are presented in Appendix 1 and 2.

The initial gravimetric water content of the intact OPA used was analysed at ETH Zurich as part of the work by Naegeli (2018) using a 3 m long drill core. Subsamples were obtained from the centre of the drill core at regular intervals along its length. No obvious trend could be identified with regard to depth. The median value of all measurements was 5.66 %. As the samples were only briefly exposed to the atmosphere during the individual processing steps of sample preparation and were then vacuum-sealed once more, it can be assumed that this value represents the initial water content of the tested samples.

In the initial stage of the sample preparation process, shorter pieces of approximately 10 cm were obtained from the drill cores through the use of a band saw. It should be

Table 4.3.: Sample geometries of prepared intact samples.

Test	Geometry	Dimensions
Swelling pressure	cylindrical	$h = 20$ mm; $d = 50$ mm
SWCC	cylindrical	$h = 7$ mm; $d = 30$ mm
Thermal conductivity	cylindrical	$h = 40$ mm; $d = 38$ mm
3D-Swelling strain	cubic	30 mm x 30 mm x 30 mm

noted that the cores were not always perfectly perpendicular or parallel to the direction of the bedding planes. Consequently, a manual correction was implemented in this phase by deviating from the standard perpendicular cut and orienting the surfaces in accordance with the bedding planes. Subsequently, the shortened pieces were clamped on a lathe and precisely reduced to the diameter of the utilised rigid rings, thereby ensuring a tight fit (Fig. 4.3a and b). Subsequently, the resulting cylinders were cut to the required height utilising a diamond band saw (Fig. 4.3c and d). The samples that were pressed into the sample rings of the swelling pressure cells or into the microcells were manufactured with a few millimetres of excess height. Subsequently, they were ground with sandpaper in order to level the sample ring or microcell height. The final cylindrical and cubic samples are illustrated in Fig. 4.3e with respect to their bedding plane orientation.

The preparation time was kept to a minimum, and the material was always vacuum-sealed between steps. The initial batch of samples was prepared at the rock mechanics laboratory of the ETH Zurich. Additional samples were prepared by Sondermaschinenbau Schudy in a manner analogous to that described above. An exception was made for the specimen oriented perpendicular to the bedding direction, which was prepared for the purpose of determining the thermal conductivity (sample I_{12}). Given the small diameter and the material's tendency to delaminate in its bedding planes, the conventional sample preparation method could not be employed. Consequently, a separate sample was produced at RWTH Aachen, Chair of Engineering Geology and Hydrogeology. In this process, the specimen was obtained directly from the drill core using a hollow drill bit with the appropriate inner diameter and then cut again to the final height using a diamond band saw.

Cubic samples were obtained by sawing shortened pieces of the drill cores with a diamond band saw, utilising the integrated brackets. Once more, the orientation of the bedding planes was manually corrected from the drill cores in order to obtain cubes with two sides that were perfectly perpendicular to the bedding planes. Consequently, the remaining four

sides are parallel to the bedding planes.
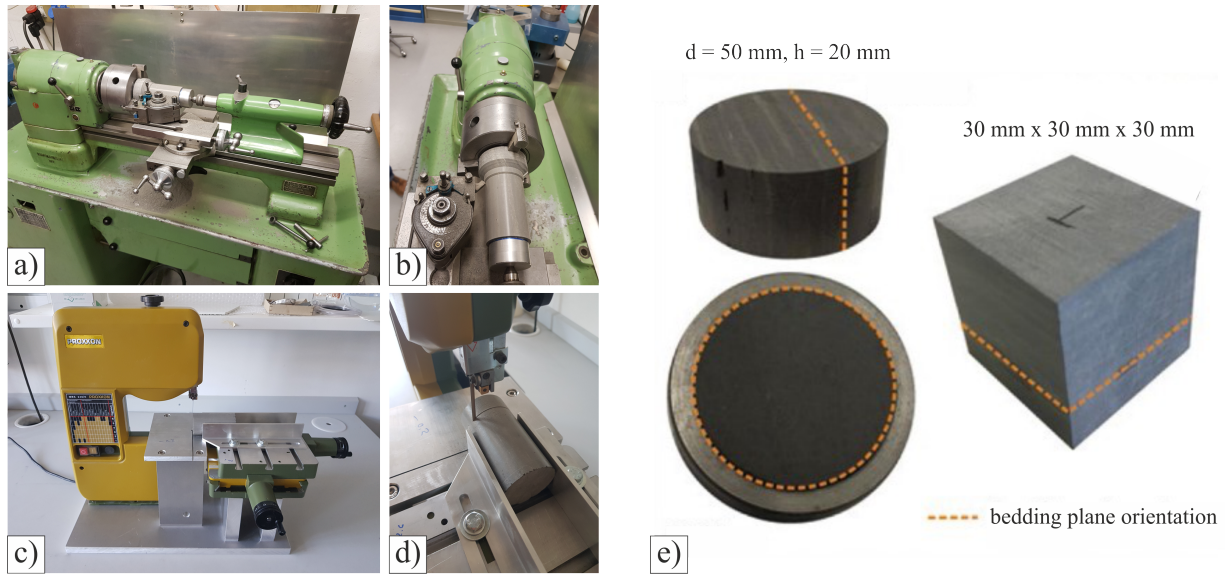
Figure 4.3.: Used devices at ETH Zurich to prepare intact OPA samples: a,b) lathe to achieve the required diameter from pre-cut drill cores and c,d) diamond band saw to cut required heights. e) Final cylindrical samples, without ring and attached in the ring, and cubic samples. Modified after Ziegler et al. (2020).

Table 4.4 lists the intact samples used in this work with their labelling, exact origin, initial dry density and void ratio. The dry density was always calculated using the aforementioned median water content of 5.66 %. The table also lists the sections in which the tests on the sample are discussed.

4.2.2. Preparation of reconstituted OPA samples

The compacted powder samples were obtained in two distinct steps. The initial stage involved milling intact OPA drill cores to prepare a powder. This was followed by compacting of the powder in order to prepare samples that met the required dimensions and exhibited defined initial conditions. The following sections provide a detailed presentation of the aforementioned steps.

4.2.2.1. Powder preparation

Two distinct methodologies were employed in the production of OPA powder. In both cases, the drill cores were initially subjected to a preliminary crushing process with a

Table 4.4.: Initial parameters of intact OPA samples tested in this study along with the sections in which the results are discussed.

Sample	Drill core	Depth	ρ_d	e	Section
	[-]	[m]	[g/cm^3]	[-]	
I_0	CP3	0.30-1.35	2.35	0.147	5.3.1
I_1	CP3	0.30-1.35	2.36	0.142	5.3.4.1
I_2	CP3	0.30-1.35	2.30	0.170	5.3.4.1
I_3	CP1	6.25-7.00	2.30	0.157	5.3.4.1
I_4	CP1	6.25-7.00	2.33	0.170	5.3.4.1
I_5	CP3	6.50-6.60	2.33	0.157	5.3.5.2
I_6	CP2	16.00-16.75	2.32	0.162	5.3.5.2
I_7	CP3	6.50-6.60	2.32	0.162	5.3.6.2
I_8	CP2	16.00-16.75	2.35	0.147	5.3.6.2
I_9	CP2	16.70-16.74	2.36	0.142	5.3.5.2
I_{10}	CP1	2.88-3.00	*	*	5.3.2
I_{11}	CP3	10.85-10.97	*	*	5.3.2
I_{12}	CP3	15.80-16.60	2.37	0.137	5.4
I_{13}	CP2	2.80-3.55	2.39	0.128	5.4

* = several small samples were used for this test series.

hammer, resulting in pieces with an approximate maximum dimension of 5×5 cm. The initial batch of OPA powder was prepared using a mortar grinder. The material was subjected to grinding for approximately ten minutes, after which it was sieved using a mesh size of 0.25 mm. The material that had been separated by sieving (material >0.25 mm) was then returned to the mortar grinder and ground again. A sedimentation analysis was subsequently conducted to ascertain the resultant grain size distribution. As the quantities of material required increased during the course of this study, and given that a single run in the mortar grinder yielded only a few grams, an alternative process was employed for the production of further powder. Subsequent batches were prepared using a jaw crusher in the laboratory of Engineering Geology and Rock Mechanics at RUB. The jaw crusher enables the production of larger quantities of powder in a shorter time. An opening width of 1 mm was employed in combination with a speed of 900 rpm. Once more, a sieve with a mesh size of 0.25 mm was employed to ensure the maximum grain size. The resulting grain size distributions were subjected to regular verification (as presented in Fig. 4.1) and

demonstrated a high degree of reproducibility across and between methods. An additional work package was conducted to investigate the impact of the grain size distribution on the hydro-mechanical behaviour of the powder (see Section 5.3.3).

4.2.2.2. Powder compaction

Subsequent to the aforementioned procedure, the powder was subjected to static compaction. The procedure for all samples was identical: a weighed mass of the material, which accounted for the initial boundary conditions specific to the test in question, was brought to a defined volume in a rigid ring or mould using a hydraulic press. Accordingly, distinct compaction sets were employed to compact the powder directly into a sample ring, which can be mounted in the cell (swelling pressure, heave, hydraulic conductivity and oedometer tests), while different moulds were utilised to obtain samples in the required geometries, which are subsequently mounted in the cell with other additional support systems, such as membranes or microcells (triaxial tests, thermal conductivity, SWCC). Table 4.5 summarises the various sample geometries, while Fig. 4.4 depicts the compaction sets and moulds employed.

Table 4.5.: Sample geometries of compacted powder samples.

Test	Geometry	Dimensions
Swelling pressure/heave	cylindrical	$h = 20$ mm; $d = 50$ mm
Oedometer	cylindrical	$h = 20$ mm; $d = 50$ mm
Hydraulic conductivity	cylindrical	$h = 20$ mm; $d = 50$ mm
SWCC	cylindrical	$h = 7$ mm; $d = 30$ mm
Thermal conductivity	cylindrical	$h = 40$ mm; $d = 38$ mm
Triaxial testing	cylindrical	$h = 80$ mm; $d = 35$ mm

The reference dry density for all tests was 2.0 g/cm^3, as samples with this initial dry density yield swelling pressures in the range of intact OPA perpendicular to the bedding plane direction and this is the highest dry density that can be achieved with the laboratory hydraulic press. In order to investigate the influence of the initial dry density on the hydro-mechanical behaviour, it was also varied to 1.8 and 2.2 g/cm^3. The dry density of 2.2 g/cm^3 was achieved with a workshop press capable of a maximum force of 50 t. However, this required great care in handling and could not be implemented with every compaction set for all types of tests due to the significant acting forces. The initial

Figure 4.4.: Compaction sets used in this study for compacting samples for: a) swelling pressure and oedometer tests directly into the sample ring, b) triaxial and thermal conductivity testing, c) the investigation of compaction induced anisotropy, d) SWCCs with direct transfer into microcells and e) swelling pressure tests in the newly developed cell for tunnelling relevant boundary conditions directly into the sample ring. f) Shows the used hydraulic jack for densities up to 2.0 g/cm^3 with an integrated load cell.

parameters for samples with the three tested dry densities are presented in Table 4.6. These parameters are no longer specified in the following sections for the corresponding tests, as they remain constant for the respective dry densities. The water content of the powder used remained relatively consistent throughout the study, with a maximum range of 2.3-2.5 %. The water content was monitored on a regular basis when new tests were initiated, but it remained largely consistent at approximately 2.3 % across the majority

of tests. However, a fluctuating initial water content with a maximum change of 0.2 % has no significant influence on the outcome of the tests. The initial degrees of saturation for the different dry densities (Table 4.6) are specified on the basis of $w_{init} = 2.3$ %. Should any tests on OPA powders deviate from the specified initial water content (e.g. in the study on the influence of grain size distribution on the hydro-mechanical behaviour of the powder, see Section 5.3.3), this will be explicitly stated.

An exception was the additional step in the preparation of the samples, both intact and reconstituted, for the determination of the thermal conductivity. To install the temperature sensors T_3-T_5 within the sample, three holes with a depth of 1 cm and a diameter of 1 mm were drilled into the sample at heights of 1, 2 and 3 cm, respectively, using a bench drill. Further details regarding this experimental configuration can be found in Section 4.3.5.

Table 4.6.: Initial parameters of reconstituted OPA samples tested in this study.

ρ_d	[g/cm^3]	1.8	2.0	2.2
e	[-]	0.497	0.348	0.225
S_r	[%]	12.3	17.6	27.2

In order to obtain samples for the investigation of compaction-induced anisotropy, OPA powder was compacted in a large cylinder with dimensions of 15 cm in diameter and 8 cm in height (see Fig. 4.4c). Subsequently, two samples were extracted from the cylinder using a hollow drill bit, with the resulting samples being perpendicular or parallel to the direction of compaction, respectively.

4.3. Experimental methods

This study employed existing methodologies and devices, but also involved the development of novel equipment specifically designed and constructed for this project. These are the swelling pressure cell for testing under tunnelling relevant boundary conditions and a cubic cell for measuring the three-dimensional deformations of an anisotropic clay shale on a single cubic sample. Furthermore, the limitations of experimental methods became apparent, prompting a more detailed consideration and adaptation for this study. This includes the immersion weighing in paraffin oil.

4.3.1. Determination of state variables

It can be assumed that the methods used to determine the common state variables in soil mechanics are well-known. However, two additional methods are presented here because they have been evaluated in detail for their suitability for this particular work (volume determination) or because they are not necessarily well-known outside the field of unsaturated soil mechanics (suction measurement).

4.3.1.1. A comparative study on the volume determination of porous media

The determination of the bulk density of a material via volume measurement is of great importance in the context of unsaturated soil testing, as it allows for the subsequent determination of the degree of saturation. This is particularly relevant in the framework of SWCCs, as outlined in Section 4.3.4.1.

The established methods for determining the bulk density of a material are length measurements using optical tools, immersion weighing (IM) and pycnometer-based methods (PM). The first method is more suitable for uniform geometries, whereas the last two require that the fluids used do not influence the measurement, due to swelling or penetration of the fluids into the pore space. In order to achieve this, non-wetting fluids, such as kerosene or previously mercury, are utilised, or the sample is covered prior to the beginning of the test, like in accordance with DIN EN ISO 17892-2 (2015) in the paraffin-coated-clod method (PCCM). The samples used in this study exhibit an uneven morphology, comprising intact OPA chips, and are in a highly dense state. The exclusion of optical volume determination necessitates the utilisation of more precise techniques, given that minor deviations can result in a considerable degree of data scattering. Furthermore, the PCCM proposed by DIN EN ISO 17892-2 (2015) and ASTM D7263-21 (2021) can be excluded, as this method has been demonstrated to systematically overestimate the actual volume, particularly for small, uneven samples (Liu and Buzzi, 2014; Solgi et al., 2018; Pires et al., 2019). Consequently, the PM in combination with kerosene as the non-wetting fluid has thus far been the prevailing method in this field, as evidenced by the literature (Sibley and Williams, 1989; Péron et al., 2007). Nevertheless, inaccuracies in this method have also been observed in the past when using pycnometers with weights significantly larger than the weight of the sample.

In light of the aforementioned issues, a study was conducted within the framework of this research project with the objective of identifying the most appropriate methodology. A detailed description of the study can be found in Christ et al. (2022). The volume of

compacted kaolin was determined using the PM with kerosene, PCCM and IW in paraffin, silicone and canola oil. Subsequently, the results were subjected to statistical analysis in three stages: I) The Shapiro-Wilk test was used to verify the assumption of normality of the observations. It is based on the analysis of variance (ANOVA) and corresponding F-test, which compares between-groups sum of squares and within-groups sum of squares, respectively, with the objective of testing for equal expected values (Shapiro and Wilk, 1965). II) The one-sample t-test was employed for testing for equal means, where the mean of observations is compared with a fixed mean. III) The Levene test is employed to test for equal variances between more than two groups (Gastwirth et al., 2009).

The average error of all methods is presented in Table 4.7. The measured volume is thus compared to an expected volume, which is determined with a high-precision caliper, given that the used samples exhibited an almost perfect cylindrical shape. This results in a tendency towards slight overestimation of the actual volume, given that imperfections in the surface of the samples were considered to be part of the volume in question. In light of these considerations, negative values of a modest magnitude, as observed in the case of IW with paraffin and silicone oil, may be indicative of a high degree of accuracy associated with these methodologies. In accordance with the literature, the error of the PCCM is notably high. The Shapiro-Wilk test indicates that the experimental data for all methods are normally distributed. However, the one-sample t-test reveals that the average error of the PCCM is significantly larger than the average of all other methods. This demonstrates that the PCCM leads to significantly larger volumes than all other methods. Accordingly, this method is not included in the subsequent comparison of variances. The Levene test, with the median as the centre and a significance level of $\alpha = 0.05$, indicates that there are differences in the variances between the groups. Subsequently, post hoc tests were conducted to identify the aforementioned differences by comparing the test series to one another. In order to avoid type II errors, it was proposed by Lee and Lee (2018) that only relevant pairs should be considered. Consequently, paraffin oil was subjected to comparison with the remaining three methods, given that it exhibited the smallest absolute error. A significant difference was identified between the IW in paraffin and canola oil, as well as between the IW in paraffin oil and the PM with kerosene. This indicates that the IW in paraffin oil yields more precise and reliable outcomes. No notable distinction was observed between the IW in paraffin and silicone oil. However, the standard deviation in Table 4.7 and the boxplots in Fig. 4.5 suggest that paraffin oil may offer a slight advantage. Consequently, the IW in paraffin oil was employed in this project for all volume determinations.

Table 4.7.: Average error of measurements of all methods.

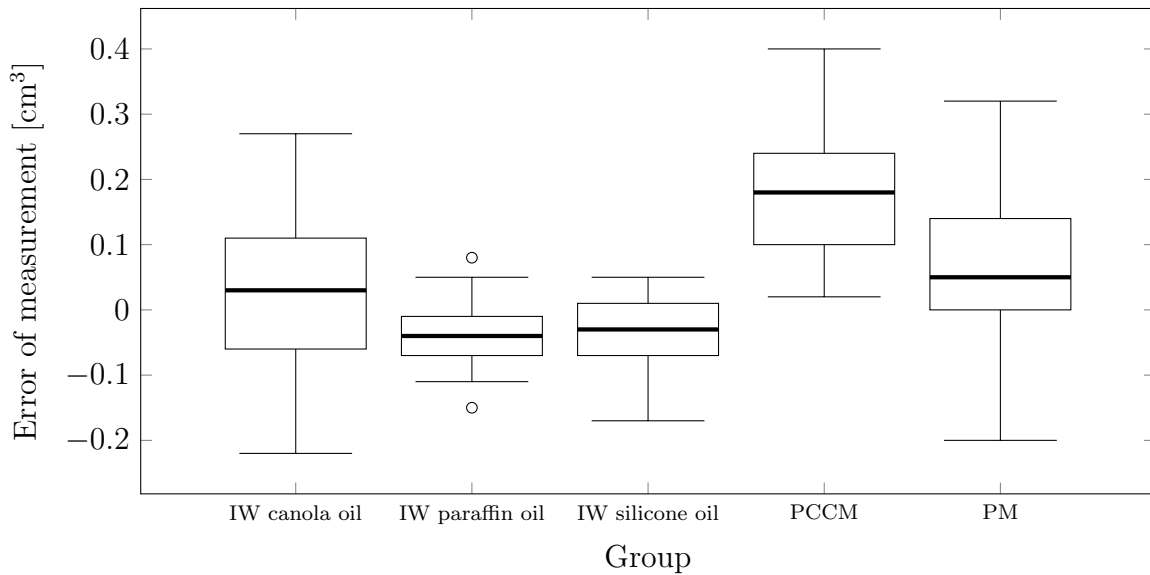| Method	Average error, cm^3	Standard deviation, cm^3
IW paraffin oil	-0.0348	0.0563
IW silicone oil	-0.0403	0.0638
IW canola oil	0.0241	0.1134
PM	0.0718	0.1226
PCCM	0.1830	-

Figure 4.5.: Boxplots of all five test series.

4.3.1.2. Suction measurement via a chilled mirror hygrometer

A chilled mirror dew point hygrometer (CMH) enables the direct measurement of the dew point temperature of a sample by condensing the air in the measuring chamber, which is in equilibrium with the water vapour in the pores of the sample, onto an inert and temperature-controlled mirror. A beam of light from a light-emitting diode is reflected by the mirror into a photodetector cell, which detects the change in reflectance that occurs when condensation forms on the mirror. Consequently, the dew point temperature is determined. The ratio of the saturated vapour pressure of water at the dew point to the saturated vapour pressure of water at the air temperature is equal to the relative humidity of the sample. This method is easy to carry out, fast, reliable and capable of ac-

commodating a wide range of suction, which makes it more advantageous than alternative techniques such as the filter paper method, pore fluid squeezing or suction probe (Agus and Schanz, 2005). In general, the method is widely used and established in unsaturated soil mechanics (Leong et al., 2003; Cardoso et al., 2007; Seiphoori et al., 2014).

The CMH device utilised in this study is the AquaLab CX-3TE manufactured by ME-TER Group Inc., previously known as Decagon Devices. The maximum deviation of the measured relative humidity is 0.3 %. The theoretical measurement range is between 3 % and 99.9 %, with reliable results achieved between 10 % and 99 %. This corresponds to a theoretical suction range of 0.14 to 476 MPa at 21°C, which is the temperature in the temperature-controlled room, and a reliable range between 1.3 and 312 MPa.

Figure 4.6.: Chilled mirror hygrometer AquaLab CX-3TE used in this study with a plastic lid for loose samples and a closed and an open microcell with meshes for samples at constant volume conditions.

In order to calculate the suction from the measured relative humidity and temperature, it is possible to employ the Kelvin equation (Eq. 2.16).

4.3.2. Microstructural investigations

The microstructure of clays and clay shales can frequently offer insight into the fundamental mechanisms underlying the hydro-mechanical behaviour of the material in question. In this study, the imaging technique of scanning electron microscopy (SEM) and mercury intrusion porosimetry (MIP) were employed to analyse the microstructure.

In both the MIP and SEM, both intact and reconstituted samples were subjected to analysis. This was conducted prior to and following the swelling pressure tests in order

to identify any microstructural alterations resulting from the hydration process. For the MIP, pieces measuring a maximum of $3\times3\times3$ mm were cut from the corresponding powder samples using a scalpel or broken from the corresponding intact material. In order to prevent the smearing of the cut surface, the samples for SEM analysis were broken rather than cut. The maximum size of these samples was $10\times10\times10$ mm. The two methods and the necessary sample preparation are presented below.

4.3.2.1. Rapid (slush) freezing and freeze drying

In order to investigate the microstructure of clays, it is essential that the sample under examination is in a dry state, as this is necessary for a number of techniques. For instance, a vacuum is employed in the process of scanning electron microscopy (SEM) imaging, and mercury is pressed into the pore spaces during the measurement of the pore size distribution (MIP). In both cases, the presence of frozen water in the pore space is a disturbance factor and prevents the respective investigation from being carried out correctly. In the event that the microstructure is of interest in its saturated or partially saturated state, it is of the greatest importance that the sample be dried in a way that is gentle on the structure, as common drying under atmospheric conditions or in an oven lead inevitably to shrinkage of the sample and therefore a change in the microstructure. One suitable technique for this purpose, which is widely used in soil mechanics, is rapid freezing followed by freeze drying (Delage et al., 1982; Shi et al., 1999; Chai and Zhang, 2019; Di Remigio et al., 2021). While rapid freezing implies the shock-freezing of the sample in liquid nitrogen at temperatures of -196°C in order to prevent the expansion of ice crystals, a corresponding device is necessary for the subsequent freeze-drying process. In order to prevent the Leidenfrost effect, in which an insulating layer of vapour forms on the sample surface due to the evaporation of liquid nitrogen caused by the high temperature difference between the sample and the liquid nitrogen, slushy nitrogen is used for rapid freezing when preparing samples for SEM imaging. The Leidenfrost effect results in a slower cooling of the sample, which can lead to the formation of ice crystals on the surface and, consequently, the generation of artefacts in SEM images (Baker et al., 2013).

In the present study, an Alpha 1-2 by Martin Christ Gefriertrocknungsanlagen GmbH (Fig. 4.7a) was employed for the process of freeze-drying. A freeze dryer controls both air pressure and temperature within the drying chamber, thereby facilitating the sublimation process and resulting in the drying of the sample. The process of sublimation implies a direct transition of water from its solid to gaseous state, occurring at a reduced ambient pressure without the intermediate stage of liquid formation. This is illustrated in the

phase diagram of water in Fig. 4.7b. The diagram illustrates the relationship between the state of aggregation of water and the variables of pressure and temperature. The water in the rapidly frozen sample is in the solid phase at atmospheric pressure (1 bar). The pressure within the freeze dryer is regulated by vacuum below the pressure corresponding to the triple point (6 mbar). Subsequently, the temperature is elevated, resulting in the sublimation of the ice. The water vapour that evaporates from the sample precipitates as ice on the integrated condenser. This process is referred to as primary drying. In other fields of application, such as medicine or biology, this is followed by secondary drying, in which more strongly bound water is removed from the material by desorption and diffusion. In soil mechanics, however, primary drying is sufficient to remove the water from a cohesive material, resulting in a water content corresponding to 0 % through oven drying. Subsequently, the sample can be subjected to examination of the microstructure using the corresponding method.
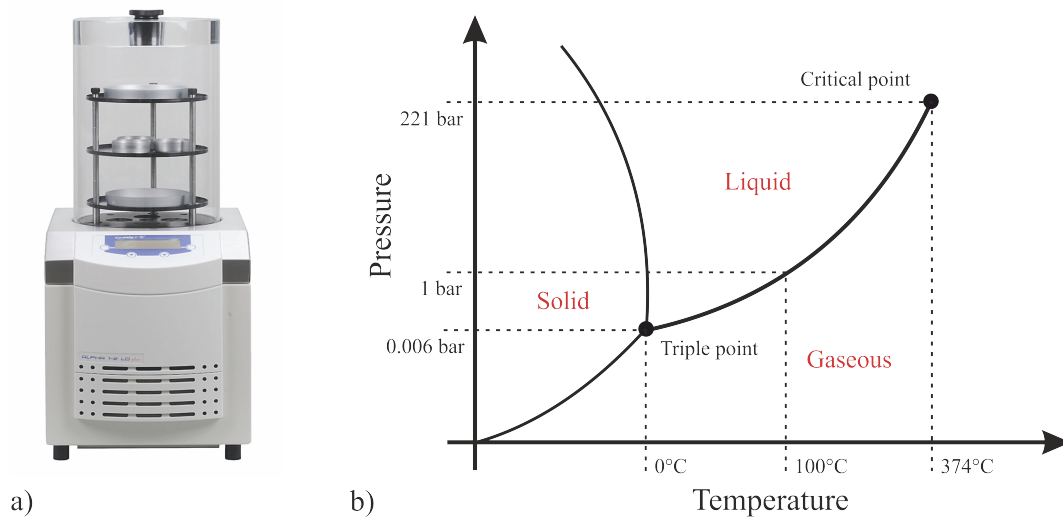
Figure 4.7.: a) Picture of the freeze dryer used and b) phase diagram of water modified after Schwarz et al. (2020).

4.3.2.2. Mercury intrusion porosimetry

Mercury intrusion porosimetry (MIP) is a technique whereby a non-wetting liquid (mercury) is pressed into the empty pore space of a sample, and the applied pressure is correlated with an entrance pore size diameter. Consequently, a pore size distribution (PSD) can be derived. The use of MIP in geotechnical engineering for fine-grained soils was first established by Delage and Lefebvre (1984), although the technique was actually pioneered

earlier by Diamond (1970). The methodology is founded upon the theoretical framework established by Washburn (1921), resulting in the formulation of the well-known Washburn equation for cylindrical pores (Romero and Simms, 2008):

$$p = -\frac{4\,\sigma_{Hg}\cos\theta_{nw}}{x} \tag{4.1}$$

where σ_{Hg} is the surface tension of mercury (σ_{Hg}=0.484 N/m at 25°C), θ_{nw} the contact angle between mercury and the pore wall, and x the entrance pore diameter.

The method is based on the assumption that the pores within the sample are interconnected, both with each other and with the surface of the sample. In addition to the fact that this is not always the case, resulting in the inability to detect closed pores, there are other disadvantages inherent to the method that can lead to erroneous results. One notable example is the phenomenon known as the ink bottle effect. As a consequence of the necessity for higher pressures to fill larger pores, which are connected to the surface or other pores via narrow entrances, these are incorrectly assigned to the volume of smaller pores (Moro and Böhni, 2002). Klaver et al. (2015) identified additional shortcomings in their study. Pores with diameters smaller than the maximum pressure that can be applied, typically around 200 MPa (equivalent to a pore entrance diameter of 7.3 nm), are disregarded. Moreover, the elevated pressures necessary to ascertain the micropores result in the overall compaction of the sample. This, in turn, results in the closure of pores or entrances to pores. The reduction in volume resulting from the compaction is reflected in the data as filled pore space. Additionally, surface imperfections resulting from the sample preparation process or the presence of cracks within the sample may be interpreted as macropores. Nevertheless, the actual geotechnical pore volume is underestimated by the MIP method, as evidenced by Delage et al. (2006). However, despite these shortcomings, MIP remains a well-established and reliable method for determining the PSD of porous media. The PSD can be presented both as a cumulative function and a density function.

4.3.2.3. Scanning electron microscopy

In this study, scanning electron microscopy (SEM) is employed in combination with MIP to yield reliable insights into the microstructural discrepancies between samples, including those that are intact and reconstituted, or dry and saturated. In SEM, an electron beam with an energy between 0.1 and 30 keV is generated by an electron gun and scans the surface of the sample to be analysed. To prevent the electrons from being deflected by molecules in the air, the test chamber is maintained under vacuum conditions. The detectors register a range of emissions resulting from scattering processes when the electrons

interact with the sample. The signals are in turn converted into images in the form of contrasts between the signal intensities. Three distinct image types can be distinguished based on the nature of the emission detected (Goldstein et al., 2018). The aforementioned categories are outlined below.

Backscattered electrons

Backscattered electrons (BSE) are electrons that enter the sample and are repeatedly deflected by elastic and inelastic processes until they finally leave the sample again at a different location. The number of backscattered electrons is observed to increase in accordance with both an increase in atomic number and an increase in the entrance angle of the electron beam. This enables the generation of images through the detection of emission, which contains information regarding both the atomic composition and surface topography.

Secondary electrons

Secondary electrons (SE) are generated at low beam energies (<50 eV) through the release of weakly bound outer shell electrons in atoms undergoing inelastic scattering as the electron beam interacts with the sample. Given the low energy of the electron beam, it only reaches a depth of a few nanometres below the surface. There is no correlation between the atomic number of the atoms and the yield of secondary electrons; however, there is a correlation between the yield of secondary electrons and the angle of inclination of the surface. This makes SE images an appropriate instrument for visualising and analysing the surface topography of a sample in detail.

Energy-dispersive X-ray spectroscopy

Should the energy of an electron beam exceed the binding energy of electrons occupying the inner shells surrounding the atomic nucleus, these electrons may be removed from their shells. The resulting gap can only be closed by the transfer of an electron from the outer shell. The required energy can be generated in two ways: either by the creation of an Auger electron or by the release of X-rays. The resulting X-rays are specific to each element and can be detected by energy-dispersive X-ray spectrometers. Consequently, the material composition of a sample can be visualised through the utilisation of energy-dispersive X-ray spectroscopy (EDS) analysis.

4.3.3. Mechanical testing

In this work, the purely mechanical behaviour of OPA plays a supporting role. The emphasis is on the hydro-mechanical processes that are initiated by mechanised tunnelling.

In order to facilitate the derivation of comprehensive parameter sets for numerical investigations in subsequent works, a series of mechanical tests was conducted on reconstituted OPA with an initial dry density of 2.0 g/cm^3. A sufficient number of studies on intact OPA have been conducted and are available in the literature. The relevant parameters of intact OPA are summarised in Section 5.2. The following sections provide a brief overview of the test conditions employed in the present study on reconstituted OPA.

4.3.3.1. Oedometer testing

A high-pressure oedometer was employed for oedometer testing (Baille et al., 2010). In order to conduct the unsaturated oedometer test, the dry, reconstituted OPA sample (with an initial dry density of 2.0 g/cm^3, diameter of 5 cm and height of 2 cm) was installed in the device and subjected to incremental loading up to 21 MPa, followed by stepwise un- and reloading. In order to conduct the saturated oedometer test, the compacted sample was saturated under constant volume conditions with deionised (DI) water upon installation. Once the swelling and saturation process was complete, as indicated by equilibrium in the swelling pressure development, the same loading, unloading and reloading path was initiated.

4.3.3.2. Triaxial testing

The device employed in this study is a High Pressure Triaxial Cell Type WF40020 ET manufactured by Wykeham Farrance Engineering Limited. One drained and one undrained triaxial test series were conducted on compacted OPA powder with an initial dry density ρ_d of 2.0 g/cm^3. The compacted samples had an initial diameter of 3.5 cm and a height of 8 cm with a water content of 2.3 %. The prepared samples were placed in a membrane within the triaxial device and a support pressure of 0.3 bar was applied for the following saturation process with a backpressure of 0.2 bar. Consequently, the samples underwent swelling under a pressure of 10 kPa. Once the swelling of the sample was complete, as determined by the displaced water in the cell and thus the volume change of the sample, the support pressure was increased to 3.2 bar and the back pressure to 3 bar. This process removed the residual air from the pore system, allowing the B-test to be conducted. Following a successful B-test ($B > 0.95$), the sample was consolidated at the effective confinement pressure (σ'_3) of the respective test. The series of tests was conducted using values of 100, 300 and 500 kPa. The volumetric deformations of the samples resulting from saturation and consolidation were incorporated into the subsequent data

analysis. A shear rate of 0.003 mm/min was employed for all tests. The initial porosities of all samples, prior to shearing but subsequent to saturation and consolidation, are presented in Table 4.8.

Table 4.8.: Porosity of samples in all conducted triaxial tests after saturation and consolidation, before shearing.

		CD			CU		
σ_3'	[kPa]	100	300	500	100	300	500
n	[-]	0.306	0.276	0.261	0.297	0.259	0.254

4.3.4. Hydro-mechanical testing

In order to study the hydro-mechanical behaviour of OPA in the context of mechanised tunnelling, a variety of devices and techniques were employed. The conventional isochoric swelling pressure cells that were already available at the chair were supplemented by new devices that were developed within the scope of this study. These comprise, on the one hand, swelling pressure cells designed for mechanised tunnelling relevant boundary conditions and, on the other hand, a cubic cell for the determination of the anisotropic swelling strains of clay shales. The following section introduces the methodologies employed.

4.3.4.1. Determination of soil-water characteristic curves

In the present study, a total of four soil-water characteristic curves (SWCCs) were determined. Two SWCCs were determined for each of the intact OPA and the reconstituted OPA with an initial dry density of 2.0 g/cm³. One SWCC determination was conducted under constant volume conditions, and the other under unconstrained conditions. The initial state for the determination of the SWCCs was the in-situ water content and suction of the intact OPA, along with the hygroscopic water content of the OPA powder and the resulting suction after compaction. Subsequently, the samples were subjected to both saturation and drying processes. These two states were selected as initial states, as they are relevant for subsequent studies. The in-situ water content and the corresponding suction of the intact material constitute the initial state for the practical background of this study, namely swelling during mechanised tunnelling. The hygroscopic water content and the corresponding suction in the compacted state of the OPA powder serve as the

basis for all hydro-mechanical tests conducted in this study. The conventional approach for determining a SWCC, which begins with drying from the slurry state (thoroughly mixed with $w = 1.1 \cdot w_l$) is rather irrelevant for the present study. The initial conditions are summarised in Table 4.9. A range is provided for intact OPA, as the initial states differ slightly for various intact samples.

Table 4.9.: Initial conditions of the determined SWCCs of intact and reconstituted OPA ($\rho_d = 2.0$ g/cm^3).

		Intact OPA	Compacted powder
ψ_{init}	[MPa]	60-65	68
S_r	[%]	63-67	18

In order to ensure constant volume conditions, samples were installed in microcells in accordance with the methodology proposed by Seiphoori et al. (2014), which can be seen in Fig. 4.6. The use of microcells precluded the application of the OM and ATT methods for determining the SWCC in this study. This is because both methods require the water in the soil sample pores to be in contact with the water in the ceramic plate (ATT) or the surrounding PEG solution (separated by a membrane; OM). Given the suitability of the VET in combination with microcells, this experimental method was employed exclusively in this study to determine the SWCCs. Consequently, only the suction range between 3 and 350 MPa was covered. However, this limitation in the methodology does not affect the accuracy of the SWCC, as the air entry values (AEV) for intact OPA samples were above 10 MPa (Ferrari, 2014). The samples of reconstituted OPA were stored in an additional step after finishing the VET in a closed container with deionised water to achieve higher degrees of saturation and thus suctions under 3 MPa.

The samples for constant volume conditions were prepared in accordance with the methodology outlined in Section 4.2 and then stored in desiccators. In the case of free swelling conditions, compacts of powder or shards of intact OPA were stored directly in small plastic containers in the desiccators. The desiccators were filled with oversaturated salt solutions, which allowed for the exposure of the samples to a defined suction. The employed oversaturated salt solutions and their corresponding relative humidities at 20°C are presented in Table 4.10. Nevertheless, the final suction of the samples was measured with a CMH (see Section 4.3.1.2) once equilibrium of the sample masses was established.

The void ratio required to determine the degree of saturation for the free swelling SWCC was determined in a manner analogous to that described in Section 4.3.1.1.

Table 4.10.: Theoretical relativ humidities and resulting suctions at 20°C for different saturated salt solutions used in this study.

Salt		K_2SO_4	KNO_3	KCl	NaCl	$NaNO_2$	LiCl
RH	[%]	97	94	86	76	66	12
Suction	[MPa]	4.1	8.4	20.4	37.1	56.1	218.7

The experimental data were fitted with the van Genuchten equation (Eq. 2.17). The air-entry value (AEV) was determined according to the definition of the commonly used graphical construction method (Pasha et al., 2016), where the AEV is defined as the intersection of the tangent through the inflection point of the SWCC and the horizontal line of $S_r = 1$. Here, however, this exact value was calculated explicitly, in accordance with the approach outlined by Soltani et al. (2021) via the first (Eq. 4.2) and second derivatives (Eq. 4.3) of the van Genuchten equation, resulting in the equation for the inflection point ψ_i of the SWCC (Eq. 4.4) and, finally, yielding Eq. 4.5 for the suction at the AEV ψ_{AEV}.

$$f'(\psi) = \frac{-nm(\alpha\psi)^n}{\psi[1+(\alpha\psi)^n]^{m+1}} \tag{4.2}$$

$$f''(\psi) = \frac{nm(\alpha\psi)n[(nm+1)(\alpha\psi)^n - (n-1)]}{\psi^2[1+(\alpha\psi)^n]^{m+2}} \tag{4.3}$$

$$\psi_i = \frac{1}{\alpha}\left(\frac{1}{m}\right)^{\frac{1}{n}} \tag{4.4}$$

$$\psi_{AEV} = \psi_i\exp\left(\frac{m+1}{nm}\left(1-\left(\frac{m+1}{m}\right)^m\right)\right) \tag{4.5}$$

where m, n and α are the Van Genuchten fitting parameters (Eq. 2.17).

Nevertheless, there are additional, more pragmatic definitions, such as the suction, which corresponds to a degree of saturation of 95 % (Ferrari et al., 2014) or as introduced in Section 2.2.2 according to Baille (2014), the suction, where air enters the pore space of the sample and thus the degree of saturation becomes less than 100 %.

An additional method to obtain information about the water retention behaviour of a soil is to derive it from the pore size distribution through the utilisation of MIP. The method associates the mercury intrusion with the drying path of a SWCC by considering

the mercury intrusion at a given pressure, p, to be equivalent to the air intrusion at a matric suction, ψ_m (Eq. 4.6) (Ferrari and Romero, 2019).

$$\psi_m = -\frac{4 \sigma \cos \theta_w}{x}; p = -\frac{4\sigma_{HG} \cos \theta_{nw}}{x} \tag{4.6}$$

where σ is the surface tension of water, θ_w the wetting coefficient for the air - water interface, σ_{HG} the surface tension of mercury and θ_{nw} the contact angle between mercury and particle surface.

The following equation is obtained by rearranging the previous equations and setting the parameters for 25°C:

$$\psi_m = -\frac{\sigma \cos \theta_w}{\sigma_{Hg} \cos \theta_{nw}} p \approx 0.196 \, p \tag{4.7}$$

The corresponding degree of saturation S_r for a suction ψ_m is given according to Romero et al. (1999) by

$$S_r = (1 - S_{r,nw}) \tag{4.8}$$

where $S_{r,nw}$ is the mercury degree of saturation as a quotient of the mercury intruded porosity by the total porosity.

To additionally consider the hygroscopic water content of strongly attracted adsorbed water to the mineral surface and the porosity that cannot be filled by mercury, the expression is modified to

$$S_r = (1 - S_{r,nw}) + S_{r,nw}\frac{w_r}{w_{sat}} \tag{4.9}$$

where w_r is the residual water content and w_{sat} the water content at full saturation.

The derivation of the matric suction-saturation relationship from MIP should be limited to the low-suction range, in which capillarity is the dominant factor governing water retention properties. From the pore size separating inter-aggregate and intra-aggregate pores (130-180 nm) in combination with the Laplace equation (Eq. 4.6) Romero et al. (1999) derived an upper limit of 2 MPa. Other studies have demonstrated that satisfactory results can be obtained for fine-grained soils with suction values up to the AEV (Garcia-Bengochea et al., 1979; Cardoso et al., 2023). For higher suctions, the predictions derived from MIP significantly underestimate the degree of saturation. This can be attributed, according to Romero and Simms (2008), to two main issues. Firstly, the utilisation of smaller samples for MIP introduces a discrepancy in accessibility of the pores when compared to the larger samples employed for the experimental determination of SWCCs. Secondly, the GSD of plastic soils undergoes a notable alteration throughout the drying and wetting phases, due to the influence of shrinkage and swelling processes. However, the deviations from

the latter are significantly reduced when employing the methodology on soils that do not experience significant volume changes during these hydraulic paths. These soils include soft rocks and clay shales like OPA.

4.3.4.2. Isochoric cells for swelling pressure tests with subsequent hydraulic conductivity tests

Basic isochoric swelling pressure cells were employed for some of the swelling pressure tests conducted under constant volume conditions (Section 5.3.4.1) and hydraulic conductivity tests (Section 5.3.1). These were constructed as part of the study of Khan (2012) and described more in detail in Schanz et al. (2013). A scheme and photography of the cell are presented in Fig. 4.8.

The rigid cells are constructed from V2A stainless steel, which exhibits resistance to corrosion. A top cap ensures volume-constant conditions and supports a load cell via a piston. The cell is equipped with two upper and two lower connections. The aforementioned connections permit the flushing and saturation of both parts of the cell. This marks the beginning of the swelling pressure test. Once equilibrium has been reached in the swelling
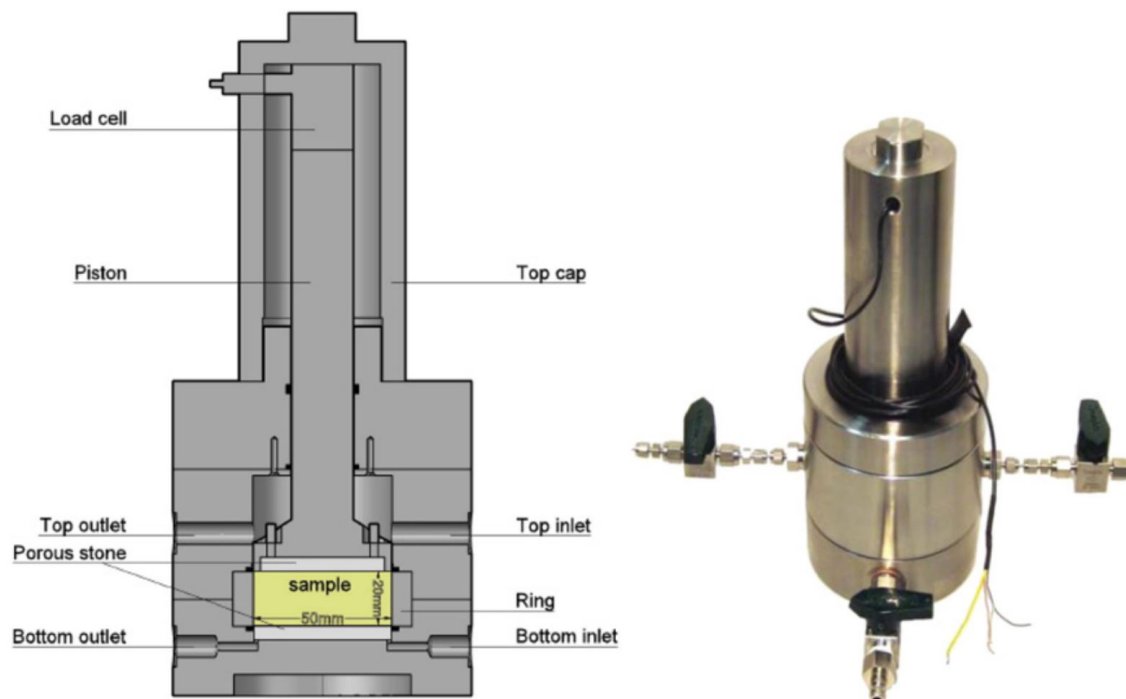

Figure 4.8.: Scheme and photography of the used isochoric cell from Schanz et al. (2013).

pressure development and the swelling pressure test has been accomplished, a volume pressure controller (VPC) can be connected at the bottom and a burette at the top. Accordingly, the sample is subjected to a controlled flow, which is measured over time in the burette attached to the top connection, and the hydraulic conductivity k can be determined via Darcy's law:

$$k = \frac{Q \cdot L}{A \cdot \Delta h} \tag{4.10}$$

where Q is the flow rate, L the length of the sample, A the area of the sample and Δh the pressure drop.

Thereby, the hydraulic gradient i is defined as

$$i = \frac{\Delta h}{L} \tag{4.11}$$

In the tests carried out, an applied pressure of 50 kPa and thus a pressure drop Δh of 5.0 m was employed. Given the dimensions of the sample, this equates to a hydraulic gradient i of 255. This hydraulic gradient was selected in order to facilitate the measurement of a reasonable flow rate, given the low expected permeability.

4.3.4.3. Swelling pressure cells for tunnelling relevant boundary conditions

In order to conduct this study, multi-purpose swelling pressure cells were designed and constructed. A total of four of these cells have been produced and are available for research. The development of the cells was oriented towards the consideration of boundary conditions pertinent to tunnelling during the swelling test, with a particular focus on mechanised tunnelling. Two significant characteristics of the cells can be identified as a consequence of this. Primarily, the combination of a spindle with a laser and a LVDT sensor provides precise control of the volumetric boundary conditions throughout the swelling process. Consequently, constant volume boundary conditions can be maintained, which represent a rigid tunnel lining. Free swelling can be allowed, which represents the case without a tunnel lining. Additionally, volumetric deformations during swelling can be allowed in a controlled manner to represent the case of a flexible tunnel support system. Furthermore, the cell enables direct saturation of the sample with water, which reflects the practical scenario of clay rock saturation along the tunnel via an advective flow or a stepwise vapour phase saturation, which represents a saturation by an unloading-induced diffusive flow in a radial direction towards the tunnel.

Fig. 4.9a and 4.9b, respectively, show a photograph of the cell and a general scheme. The sample is positioned between two porous stones. Two inlets or outlets are provided above

and below the sample for the flushing, saturation or circulation of a liquid or vapour. Consequently, two distinct saturation modes can be employed: I) water saturation via a burette (Fig. 4.9c), also referred to as single-step saturation in this study, and II) vapour saturation via the circulation of a vapour with a defined relative humidity with a peristaltic pump (Fig. 4.9d), here referred to as multi-step saturation. Thereby, the relative humidity is controlled by an oversaturated salt solution, which is integrated into the circulatory system in a gas washing bottle. The acting suction can be calculated by considering the temperature with the Kelvin equation (Eq. 2.16). The salt solutions and corresponding relative humidities employed, along with the resulting suctions, are outlined in Table 4.10. In addition to being situated within a temperature-controlled room (at 21°C), the cells are also equipped with temperature sensors. Furthermore, the four inlets and outlets at the cell also permit the performance of hydraulic conductivity tests on expansive materials.

The spindle on top of the cell can be utilised to implement volume-constant boundary conditions for a conventional swelling pressure test when being in contact with the radial ball bearing. In the event of the spindle being entirely removed, an almost free swelling heave test can be conducted. Due to the self-weight of the required top part of the cell to which the laser sensor is attached, a residual pressure of 10.5 kPa acts on the sample in the vertical direction during free swelling. A distinctive attribute of the cell is the capacity to conduct swelling pressure tests under precisely controlled volumetric deformations. For this purpose, the spindle can be utilised with a lever even under high pressures due to the installed ball bearing. Two load cells are installed, one above and one below the sample, in order to ascertain the impact of friction from the expanding sample within the sample ring during the application of volumetric deformations. However, no influence could be determined in any of the tests within this project. The difference between the measured swelling pressures of the two load cells remained constant throughout the tests. Accordingly, an averaged value from both load cells was used for the evaluation in this work. An LVDT is affixed to the spindle and is utilised to quantify the applied deformations. An additional laser sensor is attached directly above the sample, with its counterpart situated beneath the sample. This enables the exact measurement of the deformation that actually occurs in the sample to be measured. Consequently, the measurement of the laser sensor also includes the significantly small self-deformation of the cell.

All constant-volume swelling pressure cells exhibit self-deformations. Such deformations are attributable to the strain experienced by both the rigid stainless steel frame and the load cells themselves. In a load cell, a mechanical input force is converted into an electrical signal via a strain gauge. As the pressure increases, the strain gauge is subjected to greater

compression, resulting in a corresponding increase in electrical resistance. It is therefore necessary to allow for a certain amount of deformation in order to be able to measure a force with a load cell. In the majority of studies utilising constant-volume swelling pressure tests, these self-deformations are ignored. To ascertain the self-deformation of the new swelling pressure cell as a function of the acting pressure, swelling pressure tests with constant volume conditions were conducted. The observed deformations are those of the load cells, as it is assumed that the swelling pressure cell is sufficiently rigid to preclude any deformations. This resulted in the linear relationship, as presented in Fig. 4.10 and expressed by the following equation:

$$x_{sd} = 5 \cdot 10^{-5} \cdot p_s - 0.00743 \tag{4.12}$$

with the swelling pressure p_s in kPa and yielding the deformation of the device x_{sd} in mm.

4.3.4.4. Comparison of the proposed and established methods

The swelling pressure cell presented in the previous section and the associated methodology diverge from the established methods described in Huder and Amberg (1970) and Madsen (1999). In contrast to the established methods, which utilise conventional oedometer cells and are run stress-controlled, the stress-strain paths in this study are run strain-controlled in specially designed cells. The necessity of using multi-purpose swelling pressure cells in tests on compacted powder is demonstrated later in Section 5.3.5.3 through using a series of tests. Nevertheless, these cells also offer certain advantages over the established methods in tests on intact OPA. These are discussed in the following.

In their study of diagenetically solidified clay rocks, von Wolffersdorff and Fritzsche (2003) demonstrated that stress-strain correlations derived from stress-controlled tests conducted in oedometer cells and strain-controlled tests conducted in swelling pressure cells exhibit significant discrepancies. The average strain at a given stress in the stress-controlled tests was approximately eight times that observed in the strain-controlled tests. The results of the strain-controlled tests in swelling pressure cells are in closer alignment with the in-situ measured data. It can thus be concluded that this method is far more suitable for investigating and describing the in-situ swelling behaviour of diagenetically solidified clay rocks under laboratory conditions. As a potential source of error, they indicate the preloading in the stress-controlled experiments in oedometer cells, which is specified both in Huder and Amberg (1970) (preloading, unloading and reloading) and in Madsen (1999) (only preloading). It is postulated that this process results in the destruction of the diagenetic
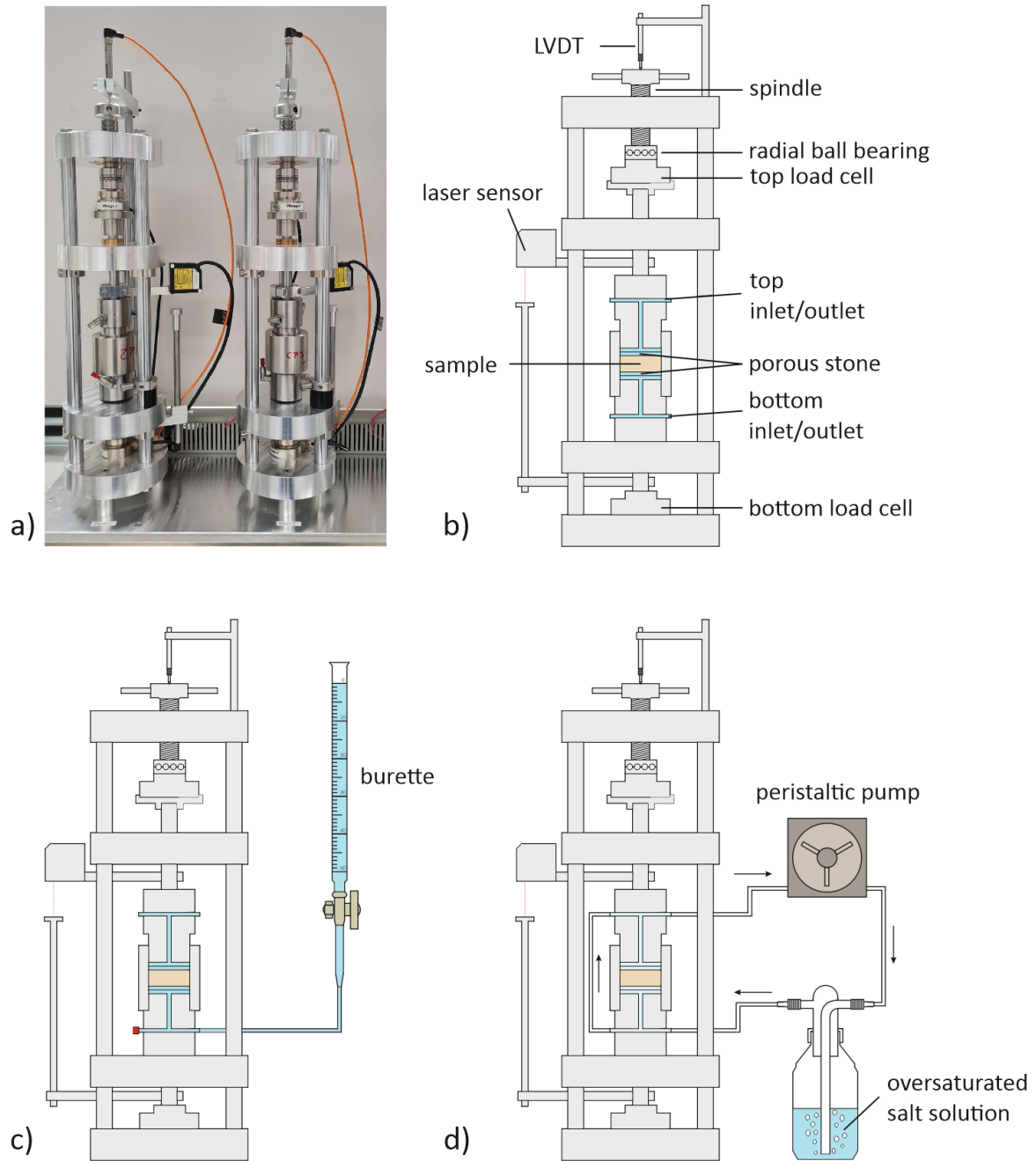
Figure 4.9.: Newly designed swelling pressure cell for tunnelling relevant boundary conditions: a) Photography of two cells, b) general scheme and setups for c) single-step and d) multi-step saturation.
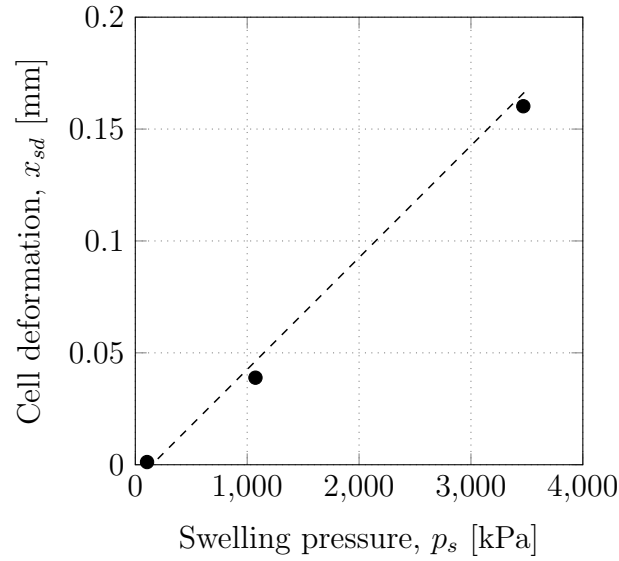
Figure 4.10.: Self-deformation of the newly developed swelling pressure cells over swelling pressure.

bonds of the intact samples, leading to a considerable overestimation of the swelling pressure (von Wolffersdorff and Fritzsche, 2003; Pimentel, 2015). Vergara (2019) proposed that the discrepancy in the stress-strain correlation between the stress- and strain-controlled tests could be reduced by incorporating explicit consideration of the purely mechanical strains. However, the initial differences in the underlying tests conducted with the two methods were considerably smaller than those observed in von Wolffersdorff and Fritzsche (2003). Vergara (2019) further highlighted the benefits of the strain-controlled method, noting that stress-controlled tests require a significantly longer time to reach equilibrium during swelling, thereby saving considerable time.

In Pimentel (2015), the emphasis was also placed on the discrepancies in the methodologies employed to ascertain the swelling pressure. Similarly, it was concluded that strain-controlled tests conducted in purpose-built swelling pressure cells represent the most appropriate methodology. In addition to the aforementioned points, the rigidity of the cells employed is highlighted as a crucial element. It is essential that the cells be sufficiently rigid to prevent the measured swelling pressure from being falsified by unwanted swelling strains. This is applicable to both swelling pressure and oedometer cells. The measurement of occurring strains and subsequent strain compensation represents an inadequate solution, as this process results in the destruction of the clay matrix within the swollen sample, thereby introducing a falsification of the results.

It is also noteworthy that the swelling pressure cell described in Vergara (2019) is highly comparable to the current study's methodology and the swelling pressure cell itself. However, the cell presented here incorporates a number of additional features that distinguish it from other models. Laser sensors are employed to enable precise measurement of the exact deformation of the sample. Furthermore, two load cells are employed, one above and one below the sample, with the objective of ascertaining any potential pressure loss due to friction. However, there are primarily two additional features that distinguish this cell from the one described in Vergara (2019). The configuration of the cell with two inlets and outlets, positioned above and below the sample, enables the circulation of a vapour around the sample at a controlled relative humidity and at a constant temperature, and therefore with a controlled suction. This allows for the gradual saturation of the sample. Furthermore, a defined volume flow of water can be applied to the bottom of the sample, while the outflow at the top can be measured, and thus the hydraulic conductivity can be determined. Strain can be applied through the spindle during the test, thus enabling the analysis of hydraulic conductivity at varying void ratios.

4.3.4.5. Cubic cell for three dimensional swelling

In order to measure the three-dimensional swelling strain of an anisotropic clay shale, a cubic swelling strain cell was developed and constructed as part of this study. The objective was to ensure a slow and homogeneous saturation and to examine the intrinsic anisotropy of the tested material. A scheme of the cell is provided in Fig. 4.11. The cubic shape of the cell is based on the cubic shape of the sample under study, which in turn is a necessary consequence of the intrinsic anisotropy of a clay shale. The sample (1 in Fig. 4.11) can be placed through the two installation hatches (2, 3) on the rectangular sample holder (4, 5, 6), which is trenched and covered by a folded filter paper. Installation hatches as well as the plexiglass discs (7) holding the horizontal LVDTs (8, 9) are fixed with knurled screws (11) and sealed with o-rings. The holder for the vertical LVDT (10) is fixed at the top plate (12) of the cubic cell. LVDTs can be directly attached to the sample.

The cell permits the sample to be saturated once more in two distinct modes: single-step saturation with water or multi-step saturation via vapour. When in direct contact with water, clay shales are prone to delamination and dissolution. Accordingly, the saturation rate must be maintained at a relatively low level. This was accomplished in the aforementioned configuration through the utilisation of two wicks and an elevated water tank (18) situated atop the cubic cell. One end of the wick is situated within the water tank,

with the wick then passing through the feedthrough (19). The end of the wick is affixed within a trench in the lateral walls (4, 5) of the sample holder, situated behind the filter paper. The filter paper ensures an even distribution of water across the entire contact surface, including both sides and the bottom, thereby facilitating homogeneous saturation of the sample. The wick in use was observed to transport water at a rate of 0.005 g/h. The multi-step saturation via vapour is once again conducted with the same salt solutions presented in Table 4.10, which are also employed for the determination of the SWCC with the VET method (Section 5.3.2) and swelling pressure tests (Section 5.3.4.3). Therefore, the salt solution is filled into a tank (20) situated beneath the sample holder. The sample holder and tank are separated by a perforated plate (21). The cubic cell is hermetically sealed with a plug in the feedthrough, and the relative humidity within the cell is regulated by means of the salt solution. The tank beneath the sample is filled with DI-water during a test with water saturation to prevent drying. Photographs of the sample holder with attached filter paper and sample are presented in Fig. 4.12a, alongside the cell in its entirety, including the installed LVDTs and the complete data acquisition system (Fig. 4.12b). A closer image of the sample with attached LVDTs is also provided (Fig. 4.12c).

The complete cell is again placed in the same temperature-controlled room at 21°C like the swelling pressure cells for tunnelling relevant boundary conditions, in order to eliminate any potential temperature-related effects.
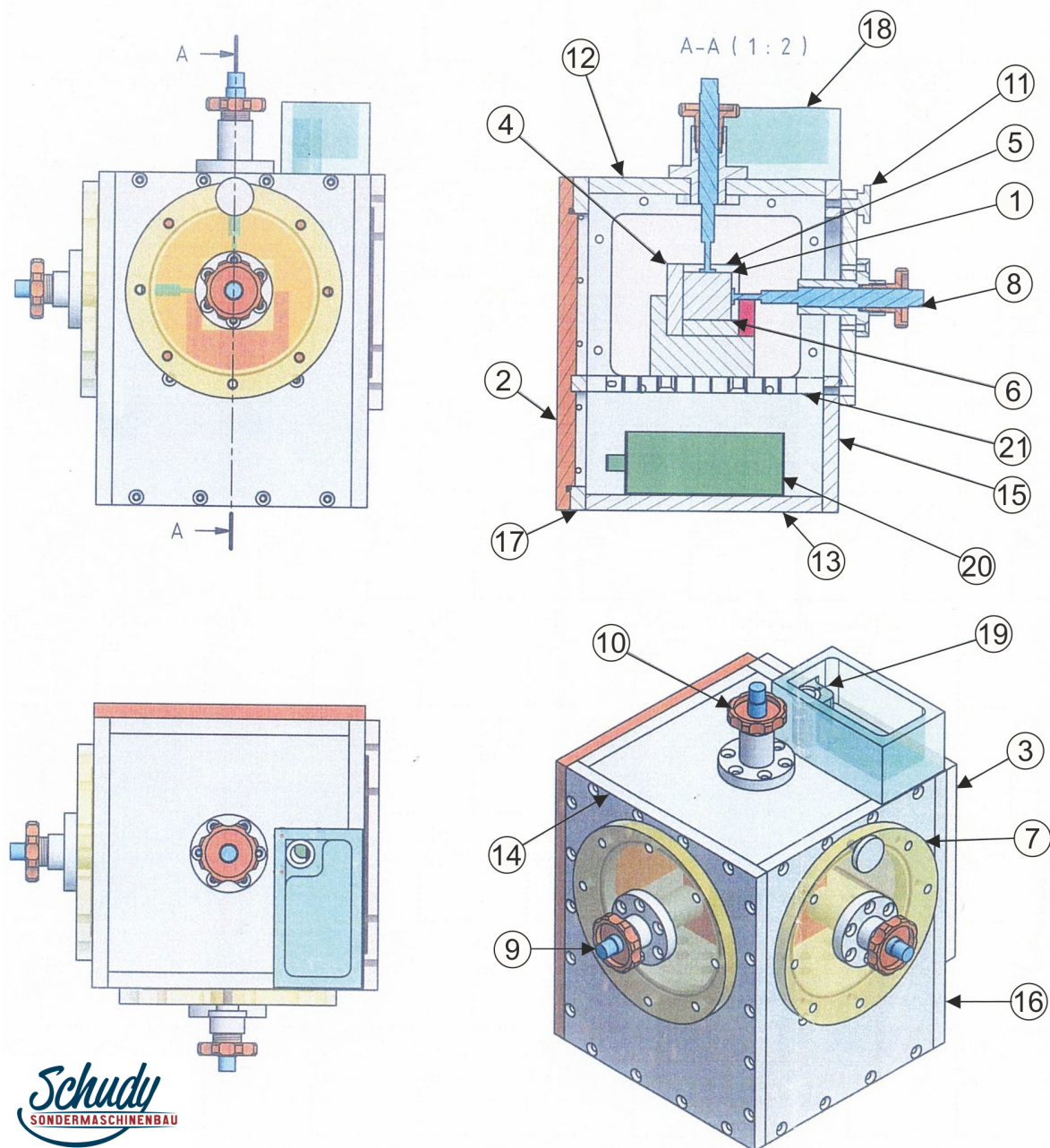
Figure 4.11.: Newly designed swelling strain cell for anisotropic clay shales: 1) Sample, 2) installation hatch Nº1, 3) installation hatch Nº2, 4) side wall Nº1 of the sample holder, 5) side wall Nº2 of the sample holder, 6) bottom plate of the sample holder, 7) plexiglass disc, 8) horizontal LVDT Nº1, 9) horizontal LVDT Nº2 10) vertical LVDT, 11) knurled screw, 12) top plate of the cubic cell, 13) bottom plate of the cubic cell, 14) side wall Nº1 of the cubic cell, 15) side wall Nº2 of the cubic cell, 16) side wall Nº3 of the cubic cell, 17) side wall Nº4 of the cubic cell, 18) upper water tank, 19) feedthrough, 20) tank for salt solution and 21) perforated plate. Sketched by Sondermaschinenbau Schudy.
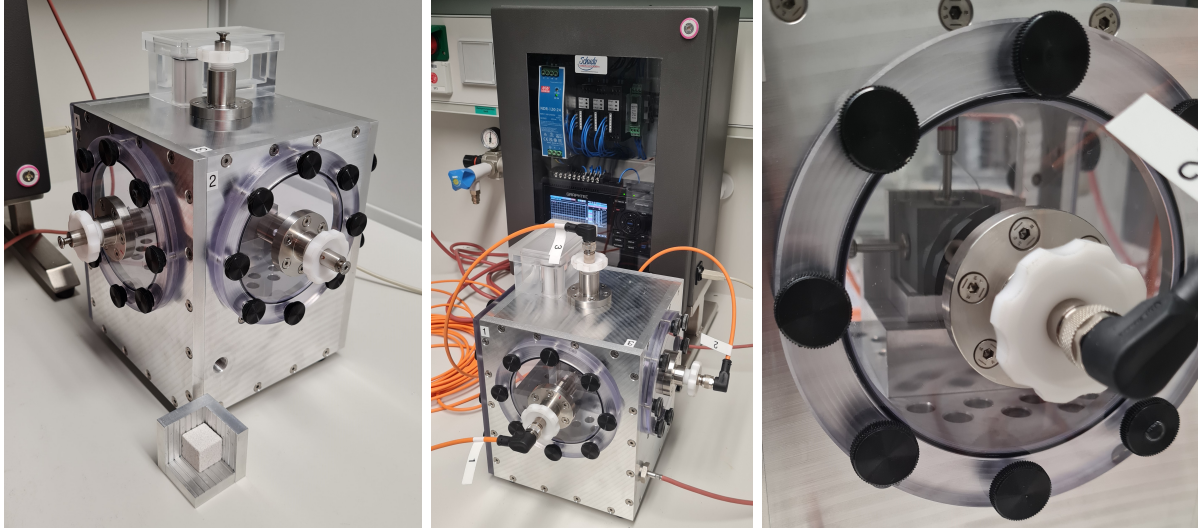
Figure 4.12.: Photographs of the newly designed cubic swelling strain cell for anisotropic clay shales. a) Cell with sample holder and dummy, b) fully equipped cell with LVDTs and data acquisition system and c) detail of the installed sample.

4.3.5. Thermal conductivity measurement

Thermal conductivity tests were conducted in the geotechnical laboratory of the Universitat Politècnica de Catalunya UPC in Barcelona, Spain. The setup was described in Sau (2021) and designed for especially testing the thermal conductivity of deep agrillaceous formations. The cell is constructed from polyetheretherketon (PEEK), which exhibits a low linear coefficient of thermal expansion, low thermal conductivity and a high mechanical stiffness. Consequently, the cell exhibits insulating and relatively rigid properties. It can be loaded in an oedometer to replicate in-situ conditions and to close bedding planes of the tested sample that may have opened due to extraction-induced unloading. A scheme of the cell is shown in Fig. 4.13. The dimensions of the tested soil samples are 38 mm in diameter and 40 mm in height. The sample is covered in a neoprene membrane to prevent water loss. A heat flux is applied at the top of the sample, and the temperature development throughout the sample is observed by a total of seven thermocouples (T_1-T_7). Thermocouples T_1 and T_2 are employed to determine the input heat flux q_{in}, while T_6 and T_7 are used to determine the output heat flux q_{out} in accordance to Fourier's law. Therefore, at the top and bottom, heat flux sensors consisting of a polycarbonate disc as reference material with a thermal conductivity of $\lambda_{poly} = 0.2$ Wm^{-1}K^{-1} and the height of $h_{poly} = 1$ mm are sandwiched by two highly conductive aluminium discs. Their thermal

gradient is assumed to be negligibly small and thus, q_{in} and q_{out} are given by:

$$q_{in} = \lambda_{poly}(T_1 - T_2)/h_{poly} \tag{4.13}$$

$$q_{out} = \lambda_{poly}(T_6 - T_7)/h_{poly} \tag{4.14}$$

The temperature in the sample is furthermore monitored at 1, 2 and 3 cm height with thermocouples T_3-T_5. For this purpose, small holes, 1 mm in diameter and 10 mm in depth, were drilled into the sample for the installation of the thermocouples. In all tests, a vertical load of 4.5 MPa was applied, which corresponds to in-situ pressure estimations in the STB. Tests were conducted with an applied temperature of 50°C and the cell was additionally encased in a heat-insulating foam.

After a steady-state is reached, the thermal conductivity λ can be calculated with Fourier's law as:

$$\lambda = (q_{in} - q_{out})h/(T_2 - T_6) \tag{4.15}$$
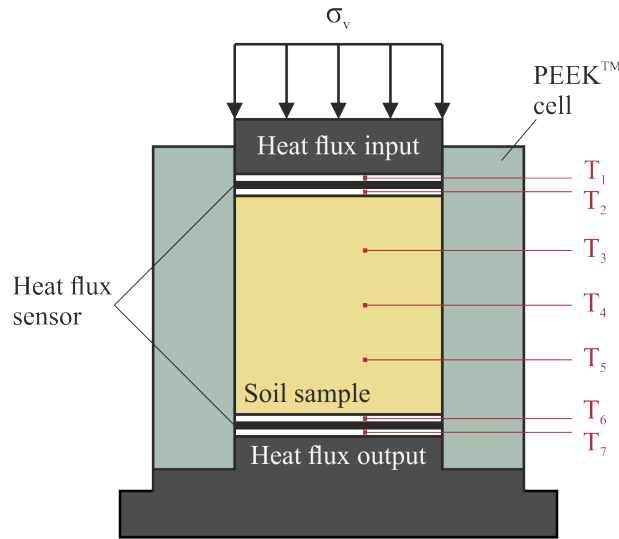
with h being the sample height.

Figure 4.13.: Scheme of the cell used at the UPC in Barcelona for determining the thermal conductivity of intact and reconstituted OPA.

5. Results and discussion

This chapter presents and discusses the most significant findings derived from this research project. Firstly, the analysed materials are subjected to an examination on the basis of microstructure investigations. In addition to intact OPA, compacted powder samples as reconstituted OPA are also subjected to analysis. The reference dry density is 2.0 g/cm^3, as this results in a comparable swelling pressure to that observed with intact OPA perpendicular to the bedding plane orientation. In order to examine the impact of the initial dry density on the hydro-mechanical behaviour, a range of 1.8 to 2.2 g/cm^3 is considered. In general, reconstituted samples are selected for investigation of the fundamental mechanisms of the hydro-mechanical behaviour, without the influence of inhomogeneities and anisotropy. This allows the development of concepts with the least influence of uncontrolled natural aspects, as the samples are free from the effects of such factors. These concepts can subsequently be applied to intact OPA (e.g., Section 5.3.6). Nevertheless, in order to ensure comprehensive coverage of the topic, mechanical investigations are conducted in order to derive complete parameter sets for potential further numerical studies.

The majority of the work is dedicated to hydro-mechanical investigations. First, the investigation focuses on two primary areas: hydraulic conductivity and water retention behaviour. Afterwards, a study is conducted to investigate the influence of the grain size distribution on the hydro-mechanical behaviour of OPA powder. The next work package examines the impact of the fabric and the initial dry density of the reconstituted OPA, a gradual saturation via the vapour phase and the initial degree of saturation through the utilisation of constant volume swelling pressure tests. The free swelling tests represent the other limit state and are employed to establish the maximum volumetric swelling potential as a function of the initial dry density for reconstituted OPA or taking into account the anisotropy, namely the bedding plane orientation, of intact OPA. The relevance of the initial microstructure is also subjected to analysis through a series of tests. This is followed by the central component of the study. The recently developed swelling pressure cells for tunnelling relevant boundary conditions are employed to examine the evolution of the swelling pressure in strain-controlled swelling pressure tests. Based on the consistent

behaviour observed in homogeneous reconstituted OPA, a concept including a simplified design chart is presented and subsequently validated on intact OPA. Finally, a study on thermal conductivity is conducted, providing a foundation for a forthcoming planned project investigating the influence of annual temperature cycles on the hydro-mechanical behaviour.

5.1. Microstructural analysis

The section presenting the microstructural investigations is intended to characterise the initial material under examination and to illustrate the differences between intact and reconstituted samples. Furthermore, the observations made on swollen samples offer insight into the fundamental processes occurring during constant volume hydration. This is achieved through a combination of quantitative and qualitative analysis. The former employs the results of mercury intrusion porosimetry (MIP), which are expressed in the form of pore size distributions and cummulative pore volumes. The latter utilises scanning electron microscope (SEM) images. In examining the microstructure, it is important to pay attention when interpreting the results obtained in the swollen state. In order to obtain a sample from the swollen material for further analysis, it is first completely unloaded due to the dismantling procedure. This naturally leads to immediate volumetric deformations, which in turn increases the pore volume.

5.1.1. Comparison of the pore-size distribution of intact and reconstituted OPA in different states

The results of the MIP on intact and reconstituted OPA with an initial dry density of $2.0 \, \text{g/cm}^3$ for the initial as well as the fully saturated state with hydration under constant volume conditions are presented in Figs. 5.1 and 5.2. Fig. 5.1 illustrates the data in terms of differential intrusion, which represents a distribution of the pore sizes. Fig. 5.2 depicts the cumulative intruded void ratio.

Fig. 5.1 shows a monomodal pore size distribution for the intact OPA in the initial state. The data indicate the presence of a single peak, representing the majority of pores of a similar size, within the micropore region, with a diameter of approximately 12 nm. This finding is consistent with observations in the literature for OPA from the same facies and similar depth, which also demonstrate a monomodal pore size distribution

with peaks in this order of magnitude (Muñoz et al., 2009; Ferrari et al., 2014; Seiphoori et al., 2017). The influence of swelling under constant volume conditions on the pore size distribution of intact OPA is found to be minimal, resulting in a modest reduction of the micropores. This phenomenon occurs because the swelling pressure is less than the actual overconsolidation pressure, which results in the structure remaining almost unchanged at this level of stress. In contrast, the reconstituted OPA sample initially exhibits a bimodal pore size distribution, which is to be expected for compacted dry clay powder (see Section 2.1.3.1). This is evidenced by the peaks observed for the macropores at a diameter of approximately 420 nm and for the micropores at a diameter of approximately 20 nm. Macropores represent inter-aggregate pores, while micropores represent intra-aggregate pores. The saturation of the compacted powder under constant volume conditions results in a notable reduction in the diameter of the macropores. Macropores close due to the swelling of the clay particles that occurs during the hydration process. In this case, the peak of macropores is reduced and shifted to a pore diameter of approximately 200 nm. No notable alteration could be indentified in the micropores. The peak is only minimally reduced, which may be attributed to the occurrence of natural smaller deviations within the material, which inevitably give rise to results that vary slightly from one another. Nevertheless, this phenomenon can also be attributed to the poor connectivity of the pore space observed in clay shales (Keller et al., 2013).
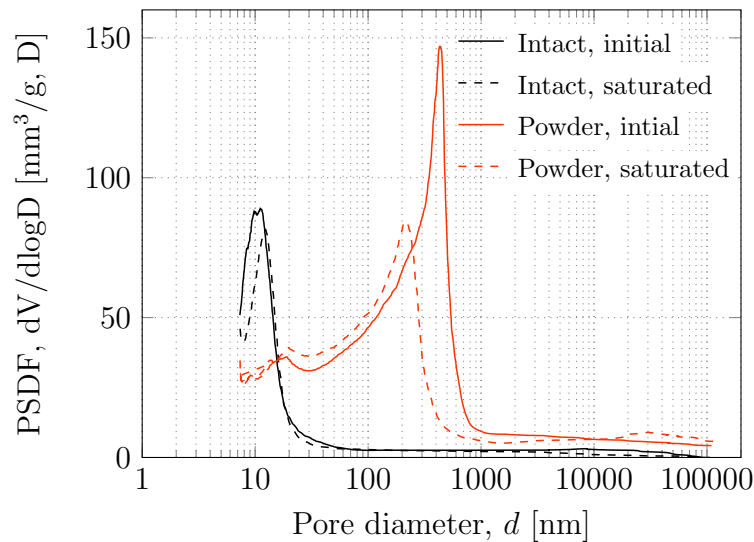

Figure 5.1.: Pore size density function (PSDF) before and after volume-constant swelling for intact as well as reconstituted OPA.

An analysis of the intruded void ratio as presented in Fig. 5.2 reveals that it is diminished for both materials following volume-constant saturation. As saturation under volume-

constant conditions does not affect the void ratio as defined in the geotechnical sense, which means that the global void ratio is the same before and after swelling, this suggests that either accessibility of the pore space is reduced or that a portion of the pore space transitions into ultramicroporosity, which is no longer discernible through MIP. Nevertheless, the reduction in the intruded void ratio for the intact OPA is of a relatively minor magnitude. This provides an initial indication that the swelling processes in this case have no significant impact on the microstructure. On the one hand, this may be attributed to the robust bonding between the particles, but on the other hand, it can be concluded that the burial diagenesis induced lack of macroporosity is the primary factor. In comparison to the geotechnical void ratio that is calculated analytically on the basis of the dry and grain density, the intruded void ratio is lower for both materials. However, this is a common occurrence and has been discussed in the literature as well. This discrepancy can be attributed to two factors: firstly, the inability of the method to detect pores smaller than 7 nm; and secondly, the initial pressurising of the sample in the MIP device, which results in the compression and penetration of pores larger than 400 nm before the mercury enters the sample as part of the actual process of the MIP (Romero and Simms, 2008). The intruded void ratio for the compacted powder was obtained as 0.336, while the geotechnical void ratio was determined to be 0.348, what indicated a negligible deviation. In the case of the intact OPA, the intruded void ratio is 0.119, in comparison to the geotechnical void ratio, which ranges from 0.142 to 0.171 for all values determined in the course of this study. A clear divergence is evident in this case. The absence of macroporosity may be indicative of the significance of the non-detectable ultramicroporosity with pore diameters smaller than 7 nm for these deviations, with reference to the argumentation of Romero and Simms (2008).

In conclusion, it can be stated that the porosity of reconstituted and intact samples is a source of different hydro-mechanical material behaviours. While swelling mechanisms occur at two levels in reconstituted OPA due to the double porosity (micro- and macropores), only the microporosity is relevant in intact OPA. The volumetric boundary conditions during the swelling process determine whether a redistribution of the porosity occurs (constant volume) or an increase (free swelling). However, this latter phenomenon was not explicitly analysed here.

5.1.2. SEM-analysis of reconstituted and intact OPA

A set of different SEM images is presented in Fig. 5.3. This serves to highlight some distinctive characteristics of the microstructure of OPA. In general, intact OPA exhibits
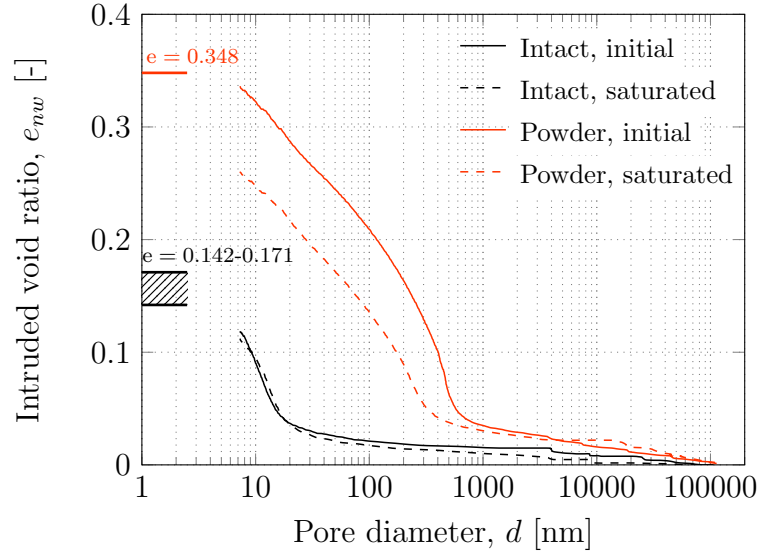
Figure 5.2.: Intruded void ratio e_{nw} before and after volume-constant swelling for intact as well as reconstituted OPA. In addition, the geotechnical void ratio e of the corresponding samples is indicated in the figure.

a dense and well-ordered clay matrix with a multitude of inhomogeneities. For example, Fig. 5.3a illustrates a substantial dispersed inclusion of cubic and octahedral pyrite (FeS_2) crystals aligned with the bedding plane orientation of the surrounding clay matrix. The bedding plane orientation can be recognised by observing the alignment of the clay particles. The orientation of the particles, and thus also of the bedding planes, is more clearly distinguishable in Fig. 5.3b, which depicts the same material at a further 10x magnification. The clay matrix appears to be highly dense, exhibiting no discernible porosity or distinctive aggregates of clay particles.

A characteristic framboid, derived from the French term 'framboise' for raspberry, of pyrite is shown in detail in Fig. 5.3c. These are the dominant texture of pyrite microcrystals, which are among the most significant authigenic minerals in marine sediments (Chang et al., 2022). Such a spherical aggregate has a diameter of 4 to 50 μm and consists of numerous microcrystals <2 μm. Other inhomogeneities that are frequently encountered include calcareous microfossils, quartz, and organic residues (Seiphoori et al., 2017). Fig. 5.3d illustrates an organic remnant, which might be coal, embedded in the clay matrix. An EDX analysis of the particle revealed that the dominant components were carbon (67.7 %) and oxygen (13.7 %), which supports the aforementioned assumption. Furthermore, a number of additional inhomogeneities that could not be definitively identified were observed within the intact OPA during the SEM analyses.

Figs. 5.3e and 5.3f present SEM images of compacted OPA powder at a dry density of
2.0 g/cm^3 and thus show the initial microstructure of the reference material for recon-
stituted samples. The images display notable differences from those of intact OPA. It
is essential to note that the inhomogeneities are no longer discernible. The analysis of
the reconstituted OPA revealed the absence of pyrite clusters, microfossils, and organic
residues. It appears that the sample preparation, particularly the grinding of the intact
rock, has resulted in their destruction. Seiphoori et al. (2016) also observed the pulveri-
sation of microfossils during the powder preparation procedure and concluded that it is
likely that the reconstitution process removes all sources of diagenetic bonding. An exper-
imental study on the influence of the remaining intrinsic bonding on the hydro-mechanical
behaviour of reconstituted OPA follows in Section 5.3.3. Moreover, the SEM images of
reconstituted OPA illustrate a more homogeneous and uniform microstructure of the clay
matrix, exhibiting no discernible anisotropy. The bedding appears to be looser than that
observed in the intact sample. Individual aggregates can be identified and their dimen-
sions correspond to the determined grain size distribution (GSD, Fig. 4.1) of the OPA
powder. For example, three aggregates are marked in Fig. 5.3e, labelled aggregates 1, 2
and 3, which have average diameters of 0.065, 0.04 and 0.03 mm, respectively. Overall,
the images reiterate that a more homogeneous material is obtained with the compacted
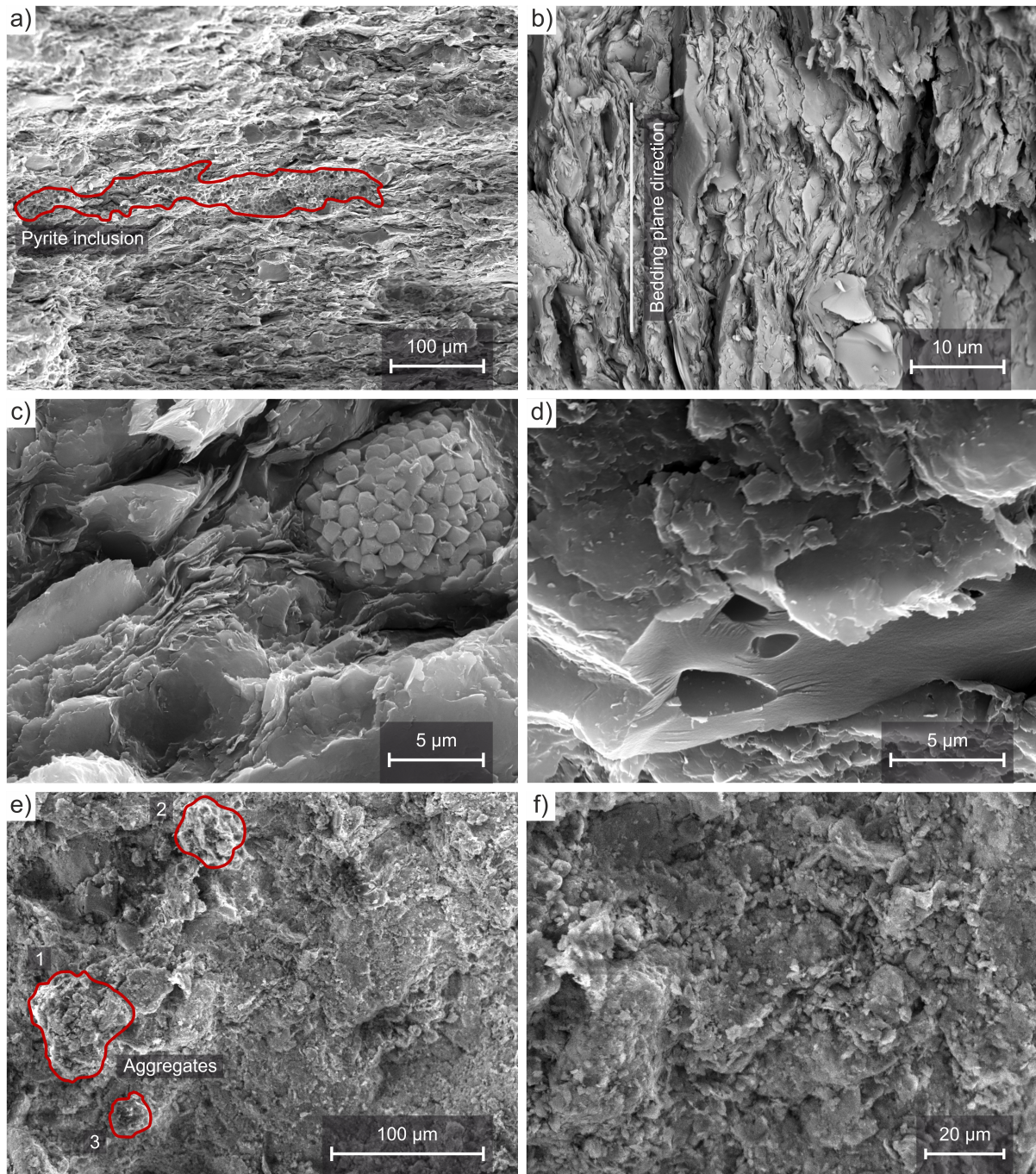powder samples (reconstituted OPA).

Figure 5.3.: SEM images of intact OPA showing a) an overview, b) a close-up of the clay matrix, c) a characteristic pyrite framboid and d) an organic remnant; and of reconstituted OPA showing e) an overview and f) a close-up of the clay matrix.

5.2. Mechanical behaviour

This thesis is concerned with the hydro-mechanical behaviour of OPA. Nevertheless, the results of elementary mechanical tests are presented in this section, and the basic parameters are derived. These form the basis for further numerical investigations, which are out of scope of the current thesis. A substantial body of literature exists on the determination of these parameters for intact OPA. For example, see Bock (2001); Bossart et al. (2002); Bossart and Thury (2008). This data is summarised in Table 5.1. However, as all tests in this study were also conducted with reconstituted OPA, this section presents mechanical tests to determine the relevant parameters for this material. All tests in this section were conducted on reconstituted OPA with an initial dry density of 2.0 g/cm^3.

5.2.1. Saturated and unsaturated compressibility of reconstituted OPA

Two different oedometer tests were conducted on reconstituted OPA as part of this research project. In one test, the material was evaluated in an unsaturated state, with the hygroscopic water content ($w = 2.27\,\%$) and the corresponding suction ($\psi = 68$ MPa), whereas in the second test, the sample was first saturated under constant volume conditions prior to initiating the oedometer test.

The results of the unsaturated oedometer test are presented in Fig. 5.4a. The sample was loaded to 25 MPa, unloaded to 0.1 MPa, and again loaded to 25 MPa. The material shows over-consolidation behaviour across the majority of the compaction curve. Given that the compaction pressure was measured as 15 MPa, it is evident that only the final load interval represents normal consolidated behaviour. The preconsolidation pressure was determined to be about 12.5 MPa following the Casagrande procedure. It can be concluded that the

Table 5.1.: Mechanical parameters of intact OPA based on data from literature.

λ	κ	p_0	c'	φ'
[-]	[-]	[MPa]	[MPa]	[°]
0.008-0.022[1,2]	0.004-0.011[1,2]	12-20[2,3]	2-4[4,5,6]	25-35[4,5,6]

[1]Favero et al. (2016), [2]Crisci et al. (2019), [3]Zhang et al. (2004)

[4]Bock (2001), [5]Bock (2009), [6]Bossart and Thury (2008)

data for compaction and preconsolidation pressure correlate well with one another. It is reasonable to assume that the transmission of forces to the sample during compaction will be partially impeded by self-deformations of the hydraulic jack employed. The values for λ_{unsat} and κ_{unsat} for the unsaturated state can be calculated as 0.1123, considering the stress range of 4.9 MPa to 25 MPa, and 0.0072, considering the stress range from 0.2 MPa to 25 MPa, respectively.

Fig. 5.4b illustrates the results obtained from the saturated oedometer test. The initial phase shows the volume-constant swelling of the sample when saturated with water. The swelling pressure measured in this test is 1.17 MPa. The initial two loading steps, applied at 1.45 and 2.2 MPa, still exhibited over-consolidated behaviour before transitioning to normal consolidation in the subsequent loading steps. It may therefore be hypothesised that these observations are artefacts introduced by the compaction of the dry sample. It can be seen in Fig. 5.4b that the preconsolidation pressure determined according to the Casagrande procedure of 1.8 MPa is significantly lower than that of the test on the unsaturated material. This is due to the process of hydration, which results in a rearrangement of the microstructure (see Section 5.3.5.3 for more details) with an associated reduction of arching effects and shear forces in interaction with the oedometer ring, and thus leads to a different material behaviour. For the saturated sample, this results in λ_{sat} and κ_{sat} values of 0.0718, considering the stress range of 1.5 MPa to 25 MPa, and 0.0236, considering the stress range of 1.2 MPa to 25 MPa, respectively.
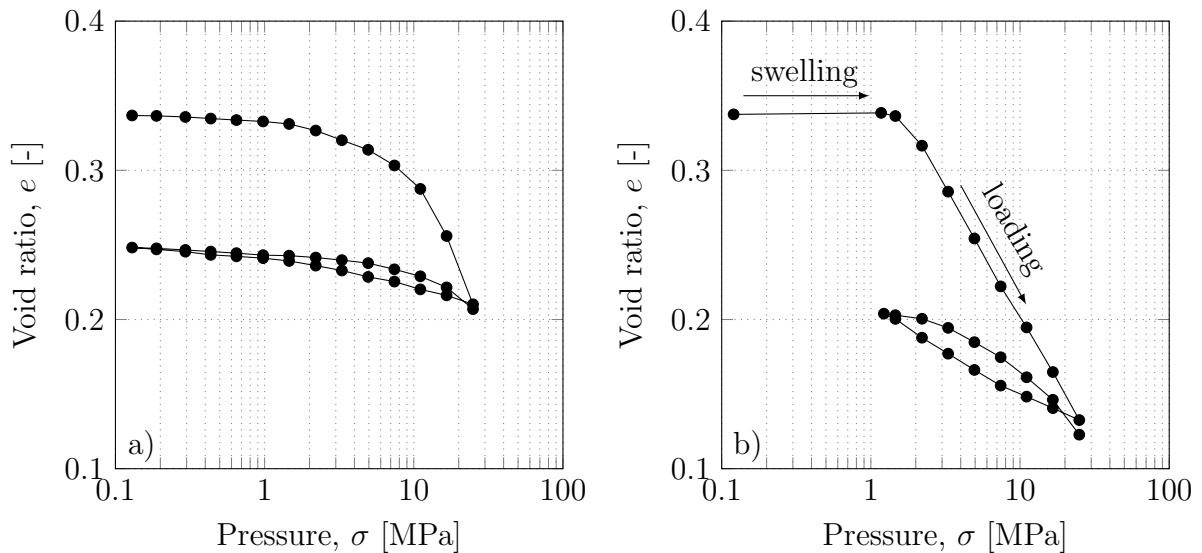

Figure 5.4.: Oedometer test results of a) unsaturated and b) saturated reconstituted OPA at an initial dry density of 2.0 g/cm^3.

5.2.2. Drained and undrained triaxial testing of reconstituted OPA

The results of the two test series, one drained (in green), the other undrained (in blue), are presented in Fig. 5.5. The values of the residual cohesion c_r' and the residual friction angle φ_r' were obtained from the drained tests as 35 kPa and 23.1°, respectively. Taking the peak values into account, the cohesion c' is 25.8 kPa and the friction angle φ' is 25.2°. All mechanical parameters resulting from the oedometer and triaxial tests are summarised in Table 5.2. In Fig. 5.5a, the initial linear increase of the effective stress paths in the undrained tests reflects elastic behaviour in the lower stress range. Fig. 5.5b shows for the tests at σ_3' of 300 and 500 kPa that a plateau of the deviatoric stress was initially reached with increasing vertical strain before softening occurs. This is not observed in the test with $\sigma_3' = 100$ kPa, but could potentially occur with further compression of the sample. The curves of volumetric response in Fig. 5.5c for the drained test series also initially show a linear increase, which indicates again elastic behaviour. The Poisson's ratio of 0.17 can be calculated based on this segment. In the further course, the test with a σ_3' of 100 kPa shows dilatancy, which implies overconsolidation. The other two tests show contractive and thus normally consolidated behaviour. In conclusion, it can be assumed that the preconsolidation pressure of the compacted and saturated samples is between 100 and 300 kPa. The preconsolidation pressure obtained from the triaxial tests is thereby significantly lower than that from the saturated oedometer test. This discrepancy can be attributed to the fact that the samples were maintained at a constant volume during saturation in the oedometer test, whereas in the triaxial test the samples were permitted to expand in all directions under a supporting pressure of 10 kPa. Minor evidence of elastic behaviour at the beginning of the tests with $\sigma_3' = 300$ and 500 kPa (Fig. 5.5c) are common and can be attributed to the consolidation under said pressure. As illustrated in Fig. 5.5d, which shows the excess pore water pressure over axial strain, all three samples exhibited dilatant behaviour following initial contraction. This phenomenon does not align with the observations made in the drained tests. Consequently, in undrained tests, the preload stress would be considerably higher.

5.3. Hydro-mechanical behaviour

This section is concerned with the hydro-mechanical behaviour of clays and clay shales under boundary conditions pertinent to tunnelling and particularly mechanised tunnelling. Consequently, the hydraulic conductivity and the water retention behaviour of the ma-
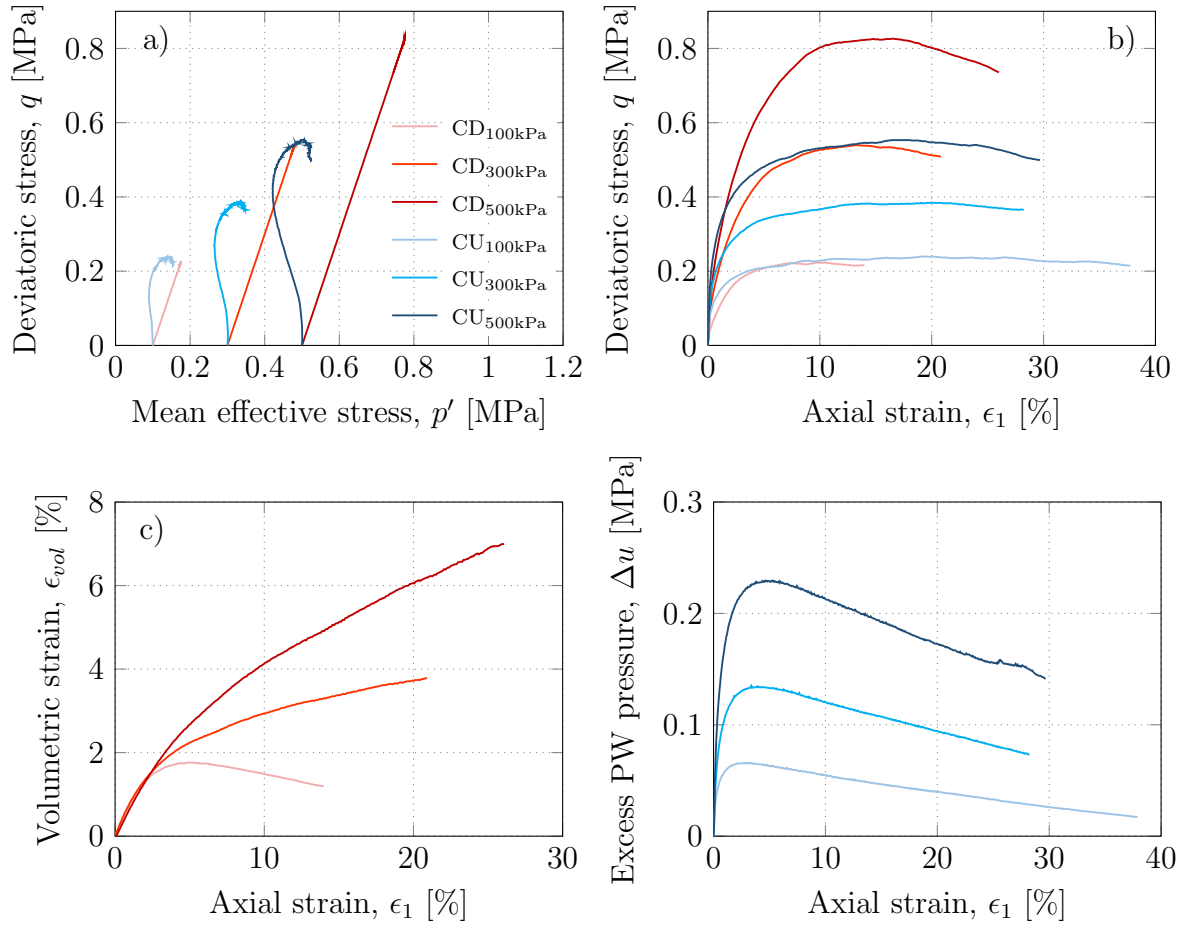
Figure 5.5.: Results of undrained (blue) and drained (green) triaxial tests with $\sigma_3' = 100$, 300 and 500 kPa on reconstituted OPA with an initial dry density of 2.0 g/cm³ as a) deviatoric over mean effective stress, b) deviatoric stress over axial strain, c) volumetric strain over axial strain and d) excess pore water pressure over axial strain.

terial are initially analysed, after which the influence of various aspects on the volume-constant swelling and thus the swelling pressure development is examined in different work packages. Following an analysis of free swelling and the development of swelling strains, the combination of swelling pressure and swelling strain is then emphasised. This implies that the swelling pressure development is examined under controlled volumetric deformations. This will facilitate an understanding of the interaction between soil and flexible tunnel support systems.

Table 5.2.: Mechanical parameters of reconstituted OPA with an initial dry density $\rho_d = 2.0$ g/cm^3.

λ_{unsat}	κ_{unsat}	$p_{0,unsat}$	λ_{sat}	κ_{sat}	$p_{0,sat}$	c'_r	φ'_r	c'	φ'
[-]	[-]	[MPa]	[-]	[-]	[MPa]	[kPa]	[°]	[kPa]	[°]
0.1123	0.0072	12.5	0.0718	0.0236	1.8	35.0	23.1	25.8	25.2

5.3.1. Hydraulic conductivity of reconstituted and intact OPA

The results of the hydraulic conductivity tests, as introduced in Section 4.3.4.2, on saturated reconstituted OPA with different initial dry densities are summarised in Table 5.3. Furthermore, an intact sample with an orientation perpendicular to the bedding plane direction (I_0) was tested. The results demonstrate a clear trend with respect to the initial dry density or the associated void ratio. A decreasing void ratio results in a corresponding decrease in hydraulic conductivity. The associated data are shown in Fig. 5.6, where the experimental data from the tests on OPA powder can be fitted best with the power function in Eq. 5.1.

$$k_{sat} = 4.61 \times 10^{-9} \cdot e^{4.25} \tag{5.1}$$

where k_{sat} is given in m/s and e is the void ratio.

Given the distinct microstructure and genesis of reconstituted compared to intact OPA, the fit is based exclusively upon the reconstituted samples. Nevertheless, the intact sample also demonstrates a high degree of correlation with the fitted trend in the diagram. The observed value is below the value that would be expected from the fit based on the reconstituted samples. However, this is a reasonable observation and might be related to the previously mentioned poorly connected pore space of clay shales (Keller et al., 2013).

Table 5.3.: Hydraulic conductivity of reconstituted OPA for different initial dry densities and intact OPA perpendicular to bedding directions.

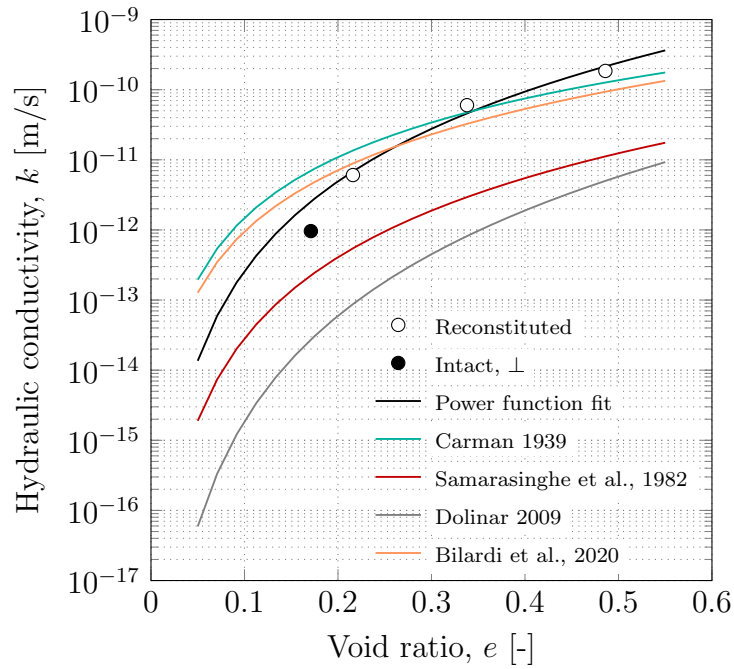|		Reconstituted			Intact
		1.8 g/cm^2	2.0 g/cm^2	2.2 g/cm^2	$\perp$
k	[m/s]	1.85×10^{-10}	6.01×10^{-11}	6.06×10^{-12}	9.62×10^{-13}

Figure 5.6.: Variation of the hydraulic conductivity over void ratio for various OPA samples including a best fit for the reconstituted samples and different analytical approaches from literature.

However, in addition to purely mathematical fitting, there are numerous theoretical approaches in the literature for estimating the hydraulic conductivity of a material, or in this case, explicitly of a clayey soil. In the following, selected approaches are presented for which the defined conditions for validity are met with the material investigated in this study. One of the earliest and most well-known approaches is the Kozeny-Carman equation from Carman (1939), which is based on Kozeny (1927). The Kozeny theory was originally formulated for sand and other fine powders, and it has been demonstrated to deliver accurate results for granular materials, while it revealed limitations when applied to clays. Consequently, Carman (1939) extended it to the Kozeny-Carman equation, which also yields reliable results for clays. The equation is as follows:

$$k_{sat} = \frac{\gamma}{\mu} \frac{1}{C} \frac{1}{S_0^2} \frac{e^3}{(1+e)} \qquad (5.2)$$

where k_{sat} is the saturated hydraulic conductivity, γ is the unit weight of the flowing fluid, μ the viscosity of the flowing fluid, C a constant considering the geometry of the porosity, S_0 the specific surface area and e the void ratio.

Another equation for the hydraulic conductivity of normally consolidated remoulded clays

is given by Samarasinghe et al. (1983) as

$$k_{sat} = 0.00104 \cdot I_p^{-5.2} \left(\frac{e^x}{1+e} \right) \tag{5.3}$$

where x is a constant between 3.97 and 6.39 (Sridharan and Nagaraj, 2005) and I_p the plasticity index.

Dolinar (2009) introduced an equation for soils containing non- or limited-swelling clay minerals

$$k_{sat} = \frac{6.31 \cdot 10^{-7}}{(I_p - 8.74p)^{3.03}} e^{2.66(I_p - 8.74p)^{0.234}} \tag{5.4}$$

where p is the percentage of clay minerals in the material. This value is derived in the original publication from the grain size distribution and thus corresponds to the clay fraction in the soil mechanical sense and not to the percentage of clay minerals.

A comprehensive overview of existing approaches is provided, along with an in-depth analysis of these approaches and the individual parameters that appear in various equations, in Bilardi et al. (2020). The analysis yields a set of equations for predicting the hydraulic conductivity, which is structured in a multilevel format: as the number of material parameters known and integrated into the equation increases, the accuracy of the prediction also increases. The equation that offers the highest accuracy while eliminating unnecessary parameters is as follows:

$$k_{sat} = 0.0338 \cdot C_F^{-2.898} \cdot e^{2.9015} \cdot w_p^{-1.377} \cdot S_F^{-0.921} \tag{5.5}$$

where C_F is the clay content, w_p the plastic limit and S_F the silt content.

The four aforementioned equations and the power function fit from Eq. 5.1 are also presented in Fig. 5.6. It can be observed that the equations proposed by Carman (1939) and Bilardi et al. (2020) deliver consistent results of the hydraulic conductivity, in comparison to the values that were actually measured in the laboratory. The equation proposed by Samarasinghe et al. (1983) gives values that are approximately one order of magnitude lower than the experimental data, while the prediction by the equation presented by Dolinar (2009) is approximately two orders of magnitude lower. The equations proposed by Carman (1939) and Bilardi et al. (2020) both yield satisfactory results for the material tested here, considering the specific surface area as a measure of the clay activity or the clay and silt fraction from the sedimentation analysis to reflect the grain size distribution, respectively. The clay mineral content is likewise a value that indirectly represents these two characteristics in a modified form. The discrepancies between the equation proposed by Dolinar (2009) and the experimental results on the OPA investigated here can be

attributed to the fact that the specific surface area in the equation is derived through a correlation with plasticity, which was experimentally deduced using clays with a dispersed microstructure. In contrast, compacted clays with water contents below the proctor maximum, as the one investigated in the present study, exhibit an aggregated and flocculated microstructure (see Section 2.1.3.1).

The value for the hydraulic conductivity of intact OPA, as determined in the laboratory, is in good agreement with values reported in the literature. These are summarised in Table 5.4, with the respective method used for the determination of the values indicated in the second column. In particular, the measured value is in close agreement with that reported by Muñoz (2006), which is the only data also determined in the laboratory with a similar set-up using Darcy's Law and is tested explicitly perpendicular to the bedding direction.

At the end of this work package, a comparative test was conducted in the newly developed swelling pressure cells for tunnelling relevant boundary conditions (Section 4.3.4.3) on compacted OPA powder with an initial dry density of 2.0 g/cm^3 to determine the hydraulic conductivity and thus check the functional suitability of the cell with regard to this specific type of test. The experiment yielded a hydraulic conductivity of 5.14×10^{-11} m/s, which is in close agreement with the previously determined value of 6.01×10^{-11} m/s. This demonstrates that the cells can also be employed with confidence in this type of experiment.

5.3.2. Influence of volumetric boundary conditions on the water retention behaviour

The soil-water characteristic curves (SWCCs) of reconstituted and intact OPA for volume-constant (I_{10}) and free swelling (I_{11}) conditions are presented in Figs. 5.7a and 5.7b, respectively. The least-squares method was employed to obtain the fitting curves, utilising the van Genuchten equation presented in Section 2.2.2. A summary of the fitting parameters is provided in Table 5.5. It should be noted that these are not the conventional SWCCs, where a material is installed as a slurry and then subjected to a drying process (initial drying), rehydration (main wetting) and a subsequent drying phase (main drying), as outlined in Section 2.2.2. The objective of the SWCCs in this study is to examine the water retention behaviour of the material upon drying and wetting beginning from field- and laboratory-relevant initial conditions, which are derived from the in-situ state in the field (intact material) or the initial state of all experimental tests conducted in this study

Table 5.4.: Literature data for the hydraulic conductivity of intact OPA.

	Test type	Hydr. conductivity [m/s]
Muñoz (2006)	Laboratory	7.35×10^{-13}
Fernàndez-Garcia et al. (2007)	Large scale ventilation	3.5×10^{-13}
Mayer et al. (2007)	Large scale ventilation	2.91×10^{-13}
Bossart and Thury (2008)	Hydraulic packer	1×10^{-12} - 2×10^{-14}
Gautschi (2017)	Large scale ventilation	2.5×10^{-13}
Yu et al. (2017)	Poiseuille-type law	1.9×10^{-14} - 5.8×10^{-13}
	Pulse withdrawal	3.1×10^{-12} - 7.3×10^{-12}

on reconstituted OPA (compacted powder). Accordingly, the samples were subjected to both, a drying and wetting process, from this initial state in order to obtain a single scanning curve.

In the case of reconstituted OPA, the initial state is characterised by a suction of 68 MPa and a degree of saturation of 18 %. A minor discrepancy between the volume-constant and free swelling boundary conditions is evident in the wetting branch. No difference is observable in the drying branch, which can be attributed to the fact that the applied volumetric boundary conditions are irrelevant for the drying process. The concept of microcells for the preservation of volume-constant boundary conditions was first introduced in Seiphoori et al. (2014) as part of an investigation into the water retention behaviour of compacted bentonite in the context of radioactive disposal. The study revealed a more pronounced impact of volumetric boundary conditions on water absorption during hydration. It was proposed that the prevention of continued subdivision of clay particles by volume-constant boundary conditions inhibits further water absorption on and between clay particles. In the current work it is demonstrated that the SWCC of reconstituted OPA at constant volume conditions exhibits a slightly elevated degree of saturation at the same total suction as the SWCC without volumetric constraints. A review of the underlying data indicates that this discrepancy can be attributed to the constrained expansion of the material. The water content is essentially identical in both cases at the same total suction. In contrast, when free swelling is permitted, the void ratio increases in a linear fashion as total suction decreases. This is in contrast to the constant volume SWCC, where the void ratio remains constant. The lesser influence of volumetric boundary conditions in this case, in comparison to the study by Seiphoori et al. (2014), can be attributed to the

differing mineralogies of the two materials under analysis. In contrast to the MX-80 bentonite studied in Seiphoori et al. (2014), which contains 85 % smectite, OPA consists of only 11-16 % illite/smectite mixed layer minerals. Smectites are clay minerals that exhibit a markedly high water absorption capacity. Consequently, MX-80 exhibits an enhanced swelling capacity, resulting in a greater sensitivity to constraints on volumetric swelling. In light of the fact that the various volumetric boundary conditions for determining the SWCC were taken into account in order to consider the tunnelling relevant volumetric boundary conditions of 'rigid lining', 'no lining' and 'deformation-tolerant lining', it can be concluded that a combined SWCC is sufficiently accurate, given the minor deviations observed.

The initial state of intact OPA samples was characterised by a total suction of 60 to 65 MPa and a corresponding degree of saturation of 63 to 67 %. The experimental data for the SWCCs, as illustrated in Fig. 5.7, demonstrate no remarkable difference between the two volumetric boundary conditions under consideration. The data points appear to be distributed along a single scanning curve. Accordingly, no distinction was made in the fitting between the two different boundary conditions; instead, all points were merged to derive a single combined parameter set. The similarity of free and constant volume swelling in the SWCC for intact OPA can be attributed to a further factor, in addition to the influence of mineralogy that has already been discussed. The decisive factor in this case is the effect of diagenesis and the resulting structure. As demonstrated in Christ
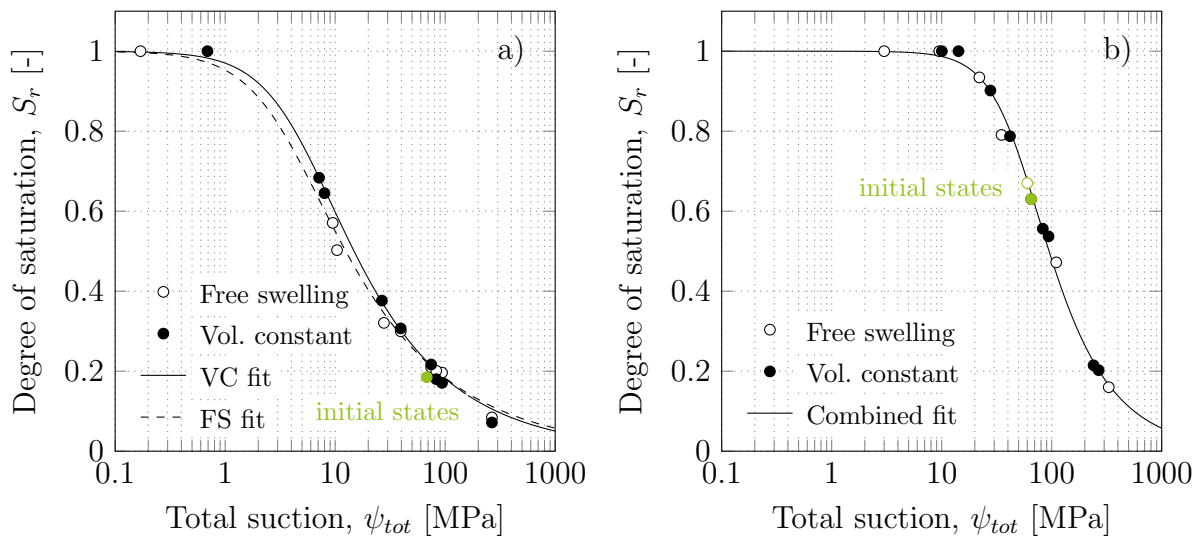

Figure 5.7.: SWCCs of OPA in a) the reconstituted state as compacted powder with $\rho_d = 2.0$ g/cm^3 and b) intact state. Initial states are plotted in green.

et al. (2024) and Section 5.3.3, the structure of the intact material exerts an additional attractive force, thereby further reducing the swelling capacity. As intact OPA is ground to a powder, the swelling pressure and the water uptake capacity according to Enslin-Neff increase significantly. Both increase more with increasing grinding fineness. Consequently, the volumetric boundary conditions no longer play a significant role in the determination of the SWCC, as the intact OPA exhibits a lower swelling capacity than the OPA powder. Actually, no influence can be identified from the data.

The air-entry values (AEVs) determined according to Eq. 4.5 are summarised in Table 5.5. From a physical point of view, the AEVs are not actual air entry values, as they were determined using the wetting path and not the drying path. Nevertheless, they are considered here to be characteristic values of an SWCC. It is noteworthy that the AEV of the intact material ($\psi_{AEV} = 26.34$ MPa) is more than ten times that of the reconstituted samples ($\psi_{AEV} = 1.98$ MPa for the combined fit). The magnitude of AEVs is affected by a number of factors, including the density, grain size distribution and aggregation (Nishimura et al., 2012), which in turn influence the size of the pore diameters. The smaller the pore diameter, the greater the suction required for air to penetrate into the pore space and thus to bring the sample into an unsaturated state. The discrepancy in the observed difference is plausibly attributed to the higher dry density of the intact material ($\rho_d = 2.3$ g/cm^3) in comparison to the compacted powder ($\rho_d = 2.0$ g/cm^3). This is supported by the pore-size distribution of the two materials. The pore diameter distribution for the powder shows a peak at 300 nm, while for the intact OPA, the most common pore diameter is only 10 nm (Fig. 5.1). Ferrari et al. (2014) assessed data from multiple studies on the water retention behaviour of intact OPA and derived the following exponential

Table 5.5.: Van Genuchten fitting parameters and AEVs for all determined SWCCs.

| | | Powder | | | Intact |
		free swelling	volume-constant	combined	combined
n	[-]	1.503	1.558	1.556	2.132
m	[-]	0.335	0.358	0.357	0.452
α	[1/MPa]	0.290	0.211	0.220	0.019
ψ_{AEV}	[MPa]	1.49	2.07	1.98	26.34
$\psi_{AEV_{S_r=95\%}}$	[MPa]	1.03	1.42	1.37	19.14

function for the development of the AEV with the void ratio:

$$\psi_{AEV} = 69.39 \cdot \exp(-9.82 \cdot e) \tag{5.6}$$

where ψ_{AEV} is the total suction at the air entry value and e the void ratio.

The exponential function is plotted with available data from the literature in Fig. 5.8a. The AEV from this study demonstrates a high degree of correlation with the data and the corresponding exponential fit. It should be noted, however, that the value in Fig. 5.8 from this study differs from the aforementioned AEVs in Table 5.5. This is due to the fact that the definition of the AEV in this figure is based on Ferrari et al. (2014). In this context, the AEV is defined as the suction that correlates to a degree of saturation of 95 % in the SWCC. The value designated as $\psi_{AEV_{S_r=95\%}}$ is also referenced in Table 5.5.

As outlined in Chapter 4.3.4.1, an SWCC can also be derived from MIP data. Consequently, the pressure exerted on the mercury to penetrate the sample's pores is transformed into matric suction. Fig. 5.8b illustrates the two SWCCs for the intact material, that means the van Genuchten fit of the total suction, and the MIP data for the matric suction. There is a notable parallelism and alignment of the inflection points between the two curves. As a result of the limitations of the MIP methodology, the SWCC of the matric suction reaches its upper boundary at approximately 40 MPa. The discrepancy between the two curves can be attributed to the osmotic suction exerted by the sample, or more specifically, the pore fluid. Ferrari et al. (2014) demonstrated through separate determination of the osmotic suction of OPA with the contact and non-contact filter paper method that this matches well quantitatively. In the present study, the proportion of osmotic suction was observed to decrease slightly as the degree of saturation increased. This was evidenced by a reduction in osmotic suction from 18.8 MPa at $S_r = 75$ % to 16.8 MPa at $S_r = 80$ %, 14.2 MPa at $S_r = 85$ %, and finally to 13.5 MPa at $S_r = 90$ %. This can be attributed to the fact that the sample is saturated via the vapour phase, which results in a reduction in the ion concentration within the pore fluid and, consequently, a decrease in the osmotic suction. Moreover, as previously stated in Section 4.3.4.1, the MIP often underestimates the degree of saturation at high suctions. Accordingly, alternative upper limits are specified in different studies, such as the AEV, in this case 26.34 MPa. It is also important to note that, in this method, mercury is theoretically substituted by air, which represents a drying path. In fact, the experimental data obtained in the low suction range can be considered as wetting paths. Nevertheless, this method provides a useful estimation of the matric suction.
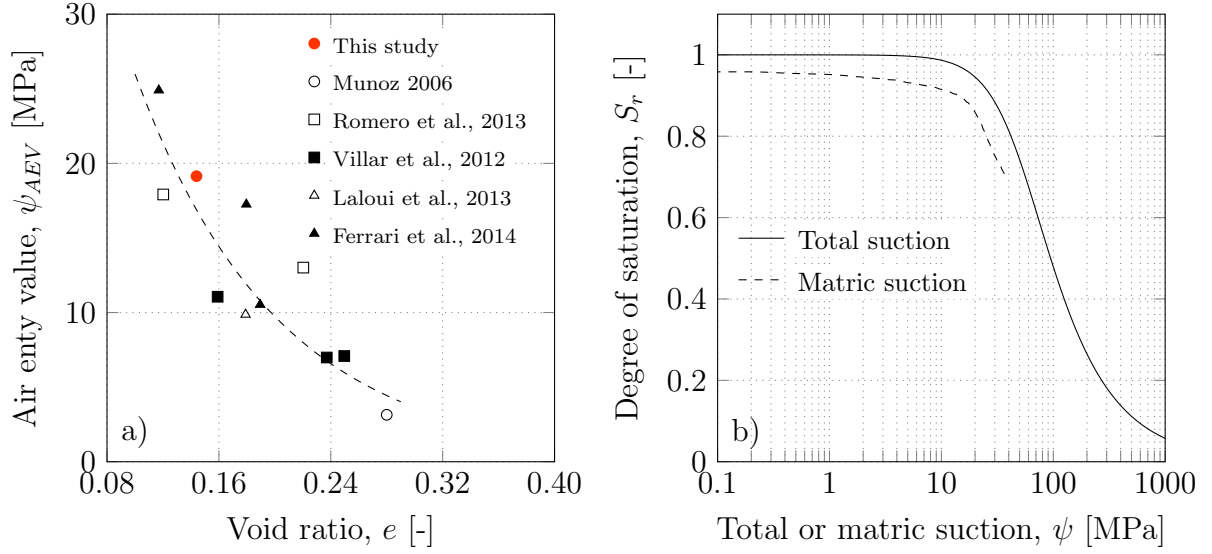
Figure 5.8.: Further analysis of the soil-water retention behaviour of intact OPA in terms of a) the air-entry value (here defined as the suction correlating to a degree of saturation of 95 %) over void ratio and b) separate consideration of matric and total suction in the context of the SWCC.

5.3.3. Influence of the grain size distribution on the hydro-mechanical behaviour

Research on reconstituted clay shales have focused on a particular grain size distribution (Favero et al., 2016; Crisci et al., 2019; Ferrari et al., 2020; Nitsch et al., 2023), but it has not been thoroughly studied what influence the used grain size distribution has on the material behaviour. This raises the question of which material characteristics are intrinsic and which are remnants of its structure that can be altered by modifying the grinding process. For this reason, a study was carried out as part of this thesis in which the hydro-mechanical behaviour of OPA powder was investigated as a function of grain size distribution using three different OPA powders. Two of the three studied grain size distributions were achieved with different settings of the used jaw crusher, 1.2 and 1.0 mm opening width at 850 rpm and 900 rpm, respectively. The third grain size distribution was prepared from a subsequent milling process in a vibration mill for 5 minutes. The final grain size distributions were then determined with a combined sieving (above 0.25 mm) and laser diffraction analysis (below 0.25 mm). For the laser diffraction analysis, the powder was ultrasonically dispersed for one minute with isopropyl alcohol as dispersant. The resulting grain size distribution curves for the OPA powders are presented in Fig. 5.9, including points from sieving (s) with filled symbols and laser diffraction analysis (l) with

empty symbols. They are categorised as fine, medium and coarse in the following. The medium powder comes closest to the reconstituted material used in the rest of the study. There, however, all grains >0.25 mm were sieved off in an additional step (see Section 4.2.2.1). The test program was designed in such a way that the influence of the grain size distribution on the hydration characteristics, the evolution of the swelling pressure and the compressibility can be analysed on the basis of mutually complementary individual tests. Therefore, in the following the individual test results are described first (Section 5.3.3.1), before they are discussed in Section 5.3.3.2 with respect to the previously mentioned topics. This entire work package is published in Christ et al. (2024).
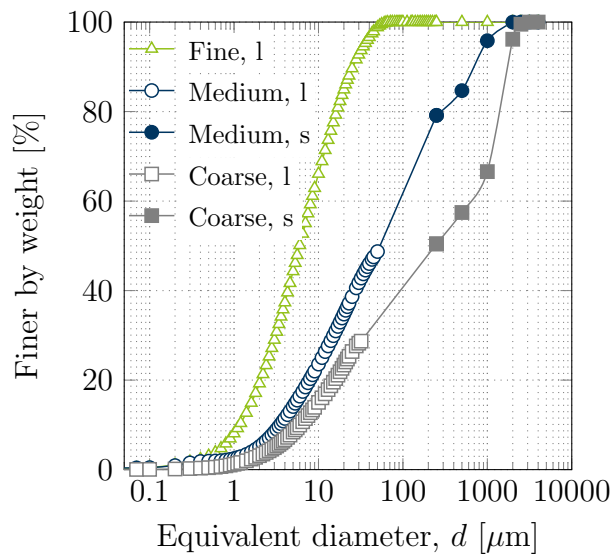
Figure 5.9.: Grain size distributions for various preparation methods, determined via combined sieving (s) and laser diffraction (l).

5.3.3.1. Experimental results

Geotechnical and chemical-physical characterisation

The outcomes of the geotechnical and chemo-physical characterisation of the reconstituted powder samples with varying grain sizes are presented in Table 5.6. The hygroscopic water contents of the three different prepared powders demonstrate an increase with an increase in grain size, from fine (2.61 %) over medium (3.12 %) to coarse (3.81 %). Conversely, the CEC decreases simultaneously from 8.07 over 6.46 to 6.01 meq/100g. As presented in Table 5.6, the liquid limit, plastic limit and plasticity index of OPA powders reduce

with an increase in grain size. Transferring these values to the Casagrande diagram (Fig. 5.10), all three points are located on a line parallel to and above the A-line. This indicates that they correspond to a clay without organic matter. The coarse and medium coarse materials can be classified as clays with low plasticity (CL), whereas the fine material can be classified as a clay with medium plasticity (CI).

Fig. 5.11 represents the water uptake capacity according to Enslin-Neff, as determined by averaging the results of duplicate tests conducted for each grain size. As can be seen, the fine-grained material demonstrates the highest rate of increase in water content at the beginning of the test and also the highest final water uptake capacity. According to Fig. 5.11, the smallest rate of water content increase and lowest maximum of water uptake was observed for the coarse-grained samples, while the results for the medium-sized grains fall between those for the fine and coarse samples.

Hydration curves

To allow the determination of the hydration curves, approximately 5 g of each powder (dried at 60°C) were stored in small plastic lids in desiccators above oversaturated salt solutions for a controlled relative humidity. Desiccators again were stored in a temperature-controlled room, resulting in a controlled atmosphere and suction. Used salt solutions contained those from Table 4.10 and additionally $MgCl_2$ which results in a suction of 96 MPa at 21°C. The material was weighed regularly and its suction was measured in a chilled mirror hygrometer. Upon reaching an equilibrium value, materials were transferred to the next desiccator with a lower suction, which led to a stepwise hydration of the samples.

Table 5.6.: Hygroscopic water content, cation exchange capacity, liquid limit, plastic limit and plasticity index for all three materials.

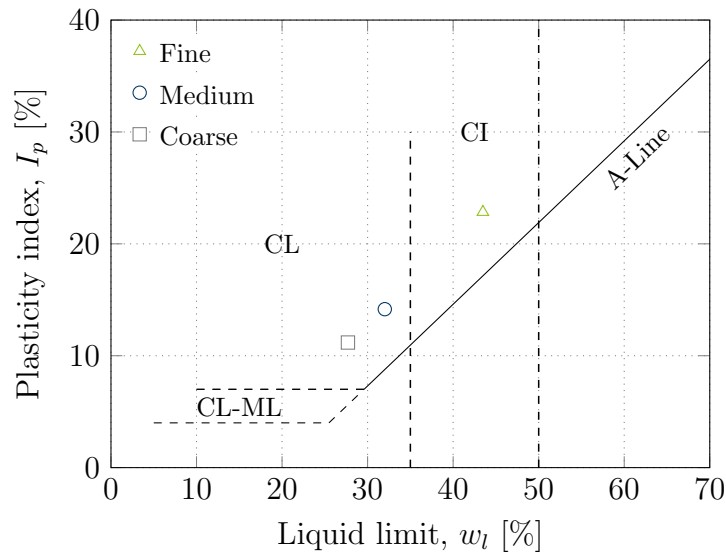|		Fine	Medium	Coarse
Hygroscopic water content, w_{hyg}	[%]	2.61	3.12	3.81
Cation exchange capacity, CEC	[meq/100 g]	8.07	6.46	6.01
Liquid limit, w_l	[%]	43.48	32.01	27.81
Plastic limit, w_p	[%]	20.64	17.85	16.52
Plasticity index, I_p	[%]	22.84	14.16	11.29

Figure 5.10.: Plasticity chart with the three OPA powder samples with different grain sizes.
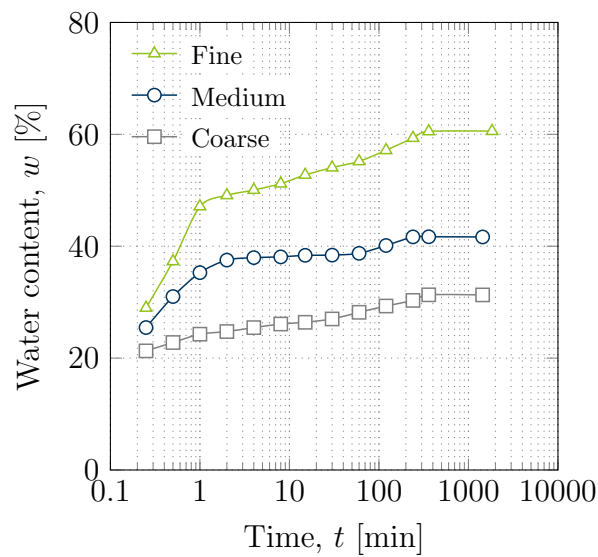
Figure 5.11.: Water uptake capacity according to Enslin-Neff with correction of Kugler et al. (2002) for the three OPA powder samples with different grain size distributions.

As presented in Fig. 5.12a, the saturation of the OPA powder proceeds in six distinct steps. The considerable rises in water content at specific points are attributed to the transfer of the samples into a desiccator with a higher relative humidity. The initially rapid increases and the subsequent almost constant levels of water content in Fig. 5.12a

reflect the rapid adaptability of the water content of the samples to changing relative humidities. While the water contents of the different materials are at a similar level at the beginning of the test (for suctions between 286 and 96 MPa), they increasingly diverge in terms of water content as the suction decreases and therefore sample saturation increases. In particular, the fine-grained sample is exhibiting a progressively greater divergence from the medium and coarse samples, with a corresponding larger increase in water content. Fig. 5.12b presents the hydration curves of the three materials, depicting the equilibrium water content across the various suction levels on a semi-logarithmic scale. A logarithmic increase in the water contents with decreasing suction for suctions higher than 20 MPa can be observed. In this rang of suction, the hydration curves are relatively independent of grain size. Nevertheless, a notable divergence between the hydration curves is evident at suctions below 20 MPa, where the hydration curve of the samples with fine grains lies significantly above those for the medium and coarse samples.
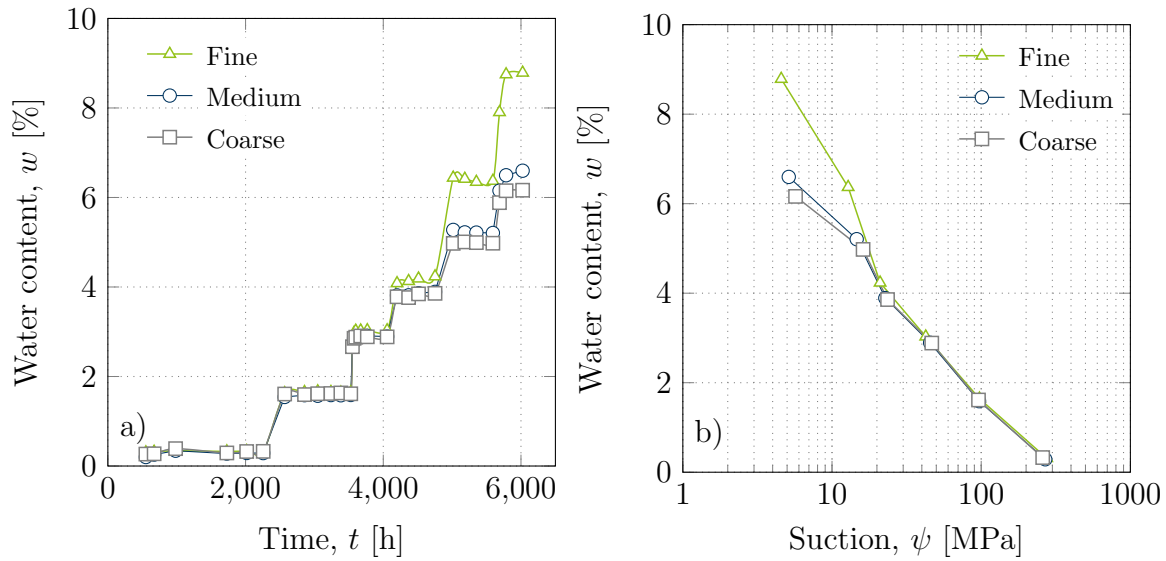

Figure 5.12.: Water content of the three studied materials a) over time and b) over suction.

Swelling pressure tests

Swelling pressure tests were conducted in the swelling pressure cells for tunnelling relevant boundary conditions (Section 4.3.4.3) at isochoric conditions. The target initial dry density for all three tests was chosen as 2.0 g/cm³, resulting in the corresponding initial void ratio of 0.34. The initial water content was chosen to be the hygroscopic water content of the three powders, which were 2.61 % for fine, 3.12 % for medium and 3.81 % for coarse. The

material was statically compacted in the ring of the swelling pressure cells. Saturation was realised with a 0.5 m water column (DI-water) in a burette.

The evolution of swelling pressure over time for the three materials is presented in Fig. 5.13a, which reveals notable differences in both the equilibrium swelling pressure and its rate of development. According to Fig. 5.13a, the equilibrium swelling pressures of the fine and medium-grained samples are approximately 1,820 and 620 kPa, respectively, while the coarse sample reaches equilibrium at 430 kPa. The aforementioned pressures are achieved within approximately 16 hours for the fine and medium-grained samples and within approximately 8 hours for the coarse sample. In the case of fine and medium-grained samples, the swelling pressure curve shows a drop of approximately 10 % at a specific pressure state (i.e., 1,730 and 650 kPa, respectively) prior to reaching equilibrium. Fig. 5.13a illustrates that the medium sample instantly reaches the equilibrium swelling pressure after the drop, whereas the fine sample demonstrates a further increase in swelling pressure before reaching the equilibrium swelling pressure. However, this phenomenon was not observed in the case of the coarse sample.

Evidently, the equilibrium swelling pressure of the fine sample is significantly higher than that of the medium and coarse samples. The equilibrium swelling pressure is plotted versus the compaction pressure required for the preparation of compacted samples with the exact same dry density in Fig. 5.13b. It is evident that an increase in grain size in powder-compacted samples results in a reduction in the required compaction pressure to fabricate samples at a given dry density. In particular, a significantly higher compaction pressure of approximately 30 MPa was required to produce the sample with a dry density of 2.0 g/cm^3 from fine OPA grains, which is approximately three times higher than the compaction pressure needed for the coarse sample. According to Fig. 5.13b, the equilibrium swelling pressure increases in a linear fashion with increasing compaction pressure. This indicates that the compaction pressure required to produce samples with an identical dry density and the corresponding equilibrium swelling pressure both increase with the reduction in grain size of OPA, while a linear relationship is observed between both pressures.

Compression behaviour

For the oedometer tests, materials were mixed with water in a ratio corresponding to approximately 1.1 to 1.2 times the liquid limit, resulting in a slurry. Subsequently, the slurry was placed in the oedometer ring, ensuring the absence of any air inclusions. The samples had a diameter of 7 cm and a height of 1.89 cm. The initial parameters obtained
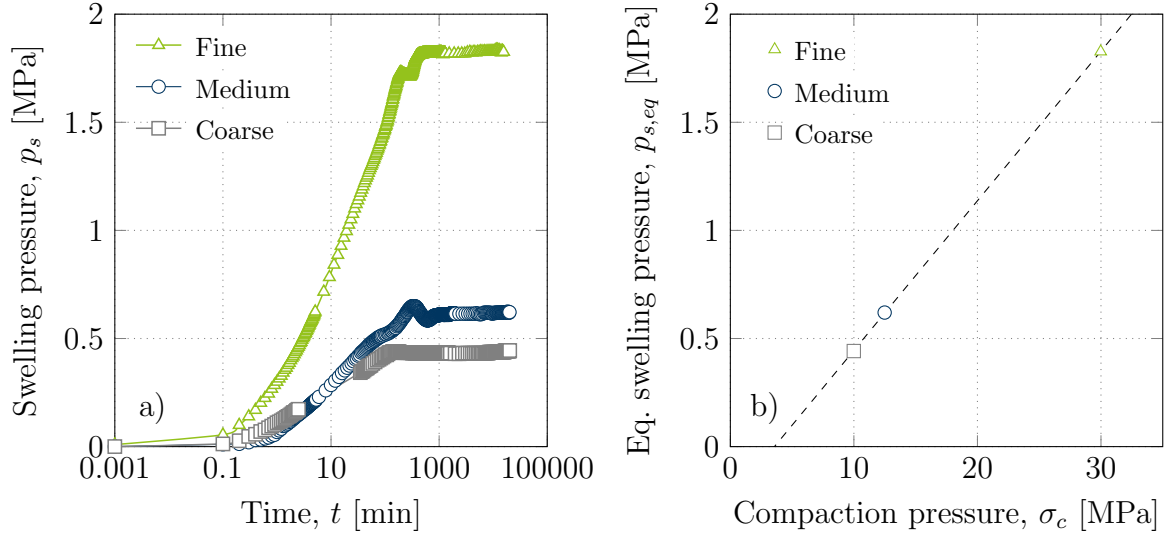
Figure 5.13.: Swelling pressure of the three studied materials a) over time and b) compared to the required compaction pressure for obtaining a sample with a dry density of 2.0 g/cm³.

through this sample preparation method are presented in Table 5.7. Subsequently, the samples were subjected to incremental loading up to 1.2 MPa, followed by an unloading back to 50 kPa, employing the same steps. The deformation was quantified using LVDTs. To ensure that the samples were fully saturated during the test, the setup was placed in a tray filled with water.

The outcomes of the oedometer tests conducted on samples with different grain sizes are presented in Fig. 5.14. The compression and swelling indices obtained from these tests are presented in Table 5.8. According to Table 5.8, both the compression and swelling indices (λ and κ) demonstrate an increase with decreasing grain size. Fig. 5.14 and Table 5.8 illustrate a comparable behavioural and parameteric trend for the medium and coarse material. The intrinsic compression line (ICL) according to Burland (1990) in Fig. 5.14b is defined with the actual experimentally identified e_{100}^* and e_{1000}^* (void ratios on the ICL at

Table 5.7.: Initial parameters of the samples in the oedometer tests.

		Fine	Medium	Coarse
Dry density, ρ_d	[g/cm³]	1.171	1.361	1.465
Void ratio, e	[-]	1.301	0.980	0.840
Water content, w_{init}	[%]	48.9	34.9	36.4

vertical stresses of 100 and 1,000 kPa, respectively) from Fig. 5.14a, according to Eq. 5.7. This leads to the conclusion that a single ICL can be identified for all three materials. In contrast, the three curves of the void index I_v shown in Fig. 5.14b consider a normalisation with the liquid limits of the three materials, by determining the normalised void ratio at a vertical stress of 100 kPa $e^*_{100,el}$ and normalised compression index $C^*_{c,el}$ in accordance with empirical relationships as proposed in Eq. 5.8 and Eq. 5.9 by Burland (1990). This means that Eq. 5.7 was also used for these three curves, but with $e^*_{100,el}$ and $e^*_{1000,el}$ instead of the experimentally determined e^*_{100} and e^*_{1000}. All materials meet the criteria for the application of these empirical equations, as their liquid limit falls within the range of 25 to 160 % and they are located above the A-Line in the plasticity chart (Fig. 5.10).

$$I_v = (e - e^*_{100})/(e^*_{100} - e^*_{1000}) \tag{5.7}$$

$$e^*_{100,el} = 0.109 + 0.679e_l - 0.089e_l^2 + 0.016e_l^3 \tag{5.8}$$

$$C^*_{c,el} = 0.256e_l - 0.04 = e^*_{100,el} - e^*_{1000,el} \tag{5.9}$$

where e_l is the void ratio at the liquid limit.

The results for e_l, $e^*_{100,el}$, $e^*_{1000,el}$ and $C^*_{c,el}$ are summarised in Table 5.9. As seen in Fig. 5.14b, the curves of void index versus vertical stress for samples with distinct grain sizes are located above the experimentally determined ICL.

To determine the constrained modulus M according to Janbu (1985), Eq. 5.10 is employed and the corresponding results have been presented in Fig. 5.14c.

$$M = \frac{\Delta\sigma'_1}{\Delta\varepsilon} \tag{5.10}$$

where $\Delta\sigma'_1$ and $\Delta\varepsilon$ are the increments of vertical effective stress and strain, respectively.

As evident in Fig. 5.14c, the constrained modulus M demonstrates a nearly linear variation with vertical stress in the diagram with double-logarithmic scale. It can be observed that there is a correlation between the vertical stress at which this linear trend is achieved and the grain size distribution. The linear trend is observed to be achieved at an earlier stage in the case of finer powder. Furthermore, a comparison of the results obtained from the present experiments with those reported by Favero et al. (2016) on remoulded OPA samples demonstrates a high level of agreement. The OPA from a shallow depth (approximately 300 m) from Mont Terri, as used by Favero et al. (2016), is comparable in terms of mineralogical composition and burial diagenesis to the material from the Sanierungstunnel Belchen used in this study. The results of the intact OPA in the same study approach the best-fit line at significantly higher vertical stresses. Fig. 5.14d shows

the measured coefficient of consolidation (c_v) as an estimate for the hydraulic permeability of the investigated materials. As anticipated, the samples with finer grains exhibited lower coefficients of consolidation. Furthermore, the coefficient of consolidation demonstrates an increases with increasing vertical stress up to approximately 500 kPa, while a contrasting trend is observed at higher pressures.

The variation of experimentally determined e_{100}^* and C_c^* values versus void ratio at the liquid limit (e_l) obtained for the samples with different grain sizes in the present study is plotted in Fig. 5.15, along with the results of Favero et al. (2016). The data sets show a good agreement. The dashed lines in Fig. 5.15, representing a fitting of the three experimental data points from the present study, lie above the regression lines as outlined in Burland (1990).

Mineralogical analysis

The XRD analysis was carried out at the Karlsruhe Institute of Technology (KIT). The three powders (fine, medium and coarse) were again divided into three fractions (>250 μm, 250-20 μm and <20 μm) and then prepared for further analysis. This was done to detect whether certain minerals fracture preferentially and thus are unevenly distributed among different fractions.

The outcomes of the XRD analysis on the various subsamples are presented in Table 5.10. The qualitative interpretation of the XRD results indicated the presence of a mineral assemblage consistent with that previously observed in OPA. The absence of gypsum in the samples indicates that they have not been subjected to any form of artificial alteration. The quantitative analysis indicates that the main phases are R1 illite-smectite (IS-R1 structure; see Ufer et al., 2012b,a) with an average content of 25 %, muscovite/illite (22 %), quartz (16 %), kaolinite (13 %), calcite (7 %) and minor phases like chlorite (5 %), feldspars (plagioclase 4 %; K-feldspar 2 %), dolomite (3 %), siderite (2 %), pyrite (1 %)

Table 5.8.: Compression (λ) and swell index (κ) from oedometer tests on remoulded OPA samples with different grain sizes.

		Fine	Medium	Coarse
Compression index, λ	[-]	0.152	0.091	0.077
Swell index, κ	[-]	0.033	0.017	0.013

Table 5.9.: Theoretically calculated $e^*_{100,el}$, $e^*_{1000,el}$ und $C^*_{c,el}$ according to equations from Burland (1990) depending on void ratio at liquid limit e_l.

		Fine	Medium	Coarse
e_l	[-]	1.166	0.858	0.746
$e^*_{100,el}$	[-]	0.805	0.636	0.572
$e^*_{1000,el}$	[-]	0.547	0.457	0.421
$C^*_{c,el}$	[-]	0.258	0.858	0.151

and anatase and rutile (both < 1 %). This composition is particularly characteristic of the OPA shaly facies. The phase contents of the fractions taken from the fine, medium, and coarse samples were found to be highly consistent with those of the intact sample, indicating that the grinding process did not result in any significant amorphisation. The greatest discrepancy in composition between different samples was observed for the IS-R1 phase. It is anticipated that a greater degree of variation in the content of this phase will be observed, given the inherent challenges associated with modelling and thus determining clay phases in XRD analyses. Moreover, the chlorite content is marginally higher in the f<20 mm sample, yet the impact on the abundance of the other phases is minimal, with a discrepancy of only +3 % observed. Such discrepancies could be attributed to imperfect sample preparation, e.g., non-uniform crystallite size in the XRD sample resulting from grinding and sieving processes, or preferential orientation in the XRD sample. No systematic variation in mineralogy was observed between the fine, medium, and coarse samples, nor between the >250, 250-20 and <20 μm size fractions. The compositions of the samples were found to be similar within the limits of the methodology's accuracy, indicating that grinding does not appear to have a selective impact on specific mineral phases.
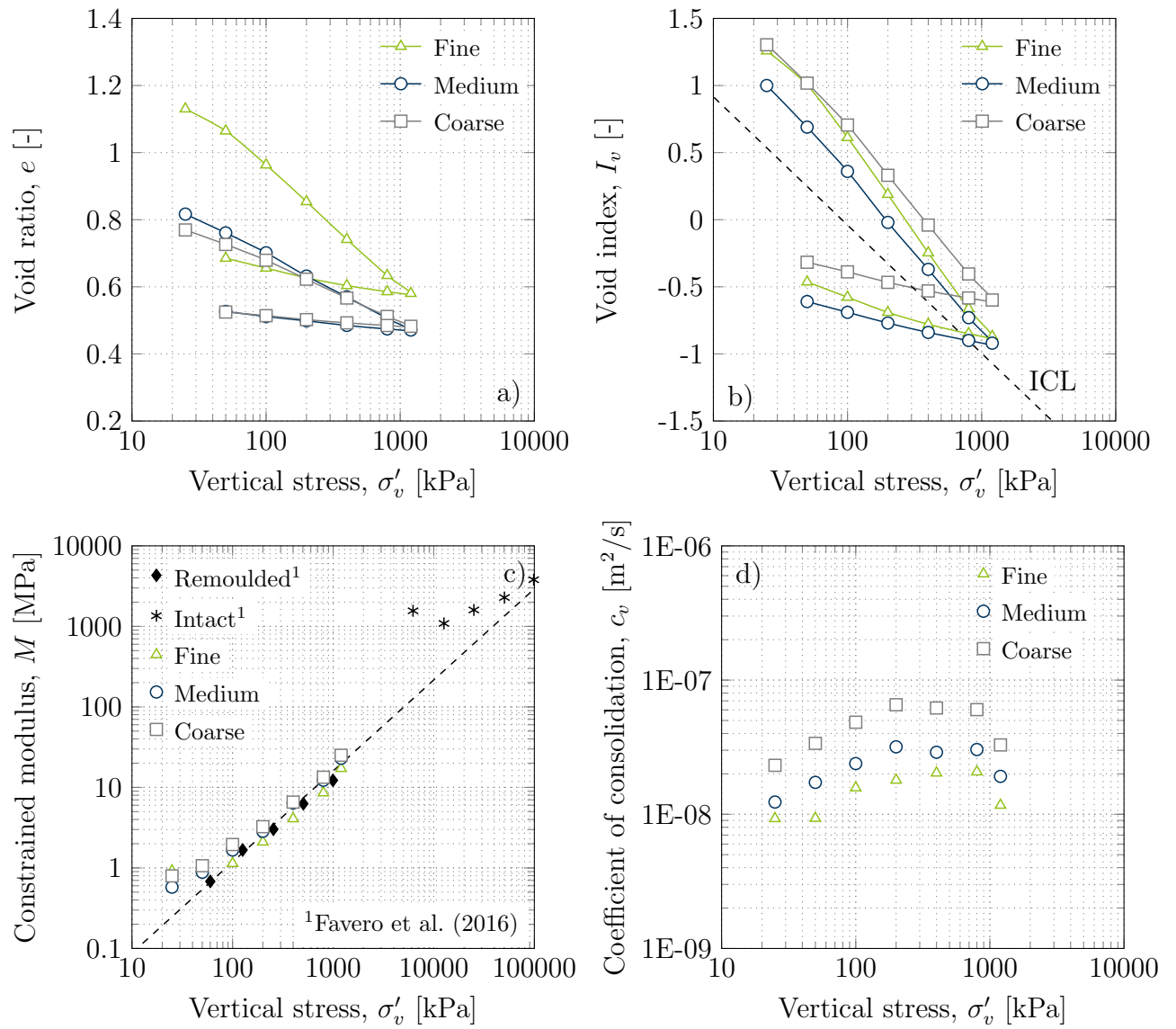
Figure 5.14.: Oedometer test results: a) void ratio e, b) void index I_v, c) constrained modulus M and d) coefficient of consolidation c_v as function of vertical stress σ'_v.
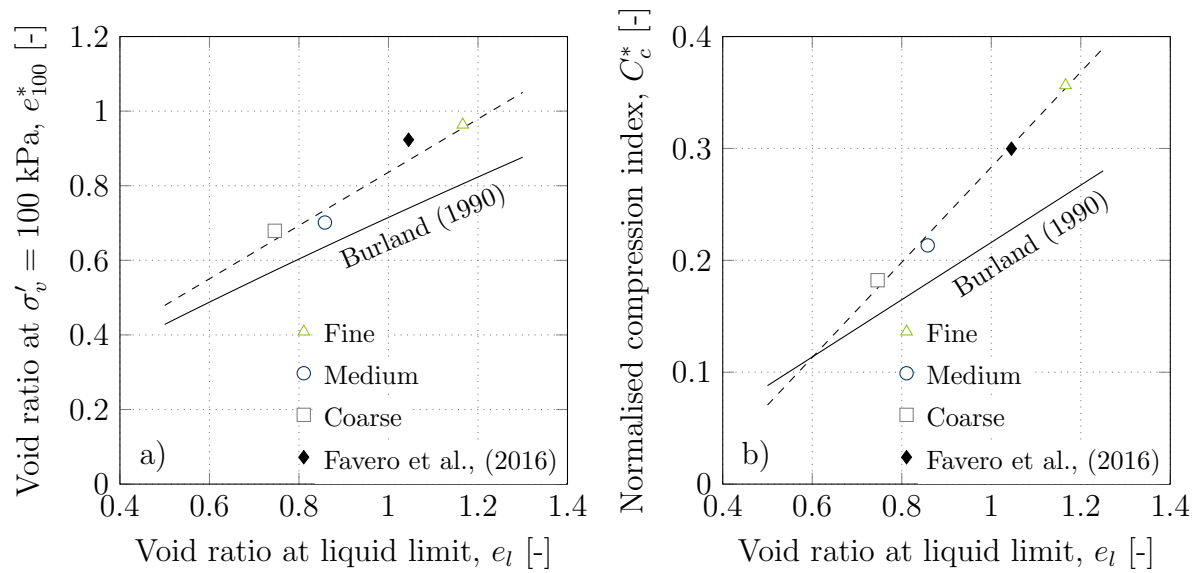
Figure 5.15.: Void ratio at liquid limit for the three materials with different grain size distributions in context to a) the void ratio on ICL at 100 kPa vertical stress and b) the normalised compression index.

Table 5.10.: Summary of the pXRD results for all tested subsamples. All values in %.

Sample	coarse			medium			fine			Intact	Mean
Fraction [µm]	>250	250-20	<20	>250	250-20	<20	>250	250-20	<20		
IS-R1	24.9	27.0	20.3	26.8	26.7	23.6	29.7	20.8	21.1	27.5	24.8
Muscovite	21.5	20.4	23.4	21.0	20.3	21.6	20.8	21.0	23.8	20.4	21.4
Kaolinite	13.1	12.3	14.7	12.9	12.4	14.3	13.1	13.6	11.6	12.3	13.0
Chlorite	4.9	4.8	4.8	4.9	4.4	3.6	4.0	4.5	7.3	4.3	4.7
Quartz	16.3	16.5	16.6	15.8	17.4	15.5	14.4	18.1	16.4	17.0	16.4
Plagioclase	3.4	3.2	3.5	3.4	3.6	4.7	3.4	4.0	3.6	3.3	3.6
K-Feldspar	2.1	2.1	2.1	1.9	2.0	3.1	1.9	2.5	2.6	2.2	2.2
Calcite	6.9	6.9	7.0	6.5	7.0	5.6	6.1	7.8	6.2	6.0	6.6
Ankerite	2.6	2.8	3.3	2.3	2.5	4.4	2.7	3.2	3.1	1.7	2.9
Siderite	1.7	1.6	1.8	2.0	1.5	1.5	1.5	1.5	1.8	2.4	1.7
Pyrite	1.1	1.1	1.0	1.2	1.0	0.8	1.1	1.6	1.0	1.7	1.1
Anatase	0.8	0.8	0.6	0.8	0.8	0.5	0.8	0.8	0.9	0.7	0.8
Rutile	0.7	0.6	0.7	0.7	0.6	0.9	0.6	0.6	0.8	0.5	0.7

Microstructural analysis

The pore size distribution of compacted OPA samples with fine and coarse grains having a dry density of $\rho_d = 2.0$ g/cm^3 was determined via MIP before and after a swelling pressure test. For this purpose, the samples were broken in small pieces and rapidly frozen by means of liquid nitrogen. Afterwards, the freeze dryer was used to remove the water while preserving the microstructure.

The pore size distributions of fine and coarse compacted OPA samples are presented in Fig. 5.16 in terms of the pore size density function for the initially compacted state (initial) and after a swelling pressure test at constant volume conditions (swollen). The curves are representative for a double-porosity structure, with a primary peak corresponding to the micropores (ultramicroporosity and microporosity collectively referred to as micropores with $r < 50$ µm) and a secondary peak pertaining to the macropores (mesoporosity and macroporosity collectively referred to as macropores with $r > 50$ µm). It is evident that no notable distinction was discerned in the micropore domain of the coarse and fine samples in their initial state. However, there is a notable difference in the macropore regimes of the fine and coarse samples in the initial state, with the coarse sample exhibiting larger macropores compared to the fine material. According to Fig. 5.16, the constant volume swelling of the samples affects the macropores in terms of the peak density (increased by swelling) and the size of the macropores (reduced by swelling) for both the coarse and fine materials.
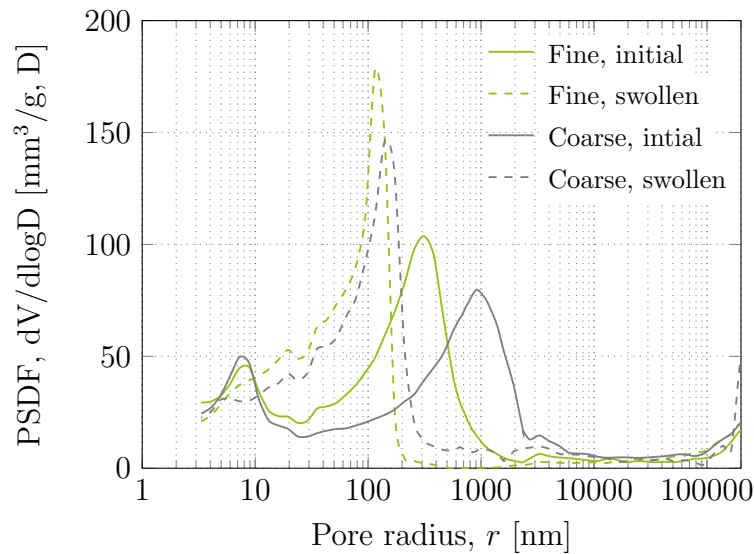

Figure 5.16.: Pore size density function (PSDF) of compacted fine and coarse OPA powder before and after swelling.

5.3.3.2. Interpreptation of experimental results

Influence of the grain size on the hydration characteristics

The water content-suction relationship presented in Fig. 5.12b indicates a comparable behaviour for all materials within the suction range exceeding 18 MPa. Conversely, notable distinctions can be observed for suctions below 18 MPa. Similarly, the free water uptake, as depicted in Fig. 5.11, demonstrated a notable correlation with the grain size of the OPA powder samples. The water adsorption of clayey soils can be attributed to effects that arise from mineralogy and exchangeable cations (e.g. hydration of surfaces and cations) on the one hand, and impact of fabric (e.g. capillarity) on the other hand. In their study, Khorshidi et al. (2017) identified three distinct water retention regimes, namely capillary water, adsorbed water and tightly adsorbed water, in increasing order of their corresponding suction range. The tightly adsorbed water is primarily governed by cation and surface interactions, and can thus be estimated using the cation exchange capacity (CEC) and specific surface area (SSA). At high suctions, the cation hydration is the decisive factor that governs the water retention behaviour. The three materials tested exhibit comparable behaviour within this range. This finding is consistent with the observation that, despite an evident increase from coarse over medium to fine, the CEC values are very close to each other in absolute terms. In relative terms, there is an increase of 33 % from fine to coarse, but in absolute terms this is not a difference that would justify a significant effect in water absorption. The XRD results presented in Section 5.3.3.1 showed no impact of the grinding process on the minerals present, nor any separation due to preferential breakage of specific clay minerals. The primary effect of grinding was found in the structure of the powder, characterised by a breakage in the bonding that gives rise to an increase in the number of smaller grains. This becomes decisive at lower suctions and thus results in the observed deviations in water content at suctions below 18 MPa. The free surface of particles that can get in contact with water is of significant relevance with regard to the hydration of the grains. The sum of free surfaces that is exposed to hydration is greater for a higher number of smaller grains than for a lower number of larger grains. By this analogy, the highest water absorption capacity of the samples with fine grains can be justified. This mechanism appears to contradict the observations made by Rouf et al. (2016), who found that bentonite granules exhibited a higher water absorption capacity than the corresponding powder. However, the inverse tendency can be attributed to the larger and more continuous pore space in the granular bentonite, which enables a well-interconnected pore structure with a higher water adsorption capacity. As evidenced by the MIP data in Fig. 5.16, the grain size distribution has no impact on the

initial micropores of the compacted OPA samples. Unlike bentonite in granular form, OPA grains exhibit a strong additional attractive force due to the rock-forming clay mineral calcite, which induces a bonding and is commonly observed in sedimentary rocks, and also documented in the present study (Table 5.10). Such bonding phenomena impede the expansion of very dense grains. Furthermore, the literature indicates that the connectivity of the pore space of clay shales is typically poor (Keller et al., 2013). Therefore, in the case of a finely ground clay rock, a reduction in the stabilising effect of the bonding coincides with a larger free surface which elevates the hydration capacity.

Influence of the grain size on the evolution of swelling pressure

The mechanisms previously discussed in the context of the different hydration behaviours also play a crucial role with respect to the rate and potential of swelling pressure evolution. As presented in Fig. 5.13, the absolute swelling pressure is notably higher for the fine OPA sample. This is consistent with the considerably higher adsorption of water by the assembly of fine grains. The discrepancy in water absorption between the OPA powders with medium and coarse grains is less pronounced in the tests on water uptake capacity (Fig. 5.11) and on hydration characteristics (Fig. 5.12). This is also evident in a smaller absolute difference in their swelling pressures (Fig. 5.13). Once more, the intrinsic bonding within the OPA grains serves to act as an additional attractive force, which reduces the swelling potential. This force also provides an explanation for the greater drop in the swelling pressure before reaching an equilibrium value observed in the fine and medium materials in comparison to the coarse material. The observed drop can be attributed to a rearrangement of particles, as evidenced by Gens and Alonso (1992). This phenomenon is characterised by the collapse of the macropores, which subsequently results in the homogenisation of the microstructure. This rearrangement is reduced in the case of larger grains due to the prevailing intrinsic bonding in them.

The coefficients of consolidation (c_v) obtained from the oedometer tests (Fig. 5.14d) indicated an increasing trend of higher hydraulic conductivities with coarser grain size distribution. This is due to the fact that the value of M remains relatively constant for the three materials under investigation, and exhibits a similar trend with respect to grain size as that observed for the coefficient of consolidation, c_v (Fig. 5.14c). However, this trend is not reflected in the courses of the constant volume swelling pressure tests, where the swelling pressure of the fine material exhibited the highest magnitude and rate of increase. As previously stated, the well-connected macropore structure in the compacted fine sample facilitates a more rapid process of hydration, while the lower bonding effect in the

fine grains allows for a greater build-up of swelling pressure. The lower free surface of the coarse powder and the lesser local permeability of the grains in comparison with the fine powder result in a deceleration of the water absorption process and evolution of swelling pressure. This mechanism is circumvented in the oedometer tests by installing the initial material in the form of a slurry. Consequently, the fine material forms a homogeneous sample with a low permeability.

According to Fig. 5.13b, the required compaction pressure to reconstitute the sample to a target dry density of 2.0 g/cm^2 increases with a reduction in grain size. This is due to the fact that the intact material has a dry density of approximately 2.3 g/cm^2 and the milled grains preserve a similar dry density. Consequently, large grains with higher dry density than the target value require less compaction pressure as well as less volume of the initial material in powder form to produce the reconstituted sample. In general, the compacted sample derived from the fine powder exhibits a significantly higher degree of homogeneity than that derived from the coarse powder. As a consequence, a linear correlation was identified between compaction pressure and corresponding swelling pressure.

Influence of the grain size on the compressibility

The oedometer test results, as presented in Fig. 5.14a, revealed notable difference in the compression behaviour of the different materials. Furthermore, a discrepancy in the initial state of the material, which commenced from a water content above the liquid limit, was observed. An evaluation of the constrained modulus, as presented in Fig. 5.14c, indicated that all materials exhibit a similar pattern at the high stress range. However, all remoulded OPA samples fabricated in this study showed effects of overconsolidation or evidence of structure at low pressures, as illustrated by a deviation from the unique linear trend indicated by the dashed line. The fine material approaches the dashed line at lower stresses (approximately 100 kPa), while such a transition is observed at a range of 200-300 kPa in the case of the coarse material. According to Fig, 5.14c, the very fine material tested by Favero et al. (2016) already reaches the linear course at 60 kPa. This can be attributed to the sieving off of the coarse material, which leads to the exclusion of any remaining structure from the samples. Furthermore, an approximation to the dashed line is also evident for the intact sample tested by Favero et al. (2016). It can thus be concluded that all materials exhibit a comparable deformation behaviour in the normally consolidated state. Conversely, despite the remoulding process, some of the reconstituted samples demonstrate the preservation of overconsolidation effects due to the strong bonding.

If the void ratio versus vertical stress plot is normalised according to the void index concept of Burland (1990), as presented in Fig. 5.14b, all remoulded materials are at the right of the intrinsic compression line, which intuitively suggests incomplete destructuring. However, when the parameters e_{100}^* and C_c^* over e_l in Fig. 5.15 are considered, which have been employed for the normalisation, a different aspect emerges. It appears that the correlation proposed by Burland (1990) fits best for the coarse material, while the fine and medium materials, as well as the material studied by Favero et al. (2016), follow a different correlation (dashed line). It is evident that with increasing liquid limit (or decreasing the grain size), both e_{100}^* and C_c^* exceed the correlation suggested by Burland (1990). This is in general agreement with the observations made by Burland (1990), who noted discrepancies from his proposed correlation at high and low liquid limits. However, this discrepancy can be attributed to the fact that the materials presented by Burland (1990) were predominantly characterised by an aggregated fabric and weak bonding between aggregates. Such relatively weak bondings can be gently removed by mixing, without entirely disturbing the intrinsic aggregated fabric. In case of OPA, the material is neither characterised by an aggregated fabric nor it is possible to remould the material in a gentle manner.

5.3.4. Swelling pressure tests under volume-constant conditions

The results of the swelling pressure tests conducted under constant volume conditions are presented in the following section. The series of tests was designed to focus on different aspects with the objective of identifying relevant influences on the swelling behaviour and improving understanding of the underlying mechanisms. Henceforth, the reconstituted OPA, as presented in Section 4.2, will be employed for all subsequent tests again in addition to intact OPA.

5.3.4.1. Influence of fabric on the swelling pressure development

Prior to the implementation of the novel advanced swelling pressure cells for tunnelling-relevant boundary conditions, an initial series of tests was conducted to assess the impact of the initial OPA fabric on the swelling behaviour. The basic isochoric cells presented in Section 4.3.4.2 were employed for this investigation.

The evolution of the swelling pressure over time is presented in Fig. 5.17 for both intact and reconstituted OPA samples, with the direction of bedding planes and the assumed

particle orientation taken into account. The definition of the direction of the reconstituted samples is based on the expected particle orientation, which is perpendicular to the compaction direction. For the reconstituted OPA samples, taking into account the fabric, larger samples with a diameter of 15 cm were first produced and then samples considering the particle orientation were drilled out. For details of the sample preparation procedure, see Section 4.2. The two intact samples, oriented perpendicular to the bedding planes (I_1 and I_2) exhibited maximum swelling pressures of 1,880 and 1,050 kPa, respectively. In comparison, the intact samples (I_3 and I_4) oriented parallel to the bedding planes achieved maximum swelling pressures of 150 and 215 kPa, respectively. Such differences in the measured maximum swelling pressures for the same orientation are attributable to the inherent inhomogeneity of intact samples. This is reflected, among other factors, in the dry density of the material, where the initial dry density ρ_d of I_1 was 2.36 g/cm^3, while that of I_2 was 2.30 g/cm^3. Additionally, the initial dry density of I_4 was higher than that of I_3, with values of 2.33 and 2.30 g/cm^3, respectively. This is evidenced by the higher maximum swelling pressure in both cases. Additionally, inhomogeneities in the composition of the material may also be a contributing factor. Despite the absence of notable variations in the mineralogical composition across all subsamples as evidenced in Section 4.1.1, the study's sample material exhibited the presence of quartz and pyrite inclusions at the mesoscale level. However, no inclusions were directly recognisable in samples I_1 to I_4 that could have been responsible for the observed variance in results. Furthermore, it is well established that even swelling pressure tests on homogeneous samples of compacted powder, which all share the same initial conditions, can show considerable variations in the measured values. In light of the small discrepancies in the initial dry density, the documented bandwidth remains within an acceptable range.

A comparison of the results from the literature presented in Section 2.4 with those obtained in this study demonstrates good agreement. In the comparatively large range for samples perpendicular to the bedding plane direction ($p_{s,max} = 0.5$ - 3.7 MPa), these values are approximately mid-range, whereas the values parallel to the bedding plane direction tend to be at the lower end of the values reported in the literature ($p_{s,max} = 0.22$ - 0.7 MPa). Evidently, the swelling pressure tests on the intact samples show a pronounced anisotropy. The anisotropy factor, defined as the ratio of the equilibrium swelling pressure perpendicular to the equilibrium swelling pressure parallel to the bedding planes, has a value of 7 in the present study for the minimum as well as for the maximum swelling pressures measured in each direction. Crisci et al. (2019) observed an anisotropy factor of 4, whereas Bock (2001) reported a value of 2. It is notable that the consideration of anisotropy in experimental studies on the swelling pressure of clay shales is rather rare.

The origins of anisotropy in clay shales were presented in Section 2.1.3.2.

The literature also documented the observation of anisotropy in artificially compacted clay samples. During the process of compaction, clay minerals became oriented perpendicular to the direction of maximum acting stress (Kawamura and Ogawa, 2004). Consequently, anisotropy was reflected in the swelling behaviour of the clay samples (Gokhale and Jain, 1972; Liu et al., 2021). The degree of anisotropy increased in conjunction with both an increase in clay content and an increase in vertical compaction pressure (Voltolini et al., 2009). Fig. 5.17 also demonstrates the impact of compaction-induced anisotropy on the swelling pressure of the reconstituted OPA samples analysed in this study. The equilibrium swelling pressure of OPA with an initial dry density of 2.0 g/cm³ perpendicular to the particle orientation is 1.1 MPa, whereas it is 680 kPa parallel to it. This corresponds to an anisotropy factor of approximately 1.6. The lower anisotropy factor in comparison to intact OPA can be attributed, as outlined in Section 2.1.3.2, to the lower compaction pressure (burial diagenesis) and the absence of physical, chemical, and biological processes, which naturally do not occur within the artificial preparation of reconstituted samples.

A comparison between the swelling pressure of intact and reconstituted OPA reveals differences in both the temporal development and the magnitude of the maximum swelling pressure. The maximum achieved swelling pressure of the reconstituted powder sample
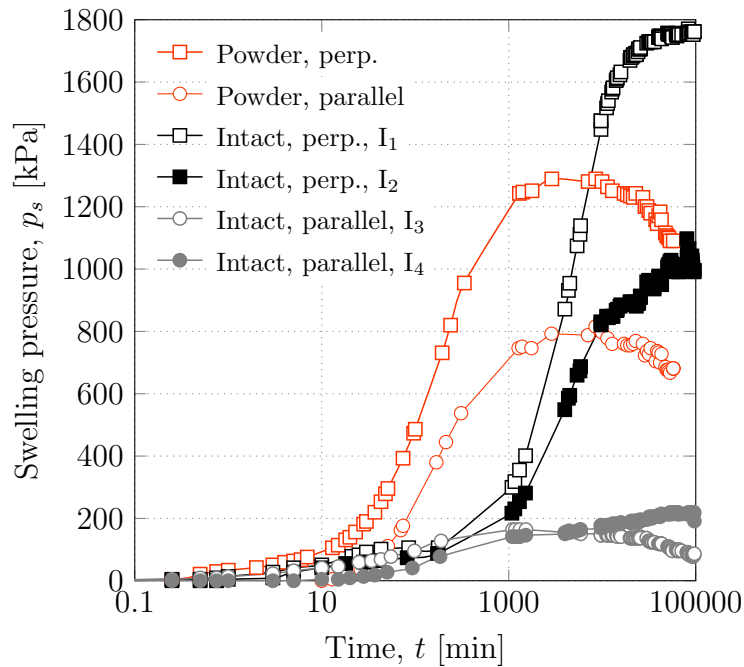
Figure 5.17.: Volume-constant swelling pressure tests on intact and compacted samples considering bedding plane orientation.

perpendicular to the particle orientation is observed to be lower than that of the intact sample perpendicular to the bedding planes. This is primarily attributed to the lower initial dry density. The reconstituted sample tested here exhibited a density of 2.0 g/cm^3, while the intact sample had a density of 2.36 g/cm^3. Assuming the same initial dry density, it can be postulated that the intact sample will exhibit a lower swelling potential. This topic is discussed deeper in Section 5.3.3, where the impact of the degradation of the intact OPA structure on its hydro-mechanical behaviour is investigated. The maximum swelling pressure of the reconstituted sample parallel to the particle orientation is approximately four times greater than that of the intact sample parallel to the bedding plane orientation. This is due to the fact that further microstructure-forming processes besides the compaction process are not initiated as a result of the artificial compaction at a comparatively low stress within a limited amount of time, and therefore the anisotropy is not as pronounced as it is in the intact samples. In this instance, the swelling pressure of intact OPA is reduced in both directions as a consequence of the strong bonding effects. However, the influence of this phenomenon is more pronounced in the direction parallel to the particle orientation, which can be attributed to the swelling mechanisms of clays. Clay particles swell primarily perpendicular to the orientation of their layers. In artificially compacted samples, the degree of anisotropy related purely to the fabric is considerably lower than in case of a marine sediment such as OPA due to its burial diagenesis. The decline in the swelling pressure of the reconstituted samples after reaching the peak cannot be reasonably attributed to the material behaviour. This phenomenon therefore suggests the presence of issues with the isochoric cells employed in this test series (see Section 4.3.4.2).

Nevertheless, there are also differences in the temporal development. Fig. 5.17 shows that the maximum swelling pressure for reconstituted samples is reached after just under 8,500 min, which corresponds to about 6 days, whereas it is 40,000 min or about 28 days for the intact samples. This is due to the difference in hydraulic conductivity. As presented in Section 5.3.1, this is strongly dependent on the void ratio and thus the dry density. There are two powers of ten between the hydraulic conductivity of the reconstituted sample with an initial dry density ρ_d of 2.0 g/cm^3 and the intact sample. As a result, it takes considerably longer for the intact sample to become completely saturated and consequently for the maximum swelling pressure to develop.

Table 5.11 presents a summary of the swelling pressures measured in this study for intact OPA, both perpendicular and parallel to the bedding plane direction (three values each), as well as for OPA powder at a dry density of 2.0 g/cm^3 (three values). In order to eval-

uate the swelling pressure of the reconstituted samples, it was necessary to consider only those samples that were compacted directly into the sample ring. This was done in order to ensure consistency. Therefore, the samples that were drilled out of larger blocks and take into account the particle orientation (Fig. 5.17) were not considered. The respective third values of the swelling pressure of the intact materials are the equilibrium swelling pressures under constant-volume conditions (initial saturation) of the strain-controlled swelling pressure tests presented later in Section 5.3.6.2. The data demonstrate that both the coefficient of variation (the ratio of the standard deviation to the mean) and the variability (the ratio of the difference between the maximum and minimum value to the mean value) of the intact OPA are significantly higher than those of the reconstituted OPA, irrespective of the sample orientation. The coefficient of variation of intact OPA is 26.9 and 30.0 %, while that of reconstituted OPA is 1.9 %. The variability of intact OPA is 53.6 and 52.4 %, while that of reconstituted OPA is 3.6 %. Based on the aforementioned values and the previously mentioned increase in test duration by a factor of four when using intact material, it is evident that the use of reconstituted OPA represents a valuable addition. This will facilitate a preliminary examination of the fundamental mechanisms of the studied hydro-mechanical behaviour in the following sections, considering boundary conditions relevant to tunnelling on an homogeneous material while saving time. Subsequently, selected tests will be repeated on intact OPA in order to facilitate the transfer of the conclusions and the derived concept to intact material, as later done in Section 5.3.6. However, due to time constraints, not all tests could be repeated on intact material within the scope of this thesis. To illustrate, the multi-step swelling pressure tests on intact OPA, as presented in Section 5.3.4.3, would have required approximately three years to complete based on the factor of four in the test duration observed here.

Table 5.11.: Minimum, maximum and average swelling pressure of all swelling pressure tests on intact OPA (parallel and perpendicular to bedding plane direction) and reconstituted OPA ($\rho_d = 2.0$ g/cm^3) as well as the coefficient of variation and variability.

	Swelling pressure				
	Min. [kPa]	Max. [kPa]	Avg. [kPa]	Coefficient of variation [%]	Variability [%]
Intact, par.	150	262	209	26.91	±53.59
Intact, perp.	1,050	1,893	1,608	30.04	±52.42
Powder, $\rho_d = 2.0$ g/cm^3	1,053	1,091	1,071	1.88	±3.55

5.3.4.2. Influence of initial dry density of reconstituted OPA

The newly developed swelling pressure cells for tunnelling relevant boundary conditions offer the potential for significantly enhanced resolution of the swelling pressure curve, thereby facilitating insight into crucial mechanisms. One reason for this is the automatic recording of measured values, which enables the generation of a continuous data set. Furthermore, the resolution of the load cells is a contributing factor. This value is now 0.5 kPa, representing a significant reduction from the 5 kPa of the previously used cell configuration. Accordingly, the progression of the swelling pressure will be more intensively assessed in the forthcoming tests. In the preceding tests (Section 5.3.4.1), primary the final magnitude was considered.

It is well documented that the swelling pressure of clays increases with increasing initial dry density (Tripathy et al., 2004; Villar and Lloret, 2008; Yigzaw et al., 2016; Zeng et al., 2023). To evaluate this trend for reconstituted OPA, three swelling pressure tests were conducted with initial dry densities of 1.8 g/cm^3, 2.0 g/cm^3 and 2.2 g/cm^3. The results are presented in Fig. 5.18a, showing a pronounced increase of maximum swelling pressure with increasing dry density. Furthermore, the impact of hydraulic conductivity on the swelling pressure development is evident. As the density decreases and the void ratio increases, the maximum swelling pressure is reached in a shorter time. In addition, it is notable that in all three tests, following the achievement of the maximum swelling pressure, the pressure drops before reaching an equilibrium state. With respect to the maximum swelling pressure, this drop is observed to decrease with increasing density, from 19.31 % at $\rho_d = 1.8$ g/cm^3, over 7.75 % at $\rho_d = 2.0$ g/cm^3 to 0.81 % at $\rho_d = 2.2$ g/cm^3. This phenomenon has been previously observed in other studies and is attributed to a reorientation of the clay particles (collapse of macrostructure) at the high pressures caused by the swelling (Gens and Alonso, 1992; Lloret et al., 2003; Agus et al., 2013). In light of the dry state compaction of reconstituted samples, as outlined in Section 2.1.3.1, it can be reasonably concluded that an aggregate structure with pronounced macropores is obtained. After the drop, the microstructure undergoes further swelling and homogenisation, resulting in a further slight increase in the swelling pressure. In their study, Liang et al. (2021) provide a more detailed analysis and conclude that at high suctions, the swelling pressure development is primarily driven by interlayer hydration. In contrast, at low suctions, the swelling pressure was found to be controlled by the formation and expansion of diffusive double layers, accompanied by the collapse of some macropores. This collapse and its accompanying decline in swelling pressure is not evident in the swelling pressure tests on intact OPA. This is due to the fact that intact OPA has a monomodal

pore size distribution comprising solely micropores (see Section 5.1.1), which precludes the collapse of macropores and any associated change in microstructure. Furthermore, it is notable that the maximum swelling pressure at a dry density of 2.2 g/cm^3 (3.8 MPa) is greater than the maximum swelling pressure of 1.9 MPa measured on intact OPA, which has a dry density of 2.36 g/cm^3. This can be attributed to the destruction of the inherent bonding by grinding, which consequently results in the absence of the supplementary attractive forces in the compacted samples, as previously discussed in Section 5.3.3.

The equilibrium swelling pressure of the three studied samples is presented in Fig. 5.18b, shown in the corresponding three shades of red. However, as previously stated a specific range of swelling pressures can be observed at a defined dry density. Consequently, additional results from constant volume swelling pressure tests conducted in various sections of this study have been incorporated in Fig. 5.18b in grey. An exponential fit is the most reasonable regression and the most widely used in the existing literature (Villar and Lloret, 2008). The relationship between equilibrium swelling pressure and dry density can be most accurately represented by the following equation:

$$p_{s,eq} = 6 \cdot 10^{-7} \cdot e^{7.14 \cdot \rho_d} \tag{5.11}$$

where the equilibrium swelling pressure $p_{s,equ}$ is given in MPa and the dry density ρ_d is entered in g/cm^3.
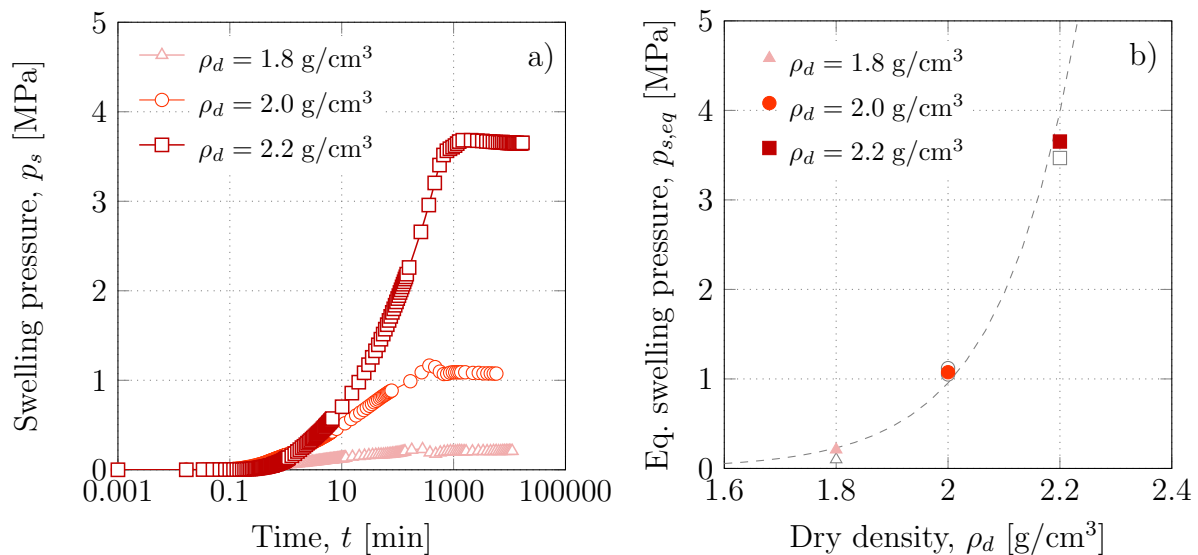
Figure 5.18.: Volume-constant swelling pressure tests of reconstituted OPA with different initial dry densities. a) Swelling pressure over time and b) equilibrium swelling pressure over initial dry density (red data: tests from a), grey data: other tests of this thesis).

5.3.4.3. Multi-step swelling pressure tests

The evolution of the swelling pressure in a constant volume swelling pressure test with vapour saturation is presented in Fig. 5.19a. The test was conducted for a total of 251 days, during which the sample was saturated in four steps, beginning with an initial suction of 68 MPa. The following suction levels were 37, 20, 8 and 3.2 MPa, respectively. The evolution of the swelling pressure is presented in Fig. 5.19a. The equilibrium swelling pressure at different suction levels is shown in Fig. 5.19b and demonstrates a logarithmic increase in swelling pressure with decreasing suction. This phenomenon can be described for the boundary conditions applying to this test by the following regression:

$$p_{s,eq} = -0.32 \cdot \ln(\psi_{tot}) + 1.49 \tag{5.12}$$

where the equilibrium swelling pressure $p_{s,eq}$ is given in MPa and the total suction ψ_{tot} is used in MPa.
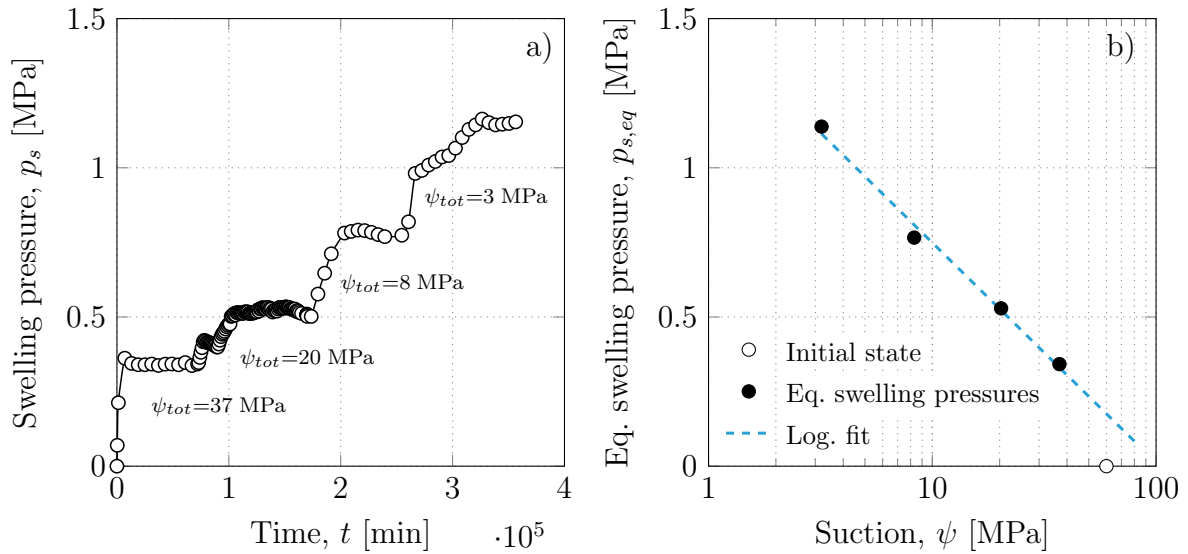
Figure 5.19.: Multi-step volume-constant swelling pressure test with vapour saturation. a) Swelling pressure development over time and b) equilibrium swelling pressure over suction.

It should be noted that the aforementioned logarithmic fit is only valid for the range of vapour saturation (VET), and therefore up to 3.2 MPa. Other studies in the literature confirm this type of trend for the VET range (Agus et al., 2013; Liang et al., 2021). In studies employing the ATT or OT at lower suctions, a linear relationship is observed (Agus et al., 2013; Schanz and Al-Badran, 2014). The utilisation of the ATT or OT to saturate the sample with lower suctions was not feasible in the present study due to the

technical constraints of the cells employed. For this purpose, the installation of porous ceramic plates (ATT) or semi-permeable membranes (OT) in the cell would be necessary, whereby these would also have to be rigid. At a suction of 3.2 MPa, the swelling pressure is already slightly greater than the final value observed in the experiment with single-step saturation. Therefore, extrapolation at this point is not a meaningful approach. The precise reason for the higher swelling pressure at this suction compared to the equilibrium value with the single step saturation remains unclear; however, it is likely attributable to the naturally occurring fluctuations in swelling pressure tests that have already been discussed.

Converting the total suction via the volume-constant SWCC of reconstituted OPA at a dry density of 2.0 g/cm^3 (Section 5.3.2) to a degree of saturation, yields a linear increase of equilibrium swelling pressure with increasing degree of saturation as shown in Fig. 5.20. This can be expressed by the following equation:

$$p_{s,eq} = 0.0141 \cdot S_r - 0.0857 \tag{5.13}$$

where the equilibrium swelling pressure $p_{s,eq}$ is given in MPa and the degree of saturation S_r is used in %.
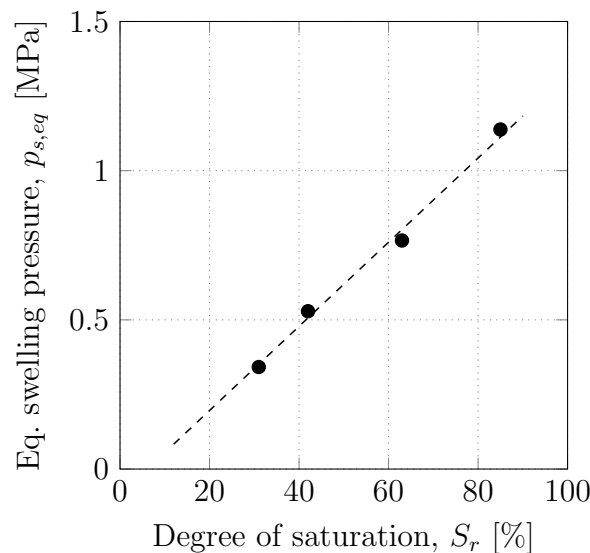
Figure 5.20.: Increase of equilibrium swelling pressure with increasing degree of saturation by using the VET.

5.3.4.4. Influence of the initial degree of saturation

This test series consisted of six constant volume swelling pressure tests, each utilising a different initial degree of saturation. The tests were conducted on reconstituted OPA with an initial dry density of 2.0 g/cm^3. Prior to the static compaction of the powder to create the final sample, the water content was adjusted.

The swelling pressures over time from the six tests is presented in Fig. 5.21a and the equilibrium swelling pressures as a function of the initial degree of saturation in Fig. 5.21b. It is worthy of note that the equilibrium swelling pressure initially increases up to 1.2 MPa for an increasing initial degree of saturation, before beginning to decrease for initial degrees of saturation exceeding 40 %. As previously discussed in Section 2.1.3.1, the structure of an artificially compacted clay sample is dependent upon the initial water content of the starting material. However, a similar phenomenon was observed in another study by Keskin et al. (2023). Proctor tests and swelling pressure tests were conducted on KarBen bentonite, a sodium bentonite sourced from Turkey. Swelling pressure tests were performed with the Proctor density at varying initial water contents. As in the present study, the water content was adjusted prior to the compacting of the samples. It was observed that the equilibrium swelling pressure over initial water content also exhibits a distinctive evolution, whereby it initially increases with rising initial water content and subsequently decreases after a specific initial water content is surpassed. The Proctor tests in the cited study demonstrated that the turning point correlates with the water content that was identified as the optimal water content. This phenomenon can be attributed to the fact that, in the absence of moisture, the particles are in edge-to-edge or edge-to-face contact, resulting in the formation of relatively large interparticle pores with the potential of swelling and water accumulation. As the initial water content increases, the size of the pores decreases, resulting in a higher swelling pressure due to the limited space between particles. The reduction in swelling pressure following the threshold value can be attributed to the fact that, at higher water contents, the material undergoes a greater degree of swelling already during sample preparation, which subsequently results in a lesser degree of swelling during the actual swelling pressure test.

It was not feasible to ascertain the optimal water content and corresponding Proctor density for the utilised OPA powder in the present study, primarily due to the quantity of powder required. Nevertheless, Gurtug and Sridharan (2015) compiled data from the literature and established a correlation between the plastic limit and the optimum water content. Accordingly, an optimum water content of approximately 23 % can be estimated for the OPA in this research project. Nevertheless, a water content of 12.6 % already
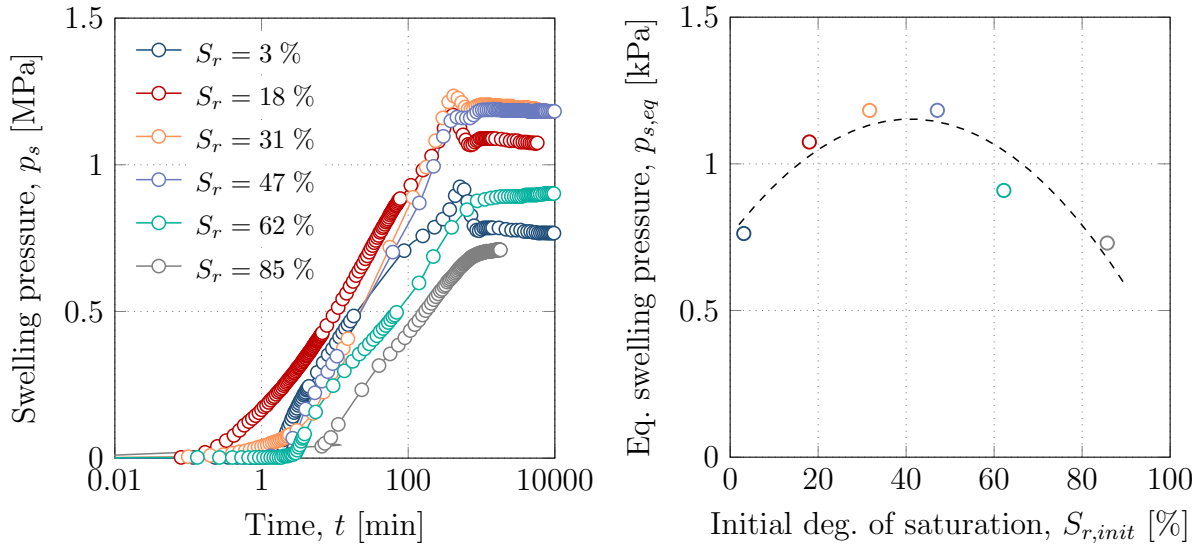
Figure 5.21.: Maximum swelling pressure as a function of the sample's initial degree of saturation.

results in the sample being fully saturated at the analysed dry density of $2.0\ \mathrm{g/cm^3}$. Nonetheless, the shape of the curve can be interpreted analogously to the argumentation presented in Keskin et al. (2023). The current study's samples collectively exhibit an aggregated microstructure with most likely edge-to-face contacts and a bimodal PSD, which can be attributed to the relatively low water content during the compaction process. Consequently, as the initial water content is increased, the larger pores that are characteristic of compaction at low water contents become smaller. This, in turn, results in an increase in the swelling pressure. This influence of the water content during compaction on the pore size distribution can also be observed indirectly in the swelling pressure curves in Fig. 5.21a. At the lowest initial degree of saturation (corresponding to the largest macropores), the drop in swelling pressure, which can be attributed to a collapse of the macropores, is the greatest. As the initial degree of saturation increases (corresponding to a decrease in the size of the macropores), the magnitude of the drop decreases. For initial degrees of saturation above $S_{r,init} = 62\ \%$ no further drops can be observed. However, above a water content of approximately $5.1\ \%$ which corresponds to a degree of saturation of approximately $40\ \%$, this effect is overlaid by another. As the water content increases, the material undergoes swelling already during the preparation stage, and the potential for swelling subsequently decreases during the actual swelling pressure test. The observed decrease in swelling pressure with increasing initial water content well below the optimum water content may be attributed to two factors. First, the inital dry density in this study

is significantly higher ($\rho_d = 2.0$ g/cm^3) compared to the study by Keskin et al. (2023). The swelling pressure tests in the aforementioned study were conducted with Proctor density ($\rho_d = 1.16$ g/cm^3). Furthermore, the observed decrease in swelling pressure below the optimum water content when using OPA may be attributed to the overall lower swelling potential of this material. The KarBen bentonite used in the study by Keskin et al. (2023) contains 75 % montmorillonite, whereas OPA consists of 11 to 16 % illite/smectite mixed layers. Nevertheless, this work package serves to highlight the significance of the initial microstructure in determining the hydro-mechanical behaviour of a clay.

5.3.5. Free swelling

The following sections examine the swelling expansion behaviour of both reconstituted and intact OPA without applying any volumetric constraint upon hydration. In the one-dimensional swelling strain tests, the swelling pressure cells for tunnelling relevant boundary conditions are employed, wherein the spindle is fully elevated at the top of the cell to allow free swelling (with the top plate of 10.5 kPa serving as the required counterpart for measuring the resulting strain). The cubic cell described in Section 4.3.4.5 is employed for the three-dimensional swelling strain tests.

5.3.5.1. Influence of the initial dry density of reconstituted OPA on swelling strains

The measured swelling strains of compacted OPA powder with initial dry densities of 1.8, 2.0 and 2.2 g/cm^3 over time are presented in Fig. 5.22a. The equilibrium values are reached after approximately 4,000 minutes, which is a later point than that observed in the swelling pressure tests. This can be attributed to the fact that, for example, in the case of the sample with an initial dry density of 2.0 g/cm^3, the water content of the saturated sample in the volume-constant swelling pressure test is 12.5 %, whereas the water content of the freely swollen sample in the swelling heave test in the saturated state is 20 % due to the expansion that has occurred. This indicates that the sample is absorbing a greater quantity of water, which is occurring over a longer period of time. The plot of equilibrium swelling strain against initial dry density in Fig. 5.22b reveals a linear increase in swelling strain. The values obtained are considered to represent the upper limit of the swelling strains that can be achieved with this material. A linear fit is provided by Eq. 5.14, which accurately represents the experimental data. A linear relationship has also been observed in the literature, for example in Komine et al. (2009) for six different bentonites.

$$\varepsilon_{max} = 30.74 \cdot \rho_d - 47.20 \tag{5.14}$$

where the dry density ρ_d is used in g/cm^3, yielding the maximum one-dimensional heave ε_{max} in %.
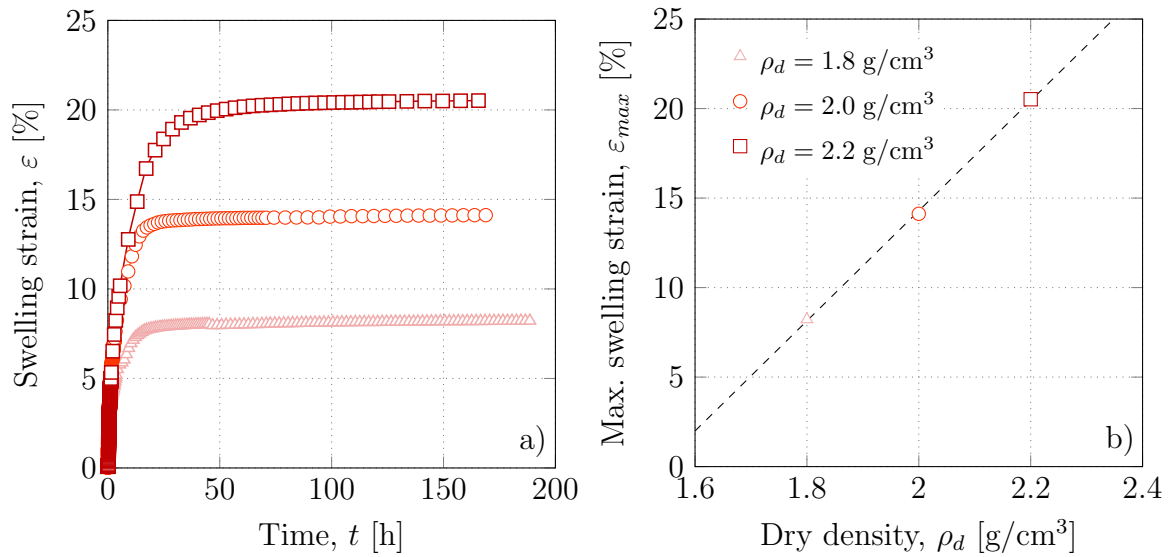

Figure 5.22.: One-dimensional swelling heave tests on compacted OPA powder with different initial dry densities. a) Swelling strain over time and b) equilibrium swelling strain over initial dry density.

A linear representation as shown in Fig. 5.22a is a more suitable method for visualising the phenomenon of swelling heave over time, allowing for the identification of the equilibrium state. This is the reason why it is also a more widely referred approach in the literature. However, for a density of 2.0 g/cm^3, the swelling curve is plotted in a semi-logarithmic scale in Fig. 5.23 to enable a comparison with the idealisation by Sridharan and Gurtug (2004) described in Section 2.1.2.3. The experimental data has been idealised as a line in order to facilitate a more accurate visual representation of the different phases. These are clearly distinguishable in the illustration. The transition from primary to secondary swelling occurs at approximately 1,000 minutes. In the present case of saturation with deionised water, the slope of the secondary swelling branch appears to be relatively flat. This may be indicative of the continued influence of ions present in the remaining pore water of the OPA following sample drilling, even when further saturated with deionised water, on the swelling process.
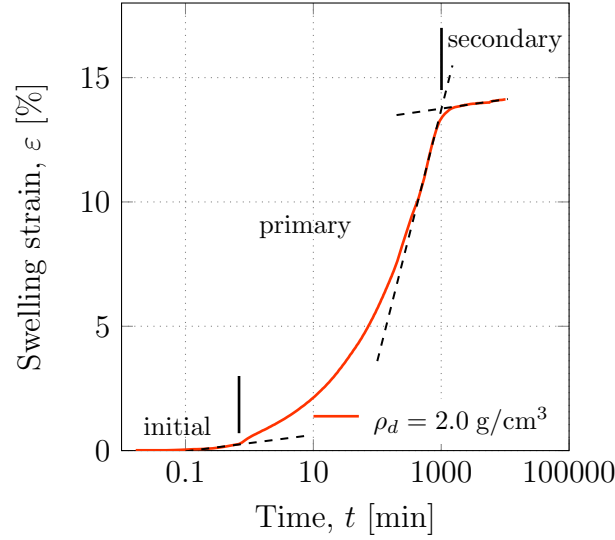
Figure 5.23.: One-dimensional swelling heave test on reconstituted OPA with an initial dry density ρ_d of 2.0 g/cm^3 with a distinction between the three phases of swelling according to Sridharan and Gurtug (2004).

5.3.5.2. Anisotropic volumetric swelling of intact OPA

The three-dimensional strains of a cubic sample of intact OPA (I$_9$) with water saturation are presented in Fig. 5.24. Fig. 5.24a illustrates the definition of the directions of the swelling strains and their relationship to the bedding plane direction. The bedding planes are indicated by means of dashed lines. Fig. 5.24b depicts the experimental outcomes. The maximum strain, occurring after just over 1.5 years, was $\varepsilon_\perp = 16.17$ % perpendicular to the bedding plane direction and $\varepsilon_{\parallel,1} = 2.90$ % and $\varepsilon_{\parallel,2} = 4.78$ % in the two directions parallel to the bedding plane direction, respectively. The three curves exhibit a comparable trajectory. The first strains could only be measured after three hours. This is due to a combination of factors, including the test setup and the slow transport of water via the used wick (see Section 4.3.4.5), as well as the low hydraulic conductivity of the intact OPA. Subsequently, an increase in strains is observed, which becomes more remarkable after approximately 30 days. This observation may be attributed to the complete saturation of the surrounding filter paper and the embedded trenches in the sample holder. Following a total period of 60 days, a notable decrease in the rate of increase was observed in all three directions. The test was ultimately concluded after 580 days. Over the last 60-day period, the increase in strain was observed to be 0.33 % in the direction of $\varepsilon_\perp$ and $\varepsilon_{\parallel,1}$, and 0.27 % in the direction of $\varepsilon_{\parallel,2}$, respectively. The final values of the strains yield a total volumetric expansion of 25 %. The anisotropy factor of the swelling strains in the perpendicular

direction to the bedding planes to the swelling strains in the parallel direction is 5.5 with regard to $\varepsilon_{\parallel,1}$ and 3.4 with regard to $\varepsilon_{\parallel,2}$.

It is not possible to make exact comparisons with existing literature due to the unique nature of the experimental apparatus and boundary conditions employed in the current study. In Wild et al. (2017), a cubic sample is tested to account for the inherent anisotropy, although the sample is saturated with vapour. As proposed by the ISRM (Fig. 2.11), Bock (2001) and Zhang et al. (2010) employed optical measurement tools (calipers) to quantify the deformations of a cylindrical sample in both the vertical and radial directions during saturation. Furthermore, Zhang et al. (2010) utilised vapour saturation (RH = 100 %), whereas the saturation method employed by Bock (2001) is not clearly defined. Additional details regarding the test procedure can be obtained from an internal report (technical note) of the Mont Terri project. However, in the test with vapour saturation on a cubic sample, as presented in Wild et al. (2017), the strain perpendicular to the bedding plane direction is 1.0 % and that parallel to it 0.2 %. In absolute terms, the values are therefore significantly lower, which may be attributed to the use of vapour with a relative humidity of 95 %. Nevertheless, the anisotropy factor of 5 that refers to the inherent anisotropy of the OPA is in excellent agreement with the values determined here. Similarly, the anisotropy factors 7 and 4, respectively, determined from the swelling strain tests on cylindrical samples by Bock (2001) and Zhang et al. (2010) are in accordance with the aforementioned values. The absolute values are again considerably lower, at 7 % (perpendicular) and 1 % (parallel), resulting in a volumetric strain of 9.15 % in Bock (2001) and 8 % (perpendicular) and 2 % (parallel), resulting in a volumetric strain of 12.36 % in Zhang et al. (2010). It is possible that this is also due to saturation via the vapour phase, although the saturation procedure is unknown for the study by Bock (2001). In comparison to the study by Wild et al. (2017), the observed strains in Zhang et al. (2010) are at least four times greater. However, it should be noted that the relative humidity of the vapour used in Zhang et al. (2010) was 100 %, whereas in Wild et al. (2017) it was 95 %.

To demonstrate the relevance of the boundary conditions, in addition to the three-dimensional swelling strain test, two one-dimensional swelling strain tests were conducted in the swelling pressure cells for tunnelling relevant boundary conditions. These tests were analogous to those conducted on reconstituted OPA in the previous Section 5.3.5.1. Two samples were prepared: one sample perpendicular (I_5) and one parallel (I_6) to the bedding plane orientation. The sample oriented perpendicular to the bedding plane exhibited a maximum vertical strain of 11.6 %, while the sample oriented parallel to the bedding plane

demonstrated a maximum vertical strain of 12.3 %. For the sake of comparison with the aforementioned test on the cubic sample the outcomes of the two one-dimensional tests are additionally presented in Fig. 5.24. However, the scaling makes it difficult to distinguish between the two curves. Given the considerable maximum swelling strain exhibited by I_6, the bedding planes were visually inspected following the dismantling of the test to obtain further information regarding the orientation. Nevertheless, this served to confirm that the orientation was indeed parallel to the bedding planes. A new sample with the same bedding plane orientation was tested, which yielded a maximum vertical strain of 12.2 % that was found to be consistent with the previous findings. This implies that the vertical strains are approximately equivalent in both directions if they are determined in a one-dimensional swelling strain test. This indicates that other mechanisms dominate here. The radial confinement results in a homogenisation of the swelling strains, whereas a considerable influence of the bedding plane orientation can still be observed in swelling pressure tests. This may be attributed to the fact that in the swelling pressure test, strains are constrained in all directions, and the prevailing particle orientation is not significantly disturbed by the swelling process. In contrast, swelling strain tests permit an unconstrained direction in which the general swelling potential can be reduced by strains without impediment. This may serve to mitigate the effects of anisotropy. Furthermore, it is evident that the temporal framework of the two experimental procedures differs considerably. In the one-dimensional swelling tests, equilibrium was reached within 20 days ($\parallel$) or 40 days ($\perp$). However, the significantly longer duration of the three-dimensional swelling test can be attributed to the slower saturation rate of 0.005 g/h, but also to the different development of the three-dimensional microstructure. Upon hydration of the sublaminate, new pores and pore networks are created in the unconstrained sample, which can then be filled with water. This process is repeated continuously until the entire sample has undergone delamination, which can be seen in fact in Fig.5.25b.

The magnitude of the measured volumetric strains in the one-dimensional swelling strain tests is approximately 50 % of that observed in the cubic sample in the three-dimensional swelling strain test investigated in this study. This discrepancy may be attributed to three potential explanations. The mechanical boundary conditions in the one-dimensional tests imply that not all of the swelling potential is reduced due to the occurrence of strains; rather, a stress increase also occurs in the radial direction within the sample ring. Moreover, in the one-dimensional swelling strain tests, the top plate exerts a load of 10.5 kPa on the sample, which serves to reduce the swelling strains. Additionally, a skin friction is generated at the sample boundaries upon free swelling. In the three-dimensional swelling strain tests, the sample exhibits unrestricted swelling, with the exception of

the negligible resistance exerted by the displacement transducers. As previously stated, the differing development of the microstructure and delamination constitutes a further contributing factor to the discrepancy in the final volumetric strain between the one-dimensional and three-dimensional swelling strain test. In comparison to the volumetric strains presented in the studies by Bock (2001) and Zhang et al. (2010), the volumetric strains determined in the one-dimensional test are significantly closer.
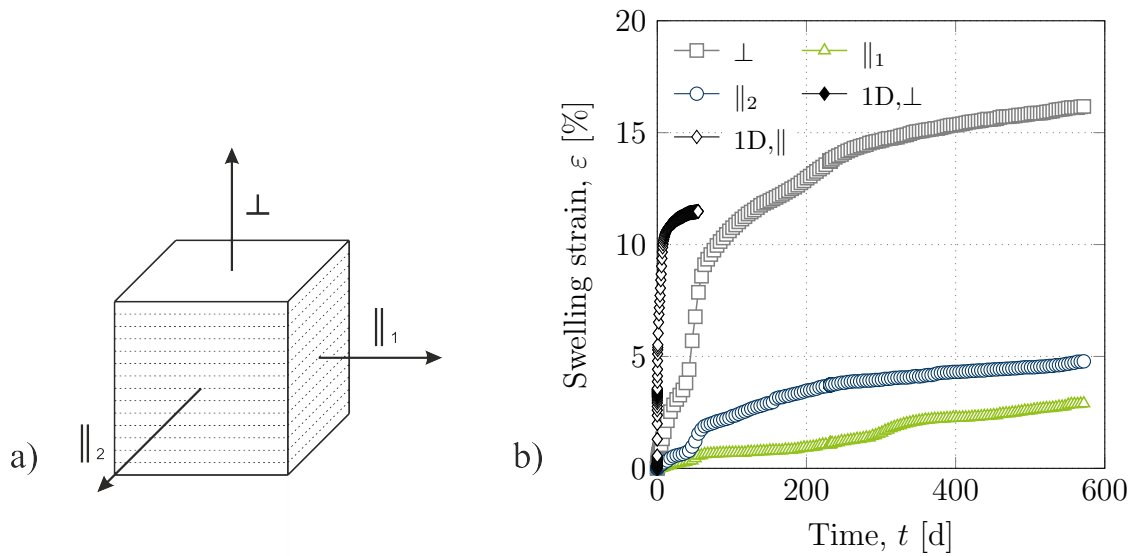

Figure 5.24.: Three-dimensional swelling strain test on intact OPA. a) Definition of the strain directions and b) experimental results of the three-dimensional swelling test and additionally two one-dimensional swelling tests.

Fig. 5.25 illustrates the state of the sample subsequent to dismantling of the test. Fig. 5.25a shows the formation of cracks in the horizontal folds along the bedding planes, as well as the transformation of the sample structure into a sublaminar format with a systematic discontinuity and opening along the bedding planes. Furthermore, the contact surfaces of the LVDTs are also discernible. The contact surfaces of the sample with the sample holder exhibit slight fraying due to the removal process. In general, the shape of the cubic sample is well preserved. However, upon lifting the sample, it became evident that the cracks were not merely superficial, but that the sample had undergone complete delamination in at least two planes (see Fig. 5.25b). A third delamination of the left of the three parts illustrated in the figure is not yet complete. However, the complete disintegration of the sample, which is often observed when clay shale is immersed in water or saturated at an excessively high rate, was successfully prevented by the experimental setup. The final water content at the end of the test was determined to be 12.95 %, which corresponds to

a degree of saturation of 85 % when considering the measured deformations. It is likely that this can be attributed to the opened fractures that lead to relatively large strains and the resulting voids are unable to be completely saturated with water by the usual soil mechanical mechanisms. Furthermore, the images in combination with the still slightly increasing curves of the swelling strain after 1.5 years in Fig. 5.24b provide additional insights that complement the observations presented in the literature (see Section 2.5.2). The phenomenon of floor heave is commonly observed during tunnelling in swelling clay rocks. During unloading, the material may swell and new fractures may open, which can facilitate further water inflow. As evidenced in the literature, this phenomenon is an ongoing process with no discernible endpoint. The upheaved area is continually removed, and after a period of months, the floor heaves up again in the same area. In the initial two tunnel tubes of the Belchen tunnel, this resulted in up to 60 cm of heave in the sections with swelling clay rock before the tunnel floor was installed. This continuously repeating process without a clearly defined endpoint is also evident in the three-dimensional swelling strain test on the laboratory scale.

a)   b)
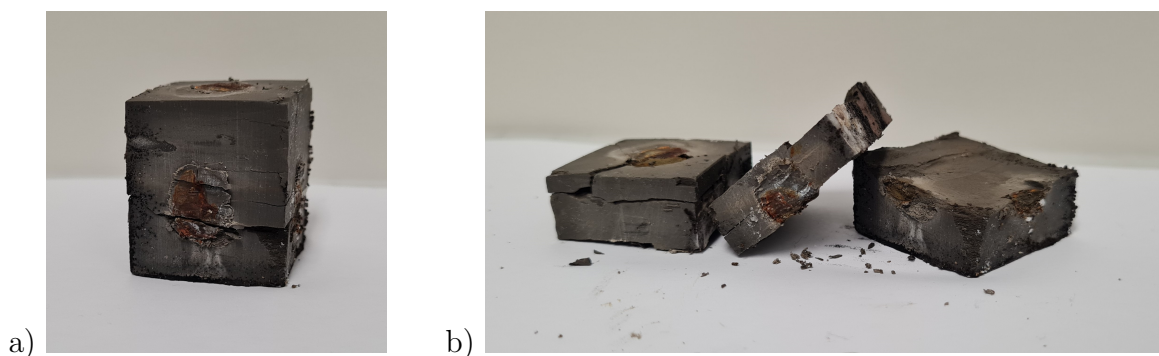
Figure 5.25.: Cubic sample of the free swelling test after dismantling. a) Complete sample and b) the three parts separated along the delaminated bedding planes.

A planned subsequent phase of the study will involve repeating the procedure in the cubic cell in order to determine the three-dimensional strains that depend on the degree of saturation with stepwise saturation via the vapour phase, namely multi-step saturation. The identical suction stages should be selected as those employed in the multi-step swelling pressure test described in Section 5.3.4.3. However, due to time constraints, this could not be conducted in the framework of this experimental campaign, as no further cubic samples were available in time. Additionally, it is anticipated that the saturation of intact OPA via the vapour phase will require a significant time investment.

5.3.5.3. Importance of initial microstructure for volumetric swelling

Before proceeding to the subsequent section, which will address swelling pressure tests with controlled volumetric deformations representing tunnelling-induced unloading and flexible tunnel support systems, it is first necessary to examine the significance of the initial microstructure for the swelling potential. The influence of the microstructure on the swelling pressure has already been demonstrated in Section 5.3.4.4 based on tests with different initial water contents, while the present section will focus on swelling strains. In the tests carried out, swelling pressure tests initiated under identical initial conditions ($\rho_d = 2.0$ g/cm^3) were fully unloaded at different stages throughout their swelling pressure development. The deformations that occur during the subsequent free swelling were measured. The points at which the sample was unloaded during the swelling pressure test are indicated by coloured crosses in Fig. 5.26a. These are at approximately 500 kPa and 750 kPa, which correspond to approximately 50 % and 66 % of the equilibrium swelling pressure, respectively, and at the equilibrium swelling pressure of 1,053 kPa. Furthermore, the free swelling test presented in Fig. 5.22a is included for the sake of comparison.

Fig. 5.26b presents the outcomes of the four swelling heave tests. It is notable that three of the tests exhibited a high degree of similarity. It is evident that the swelling heave test, which was initiated subsequent to complete saturation under constant volume conditions, i.e., after reaching equilibrium swelling pressure, exhibits a considerably reduced maximum swelling strain. This highlights two key points. Firstly, it can be observed that the particle reorientation, which was previously discussed in order to explain the drop in swelling pressure following the achievement of a maximum value, is not a gradual process; rather, it is characterised by an abrupt occurrence. Irrespective of the point in time at which the swelling strain test is initiated (i.e., the complete unloading takes place), the subsequent heave of the sample is identical provided that this occurs before the equilibrium swelling pressure is reached. The collapse of the macropores and the subsequent reorganisation of the microstructure occur abruptly. As demonstrated in this study, this process has a significant influence on the swelling potential of the material. Furthermore, the series of tests highlights the significance of the swelling pressure cell and methodology introduced in this study for boundary conditions pertinent to tunnel construction, particularly for mechanised tunnelling: In the field, the clay is typically already fully saturated, thus exhibiting the same state as that simulated by the initially constant volume swelling observed in the cell. The expansion resulting from the swelling process is inhibited by the overburden pressure. The sample in the cell is therefore in a state that is close to the potential in-situ state. Additional swelling is only observed as a result of unloading,

which can be simulated in the cell through the use of a spindle. Subsequently, the swelling deformations are either completed with the installation of the tunnel lining or, in the case of flexible tunnel support systems, further controlled deformations occur. Moreover, the test protocol considers scenarios in which, for instance, a clay barrier composed of compacted bentonite is subsequently subjected to deformation following complete hydration. In swelling pressure tests in accordance with the methodologies outlined by Huder and Amberg (1970) and Madsen (1999), this initial swelling does not occur under constant volume boundary conditions. Consequently, the unloading occurs at a different initial microstructure of the sample, resulting in a distinct stress-strain correlation. It is noteworthy that Sridharan et al. (1986) had already observed this phenomenon. The combination of Methods III and I (as presented in Section 2.3.2), namely an initial constant volume swelling prior to the material undergoing volumetric swelling and the determination of swelling pressure using Method I, resulted in lower swelling pressures than those obtained through the direct application of Method I. At this stage, a stress path dependency was postulated, although the potential underlying mechanisms were not subjected to further analysis.
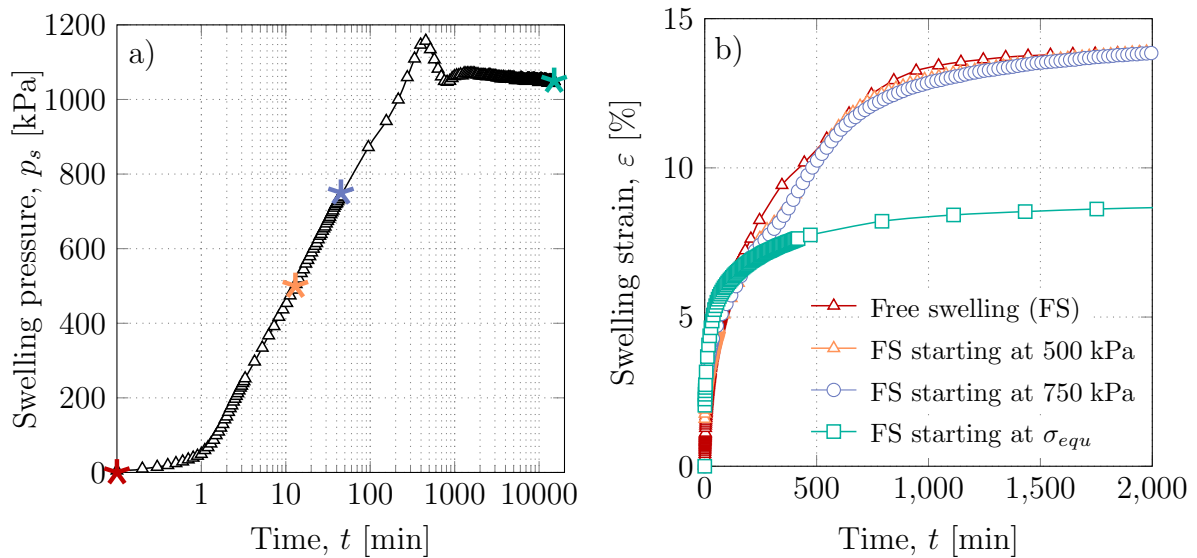
Figure 5.26.: a) Volume-constant swelling pressure test on OPA powder ($\rho_d = 2.0$ g/cm^3) and b) results of heave tests initiated at different states of a swelling pressure test: immediate free swelling, free swelling after reaching a swelling pressure of 500 kPa, 750 kPa and the equilibrium state.

For intact OPA, it can be reasonably assumed that initial swelling is not a necessary step to obtain a relevant initial microstructure, given that the material already exhibits

a monomodal pore size distribution without macropores that could potentially collapse. Nevertheless, a constant volume swelling with volumetric deformations that only occur in the fully saturated state is a more realistic representation of the processes that actually occur during mechanised tunnelling in a previously saturated clay shale. As previously stated, there is evidence in the literature indicating that strain-controlled swelling pressure tests yield results more closely aligned with in-situ data than load-controlled swelling pressure tests. Furthermore, the method, as discussed in Section 4.3.4.4, offers a number of advantages over those presented in Huder and Amberg (1970) and Madsen (1999).

In addition to the swelling heave tests presented in Section 5.3.5.1, the reduced maximum one-dimensional swelling strains of reconstituted OPA after initial volume-constant hydration over the initial dry density are presented in Fig. 5.27. The empty symbols represent data obtained from direct free swelling, while the filled symbols depict data obtained from free swelling subsequent to initial swelling at constant volume conditions. The data illustrate a distinct decline in the maximum strains. As the density increases, an increase in absolute terms and a decrease in relative terms are both observed. In the context of strain-controlled swelling pressure tests, the maximum swelling strains to be achieved are therefore the reduced values indicated by the filled symbols in Fig. 5.27.
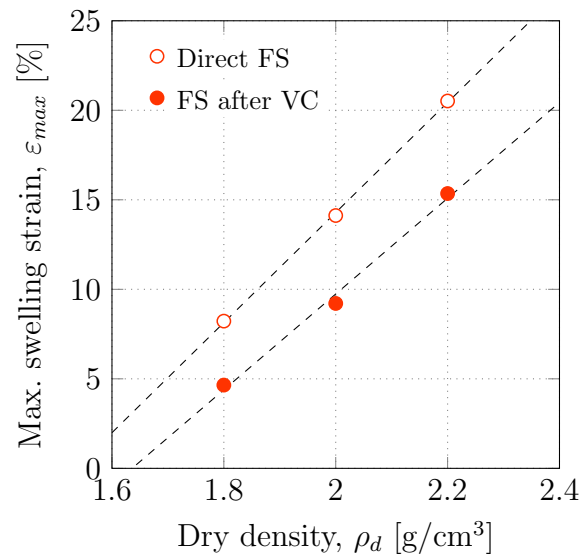
Figure 5.27.: Comparison of the maximum swelling strains of reconstituted OPA with an initial dry density of $2.0 \, \text{g/cm}^3$ for direct free swelling (FS) and free swelling after a previous volume-constant saturation.

5.3.6. Swelling pressure development under controlled volumetric deformations

The following section presents the results of the strain-controlled swelling pressure tests conducted in the newly developed multi-purpose swelling pressure cells. Tests were conducted on reconstituted OPA at three distinct initial densities, as well as on intact OPA both perpendicular and parallel to the bedding plane direction. The experiments on the reconstituted OPA serve the purpose of investigating the fundamental mechanisms and eliminating the influence of inhomogeneities. The concept is then applied to intact material.

5.3.6.1. Swelling pressure-strain correlation of reconstituted OPA

To visualise the test procedure, Fig. 5.28 depicts an illustrative curve of the test with an initial dry density of 2.0 g/cm^3 in the three-dimensional space, considering time, swelling pressure and strain. Fig. 5.29 presents the three projections of the representation as a) swelling pressure over time, b) swelling strain over time and c) swelling pressure over swelling strain.
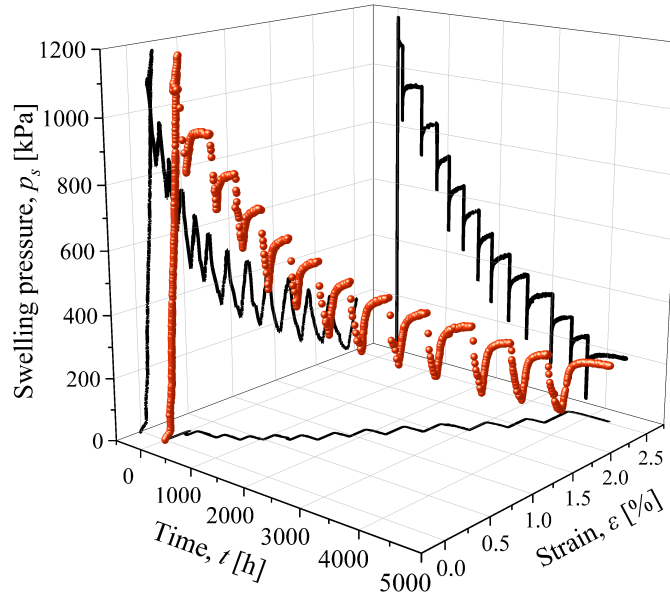
Figure 5.28.: Three-dimensional representation of the swelling pressure-strain-time relation of reconstituted OPA with an initial dry density of 2.0 g/cm^3.
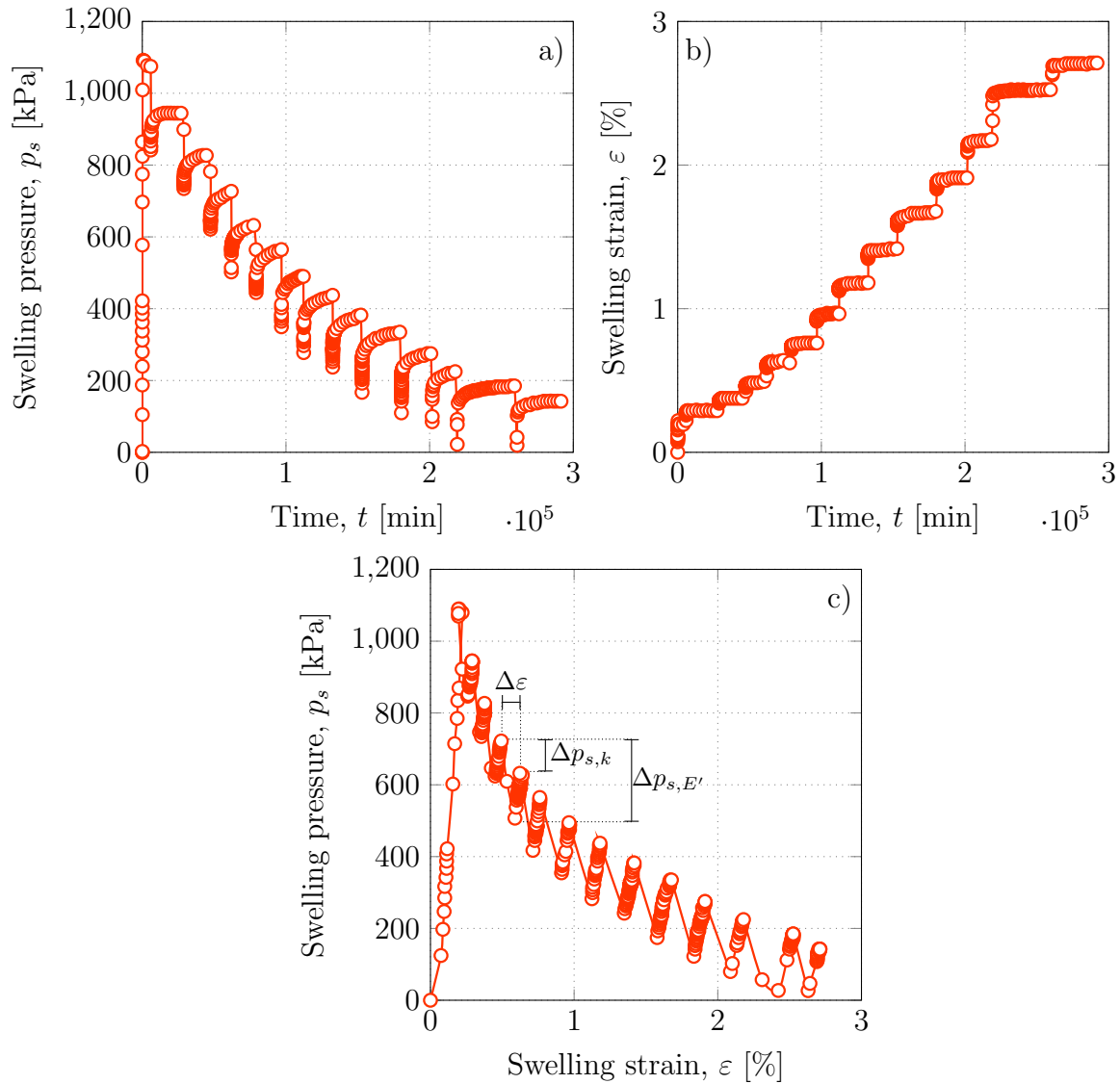
Figure 5.29.: The results of a strain-controlled swelling pressure test on reconstituted OPA ($\rho_d = 2.0 \ g/cm^3$) in the two-dimensional representation as a) swelling pressure over time, b) swelling strain over time and c) swelling pressure over swelling strain.

Fig. 5.29a presents the swelling pressure development in response to strain-controlled un-loading. Initially, the material exhibits a constant volume swelling pressure build-up to a maximum value of approximately 1,180 kPa, after which it reaches an equilibrium value of approximately 1,100 kPa. This minor reduction occurs as a result of the restructuring of clay particles due to the collapse of the macrostructure. A target value of 20 % of the equilibrium swelling pressure, equating to approximately 220 kPa, was selected for a single strain-controlled unloading step. Although the test was conducted in a strain-controlled manner, a stress value was defined as the target value in order to ensure the

uniformity of the steps in the swelling pressure curve. As the pressure was unloaded man-
ually, there were instances where the target value was not reached precisely. Nevertheless,
the precise data were recorded. The unloading step is initially accompanied by an im-
mediate decrease in the swelling pressure. Subsequently, the swelling pressure increases
again due to the reduced hindrance to the hydration of the clay particle surfaces and
the associated osmotic swelling. An equilibrium value is reached over time. Subsequently,
a further unloading step is applied. Fig. 5.29b presents the corresponding strains of the
sample over time. It is notable that a strain of approximately 0.3 % is observed with
constant volume swelling, which represents the inherent self-deformation of the device.
As previously stated in Section 4.3.4.3, this phenomenon is typical for swelling pressure
cells and is attributed to the operational characteristics of load cells. Nevertheless, this
phenomenon is frequently neglected and a perfectly constant volume is assumed in the
majority of studies. However, the initial unloading corresponds to a sudden increase in
strain. Subsequently, the strain remains almost constant, but exhibits a slight increase
over time while the material continues to build up its swelling pressure until reaching
the equilibrium value. It is evident that the strain observed during an unloading step in-
creases with the number of repetitions. This indicates that the strain necessary to reduce
the swelling pressure by approximately 220 kPa increases in proportion to the cumulative
strain of the sample. An exception to this is the final unloading step, in which a lower
magnitude of stress (180 kPa) was unloaded. Fig. 5.29c illustrates the interaction of the
aforementioned mechanisms, as evidenced by the relationship between swelling pressure
and swelling strain. The linear increase in strain with increasing swelling pressure, evident
also in the constant volume phase of the swelling pressure test, is clearly demonstrated
here. Similarly, following an unloading step, the swelling pressure once again increases in
a linear fashion with respect to strain, until an equilibrium value is reached. The swelling
pressure-strain correlation observed here is path-independent, i.e., it is independent of the
number and magnitude of unloading steps taken, provided that the total unloaded stress
remains the same. This hypothesis will be validated in Section 5.3.6.3 using two series of
tests on different materials.

The equilibrium states are represented by a pair of swelling pressure and swelling strain
values, which are plotted in Fig. 5.30. Additionally, the figure presents the outcomes of
the tests conducted with initial dry densities of 1.8 and 2.2 g/cm^3. The resulting relation-
ships can be described with adequate accuracy using a logarithmic fit, and are unique
for a certain initial dry density. This indicates that all potential combinations of swelling
pressure and swelling strain can be predicted. The predictions are represented by dashed
lines and are described using a logarithmic function, otherwise known as Grob's swelling

law (see Eq. 2.20). In order to determine the parameters of the swelling law as outlined by Grob (1972), the swelling pressure for constant volume boundary conditions (σ_0), corresponding to a strain of 0 %, was extrapolated. As previously stated, it is not possible for a swelling pressure cell to maintain exactly constant volume conditions, due to the fact that load cells must deform in order to measure loads. The aforementioned deformations were measured and incorporated into the analysis. The essential parameters are presented in Table 5.12 for all three initial dry densities. A comparison of the results obtained for the three dry densities reveals a correlation between decreasing dry density and a corresponding decrease in the gradient of the swelling pressure-strain correlation, represented by the parameter k. Although the difference in k between the dry densities of 2.0 and 2.2 g/cm^3 is only marginal, k is significantly reduced for 1.8 g/cm^3. This is a reasonable outcome, given the observed exponential increase in swelling pressure with increasing density. At a dry density of 1.8 g/cm^3, the swelling pressure at constant volume is already comparatively very low (Fig. 5.18) and continues to approach zero below this initial dry density.
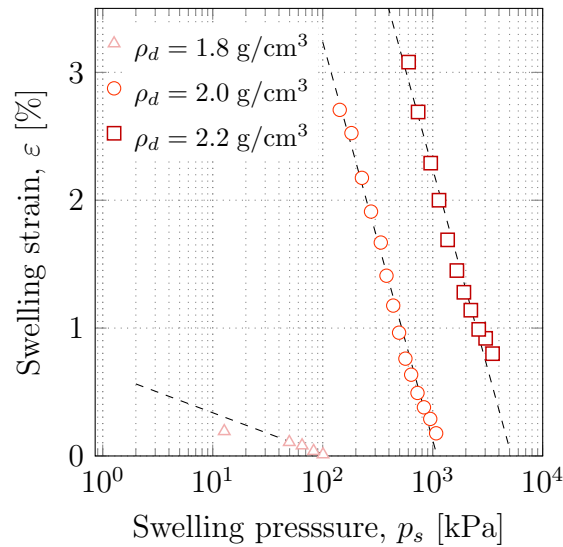
Figure 5.30.: Equilibrium states of swelling strain over swelling pressure of reconstituted OPA with initial dry densities of 1.8, 2.0 and 2.2 g/cm^3.

In calculating the gradient k, only equilibrium states are considered (see Section 2.3.3). The relationship between swelling pressure and swelling strain in the equilibrium state can thus be described; however, the complete coupled process of an unloading step remains unclear. As presented in Fig. 5.29a, there is an immediate reduction in stress before the material exhibits swelling, reaching an equilibrium swelling pressure only after a specific time interval. The average duration of this interval is approximately two weeks. In order

Table 5.12.: Parameters for Grob's swelling law for reconstituted OPA.

ρ_d	[g/cm^3]	1.8	2.0	2.2
k	[-]	0.140	1.352	1.360
σ_0	[kPa]	111	1,096	5,213

to describe the entire coupled process and not just the equilibrium states, it is reasonable to derive a stiffness parameter analogous to E from an oedometer test. This parameter, henceforth designated as E', is thus a hydro-mechanical parameter, as both mechanical (mechanical unloading) and hydraulic processes (unloading-induced build-up of a negative pore water pressure or suction and its dissipation, depending on the hydraulic conductivity) interact (stiffness increase due to suction increase). This parameter explicitly refers to the immediate material response subsequent to unloading, and thus distinguishes from a state of equilibrium as indicated by E in the oedometer test. It should be noted that this parameter is also dependent on the rate of unloading and is therefore only applicable in the context of immediate unloading and therefore undrained conditions. In the course of this study, all unloading steps were conducted within a time frame of one to three seconds, with a maximum of three seconds if re-adjustment was necessary. It should be noted that unloading carried out at a considerably slower rate will yield different values.

To illustrate the increments to which the two parameters k and E' relate, they are shown in Fig. 5.29c. E', however, is calculated analogous to the oedometer test by the following equation:

$$E' = \frac{\Delta \sigma_{E'}}{\Delta \varepsilon} \tag{5.15}$$

where $\Delta \sigma_{E'}$ is the immediate stress reduction due to unloading and $\Delta \varepsilon$ the corresponding strain of the sample.

In order to maintain consistency within the framework, the incremental strain applied to the parameters k and E' must remain constant. Consequently, the gradient E' is including the self deformation of the cell. Nevertheless, Fig. 5.29b illustrates that this supplementary strain, which increases over time in accordance with the swelling pressure, is in an acceptable order of magnitude. It can therefore be concluded that this assumption does not have a significant impact on the results. Furthermore, the parameter E' enables the prediction of material behaviour in a stress-controlled unloading event with subsequent volume-constant swelling.

A dependency on the current stress state becomes apparent when E' is calculated for each unloading step. This is demonstrated in Fig. 5.31 for the test with an initial dry density of 2.0 g/cm^3, showing an almost linear increase of E' with increasing swelling pressure. It should be noted that the pressure in this context refers to the initial state from which the unloading process is initiated. The upper and lower load cells were employed to ascertain whether this dependency on the current stress state could be attributed to friction. However, the data demonstrate that the discrepancy between the recorded pressures in the upper and lower load cells remains relatively consistent throughout the entirety of the test, exhibiting only minor fluctuations between 5 and 10 kPa. It can therefore be concluded that this tendency is exclusively attributable to the behaviour of the studied material. A linear fit, analogous to the typical linear stiffness-stress relationship of clays, offers an accurate description of the correlation shown in Fig. 5.31 and can now be used to map the coupled unloading process. The corresponding linear fit is as follows:

$$E'_{rec} = 2.433 \cdot p_s + 17.461 \tag{5.16}$$

where the current pressure p_s is used in kPa and the immediate mechanical unloading stiffness E' is given in kPa.

An exemplary design chart, using k for the solid and E' for the dashed lines, is presented in Fig. 5.32 for the test with the initial dry density of 2.0 g/cm^3. From any initial condi-
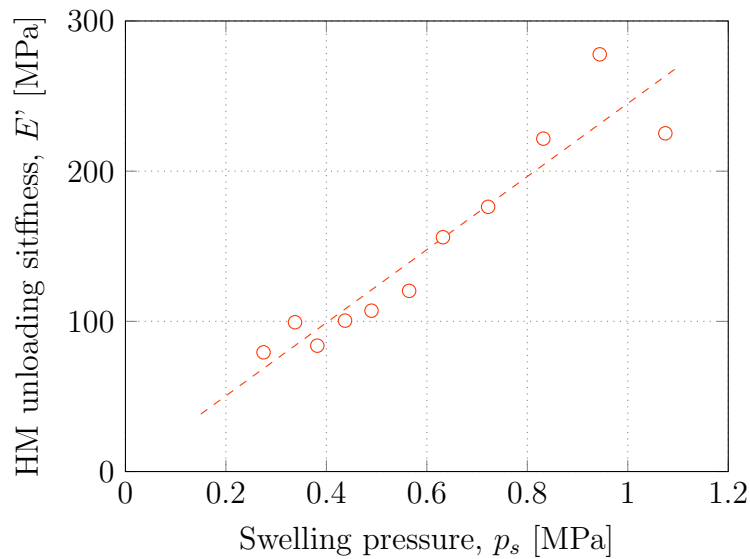
Figure 5.31.: Immediate hydro-mechanical unloading stiffness E' as a function of swelling pressure.

tion, it is possible to predict the material's response to unloading under strain-controlled and stress-controlled conditions, including subsequent volume-constant swelling. Two examples will serve to illustrate this point. The coloured lines in Fig. 5.32 serve this purpose. The first example (depicted in blue) concerns a scenario in which the pressure exerted on the tunnel lining is diminished by a specified amount, potentially as a consequence of structural enhancements such as refurbishment. This gives rise to the question of the maximum pressure that can be re-established over time when saturation is complete. The initial state, indicated by a) in Fig. 5.32, is characterised by a swelling pressure of 530 kPa and a previous strain of 1 %. Subsequently, if the material is unloaded by a further 400 kPa, i.e., to 130 kPa, the strain that will occur can be determined using the design line '$\Delta\sigma \downarrow 400$ kPa' by identifying the intersection of a horizontal line extending from the starting point and said design line. In this instance, the resulting strain when unloading 400 kPa at 530 kPa is 1.42 %. From this point onwards, the intersection of a vertical line with the σ-ε correlation can be used to predict the state of equilibrium or the maximum possible swelling pressure after full saturation c), in this case 382 kPa.

The diagram can also be employed to determine the required unloaded pressure in the short term, in order to guarantee the long-term integrity of the structure (green lines). To illustrate, the following example is provided: after several years of operation, the pressure exerted on a tunnel support system is 800 kPa, while the maximum capacity of the tunnel lining is 850 kPa. In order to enhance the factor of safety, it is necessary to ensure that the pressure does not exceed 600 kPa. For this purpose, the intersection f) of a horizontal line from the starting point d) and a vertical line from the target point e) is employed. In this instance, the point f) is located in close proximity to the design line of 500 kPa unloading. Accordingly, an unloading of 500 kPa is necessary to ensure that the target value of 600 kPa is not exceeded over the long term. In the event of a position lying between two design lines, interpolation is a viable option. This evaluation of OPA powder with an initial dry density of 2.0 g/cm^3 is intended to facilitate comprehension of the fundamental mechanisms utilising a homogeneous starting material and to introduce the concept of the tunnel support design diagram. It is evident that a design diagram of this type is of significant interest when considering intact materials. Such a diagram is also derived and presented in the following section, with the corresponding tests on intact OPA.

Any swelling strain during a swelling pressure test with stepwise unloading can be converted directly into the current dry density of the sample. This is demonstrated for the initial dry densities of 1.8, 2.0 and 2.2 g/cm^3 in Fig. 5.33. By employing the data presented
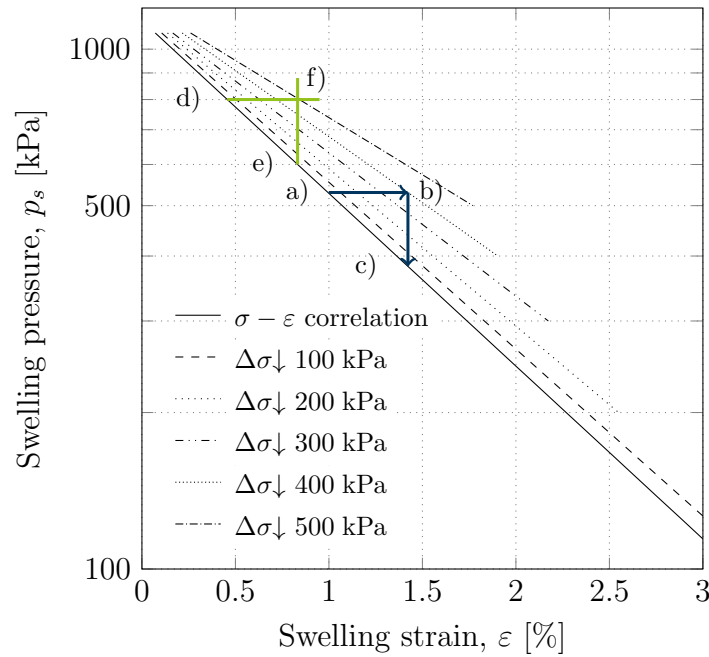
Figure 5.32.: Dimensioning chart for reconstituted OPA ($\rho_d = 2.0$ g/cm³) showing the original stress-strain correlation with design lines to read the deformation associated with a defined unloading and the subsequent swelling pressure equilibrium value.

in Section 5.3.5.3 and Fig. 5.27, it is possible to determine the dry density at which no further swelling pressure can be expected. To achieve this, the maximum strain observed in the tests is converted into the minimum dry density. This results in the three different densities 1.72 g/cm³ ($\rho_{d,init} = 1.8$ g/cm³), 1.83 g/cm³ ($\rho_{d,init} = 2.0$ g/cm³) and 1.91 g/cm³ ($\rho_{d,init} = 2.2$ g/cm³). These values represent the theoretical limit at which the swelling pressure is zero. However, in Fig. 5.33 the swelling pressure tests with constant volume boundary conditions are shown as black diamonds with the corresponding exponential fit as the black dashed line. There is a clear deviation in the swelling pressure-dry density correlation between the tests with stepwise unloading and those with constant volume conditions. As previously discussed in more detail, this difference is due to the different development of the microstructures. In other words, whether swelling strains occur from the bi-modal pore size distribution directly after compaction or from the restructured microstructure after the collapse of the macropores at constant-volume swelling. Based on the data presented in Fig. 5.22, it can be assumed that the swelling pressure of constant volume tests will remain zero at an initial dry density of 1.53 g/cm³.
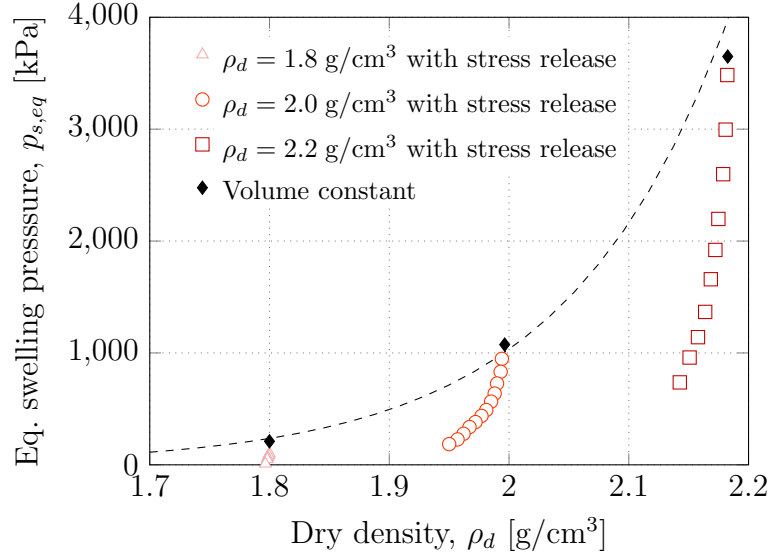
Figure 5.33.: Equilibrium swelling pressure over dry density for volume-constant swelling pressure tests and swelling pressure tests with strain-controlled unloading on reconstituted OPA.

5.3.6.2. Swelling pressure-strain correlation of intact OPA

The test procedure described in the preceding section was carried out in an analogous manner on intact OPA, with due consideration of the bedding plane orientation. The evaluation and concept presented on reconstituted OPA were then applied to the results of the tests with intact material. Fig. 5.34 depicts the complete curves of two swelling pressure tests with stepwise unloading on intact OPA, both perpendicular (I_7) and parallel (I_8) to the bedding plane direction in the three-dimensional swelling pressure-swelling strain-time space. For the sake of clarity, the projections are not included in this figure; they can be seen in Figs. 5.35a to 5.35c as the two-dimensional representations. It is evident that the material exhibits a pronounced anisotropy in its behaviour. The sample oriented parallel to the bedding plane direction exhibited considerably less swelling pressure and corresponding strain. In accordance with volume-constant boundary conditions, the equilibrium swelling pressure perpendicular to the bedding plane direction is 1,893 kPa, while it is 262 kPa parallel to it. This corresponds to an anisotropy factor of 7.2, whereby this is defined as the swelling pressure perpendicular to the bedding plane direction divided by the swelling pressure parallel to it. The magnitude of the unloaded pressure per unloading step is again in both cases 20 % of the equilibrium swelling pressure. In general, the curves do not exhibit the same degree of uniformity as those observed in compacted

powder. At the seventh unloading step of the test on intact OPA perpendicular to the bedding plane direction, the equilibrium swelling pressure is observed to be even higher than that recorded prior to unloading. This is possibly due to both inhomogeneities and changes in the microstructure of the material, e.g., delaminating. Furthermore, the extended test duration with intact OPA is noteworthy. The tests were conducted for a total of 440 days, which equates to an average of 49 days per unloading step. In comparison, the mean duration of each unloading step in the test with reconstituted OPA was 14 days.

As can be seen in Fig. 5.35b, for some stress levels the strain decreases with time. This again emphasises the significance of the tests on reconstituted OPA for the derivation of the concept. This approach enabled the exclusion of such inconsistencies in the fundamental tests. Only positive deformations were applied via the spindle during the test. The decline in strain can possibly be attributed to inhomogeneities, such as fissures present within the analysed sample, which resulted due to the increasing pressure in sagging and the associated reduction in volume respectively negative strain.

The equilibrium states of swelling pressure and swelling strain for intact OPA in both perpendicular and parallel directions to the bedding plane direction are presented in Fig. 5.36. This representation allows the parameters for Grob's swelling law to be derived once more. These results are summarised in Table 5.13. The slope of the strain-log pressure
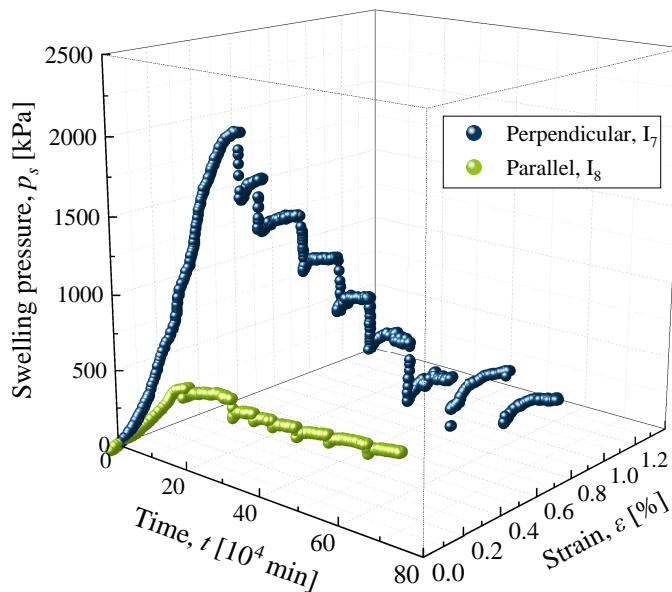
Figure 5.34.: Three-dimensional representation of the swelling pressure-strain-time relation of intact OPA perpendicular and parallel to the bedding plane direction.
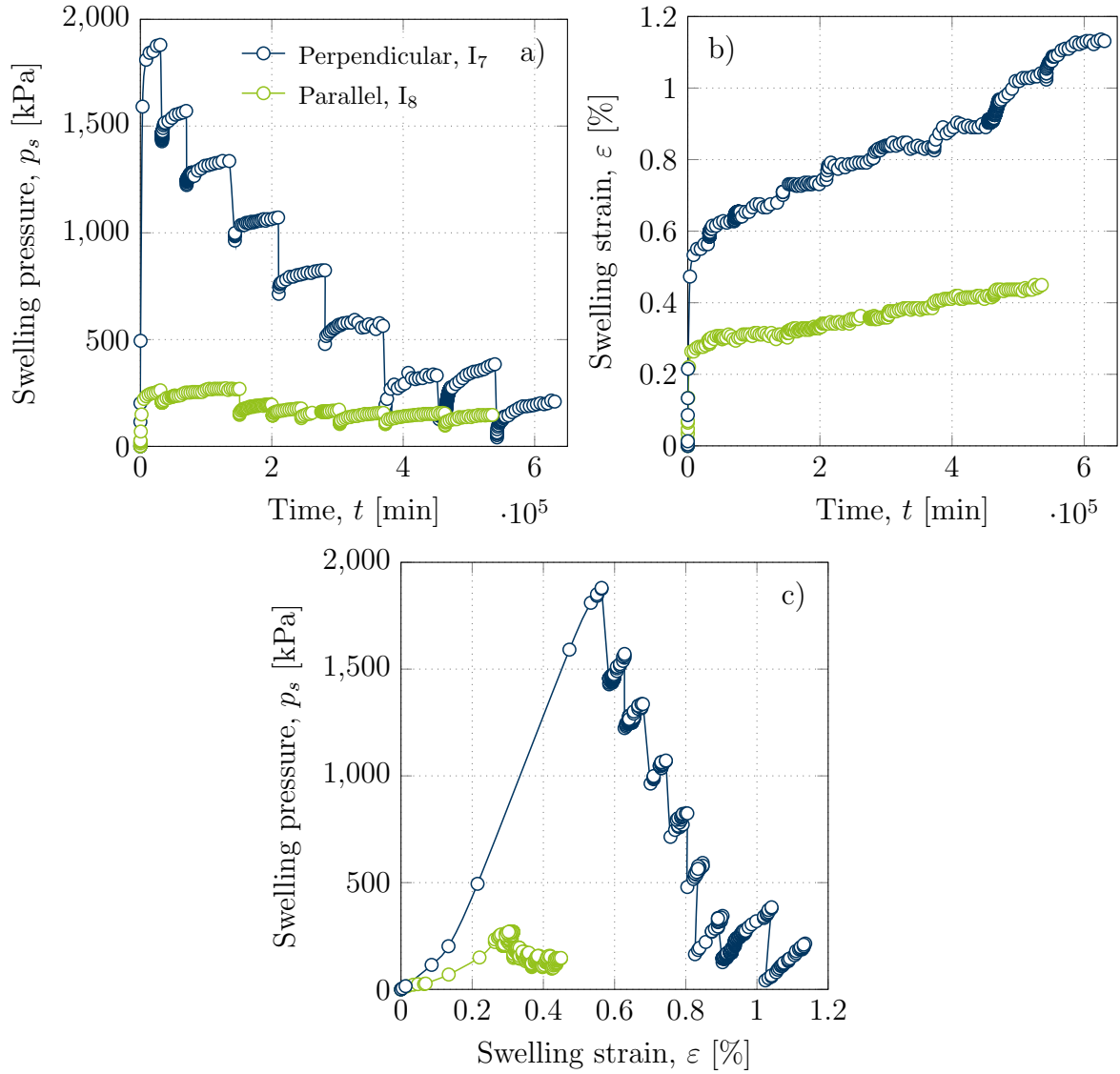
Figure 5.35.: The results of strain-controlled swelling pressure tests on intact OPA parallel as well as perpendicular to bedding plane directions in the two-dimensional representation as a) swelling pressure over time, b) swelling strain over time and c) swelling pressure over swelling strain.

line, designated as k, for the material in a direction perpendicular to the bedding plane is observed to be slightly larger than that in a direction parallel to it. However, both are within a very similar range. The determined slopes yield maximum swelling pressure values σ_0 of 1.1 and 25.5 MPa for the material parallel and perpendicular to the bedding plane direction, respectively, which appear to be significantly higher than the maximum measured pressures. This effect is a consequence of the nature of the analytical model

employed in combination with the self-deformation of the device and the high sensitivity of the swelling pressure of the intact material to occurring strains.
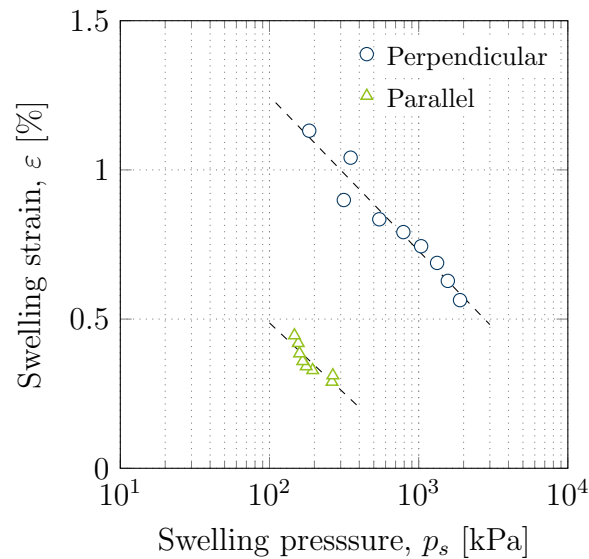
Figure 5.36.: Equilibrium states of swelling pressure and swelling strain of intact OPA perpendicular as well as parallel to bedding plane direction.

Fig. 5.37 presents the corresponding E' values for both samples that were subjected to testing. In particular, the sample oriented perpendicular to the bedding plane exhibits a pronounced scattering around the linear trend. This highlights the significance of the fact that the concept was initially developed and presented on homogeneous powder samples in the preceding section. The experimental results on inhomogeneous samples of intact OPA do not always allow a clear trend to be discerned, but a linear fit can be employed with confidence in light of the aforementioned observations on reconstituted OPA. However, the sample oriented parallel to the bedding plane direction also exhibits a data point that deviates significantly, particularly when considering the compressed scaling for this data set. Only the empty symbols were employed in the fitting of a linear trend. The

Table 5.13.: Parameters for Grob's swelling law for intact OPA considering the bedding plane direction.

		Parallel	Perpendicular
k	[-]	0.204	0.225
σ_0	[kPa]	1,084	25,506

filled symbols were identified as outliers and excluded from the subsequent analysis. The determined E' values can be described as a function of pressure to predict the material behaviour during unloading. The following linear dependencies for E' are proposed for intact OPA perpendicular and parallel to the bedding plane, respectively:

$$E'_{perpendicular} = 1.68 \cdot p_s + 2,004 \tag{5.17}$$

$$E'_{parallel} = 54.18 \cdot p_s - 6,738 \tag{5.18}$$

where the current pressure p_s is used in kPa and the immediate mechanical unloading stiffnesss E' is given in kPa.

The steep slope for the parallel sample is clearly discernible. This indicates that the immediate hydro-mechanical unloading stiffness E' of the corresponding sample is particularly responsive to changes in the pressure state. Fig. 5.36 presents that, in contrast, the slope of the strain-log pressure line for equilibrium states is similar for both materials, indicating that they react equally sensitive to strain increments in the long term.

For pressures below 125 kPa for the parallel sample, the results of the present method yield negative E' values. It can be reasonably concluded that the proposed concept has reached its limits at this point. Fig. 5.37b presents the data with the normalised swelling
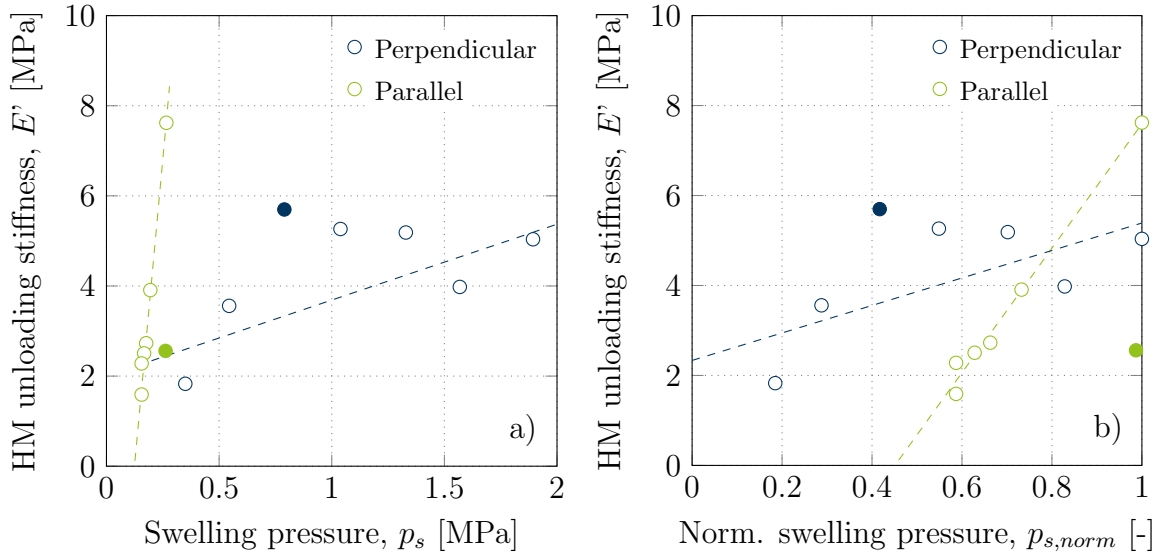
Figure 5.37.: Immediate mechanical unloading stiffness E' for intact OPA parallel as well as perpendicular to the bedding plane direction a) as a function of swelling pressure and b) as a function of normalised swelling pressure. Filled symbols are considered as outliers and are not taken into account for the fits.

pressure (normalised with the maximum swelling pressure). In this representation, the outlier of the sample with an orientation parallel to the bedding plane direction (filled green symbol) is more discernible. Furthermore, it is evident that a stiffness of zero is reached at approximately 45 % of the maximum swelling pressure. This is not a physically plausible outcome, indicating that the trend is likely to change and flatten out in the lower stress range. Therefore, the subsequent steps do not entail extrapolation, but rather interpolation in the experimentally covered range. A comparison with the data from the test on reconstituted OPA with an initial dry density of 2.0 g/cm^3 (Fig. 5.31) reveals a more consistent material behaviour for reconstituted OPA. The data demonstrate a near-perfect fit through the zero point ($E' = 0$ at -7 kPa). This is not the case in Fig. 5.37 for any of the intact samples. The data clearly demonstrate the impact of microstructure and inhomogeneities on the variability and non-uniformity of experimental outcomes. It can therefore be concluded that the procedure of initially investigating the concept on homogeneous reconstituted OPA is confirmed as the appropriate method for obtaining an unbiased picture and clear trends.

The E' values were employed to develop a design diagram for intact OPA that is analogous to that for reconstituted OPA with an initial dry density of 2.0 g/cm^3 as presented in the previous section (Fig. 5.32). The diagram for intact OPA perpendicular to the bedding plane direction is presented in Fig. 5.38 while that for intact OPA parallel to the bedding plane direction is shown in Fig. 5.39. The diagrams may be employed to predict the impact of changes in the stress or strain state of the intact rock mass surrounding the tunnel on the support system. Given the considerable scatter in the data and the non-uniform behaviour of the intact material, it was deemed inappropriate to employ extrapolation in this instance. This implies that two stop criteria have been established for the length of the design lines in the corresponding plots. The lines stop when unloading by the corresponding magnitude is no longer possible, as the current pressure is less than the magnitude of the unloading step (e.g., the line for an unloading of 1000 kPa in Fig. 5.38). In addition, the lines stop when unloading would result in the experimentally covered stress range being exceeded (e.g., the line for an unloading of 200 kPa in Fig. 5.38 and all lines in Fig. 5.39).

The tests conducted on intact OPA provide a comprehensive qualitative assessment of the material's behaviour, facilitating the prediction of this to a certain extent. Nevertheless, the quantitative significance should be treated with caution due to the pronounced inhomogeneity and variability of OPA in the scale of the swelling pressure tests.
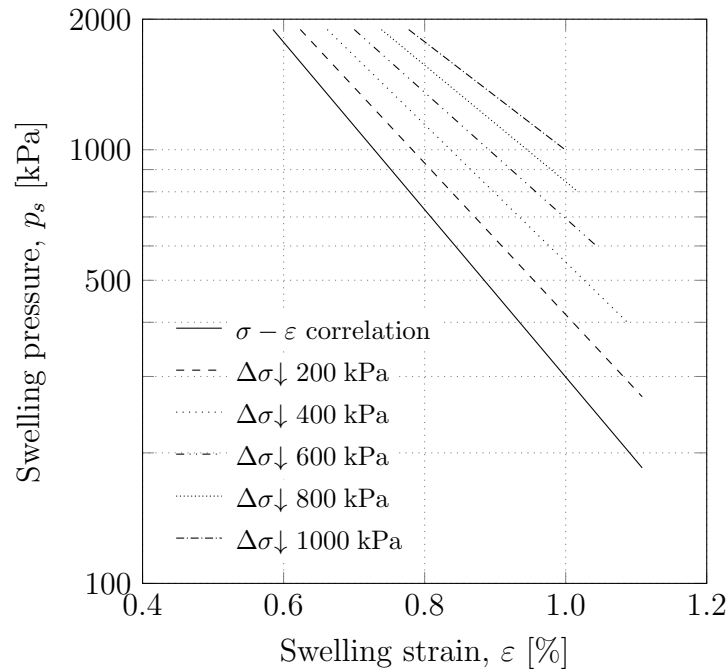
Figure 5.38.: Dimensioning chart for intact OPA perpendicular to bedding plane direction showing the original stress-strain correlation with design lines to read the deformation associated with a defined unloading and the subsequent equilibrium swelling pressure.

5.3.6.3. Verification of the path-independence of the swelling pressure-strain correlation after initial volume-constant swelling

As previously discussed, there is a distinction in the dry density-swelling pressure relationship depending on whether the material is initially saturated under constant volume conditions or not (see Section 5.3.5.3). To demonstrate that this relationship is path independent, assuming that volume-constant swelling has already been completed, two series of tests were conducted on homogeneous starting materials. The initial conditions for the first series of tests were as follows: four identical reconstituted OPA samples with an initial dry density of 2.05 g/cm^3 were initially saturated at constant volume conditions and then gradually unloaded. The total magnitude of the unloading was consistently identical (750 kPa), yet the paths varied. In test I, three unloading steps of 250 kPa were applied. In test II, 250 kPa and then 500 kPa were unloaded. In test III, 500 and then 250 kPa were unloaded. In test IV 750 kPa were unloaded in a single step. A second series of tests was conducted with a different material. The considered bentonite was of a highly swellable variety, specifically a calcium saponite originating from the Westerwald region in western Germany. The maximum swelling pressure of the bentonite, with a dry density
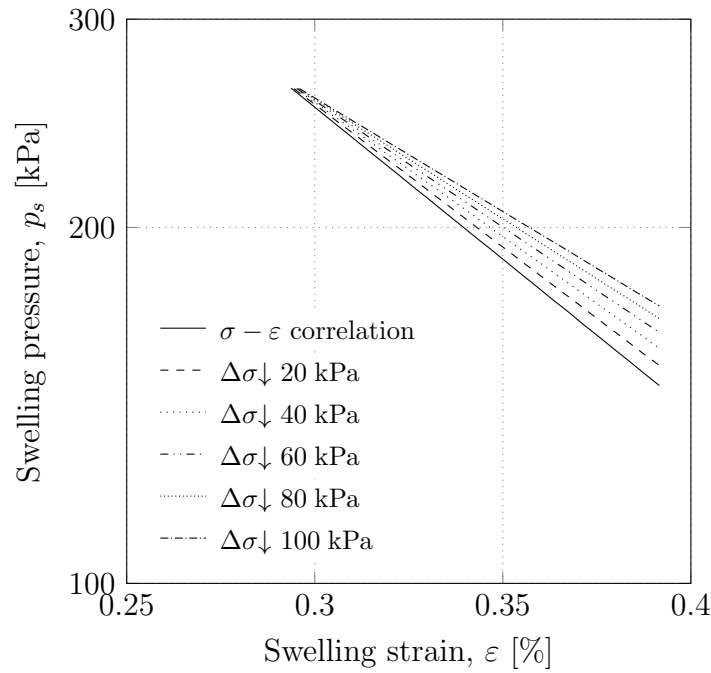
Figure 5.39.: Dimensioning chart for intact OPA parallel to bedding plane direction showing the original stress-strain correlation with design lines to read the deformation associated with a defined unloading and the subsequent equilibrium swelling pressure.

of 1.55 g/cm^3, is approximately 4.5 MPa. Similarly to the aforementioned test series with OPA, four tests were conducted, in which the pressure was unloaded by 3 MPa along different paths. In test I, the pressure was unloaded three times by 1 MPa. In test II 1 MPa and then 2 MPa were unloaded. In test II, 2 MPa and then 1 MPa were unloaded. In test IV, 3 MPa were unloaded in a single step. In both test series, the deformations of the samples associated with the unloading were recorded.

The time-dependent swelling pressure for the four tests on reconstituted OPA is presented in Fig. 5.40a, while the corresponding swelling strain over time is shown in Fig. 5.40b. Similarly, the outcomes of the test series on the bentonite are presented in Fig. 5.40c as swelling pressure over time and in Fig. 5.40d as swelling strain over time. The results demonstrate that irrespective of the number of steps or step size of the unloading, the resulting deformations are identical provided that the sum of unloaded pressure is equivalent at the end. Additionally, the equilibrium swelling pressure at the end of the test is the same. Therefore, the curves in Fig. 5.30 and Fig. 5.36 are specific to the reconstituted and intact OPA, respectively, provided that unloading occurs subsequent to a completed volume-constant swelling.
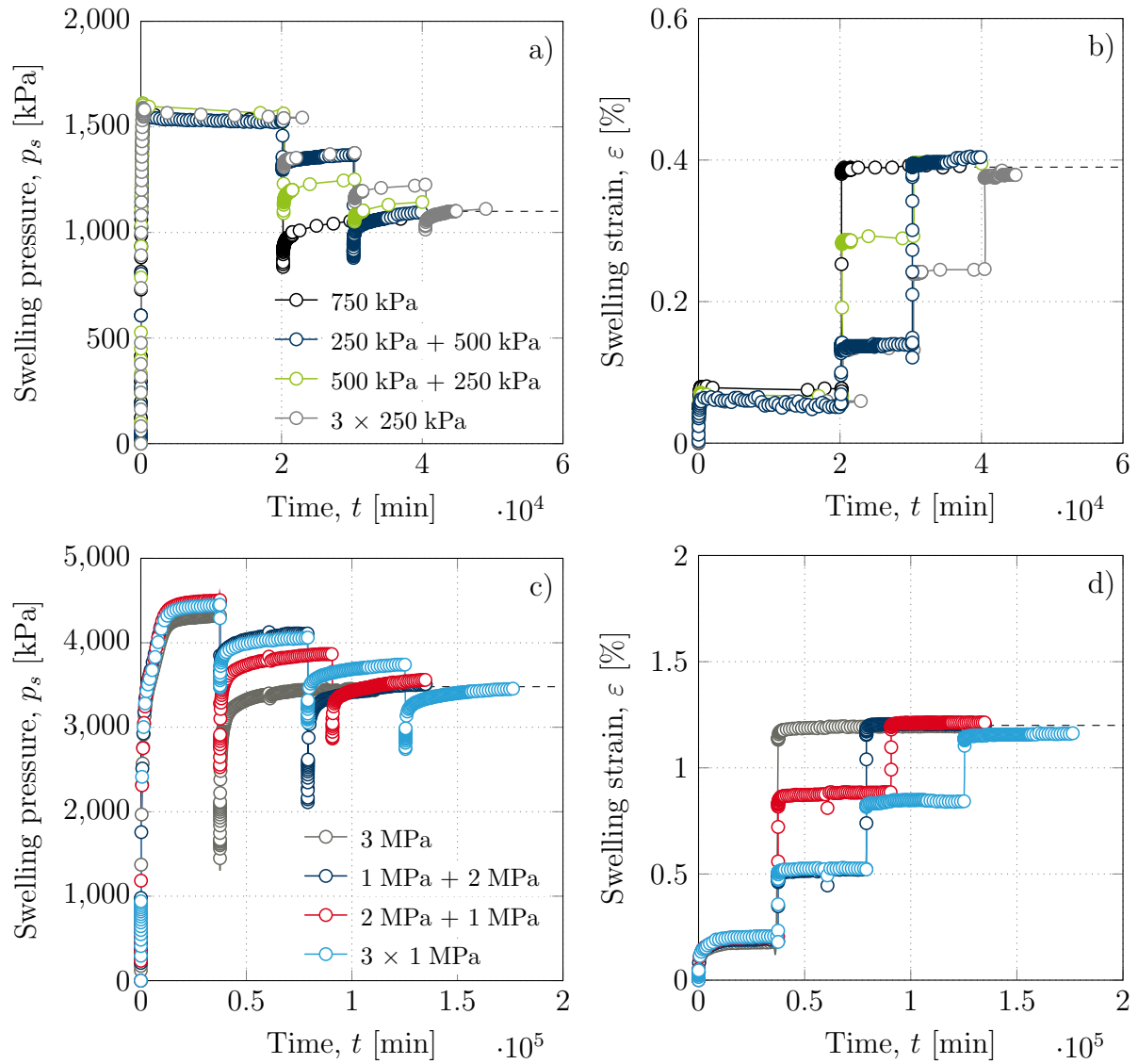
Figure 5.40.: Development of a) swelling pressure and b) corresponding strain over time for reconstituted OPA ($\rho_d = 2.0\,\mathrm{g/cm^3}$) and c) swelling pressure and d) corresponding strain over time for a bentonite with different unloading paths.

5.4. Thermal conductivity of OPA

In a long-term study of the Sanierungstunnel Belchen, Ziegler et al. (2022b) observed fluctuations in the total pressure on the tunnel lining that correlated with steps of the building process in the construction phase and annual temperature cycles in the operation phase. This observation demonstrates the impact of even minor temperature changes and their reversibility. This section presents an initial investigation into the impact of moisture distribution around the tunnel, characterised by the degree of saturation, on the thermal conductivity using reconstituted OPA. Furthermore, intact OPA is analysed in consideration of its bedding plane orientation. The full study is published in Sau et al. (2023).

Curves for the temperature development over the height of a sample (here: OPA powder with $S_{r,init} = 50\%$) are shown in Fig. 5.41 as an example. The thermal conductivity of the reconstituted OPA sample exhibited an inhomogeneous behaviour with respect to its height. This is evidenced by the temperature differences observed at steady-state conditions between the sample's internal points (ΔT of T_3-T_4 and T_4-T_5), which were not constant. This can be attributed to changes in the local soil density and water content during the test in powder samples and additionally inhomogeneities in the intact samples (Romero et al., 2016; Sau et al., 2019). In fact, after dismantling tests, the water content in the powder samples was determined, showing increasing values from the top, close to the heater, to the bottom. The corresponding development of the heat influx and outflux over time is shown in Fig. 5.42. The radial heat loss at the end of the test was rather high with $\Delta q/q_{in} = (q_{out} - q_{in})/q_{in} = 44\%$. A steady-state was reached after approximately 275 min. Therefore, the final thermal conductivity λ of the test was averaged from minute 275 to the end of the test, which was usually after around 390 minutes.

Results of the thermal conductivity tests for reconstituted OPA with different inital degrees of saturation, varying initial dry density and intact samples considering bedding plane direction (I_{12} as $\perp$ and I_{13} as $\parallel$), are summarised in Fig. 5.43. A reduction in thermal conductivity with decreasing degree of saturation can be observed in the reconstituted samples. This trend is in accordance with the fact, that the thermal conductivity of water ($\lambda_{water} = 0.598$ Wm/K) is one degree higher than that of air ($\lambda_{air} = 0.026$ Wm/K at 20°C). The geometric mean model (Farouki, 1981) in Eq. 5.19 was used for the black dashed trend line. A fit based on the available data results in a dry thermal conductivity of 1.43 W/mK and a saturated thermal conductivity of 2.41 W/mK.
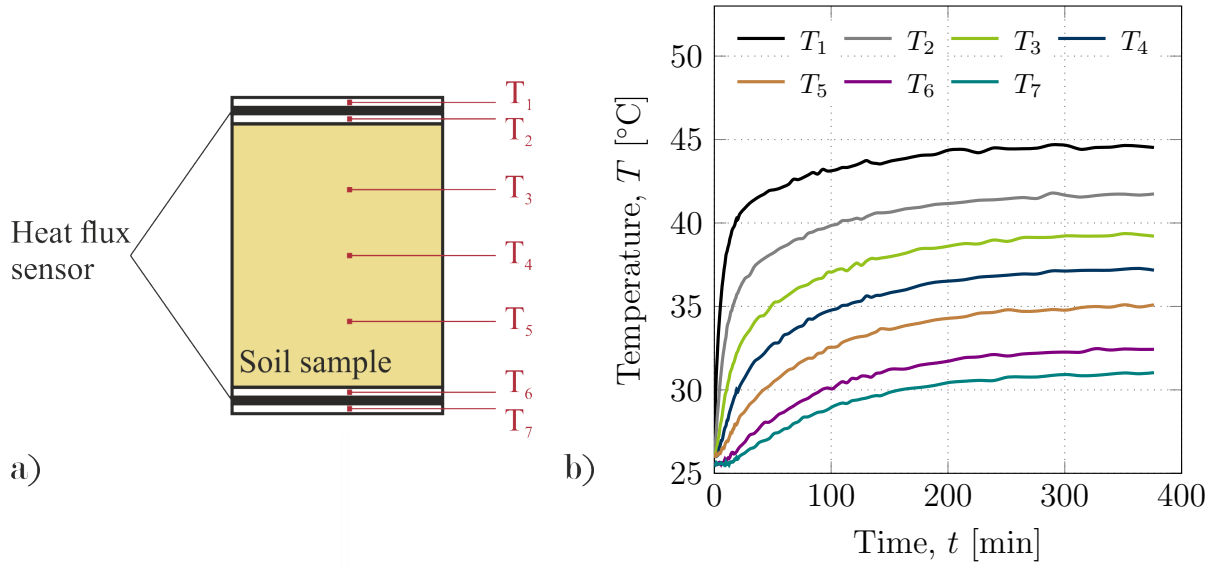
Figure 5.41.: a) Location of the seven used temperature sensors and b) their temperature development in the test on reconstituted OPA with $S_{r,init} = 50$ %.
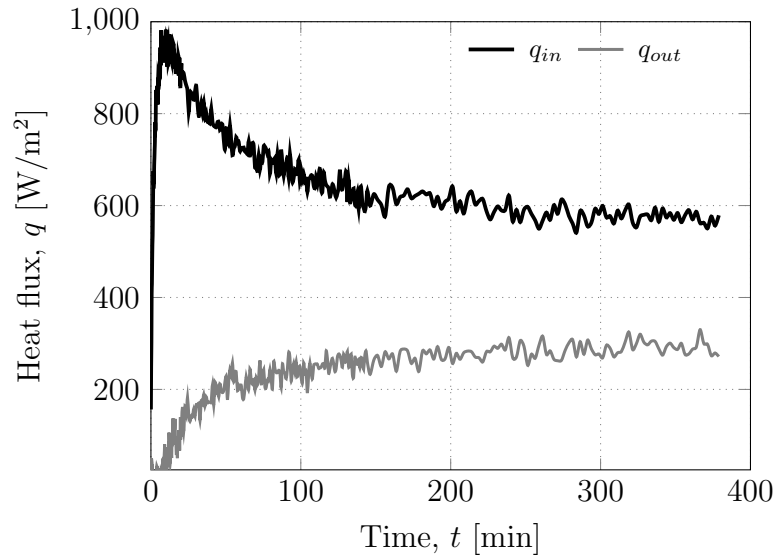

Figure 5.42.: Heat flux in- and outflow of the test on reconstituted OPA with $S_{r,init} = 50$ %.

$$\lambda = \lambda_{sat}^{S_r} \cdot \lambda_{dry}^{1-S_r} \tag{5.19}$$

where λ_{sat} is the saturated thermal conductivity in W/mK, λ_{dry} is the dry thermal conductivity in W/mK and S_r the dimensionless degree of saturation.

Furthermore, the thermal conductivity of reconstituted OPA with an initial dry density

of $\rho_d = 1.9$ g/cm^3 is lower and that for $\rho_d = 2.1$ g/cm^3 is higher than the fitted thermal conductivity trend by $\rho_d = 2.0$ g/cm^3 with the same initial degree of saturation. This in turn can be explained by the fact that the thermal conductivity of the minerals in the soil sample is greater than that of the replaced air. The thermal conductivity of the main constituents is $\lambda = 1.85 \sim 4.05$ W/mK for different clay minerals and $\lambda = 7.7$ W/mk for quartz.

Fig. 5.43 also shows the influence of the orientation of the bedding plane direction to the heat flow. The thermal conductivity of intact OPA parallel to the bedding plane direction $\lambda_{\parallel}$ is significantly larger than $\lambda_{\perp}$ perpendicular to the bedding direction. This can be attributed to the disturbance of the contact between the relatively more conductive minerals caused by the bedding planes in perpendicular direction. This is in good agreement with literature data for intact OPA and other clay sediments or clay rocks like Callovo-Oxfordian, Boom Clay and Ypresian clay (Dao et al., 2014; Garitte et al., 2014; Jobmann et al., 2016; Romero et al., 2016; Conil et al., 2020). The fully saturated thermal conductivity of intact OPA parallel to bedding directions was assumed in this study to be $\lambda_{\parallel,sat} = 3.0$ W/mK, considering a tendency parallel to that of the tested reconstituted OPA. The thermal conductivity of OPA perpendicular to the bedding plane orientation therefore corresponds to about 1.6 W/mK. Therefore, the measured degree of anisotropy in thermal conductivity is $\eta_{tc} = 1.87$. Literature data for fully saturated intact OPA from the shaly facies with respect to the bedding plane orientation is summarised in Fig. 5.44 (NAGRA, 2001; Mügler et al., 2006; Wileveau and Rothfuchs, 2007; Gens et al., 2017). The data from the current tests is in very good agreement with respect to the anisotropy factor, but rather high in absolute values. This is most likely the case due to naturally occurring variations in mineralogy or porosity. As already mentioned, different mineralogical components have different thermal conductivities, whereby the thermal conductivity of quartz is higher than that of the other occuring clay minerals. This could possibly indicate that the quartz content in the samples is greater than those reported in the literature, which were used here for the comparison. Another possibility is that the porosity is slightly lower, which also results in a greater total thermal conductivity, as the thermal conductivity of water in the pores is lower.
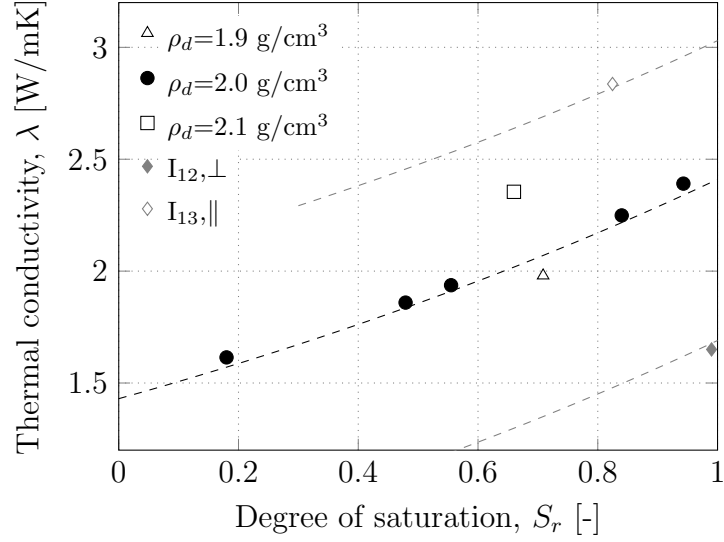
Figure 5.43.: Thermal conductivity of reconstituted OPA with different dry densities and intact OPA over the degree of saturation.
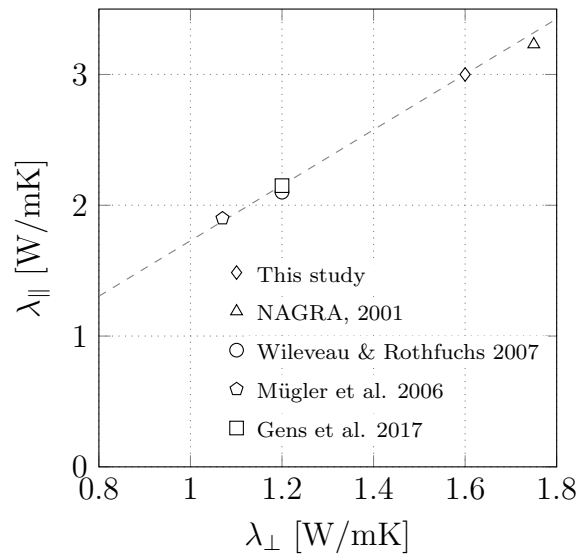

Figure 5.44.: Thermal conductivity of intact OPA considering bedding plane orientation.

6. Summary, conclusions and outlook

6.1. General

Tunnelling and underground construction in general are becoming increasingly important. The installation of underground infrastructure presents a multitude of advantages, particularly in densely populated urban environments. Similarly, natural obstacles in rural areas no longer have to be bypassed through longer distances, which has economic and ecological advantages. However, underground construction in swelling rock, and especially mechanised tunnelling, poses a particular challenge. For a long time, conventional tunnelling was used in this case to reduce the final forces acting on the tunnel structure with customised solutions like compressible zones in the tunnel floor. However, this often resulted in enormous costs and a high expenditure of time. The recent developments of deformation-tolerant segments have made it possible to utilise mechanised tunnelling in swelling rock, thereby capitalising on the advantages of a swelling pressure reduction through controlled deformations and benefiting from the economic advantages of mechanised tunnelling.

This PhD thesis first summarised the basic state of the art on the swelling of clays and clay rocks and provided a brief insight into mechanised tunnelling. The reference project from which the samples analysed in the experiments were obtained was then presented, and the material and methods used were described in detail. The focus in this part of the thesis was on sample preparation, relevant initial parameters and the new test equipment developed for this study.

The main part of the thesis dealt with the presentation and discussion of the results obtained from the comprehensive testing programme on Opalinus clay shale (OPA) in its intact and reconstituted states under boundary conditions relevant to tunnelling, including specific boundary conditions for mechanised tunnelling. Microstructural investigations showed the microstructural features of intact OPA and the differences to the reconstituted OPA that was also investigated. The results of the mechanical investigations enabled

the derivation of complete parameter sets, in particular the stiffness and shear strength parameters, which were used in a complementary numerical partner project (Schoen, 2025). Subsequently, the hydraulic conductivity as a function of the void ratio and the water retention behaviour as a function of the volumetric constraints were investigated for both types of material. Both mechanisms influence the further investigated swelling behaviour. Reconstituted claystone is also used in several studies in the literature, but the influence of the grinding fineness on the hydro-mechanical behaviour is rarely discussed. Therefore, a supplementary study was carried out at this point to investigate the influence of the grain size distribution on the hydro-mechanical behaviour.

The two limiting cases of constant volume and free swelling were then analysed, again using intact and reconstituted OPA. For constant volume swelling, the influences of fabric, initial dry density, saturation mode and initial degree of saturation were analysed. In the case of free swelling, the influences of the initial density with reconstituted OPA, the inherent anisotropy and initial microstructure were considered in particular. The main focus of the study was on the swelling pressure development under controlled volumetric deformations. Strain-controlled swelling pressure tests in the specially designed new swelling pressure cells simulated flexible tunnel support systems. This allowed the development of a concept including a design diagram to be derived from tests on reconstituted OPA, which predicts the immediate reduction as well as the equilibrium state of the swelling pressure in response to volumetric deformations. This was validated on the basis of corresponding tests on intact OPA, taking into account the bedding plane orientation. A path in dependency could be proven.

The final step was a small test programme to determine the thermal conductivity of reconstituted OPA as a function of the degree of saturation and intact OPA as a function of the bedding plane orientation. This served as an initial outlook for potential further studies.

6.2. Key findings

The following conclusions can be drawn on the basis of the investigations carried out in this work and their results:

Influence of the volumetric boundary conditions on the soil-water retention behaviour

The soil-water retention behaviour of intact and reconstituted OPA has been assessed in free and volume-constrained conditions. The experimental results indicated a minor influence of the volumetric boundary conditions on the SWCC of reconstituted OPA and no influence on the SWCC of intact OPA. However, a remarkable discrepancy in this respect was observed in Seiphoori et al. (2014). This was attributed to the analysis of bentonite, which exhibited a higher swelling potential than OPA, both in its intact and reconstituted state. The mineralogy of OPA contributes to its lower swelling potential. However, a slight difference was still discernible in the reconstituted OPA. This was no longer the case for intact OPA, where the clay shale bonding further reduces the swelling potential. Additionally, the air-entry value obtained from the current experiments was found to be consistent with other measurements reported in the literature.

Influence of the grain size distribution on the hydro-mechanical behaviour of reconstituted OPA

A study on the influence of the grain size distribution on the hydro-mechanical behaviour and compressibility of reconstituted OPA (three batches: fine, medium, and coarse) revealed clear trends from the fine to the coarse material in all tests. The XRD investigations indicated that both preferential breakage of specific clay minerals and amorphisation are negligible. The tested subsamples demonstrated no evidence of uneven mineral segregation. The intrinsic bonding that persists in the larger grains of OPA in coarse material served as an additional attractive force, thereby counteracting the expansion that occurs upon hydration. Furthermore, the larger free surface area of the finer material facilitated the hydration process, resulting in a generally higher water absorption capacity. This is in contrast to observations made with bentonite, where the pore space of the granules facilitates water absorption. The differences in the hydration process of samples with varying grain sizes were also reflected in the magnitude of the swelling pressure. The enhanced water adsorption capacity of fine material elevated the swelling pressure, whereas the

supplementary attractive force resulting from the residual bonding in the larger grains of coarse material mitigated the swelling pressure. The constrained moduli from oedometric compression tests in the high stress regime for varying grain sizes demonstrated similar behaviour in the normally consolidated state. However, the residual bonding of grains resulted in discernible overconsolidation effects at lower stresses. The investigation revealed that the finest material showed the weakest effects of overconsolidation. The influence was even less evident in a data set from Favero et al. (2016), in which the material was sieved prior to testing, thereby excluding coarse grains. In conclusion, it could be stated that finer powders should be preferred for investigations on the intrinsic behaviour of ground clay shale, given that the effects of overconsolidation are still visible in the coarse powders. It was discovered that the coarse material could be removed through a sieving process, as this did not affect the mineralogical composition of the powder due to the preferential crushing of specific clay minerals.

Key advantages of reconstituted over intact material to study basic mechanisms

In the course of this study, several advantages of using reconstituted instead of intact OPA samples have emerged. Of course, the investigation of intact OPA is essential in order to make reliable statements about the field behaviour and thus for practical application. Furthermore, the microstructure adds properties that lend additional relevant aspects to the material behaviour. However, there are some aspects that make it considerably more difficult to obtain reproducible results in an economically justifiable period of time and to investigate and understand basic mechanisms first. Due to the inherent inhomogeneity of the clay shale, repeated tests often show significantly different results. In swelling pressure tests with intact OPA, the variability of the results was $\pm 53.59\,\%$ with an average value of 209 kPa and $\pm 52.42\,\%$ with an average value of 1,608 kPa for samples oriented parallel or perpendicular to the bedding plane orientation, respectively. When using reconstituted OPA, however, the variability was only $\pm 3.55\,\%$ with an average value of 1,071 kPa. Furthermore, it is essential to consider the orientation of the bedding planes in the sample when evaluating intact OPA. Consequently, the test must be performed at least twice, with orientations perpendicular and parallel to the bedding plane direction, respectively. Furthermore, the duration of the test was approximately four times longer with intact than with reconstituted OPA. The aforementioned factors collectively indicated that it is prudent to conduct specific tests on reconstituted OPA initially, with the objective of acquiring a fundamental understanding of the material behaviour in a reasonable timeframe. This approach allows for the identification of patterns

and the formulation of concepts based on these observations. With these insights in mind, they can afterwards be transferred to intact OPA for validation. This step is of great importance, as qualitative observations on the reconstituted material can be transferred, whereas quantitative observations are of limited value.

Relevance of volumetric boundary conditions with regard to anisotropic strains

The results of tests conducted to determine the maximum swelling strains on intact anisotropic clay shale samples have demonstrated that these results are significantly influenced by the volumetric boundary conditions. Tests on cubic samples, carried out in a specialised cell in which the strains were analysed simultaneously in three directions, clearly demonstrated the presence of anisotropy. In contrast, anisotropy could not be detected in cylindrical samples produced according to the orientation of the bedding planes and subsequently analysed in one-dimensional swelling tests. This was attributed to the fact that the radial confinement and the possible restructuring of the clay particles in the one-dimensional swelling heave samples resulted in a homogenisation of the strains due to the reduction of swelling potential in one direction. However, both cases may be relevant in practice. The potential for expansion in only one direction or in several directions depends on the type of excavation.

Influence of initial microstructure on the HM-behaviour of reconstituted samples

Two test series on reconstituted OPA demonstrated the impact of the initial microstructure on the hydro-mechanical behaviour. One of these exhibited initially an increasing equilibrium swelling pressure in swelling pressure tests with the same initial dry density but increasing initial degree of saturation, which was contrary to the expected outcome. This was attributed to the initial microstructure created by the compaction of the samples with water contents on the dry side of the optimum water content. This results in an aggregated microstructure with edge-to-face contact and a bimodal pore size distribution. Consequently, the comparatively large pores between the particles, which are typical of compaction at low water content, initially become smaller with increasing initial water content. This, in turn, results in a higher swelling pressure. Only at a later stage does the equilibrium swelling pressure begin to decrease as the initial water content continuously increases. In the second series of tests, it was demonstrated that prior constant-volume swelling of a clay sample resulted in a lasting alteration to the microstructure, as evidenced by a notable reduction in the maximum strains observed in subsequent free swelling tests.

This phenomenon may be associated with the characteristic drop in the swelling pressure curve observed in compacted bimodal clay samples, which can also be attributed to a restructuring of the clay particles.

Impact of flexible tunnel support systems on the HM-behaviour

Using the new test equipment, it was possible to gain important insights into the influence of flexible tunnel support systems on the reduction of the swelling pressure acting on the tunnel structure. Although Grob's swelling law, which is a log function, accurately describes equilibrium states of swelling strain and swelling pressure, a hydro-mechanical immediate unloading stiffness was introduced to predict the complete process of unloading, the immediate resulting pressure drop and the long-term equilibrium state. On this basis, it was possible to derive a simplified design diagram for reading the relevant information. To illustrate, the immediate reduction in pressure that results from a remediation measure can be employed to estimate the swelling pressure that will be restored over time following complete hydration. Alternatively, the required radial deformation can be determined in order to ensure that the swelling pressure does not exceed a defined limit value over the long term. Subsequently, it has been demonstrated that the unloading process is path independent. The concept was initially derived for reconstituted OPA, where uniform material behaviour was observed. It was then validated on intact OPA, with consideration given to the bedding plane orientation. In the case of intact OPA, trends were still discernible, although in some instances, they were less apparent. It was observed that the swelling pressure of OPA parallel to the bedding plane orientation exhibited a considerably more pronounced sensitivity to strains than that perpendicular to it.

Preliminary findings on the thermal conductivity

The results of this work package were in good agreement with the existing literature with regard to the measured absolute values, the anisotropy of the intact material and an increasing thermal conductivity of the reconstituted material with an increasing degree of saturation. This is due to the higher thermal conductivity of water compared to air. At the same degree of saturation, a significantly higher thermal conductivity was observed for intact OPA when oriented perpendicular to the bedding plane direction, compared to when oriented parallel to it. The reconstituted OPA exhibited a value that was approximately midway between the two observed values. Additionally, an increase in thermal conductivity was noted with an increase in initial dry density for the reconstituted samples. The

findings of the study demonstrated the impact of the degree of saturation on the thermal conductivity, thereby highlighting the role of moisture distribution in the vicinity of the tunnel in shaping the resulting temperature profile. Furthermore, it was demonstrated that the maximum range of thermal conductivity for typical degrees of saturation in the context of tunnel construction of $S_r = 70\text{-}100\,\%$ is approximately 0.5 W/mK.

6.3. Recommendations for further studies

The work on this project raised further questions which can be regarded as recommendations for future investigations and will systematically improve research on this topic. Suggested tasks are:

Influence of annual temperature cycles on the HM-behaviour

In Ziegler et al. (2022b), measurement data regarding the stress evolution around the Sanierungstunnel Belchen during the first four years of the operation phase were analysed. It was observed that annual air temperature cycles have an influence on the radial pressures on the tunnel structure. This was attributed to the rock formation and concrete lining expanding and contracting with rising and falling temperatures. There are numerous studies on the influence of temperature on the hydro-mechanical behaviour of clay shales in the context of radioactive waste disposal. There, temperatures of 100°C are usually used, which are maintained for a certain period of time after the heating phase and then allowed to decrease after the heaters are switched off (Gens et al., 2017). This is intended to represent the initially high temperature of radioactive waste, which subsequently declines over time. Likewise, in Germany, the maximum permitted temperature for radioactive waste has been set at 100°C by the Bundesgesellschaft Für Endlagerung (2024). However, the minimum measured temperatures in the rock mass surrounding the Sanierungstunnel Belchen were around 7°C and the maximum temperatures were only 17°C. In addition, this is a different load case, as the temperature changes occur cyclically. Therefore, studies on the influence of annual temperature cycles at lower absolute temperatures on the hydro-mechanical behaviour of the rock mass and thus the forces acting on the tunnel structure are highly recommended.

Self-healing capacity of fractured clay shales

The unloading during mechanised tunnelling creates an EDZ around the tunnel in which fractures open up in the clay shale and thus create preferential flow paths. These in turn can bring water from water-bearing layers into formerly dry layers of swellable clay shales, which initiates swelling processes. However, the preferential flow paths close again over time as a result of the swelling process. It would be highly interesting to specifically analyse this change in hydraulic conductivity in the EDZ or generally fractures. This explicitly raises the question to what extent changes in hydraulic properties are reversible and to what extent they are permanent, and what the time frame for these processes is.

Supplementary tests for the complete calibration of a BBM parameter set

In a related thesis (Schoen, 2025), the knowledge gained here and the experiments carried out are used to conduct numerical investigations. The focus of that work is on the influence of mechanised tunnelling on the development of the EDZ and the hydro-mechanical processes in the near field of the tunnel. The Barcelona Basic Model (BBM) is used as the constitutive model for this purpose. However, in order to be able to calibrate a complete set of parameters, e.g., for reconstituted OPA, various suction-controlled tests, that were of no great relevance in the context of the current study, are missing. According to Alonso et al. (1990), these are: isotropic drained compression tests at several constant suction values, tests with drying-wetting cycles at a given constant mean net stress and drained shear strength tests at different suction values. The results of these experiments would provide a significant contribution to the conducted numerical investigations.

Assessment of the evolution of K_0 during swelling tests

Constitutive models are usually calibrated using mean stress or net mean stress rather than vertical stress. However, the horizontal stresses in oedometer or swelling pressure tests are not regularly measured, so assumptions are made for K_0. These are based on a constant value. It would be worth analysing this assumption and the K_0-value in general in more detail using experimental data from swelling tests in modified test devices measuring the horizontal stresses, preferably including free swelling tests, constant volume swelling pressure tests and strain-controlled swelling pressure tests.

Influence of the pore water chemistry on the hydro-mechanical behaviour

It is known that the ion concentration in the fluid used to saturate a clay or claystone has an influence on its hydro-mechanical behaviour. In mechanised tunnelling, there are different sources of water which can initiate swelling of the surrounding rock mass. This can be, for example, the in-situ groundwater or the bleeding water of the grout used. In addition, deionised water is often used in laboratories, as in this study, in order to obtain comparable results. It would be recommended to carry out a detailed study on the influence of the ion concentration and the resulting pH value of the fluid used for saturation on the hydro-mechanical behaviour of a clay rock under boundary conditions relevant to mechanised tunnelling.

A. Appendix
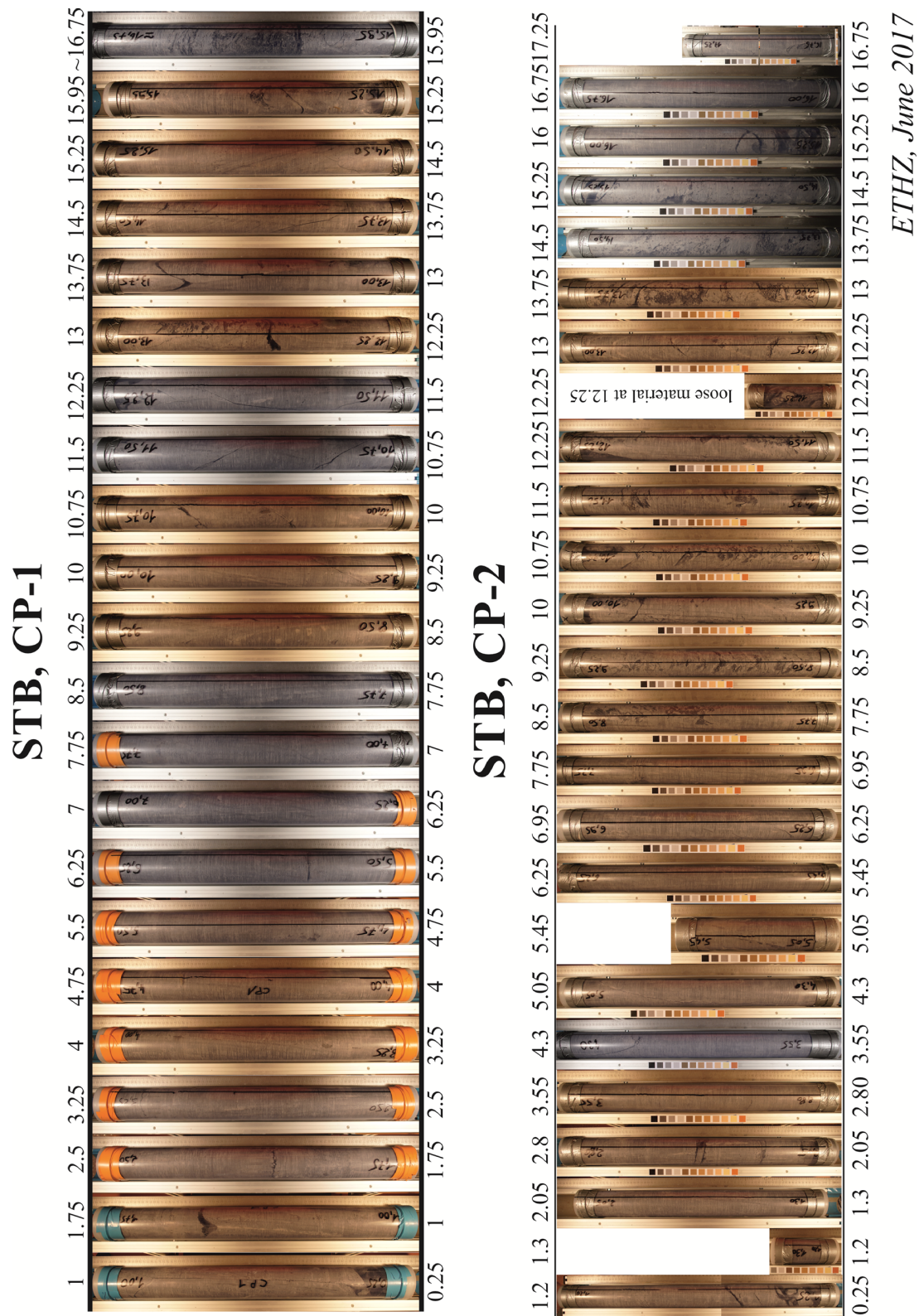
Figure 1.: Drilling cores CP1 and CP2 parallel to bedding direction from Soares (2017).
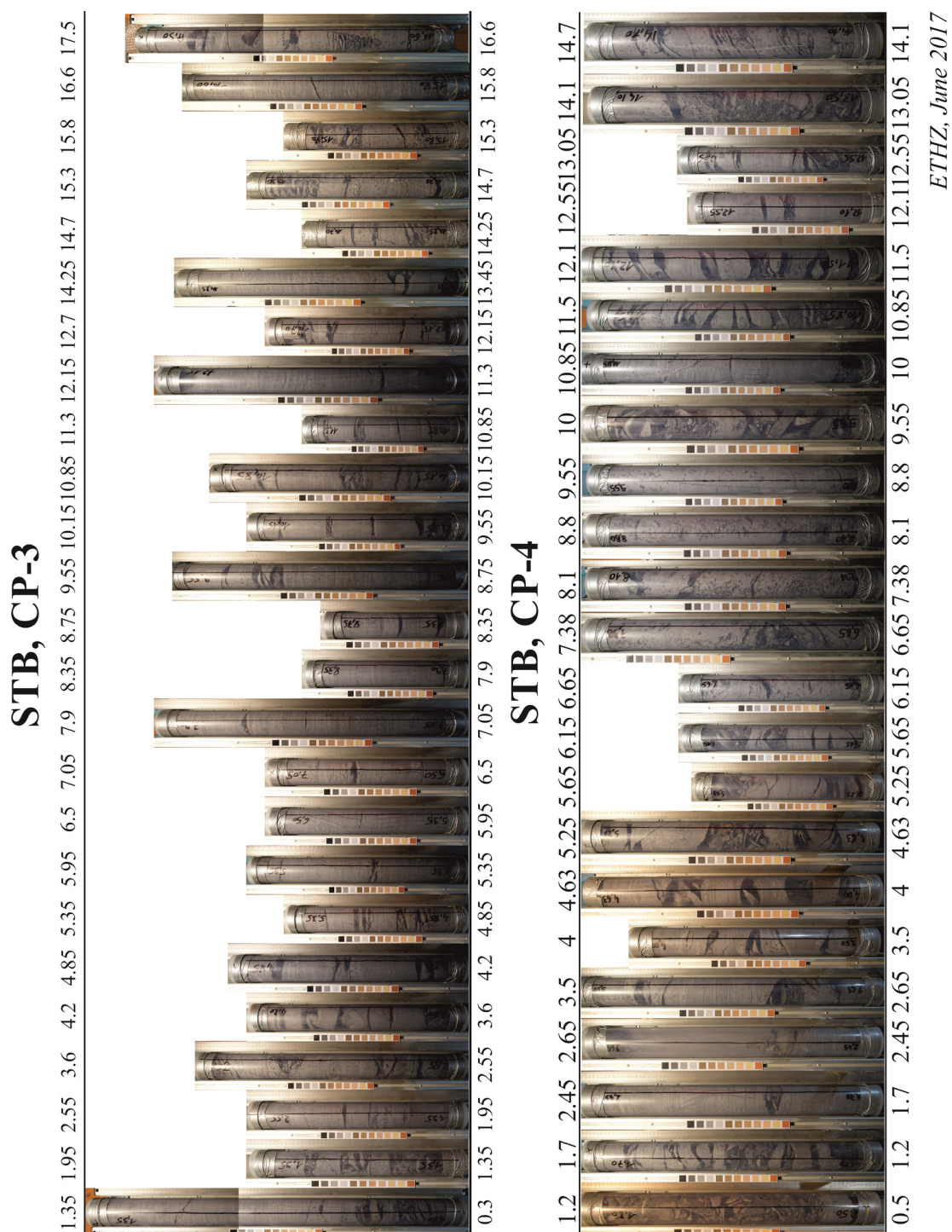
Figure 2.: Drilling cores CP3 and CP4 perpendicular to bedding direction from Soares (2017).

Bibliography

Acikel, A. S., Gates, W. P., Singh, R. M., Bouazza, A., Fredlund, D. G., and Rowe, R. K. (2018). Time-dependent unsaturated behaviour of geosynthetic clay liners. *Canadian Geotechnical Journal*, 55(12):1824–1836.

Agus, S. S., Arifin, Y. F., Tripathy, S., and Schanz, T. (2013). Swelling pressure–suction relationship of heavily compacted bentonite–sand mixtures. *Acta Geotechnica*, 8(2):155–165.

Agus, S. S. and Schanz, T. (2005). Comparison of Four Methods for Measuring Total Suction. *Vadose Zone Journal*, 4(4):1087–1095.

Aitchison, G. D., editor (1965). *Moisture Equilibria and Moisture Changes in Soils Beneath Covered Areas: A Symposium in Print*. Butterworths, Australien.

Alonso, E. E., Berdugo, I. R., and Ramon, A. (2013a). Extreme expansive phenomena in anhydritic-gypsiferous claystone: The case of Lilla tunnel. *Géotechnique*, 63(7):584–612.

Alonso, E. E., Gens, A., and Josa, A. (1990). A constitutive model for partially saturated soils. *Géotechnique*, 40(3):405–430.

Alonso, E. E., Pinyol, N. M., and Gens, A. (2013b). Compacted soil behaviour: Initial state, structure and constitutive modelling. *Géotechnique*, 63(6):463–478.

Altaner, S. P. and Ylagan, R. F. (1997). Comparison of Structural Models of Mixed-Layer Illite/Smectite and Reaction Mechanisms of Smectite Illitization. *Clays and Clay Minerals*, 45(4):517–533.

Amstad, C. and Kovári, K. (2001). Untertagebau in quellfähigem Fels: Institut für Geotechnik, ETH Zürich, Forschungsauftrag 52/94, 5408.01 von Eidgenössisches Department für Umwelt, Verkehr, Energie und Kommunikation (UVEK) und Bundesamt für Strassen (ASTRA).

Anagnostou, G. (1991). Untersuchungen zur Statik des Tunnelbaus in quellfähigem Gebirge: PhD thesis at ETH Zürich, Zürich, Switzerland.

Anagnostou, G. (1993). A model for swelling rock in tunnelling. *Rock Mechanics and Rock Engineering*, 26(4):307–331.

Anagnostou, G. (1995). Seepage flow around tunnels in swelling rock. *International Journal for Numerical and Analytical Methods in Geomechanics*, 19(10):705–724.

ASTM D7263-21 (2021). Standard Test Methods for Laboratory Determination of Density and Unit Weight of Soil Specimens. ASTM International, D18 Committee, West Conshohocken, PA.

Baille, W. (2014). Hydro-Mechanical Behaviour of Clays - Significance of Mineralogy: PhD thesis at Ruhr-Universität Bochum, Bochum, Germany.

Baille, W., Tripathy, S., and Schanz, T. (2010). Swelling pressures and one-dimensional compressibility behaviour of bentonite at large pressures. *Applied Clay Science*, 48(3):324–333.

Baker, M. J., Denton, T. T., and Herr, C. (2013). An explanation for why it is difficult to form slush nitrogen from liquid nitrogen used previously for this purpose. *Cryobiology*, 66(1):43–46.

Benett, R. H., O'Brien, N. R., and Hulbert, M. H. (1991). Determinants of Clay and Shale Microfabric Signatures: Processes and Mechanisms. In Bennett, R. H., Bryant, W. R., Hulbert, M. H., Chiou, W. A., Faas, R. W., Kasprowicz, J., Li, H., Lomenick, T., O'Brien, N. R., Pamukcu, S., Smart, P., Weaver, C. E., and Yamamoto, T., editors, *Microstructure of Fine-Grained Sediments*, Frontiers in Sedimentary Geology. Springer, New York, NY.

Bergaya, F., Theng, B. K., and Lagaly, G. (2006). Handbook of Clay Science: Elsevier.

Bilardi, S., Ielo, D., and Moraci, N. (2020). Predicting the Saturated Hydraulic Conductivity of Clayey Soils and Clayey or Silty Sands. *Geosciences*, 10(10):393.

BMDV (2023). Bundesministerium für Digitales und Verkehr. Wissing: „Verkehr in Deutschland wird zunehmen": https://bmdv.bund.de/SharedDocs/DE/Pressemitteilungen/2023/017-wissing-pk-verkehrsentwicklung-deutschland.html: Last checked: 20.11.2024.

Bock, H. (2001). RA Experiment - Rock Mechanics Analyses and Synthesis: Data Report on Rock Mechanics: Mont Terri Project, Technical Report 2000-02.

Bock, H. (2009). RA Experiment: Updated review of the rock mechanics properties of the Opalinus clay of the Mont Terri URL based on laboratory and field testing: Mont Terri Project, Technical Report 2008-04.

Bolt, G. H. (1956). Physico-Chemical Analysis of the Compressibility of Pure Clays. *Géotechnique*, 6(2):86–93.

Bossart, P., Bernier, F., Birkholzer, J., Bruggeman, C., Connolly, P., Dewonck, S., Fukaya, M., Herfort, M., Jensen, M., Matray, J.-M., Mayor, J. C., Moeri, A., Oyama, T., Schuster, K., Shigeta, N., Vietor, T., and Wieczorek, K. (2017a). Mont Terri rock laboratory, 20 years of research: Introduction, site characteristics and overview of experiments. *Swiss Journal of Geosciences*, 110(1):3–22.

Bossart, P., Jaeggi, D., and Nussbaum, C. (2017b). Experiments on thermo-hydro-mechanical behaviour of Opalinus Clay at Mont Terri rock laboratory, Switzerland. *Journal of Rock Mechanics and Geotechnical Engineering*, 9(3):502–510.

Bossart, P., Meier, P. M., Moeri, A., Trick, T., and Mayor, J.-C. (2002). Geological and hydraulic characterisation of the excavation disturbed zone in the Opalinus Clay of the Mont Terri Rock Laboratory. *Engineering Geology*, 66(1-2):19–38.

Bossart, P. and Milnes, A. G., editors (2018). *Mont Terri Rock Laboratory, 20 Years*. Swiss Journal of Geosciences Supplement. Springer International Publishing, Cham.

Bossart, P. and Thury, M. (2008). Project, programme 1996 to 2007 and results. *Wabern: Reports of the Swiss Geological Survey no. 3.*

Bossart, P., Trick, T., Meier, P. M., and Mayor, J. C. (2004). Structural and hydrogeological characterisation of the excavation-disturbed zone in the Opalinus Clay (Mont Terri Project, Switzerland). *Applied Clay Science*, 26(1-4):429–448.

Buckingham, E. (1907). Studies on the Movement of Soil Mositure. *Bureau of Soils - Bulletin No. 38.*

Bundesamt für Landestopografie swisstopo (2023). Lithostratigraphisches Lexikon der Schweiz: Opalinus-Ton [CH]: https://www.strati.ch/de/stratigraphic/opalinus-ton-ch: Last checked: 20.11.2024.

Bundesgesellschaft Für Endlagerung (2024). Auslegungstemperaturen in Schritt 2 Phase I des Standortauswahlverfahrens: Einordnungen zum Umgang mit der Grenztemperatur. *Grundlagenbericht*.

Burland, J. B. (1990). On the compressibility and shear strength of natural clays. *Géotechnique*, 40(3):329–378.

Butscher, C., Breuer, S., and Blum, P. (2018). Swelling laws for clay-sulfate rocks revisited. *Bulletin of Engineering Geology and the Environment*, 77(1):399–408.

Butscher, C., Mutschler, T., and Blum, P. (2016). Swelling of Clay-Sulfate Rocks: A Review of Processes and Controls. *Rock Mechanics and Rock Engineering*, 49(4):1533–1549.

Caenn, R., Darley, H. C. H., and Gray, G. R. (2017). *Composition and Properties of Drilling and Completion Fluids*. Gulf Professional Publishing, seventh edition.

Cardoso, R., Romero, E., Lima, A., and Ferrari, A. (2007). A Comparative Study of Soil Suction Measurement Using Two Different High-Range Psychrometers. *Proc. 2nd Int. Conf. Mech. Unsaturated Soils*, edited by T. Schanz (Springer Proceeding in Physics, Weimar, Germany, 2007):79–93.

Cardoso, R., Vieira, J., Calheiros, F., Borges, I., and Bardanis, M. (2023). A simple model for the water retention curve of compressible biocemented sands using MIP results. *E3S Web of Conferences*, 382(7):09001.

Carman, P. C. (1939). Permeability of saturated sands, soils and clays. *The Journal of Agricultural Science*, 29(2):262–273.

Cetin, H., Fener, M., Söylemez, M., and Günaydin, O. (2007). Soil structure changes during compaction of a cohesive soil. *Engineering Geology*, 92(1-2):38–48.

Chai, M. and Zhang, J. (2019). Improvement of Compressibility and Thaw-Settlement Properties of Warm and Ice-Rich Frozen Soil with Cement and Additives. *Materials (Basel, Switzerland)*, 12(7).

Chang, J., Li, Y., and Lu, H. (2022). The Morphological Characteristics of Authigenic Pyrite Formed in Marine Sediments. *Journal of Marine Science and Engineering*, 10(10):1533.

Chen, Y.-G., Dong, X.-X., Zhang, X.-D., Ye, W.-M., and Cui, Y.-J. (2019). Cyclic thermal and saline effects on the swelling pressure of densely compacted Gaomiaozi bentonite. *Engineering Geology*, 255(1-4):37–47.

Chiaverio, F., Straumann, U., Böheim, S., and Massignani, S. (2017). Dritte Belchentunnelröhre: Neue Lösungen für Vortrieb und Konstruktion beim Tunnelbau in stark quellendem Gebirge. *STUVA-Tagung 2017, Stuttgart, 6. - 8. Dezember*.

Christ, F., Lieske, W., Herz, C., and Wichtmann, T. (2022). Evaluation of the Penetration Behavior of Viscous Fluids into Porous Media in the Context of Volume Determination. *Geotechnical Testing Journal*, 45(4).

Christ, F., Lieske, W., Lavasan, A. A., Bakker, E., and Wichtmann, T. (2024). Impact of Reconstitution on the Hydro-Mechanical Behaviour of Opalinus Clay Shale. *under preparation*.

Civan, F. (2007). *Reservoir Formation Damage*. Gulf Professional Publishing, second edition.

Columbu, S., Mulas, M., Mundula, F., and Cioni, R. (2021). Strategies for helium pycnometry density measurements of welded ignimbritic rocks. *Measurement*, 173:108640.

Conil, N., Vitel, M., Plua, C., Vu, M. N., Seyedi, D., and Armand, G. (2020). In Situ Investigation of the THM Behavior of the Callovo-Oxfordian Claystone. *Rock Mechanics and Rock Engineering*, 53(6):2747–2769.

Crisci, E., Ferrari, A., Giger, S., and Laloui, L. (2018). On the Swelling Behavior of Shallow Opalinus Clay Shale. *7th International Conference on Unsaturated Soils, HKUST, Hong Kong, August, 3-5, 2018*.

Crisci, E., Ferrari, A., Giger, S. B., and Laloui, L. (2019). Hydro-mechanical behaviour of shallow Opalinus Clay shale. *Engineering Geology*, 251:214–227.

Dao, L.-Q., Delage, P., Tang, A.-M., Cui, Y.-J., Pereira, J.-M., Li, X.-L., and Sillen, X. (2014). Anisotropic thermal conductivity of natural Boom Clay. *Applied Clay Science*, 101(57):282–287.

DAUB (2020). Empfehlungen zur Auswahl von Tunnelbohrmaschinen. *Deutscher Ausschuss für unterirdisches Bauen e. V. (Hrsg.)*.

Dazas, B., Ferrage, E., Delville, A., and Lanson, B. (2014). Interlayer structure model of tri-hydrated low-charge smectite by X-ray diffraction and Monte Carlo modeling in the Grand Canonical ensemble. *American Mineralogist*, 99(8-9):1724–1735.

Delage, P., Howat, M., and Cui, Y. (1998). The relationship between suction and swelling properties in a heavily compacted unsaturated clay. *Engineering Geology*, 50(1-2):31–48.

Delage, P. and Lefebvre, G. (1984). Study of the structure of a sensitive Champlain clay and of its evolution during consolidation. *Canadian Geotechnical Journal*, 21(1):21–35.

Delage, P., Marcial, D., Cui, Y. J., and Ruiz, X. (2006). Ageing effects in a compacted bentonite: A microstructure approach. *Géotechnique*, 56(5):291–304.

Delage, P., Tessier, D., and Marcel-Audiguier, M. (1982). Use of the Cryoscan apparatus for observation of freeze-fractured planes of a sensitive Quebec clay in scanning electron microscopy. *Canadian Geotechnical Journal*, 19(1):111–114.

DGGT (1986). Empfehlung Nr. 11 des Arbeitskreises 19 - Versuchstechnik Fels - der Deutschen Gesellschaft für Erd- und Grundbau e.V. Quellversuche an Gesteinsproben. *Bautechnik*, 3:100–104.

Di Maio, C. (1996). Exposure of bentonite to salt solution: osmotic and mechanical effects. *Géotechnique*, 46(4):695–707.

Di Remigio, G., Rocchi, I., and Zania, V. (2021). Scanning Electron Microscopy and clay geomaterials: From sample preparation to fabric orientation quantification. *Applied Clay Science*, 214:106249.

Diamond, S. (1970). Pore Size Distributions in Clays. *Clays and Clay Minerals*, 18(1):7–23.

DIN 18312:2019-09 (2019). VOB Vergabe- und Vertragsordnung für Bauleistungen - Teil C: Allgemeine Technische Vertragsbedingungen für Bauleistungen (ATV) - Untertagebauarbeiten: Deutsche Institut für Normung e. V. (DIN), Beuth Verlag GmbH, Berlin.

DIN EN ISO 14688-1:2020-11 (2020). Geotechnische Erkundung und Untersuchung - Benennung, Beschreibung und Klassifizierung von Boden — Teil 1: Benennung und Beschreibung: Deutsche Institut für Normung e. V. (DIN), Beuth Verlag GmbH, Berlin.

DIN EN ISO 17892-12 (2020). Geotechnische Erkundung und Untersuchung - Laborversuche an Bodenproben - Teil 12: Bestimmung der Fließ- und Ausrollgrenzen: Deutsche Institut für Normung e. V. (DIN), Beuth Verlag GmbH, Berlin.

DIN EN ISO 17892-2 (2015). Geotechnische Erkundung und Untersuchung - Laborversuche an Bodenproben - Teil 2: Bestimmung der Dichte des Bodens: Deutsche Institut für Normung e. V. (DIN), Beuth Verlag GmbH, Berlin.

DIN EN ISO 17892-3:2016-07 (2016). Geotechnische Erkundung und Untersuchung - Laborversuche an Bodenproben - Teil 3: Bestimmung der Korndichte: Deutsche Institut für Normung e. V. (DIN), Beuth Verlag GmbH, Berlin.

DIN EN ISO 17892-4:2017-04 (2017). Geotechnische Erkundung und Untersuchung - Laborversuche an Bodenproben - Teil 4: Bestimmung der Korngrößenverteilung (ISO 17892-4:2016): Deutsche Institut für Normung e. V. (DIN), Beuth Verlag GmbH, Berlin.

Dobrowolsky, M. (2008). Quellverhalten teilgesättigter bindiger Böden mit mittlerem Quellpotential: PhD thesis at Technische Universität Kaiserslautern, Kaiserslautern, Germany.

Dolinar, B. (2009). Predicting the hydraulic conductivity of saturated clays using plasticity-value correlations. *Applied Clay Science*, 45(1-2):90–94.

Drits, V. A., Lindgreen, H., and Salyn, A. L. (1997). Determination of the content and distribution of fixed ammonium in illite-smectite by X-ray diffraction; application to North Sea illite-smectite. *American Mineralogist*, 82(1-2):79–87.

Emsley, S., Olsson, O., Stenberg, L., Alheid, H., and Falls, S. (1997). ZEDEX: A Study of Damage and Disturbance from Tunnel Excavation by Blasting and Tunnel Boring. *SKB Technical Report 97-30*.

Farouki, O. T. (1981). Thermal properties of soils. *U.S. Army Corps of Engineers, Cold Regions Research and Engineering Laboratory*.

Favero, V., Ferrari, A., and Laloui, L. (2016). On the hydro-mechanical behaviour of remoulded and natural Opalinus Clay shale. *Engineering Geology*, 208(3):128–135.

Favero, V., Ferrari, A., and Laloui, L. (2018). Anisotropic Behaviour of Opalinus Clay Through Consolidated and Drained Triaxial Testing in Saturated Conditions. *Rock Mechanics and Rock Engineering*, 51(5):1305–1319.

Fernàndez-Garcia, D., Jaime Gómez-Hernández, J., and Mayor, J.-C. (2007). Estimating hydraulic conductivity of the Opalinus Clay at the regional scale: Combined effect of desaturation and EDZ. *Physics and Chemistry of the Earth, Parts A/B/C*, 32(8-14):639–645.

Ferrage, E. (2016). Investigation of the Interlayer Organization of Water and Ions In Smectite from the Combined Use of Diffraction Experiments And Molecular Simulations. a Review of Methodology, Applications, And Perspectives. *Clays and Clay Minerals*, 64(4):348–373.

Ferrari, A., Favero, V., Marschall, P., and Laloui, L. (2014). Experimental analysis of the water retention behaviour of shales. *International Journal of Rock Mechanics and Mining Sciences*, 72(2):61–70.

Ferrari, A. and Romero, E. M. (2019). Thermo–Hydro–Mechanical Testing of Shales. In Dewers, T., Heath, J., and Sánchez, M., editors, *Shale*, Geophysical Monograph Series, pages 83–97. Wiley.

Ferrari, A., Rosone, M., Ziccarelli, M., and Giger, S. B. (2020). The shear strength of Opalinus Clay shale in the remoulded state. *Geomechanics for Energy and the Environment*, 21(5):100142.

Fleureau, J.-M., Kheirbek-Saoud, S., Soemitro, R., and Taibi, S. (1993). Behavior of clayey soils on drying–wetting paths. *Canadian Geotechnical Journal*, 30(2):287–296.

Fredlund, D. G. and Rahardjo, H. (1993). *Soil mechanics for unsaturated soils*. Wiley, New York.

Fredlund, D. G. and Xing, A. (1994). Equations for the soil-water characteristic curve. *Canadian Geotechnical Journal*, 31(4):521–532.

Garbotz, G. (1975). Baumaschinen einst und jetzt - 100 Jahre Baumaschinen im Spiegel der Bauwirtschaftsentwicklung: 5. Teil: Mechanisierung im Tunnel- und Stollenbau. *Baumaschine + Bautechnik*, 22(5):153–168.

Garcia-Bengochea, I., Altschaeffl, A. G., and Lovell, C. W. (1979). Pore Distribution and Permeability of Silty Clays. *Journal of the Geotechnical Engineering Division*, 105(7):839–856.

Garitte, B., Gens, A., Vaunat, J., and Armand, G. (2014). Thermal Conductivity of Argillaceous Rocks: Determination Methodology Using In Situ Heating Tests. *Rock Mechanics and Rock Engineering*, 47(1):111–129.

Gastwirth, J. L., Gel, Y. R., and Miao, W. (2009). The Impact of Levene's Test of Equality of Variances on Statistical Theory and Practice. *Statistical Science*, 24(3).

Gattermann, J. (1998). Theorie und Modellversuch für ein Abdichtungsbauwerk aus hochverdichteten Bentonitformsteinen. *Geotechnik in Forschung und Praxis, WBI-PRINT*, Essen, Verlag Glückauf GmbH.

Gautschi, A. (2017). Safety-relevant hydrogeological properties of the claystone barrier of a Swiss radioactive waste repository: An evaluation using multiple lines of evidence. *Grundwasser*, 22(3):221–233.

Gens, A. and Alonso, E. E. (1992). A framework for the behaviour of unsaturated expansive clays. *Canadian Geotechnical Journal*, 29(6):1013–1032.

Gens, A., Jouanna, P., and Schrefler, B. A. (1995). *Modern Issues in Non-Saturated Soils*. Springer Vienna, Vienna.

Gens, A., Wieczorek, K., Gaus, I., Garitte, B., Mayor, J. C., Schuster, K., Armand, G., García-Siñeriz, J. L., and Trick, T. (2017). Performance of the Opalinus Clay under thermal loading: Experimental results from Mont Terri rock laboratory (Switzerland). *Swiss Journal of Geosciences*, 110(1):269–286.

Giger, S. B., Marschall, P., Laloui, L., Ferrari, A., and Favero, V. (2014). Overview of geomechanical test results from Opalinus Clay core samples. *ENSI/EGT Symposium, Zurich, February 14th 2014*.

Gokhale, K. and Jain, K. K. (1972). Anisotropic Swelling in Black Cotton Soils. *Bulletin of the International Association of Engineering Geology*, (5):63–72.

Goldstein, J. I., Newbury, D. E., Michael, J. R., Ritchie, N. W., Scott, J. H. J., and Joy, D. C. (2018). *Scanning Electron Microscopy and X-Ray Microanalysis*. Springer New York, New York, NY.

Grim, R. E. (1968). *Clay Mineralogy*. 2nd edition edn, McGraw-Hill Book Company.

Grob, H. (1972). Schwelldruck im Belchentunnel. *Proceedings Internationales Symposium für Untertagebau*, Luzern:99–119.

Grob, H. (1976). Swelling and heave in Swiss tunnels. *Bulletin of the International Association of Engineering Geology*, (13):55–60.

Guggenheim, S. and Martin, R. T. (1995). Definition of Clay and Clay Mineral: Joint Report of the AIPEA Nomenclature and CMS Nomenclature Committees. *Clays and Clay Minerals*, 43(2):255–256.

Gurtug, Y. and Sridharan, A. (2015). Prediction of Compaction Behaviour of Soils at Different Energy Levels. *Uluslararası Muhendislik Arastirma ve Gelistirme Dergisi*, pages 15–18.

Hasenpatt, R., Degen, W., and Kahr, G. (1989). Flow and diffusion in clays. *Applied Clay Science*, 4(2):179–192.

Henke, K. F. (1976). Magnitude and rate of heave in tunnels in calcium sulphate bearing rocks. *Bulletin of the International Association of Engineering Geology*, (13).

Herbert, H.-J., Kasbohm, J., Sprenger, H., Fernández, A. M., and Reichelt, C. (2008). Swelling pressures of MX-80 bentonite in solutions of different ionic strength. *Physics and Chemistry of the Earth, Parts A/B/C*, 33(4):S327–S342.

Herrenknecht AG (2023). https://www.herrenknecht.com/en/products/productdetail/single-shield-tbm/: last checked on 20.11.2024.

Horseman, S. T., Harrington, J. F., Birchall, D. J., Noy, D. J., and Cuss, R. J. (2005). Consolidation and rebound properties of Opalinus Clay: A long-term, fully-drained test. *British Geological Survey Technical Report CR/05/128*.

Huder, J. and Amberg, G. (1970). Quellung in Mergel, Opalinuston und Anhydrit. *Schweizerische Bauzeitung*, 88(43).

Hueckel, T. and Borsetto, M. (1990). Thermoplasticity of Saturated Soils and Shales: Constitutive Equations. *Journal of Geotechnical Engineering*, 116(12):1765–1777.

Jaeggi, D., Bossart, P., and Wymann, L. (2014). Kompilation der lithologischen Variabilität und Eigenschaften des Opalinus-Ton im Felslabor Mont Terri: Expertenbericht von swisstopo, Landesgeologie zu Händen des Eidgenössischen Nuklearsicherheitsinspektorates ENSI.

Janbu, N. (1985). Soil models in offshore engineering. *Géotechnique*, 35(3):241–281.

Jo, H. Y., Katsumi, T., Benson, C. H., and Edil, T. B. (2001). Hydraulic Conductivity and Swelling of Nonprehydrated GCLs Permeated with Single-Species Salt Solutions. *Journal of Geotechnical and Geoenvironmental Engineering*, 127(7):557–567.

Jobmann, M., Sha Li, M. P., Breustedt, M., Schlegel, R., Vymlatil, P., and Will, J. (2016). Using Statistical Methods for Rock Parameter Identification to Analyse the THM Behaviour of Callovo-Oxfordian Claystone due to Heating. *Journal of Geological Resource and Engineering*, 4(3).

Kahr, G., Kraehenbuehl, F., Stoeckli, H. F., and Müller-Vonmoos, M. (1990). Study of the water-bentonite system by vapour adsorption, immersion calorimetry and X-ray techniques: II. Heats of immersion, swelling pressures and thermodynamic properties. *Clay Minerals*, 25(4):499–506.

Kassiff, G. and Shalom, A. B. (1971). Experimental Relationship Between Swell Pressure and Suction. *Géotechnique*, 21(3):245–255.

Kawamura, K. and Ogawa, Y. (2004). Progressive change of pelagic clay microstructure during burial process: examples from piston cores and ODP cores. *Marine Geology*, 207(1-4):131–144.

Keller, L. M., Schuetz, P., Erni, R., Rossell, M. D., Lucas, F., Gasser, P., and Holzer, L. (2013). Characterization of multi-scale microstructural features in Opalinus Clay. *Microporous and Mesoporous Materials*, 170:83–94.

Keskin, İ., Salimi, M., Ateyşen, E. Ö., Kahraman, S., and Vakili, A. H. (2023). Comparative Study of Swelling Pressure in Expansive Soils considering Different Initial Water Contents and BOFS Stabilization. *Advances in Civil Engineering*, 2023:1–11.

Khan, M. I. (2012). Hydraulic Conductivity of Moderate and Highly Dense Expansive Clays: PhD thesis at Ruhr-Universität Bochum, Bochum, Germany.

Khorshidi, M., Lu, N., Akin, I. D., and Likos, W. J. (2017). Intrinsic Relationship between Specific Surface Area and Soil Water Retention. *Journal of Geotechnical and Geoenvironmental Engineering*, 143(1).

Kiehl, J. R. (1990). A three-dimensional constitutive law for swelling rock and its application for underground constructions. *9. Nationales Felsmechanik Symposium der DGGT*, pages 185–207.

Kirschke, D. (1995). Neue Versuchstechniken und Erkentnisse zum Anhydritschwellen. *Taschenbuch für den Tunnelbau 1996*, Verlag Glückauf, Essen, Germany:203–225.

Klaver, J., Hemes, S., Houben, M., Desbois, G., Radi, Z., and Urai, J. L. (2015). The connectivity of pore space in mudstones: Insights from high-pressure Wood's metal

injection, BIB-SEM imaging, and mercury intrusion porosimetry. *Geofluids*, 15(4):577–591.

Kneuker, T. and Furche, M. (2021). Capturing the structural and compositional variability of Opalinus Clay: Constraints from multidisciplinary investigations of Mont Terri drill cores (Switzerland). *Environmental Earth Sciences*, 80(11):943.

Komine, H. and Ogata, N. (1996). Prediction for swelling characteristics of compacted bentonite. *Canadian Geotechnical Journal*, 33:11–22.

Komine, H., Yasuhara, K., and Murakami, S. (2009). Swelling characteristics of bentonites in artificial seawater. *Canadian Geotechnical Journal*, 46(2):177–189.

Kovári, K., Amstad, C., and Anagnostou, G. (1987). Tunnelbau in quellfähigem Gebirge. *Mitteilung der Schw. Gesellschaft für Boden- und Felsmechanik*, (115).

Kovári, K. and Ehrbar, H. (2008). Gotthard Basistunnel, Teilabschnitt Sedrun - Die druckhaften Strecken im TZM Nord - Projektierung und Realisierung. *Swiss Tunnel Congress*, pages 39–47.

Kozeny, J. (1927). Über kapillare Leitung des Wassers im Boden. *Sitzungsber Akad. Wiss.*, 136(2a):271–306.

Kugler, H., Schwaighofer, B., and Gruber, S. (2002). Die Modifizierung des Wasseraufnahmeversuches nach Enslin-Neff. *in Ottner, F., Gier, S. (Hrsg.), Berichte der Deutschen Ton- imd Tonmineralgruppe e.V., Band 9, Beiträge zur Jahrestagung Wien*, pages 125–141.

Laird, D. A. (2006). Influence of layer charge on swelling of smectites. *Applied Clay Science*, 34(1-4):74–87.

Laloui, L. and Ferrari, A., editors (2013). *Multiphysical Testing of Soils and Shales*. Springer Series in Geomechanics and Geoengineering. Springer Berlin Heidelberg, Berlin, Heidelberg.

Lambe, T. W. (1958). The Structure of Compacted Clays. *Journal of the Soil Mechanics and Foundations Division*, 84(2):453.

Lee, S. and Lee, D. K. (2018). What is the proper way to apply the multiple comparison test? *Korean journal of anesthesiology*, 71(5):353–360.

Leong, E.-C., Tripathy, S., and Rahardjo, H. (2003). Total suction measurement of unsaturated soils with a device using the chilled-mirror dew-point technique. *Géotechnique*, 53(2):173–182.

Liang, W.-y., Yan, R.-t., Xu, Y.-f., Zhang, Q., Tian, H.-h., and Wei, C.-f. (2021). Swelling pressure of compacted expansive soil over a wide suction range. *Applied Clay Science*, 203:106018.

Lieske, W., Tripathy, S., Baille, W., and Schanz, T. (2020). An alternative approach for determining suction of polyethylene glycols for soil testing. *Géotechnique Letters*, 10(1):45–49.

Liu, X. and Buzzi, O. (2014). Use of Hand-Spray Plaster as a Coating for Soil Bulk Volume Measurement. *Geotechnical Testing Journal*, 37(3):20130091.

Liu, Z., Zhang, R., Liu, Z., Zhang, Y., and Liu, P. (2021). Experimental Study on Swelling Behavior and Its Anisotropic Evaluation of Unsaturated Expansive Soil. *Advances in Materials Science and Engineering*, 2021(8):1–13.

Lloret, A., Villar, M. V., Sánchez, M., Gens, A., Pintado, X., and Alonso, E. E. (2003). Mechanical behaviour of heavily compacted bentonite under high suction changes. *Géotechnique*, 53(1):27–40.

Low, P. F. (1961). Physical Chemistry of Clay-Water Interaction. *Advances in Agronomy*, 13:269–327.

Low, P. F. and Margheim, J. F. (1979). The Swelling of Clay: I. Basic Concepts and Empirical Equations. *Soil Science Society of America Journal*, 43(3):473–481.

Lu, N. and Likos, W. J. (2004). *Unsaturated soil mechanics*. Wiley, Hoboken, NJ.

Madsen, F. T. (1999). Suggested Methods for Laboratory Testing of Swelling Rocks. *International Journal of Rock Mechanics and Mining Sciences*, 36(3):291–306.

Madsen, F. T. and Müller-Vonmoos, M. (1989). The swelling behaviour of clays. *Applied Clay Science*, 4(2):143–156.

Maidl, B., Herrenknecht, M., Maidl, U., Wehrmeyer, G., and Sturge, D. (2012). *Mechanised Shield Tunnelling*. Wiley, Hoboken, 2nd ed. edition.

Maidl, B., Thewes, M., and Maidl, U. (2013). *Handbook of Tunnel Engineering I: Structures and Methods*. Ernst Sohn, s.l., 1. aufl. edition.

Marti Gruppe (2017). Belchentunnel (Schweiz) - Projektfilm [Video], YouTube: https://www.youtube.com/watch?v=HEe-3QfeiW0 [18.07.2024].

Martin, C. D. and Lanyon, G. W. (2003). Measurement of in-situ stress in weak rocks at Mont Terri Rock Laboratory, Switzerland. *International Journal of Rock Mechanics and Mining Sciences*, 40(7-8):1077–1088.

Mayer, G., Klubertanz, G., and Croisé, J. (2007). Modelling of an in situ ventilation experiment in the Opalinus Clay. *Physics and Chemistry of the Earth, Parts A/B/C*, 32(8-14):629–638.

Meier, L. P. and Kahr, G. (1999). Determination of the Cation Exchange Capacity (CEC) of Clay Minerals Using the Complexes of Copper(II) Ion with Triethylenetetramine and Tetraethylenepentamine. *Clays and Clay Minerals*, 47(3):386–388.

Mezger, F., Ramoni, M., and Anagnostou, G. (2018). Options for deformable segmental lining systems for tunnelling in squeezing rock. *Tunnelling and Underground Space Technology*, 76(5):64–75.

Minardi, A., Crisci, E., Ferrari, A., and Laloui, L. (2016). Anisotropic volumetric behaviour of Opalinus clay shale upon suction variation. *Géotechnique Letters*, 6(2):144–148.

Mitchell, J. K. and Soga, K. (2005). Fundamentals of Soil Behaviour: 3. edn, John Wiley & Sons, Hoboken.

Mohajerani, M., Delage, P., Monfared, M., Tang, A. M., Sulem, J., and Gatmiri, B. (2011). Oedometric compression and swelling behaviour of the Callovo-Oxfordian argillite. *International Journal of Rock Mechanics and Mining Sciences*, 48(4):606–615.

Moro, F. and Böhni, H. (2002). Ink-bottle effect in mercury intrusion porosimetry of cement-based materials. *Journal of colloid and interface science*, 246(1):135–149.

Mügler, C., Filippi, M., Montarnal, P., Martinez, J.-M., and Wileveau, Y. (2006). Determination of the thermal conductivity of opalinus clay via simulations of experiments performed at the Mont Terri underground laboratory. *Journal of Applied Geophysics*, 58(2):112–129.

Muñoz, J., Alonso, E. E., and Lloret, A. (2009). Thermo-hydraulic characterisation of soft rock by means of heating pulse tests. *Géotechnique*, 59(4):293–306.

Muñoz, J. J. (2006). Thermo-hydro-mechanical analysis of soft rock. Application to a large scale heating test and large scale ventilation test: PhD thesis at Universitat Politècnica de Catalunya, Barcelona, Spain.

Naegeli, F. (2018). Investigation of in-situ and laboratory water content of Opalinus Clay shale from a borehole drilled at the new Belchen highway tunnel: BSc thesis at ETH Zurich, Zurich, Switzerland.

NAGRA (2001). Technischer Bericht 00-01: Sondierungsbohrung Benken Untersuchungs-bericht.

NAGRA (2002). Projekt Opalinuston: Synthese der geowissenschaftlichen Unter-suchungsergebnisse. Entsorgungsnachweis für abgebrannte Brennelemente, verglaste hochaktive sowie langlebige mittelaktive Abfälle. *Technical Report 02-03*, page 659.

Nieto, F., Pilar Mata, M., Bauluz, B., Giorgetti, G., Árkai, P., and Peacor, D. R. (2005). Retrograde diagenesis, a widespread process on a regional scale. *Clay Minerals*, 40(1):93–104.

Nishimura, T., Koseki, J., and Rahardjo, H. (2012). Determination of Air-Entry Value for Different Compacted Unsaturated Soil. *2nd International Conference on Transportation Geotechnics (ICTG)), Hokkaido, Japan*, pages 604–609.

Nitsch, A., Leuthold, J., Machaček, J., and Grandas Tavera, C. E. (2023). Experimental Investigations on Hydro-mechanical Processes in Reconstituted Clay Shale and Their Significance for Constitutive Modelling. *Rock Mechanics and Rock Engineering*, 40(3):405.

Orellana, L. F., Nussbaum, C., Grafulha, L., Henry, P., and Violay, M. (2022). Physical characterization of fault rocks within the Opalinus Clay formation. *Scientific reports*, 12(1):4389.

Pasha, A. Y., Khoshghalb, A., and Khalili, N. (2016). Pitfalls in Interpretation of Gravimetric Water Content–Based Soil-Water Characteristic Curve for Deformable Porous Media. *International Journal of Geomechanics*, 16(6).

Péron, H., Hueckel, T., and Laloui, L. (2007). An Improved Volume Measurement for Determining Soil Water Retention Curves. *Geotechnical Testing Journal*, 30(1):100167.

Péron, H., Salager, S., Nuth, M., Marschall, P., and Laloui, L. (2009). Analysis of the Swelling Pressure Development in Opalinus Clay – Experimental and Modelling Aspects. In *2nd EAGE International Conference on Fault and Top Seals - From Pore to Basin Scale 2009*. European Association of Geoscientists & Engineers.

Pimentel, E. (1996). Quellverhalten von diagenetisch verfestigtem Tonstein: PhD thesis at Karlsruher Institut für Technologie, Karlsruhe, Germany.

Pimentel, E. (2007). A Laboratory Testing Technique And a Model For the Swelling Behavior of Anhydritic Rock. *11th Congress of the International Society for Rock Mechanics 2007*, Lisbon, Portugal.

Pimentel, E. (2015). Existing Methods for Swelling Tests – A Critical Review. *Energy Procedia*, 76:96–105.

Pineda, J. A., Alonso, E. E., and Romero, E. (2014). Environmental degradation of claystones. *Géotechnique*, 64(1):64–82.

Pires, L. F., Mooney, S. J., Auler, A. C., Atkinson, B., and Sturrock, C. J. (2019). X-ray microtomography to evaluate the efficacy of paraffin wax coating for soil bulk density evaluation. *Geoderma*, 337:935–944.

Radončić, N., Schubert, W., and Moritz, B. (2009). Ductile support design. *Geomechanics and Tunnelling*, 2(5):561–577.

Rao, S. M. and Thyagaraj, T. (2007). Swell–compression behaviour of compacted clays under chemical gradients. *Canadian Geotechnical Journal*, 44(5):520–532.

Rao, S. M., Thyagaraj, T., and Thomas, H. R. (2006). Swelling of compacted clay under osmotic gradients. *Géotechnique*, 56(10):707–713.

Rauh, F., Spaun, G., and Thuro, K. (2006). Assessment of the swelling potential of anhydrite in tunnelling projects. *10th Congress of the International Association for Engineering Geology and the Environment (IAEG) 2006, Geological Society, London.*

Renz, T., Ziegler, M., and Loew, S. (2019). Investigations in the new TBM-excavated Belchen highway tunnel - Status update (Part 3): ENSI Research and Experience 2018. (ENSI-AN-10577):315–325.

Romero, E., Gens, A., and Lloret, A. (1999). Water permeability, water retention and microstructure of unsaturated compacted Boom clay. *Engineering Geology*, 54(1-2):117–127.

Romero, E., Sau, N., Lima, A., van Baelen, H., Sillen, X., and Li, X. (2016). Studying the thermal conductivity of a deep Eocene clay formation: Direct measurements vs back-analysis results. *Geomechanics for Energy and the Environment*, 8(2):62–75.

Romero, E., Senger, R., Marschall, P., and Gómez, R. (2013). Air Tests on Low-Permeability Claystone Formations. Experimental Results and Simulations. In Laloui, L. and Ferrari, A., editors, *Multiphysical Testing of Soils and Shales*, Springer Series in Geomechanics and Geoengineering, pages 69–83. Springer Berlin Heidelberg, Berlin, Heidelberg.

Romero, E. and Simms, P. H. (2008). Microstructure Investigation in Unsaturated Soils: A Review with Special Attention to Contribution of Mercury Intrusion Porosimetry and Environmental Scanning Electron Microscopy. *Geotechnical and Geological Engineering*, 26(6):705–727.

Rouf, M. A., Bouazza, A., Singh, R. M., Gates, W. P., and Rowe, R. K. (2016). Water vapour adsorption and desorption in GCLs. *Geosynthetics International*, 23(2):86–99.

Samarasinghe, A. M., Huang, Y. H., and Drnevich, V. P. (1983). Permeability and consolidation of normally consolidated soils. *International Journal of Rock Mechanics and Mining Sciences & Geomechanics Abstracts*, 20(1).

Sánchez, M., Gens, A., and Olivella, S. (2012). THM analysis of a large-scale heating test incorporating material fabric changes. *International Journal for Numerical and Analytical Methods in Geomechanics*, 36(4):391–421.

Sau, N. (2021). Thermo-Hydro-Mechanical Behaviour of a Deep Argillaceous Formation: PhD thesis at Universitat Politècnica de Catalunya, Barcelona, Spain.

Sau, N., Christ, F., Romero, E., and Lavasan, A. A. (2023). Thermal conductivity of compacted Opalinus Clay at different degrees of saturation. *E3S Web of Conferences*, 382:18002.

Sau, N., Romero, E., van Baelen, H., Tarantino, A., and Ibraim, E. (2019). Coupled thermo-hydro-mechanical behaviour of a deep clay. *E3S Web of Conferences*, 92:10001.

Schanz, T. and Al-Badran, Y. (2014). Swelling pressure characteristics of compacted Chinese Gaomiaozi bentonite GMZ01. *Soils and Foundations*, 54(4):748–759.

Schanz, T., Khan, M. I., and Al-Badran, Y. (2013). An alternative approach for the use of DDL theory to estimate the swelling pressure of bentonites. *Applied Clay Science*, 83-84:383–390.

Schanz, T. and Tripathy, S. (2009). Swelling pressure of a divalent-rich bentonite: Diffuse double-layer theory revisited. *Water Resources Research*, 45(5):1752.

Schoen, M. (2025). Numerical analysis of tunnel excavation in swellable clay shales: PhD thesis at Ruhr-Universität Bochum, Bochum, Germany.

Schuster, V., Rybacki, E., Bonnelye, A., Kwiatek, G., Schleicher, A. M., and Dresen, G. (2023). Strain Partitioning and Frictional Behavior of Opalinus Clay During Fault Reactivation. *Rock Mechanics and Rock Engineering*, 56(3):2065–2101.

Schwarz, A., Bluhm, J., and Schröder, J. (2020). Modeling of freezing processes of ice floes within the framework of the TPM. *Acta Mechanica*, 231(8):3099–3121.

Seiphoori, A., Ferrari, A., and Laloui, L. (2014). Water retention behaviour and microstructural evolution of MX-80 bentonite during wetting and drying cycles. *Géotechnique*, 64(9):721–734.

Seiphoori, A., Moradian, Z., Einstein, H. H., and Whittle, A. (2016). Microstructural Characterization of Opalinus Shale. *50th U.S. Rock Mechanics/Geomechanics Symposium, Houston, Texas*.

Seiphoori, A., Whittle, A., Krakowiak, K., and Einstein, H. (2017). Insights Into Diagenesis and Pore Structure of Opalinus Shale Through Comparative Studies of Natural and Reconstituted Materials. *Clays and Clay Minerals*, 65(2):135–153.

Shapiro, S. S. and Wilk, M. B. (1965). An analysis of variance test for normality (complete samples). *Biometrika*, 52(3-4):591–611.

Shi, B., Wu, Z., Inyang, H., Chen, J., and Wang, B. (1999). Preparation of soil specimens for SEM analysis using freeze-cut-drying. *Bulletin of Engineering Geology and the Environment*, 58(1):1–7.

Sibley, J. W. and Williams, D. J. (1989). A Procedure for Determining Volumetric Shrinkage of an Unsaturated Soil. *Geotechnical Testing Journal*, 12(3):181.

Siddiqua, S., Blatz, J., and Siemens, G. (2011). Evaluation of the impact of pore fluid chemistry on the hydromechanical behaviour of clay-based sealing materials. *Canadian Geotechnical Journal*, 48(2):199–213.

Skempton, A. (1953). The Colloidal "Activity" of Clays. *3rd International Conference on Soil Mechanics and Foundation Engineering (Switzerland)*, pages 57–61.

Soares, C. (2017). Investigations of Opalinus clay structural geology and tunnel face stability along the new Belchen N2 highway tunnel, folded Jura. MSc thesis at the Department of Earth sciences, Chair of Engineering Geology, ETH Zurich, Zurich, Switzerland.

Solgi, A., Naghdi, R., Labelle, E. R., Tsioras, P. A., and Salehi, A. (2018). Comparison of Sampling Methods Used to Evaluate Forest Soil Bulk Density. *Croatian Journal of Forest Engineering*, 39(2):247–254.

Soltani, A., Azimi, M., Boroomandnia, A., and O'Kelly, B. C. (2021). An objective framework for determination of the air-entry value from the soil–water characteristic curve. *Results in Engineering*, 12:100298.

Souza, R. and Pejon, O. J. (2020). Pore size distribution and swelling behavior of compacted bentonite/claystone and bentonite/sand mixtures. *Engineering Geology*, 275:105738.

Sridharan, A. and Gurtug, Y. (2004). Swelling behaviour of compacted fine-grained soils. *Engineering Geology*, 72(1-2):9–18.

Sridharan, A. and Jayadeva, M. S. (1982). Double layer theory and compressibility of clays. *Géotechnique*, 32(2):133–144.

Sridharan, A. and Nagaraj, H. B. (2005). Hydraulic conductivity of remolded fine-grained soils versus index properties. *Geotechnical and Geological Engineering*, 23(1):43–60.

Sridharan, A., Rao, A. S., and Sivapullaiah, P. V. (1986). Swelling Pressure of Clays. *Geotechnical Testing Journal*, 9(1):24.

Steiner, W. (2020). Sulphate-bearing rocks in tunnels - Lessons from field observations and in-situ swelling pressures: Verhalten von Sulfatgestein im Tunnelbau - Erfahrungen aus Feldbeobachtungen und In–situ–Quelldrücke. *Geomechanics and Tunnelling*, 13(3):286–301.

Steiner, W., Kaiser, P. K., and Spaun, G. (2011). Role of brittle fracture in swelling behaviour: Evidence from tunnelling case histories / Sprödbruch in wenig festem Fels als Auslöser von Quellvorgängen: Erkenntnisse aus Fallstudien. *Geomechanics and Tunnelling*, 4(2):141–156.

Steuter, A. A. (1981). Water potential of aqueous polyethylene glycol. *Plant physiology*, 67(1):64–67.

Studds, P. G., Stewart, D. I., and Cousens, T. W. (1998). The Effects of Salt Solutions on the Properties of Bentonite-Sand Mixtures. *Clay Minerals*, 33(4):651–660.

Tripathy, S., Sridharan, A., and Schanz, T. (2004). Swelling pressures of compacted bentonites from diffuse double layer theory. *Canadian Geotechnical Journal*, 41(3):437–450.

Tsang, C.-F., Bernier, F., and Davies, C. (2005). Geohydromechanical processes in the Excavation Damaged Zone in crystalline rock, rock salt, and indurated and plastic clays—in the context of radioactive waste disposal. *International Journal of Rock Mechanics and Mining Sciences*, 42(1):109–125.

Ufer, K., Kleeberg, R., Bergmann, J., and Dohrmann, R. (2012a). Rietveld Refinement of Disordered Illite-Smectite Mixed-Layer Structures by a Recursive Algorithm. I: One-Dimensional Patterns. *Clays and Clay Minerals*, 60(5):507–534.

Ufer, K., Kleeberg, R., Bergmann, J., and Dohrmann, R. (2012b). Rietveld Refinement of Disordered Illite-Smectite Mixed-Layer Structures by a Recursive Algorithm. II: Powder-Pattern Refinement and Quantitative Phase Analysis. *Clays and Clay Minerals*, 60(5):535–552.

van Genuchten, M. T. (1980). A Closed-form Equation for Predicting the Hydraulic Conductivity of Unsaturated Soils. *Soil Science Society of America Journal*, 44(5):892–898.

Vergara, M. R. (2019). Experimental and Numerical Investigations on the Swelling Behavior of Claystone and Sulfate Rock: PhD thesis at Karlsruher Institut für Technologie, Karlsruhe, Germany.

Vergara, M. R., Balthasar, K., and Triantafyllidis, T. (2014). Comparison of experimental results in a testing device for swelling rocks. *International Journal of Rock Mechanics and Mining Sciences*, 66:177–180.

Villar, M. V. and Lloret, A. (2008). Influence of dry density and water content on the swelling of a compacted bentonite. *Applied Clay Science*, 39(1-2):38–49.

Villar, M. V., Romero, F. J., and Volckaert (2012). Opalinus clay 2-phase flow parameters. *WP5 Final Report: Experiments and modelling of gas migration processes in undisturbed rocks. FORGE Report D5.15, D5.18 and D5.19 - VER.1.0.*

Voltolini, M., Wenk, H.-R., Mondol, N. H., Bjørlykke, K., and Jahren, J. (2009). Anisotropy of experimentally compressed kaolinite-illite-quartz mixtures. *GEO-PHYSICS*, 74(1):D13–D23.

von Wolffersdorff, P. and Heidkamp, H. (2005). Quellverhalten diagenetisch verfestigter Tonsteine in den Einschnitten der Neubaustrecke Nürnberg - Ingolstadt der Deutschen Bahn AG. *Festschrift zum 60. Geburtstag von Professor Dr.-Ing. Hans-Georg Kempfert*, pages 35–52.

von Wolffersdorff, P. A. and Fritzsche, S. (2003). Laboratory swell tests on overconsolidated clay and diagenetic solidified clay rocks. *Proc. Geotechnical Measurements and Modelling*, pages 407–412.

Vu, G., Iskhakov, T., Timothy, J. J., Schulte-Schrepping, C., Breitenbücher, R., and Meschke, G. (2020). Cementitious Composites with High Compaction Potential: Modeling and Calibration. *Materials (Basel, Switzerland)*, 13(21).

Wang, Y.-H. and Siu, W.-K. (2006a). Structure characteristics and mechanical properties of kaolinite soils. I. Surface charges and structural characterizations. *Canadian Geotechnical Journal*, 43(6):587–600.

Wang, Y.-H. and Siu, W.-K. (2006b). Structure characteristics and mechanical properties of kaolinite soils. II. Effects of structure on mechanical properties. *Canadian Geotechnical Journal*, 43(6):601–617.

Washburn, E. W. (1921). Note on a Method of Determining the Distribution of Pore Sizes in a Porous Material. *Proceedings of the National Academy of Sciences of the United States of America*, 7(4):115–116.

Wijaya, M., Leong, E. C., and Rahardjo, H. (2015). Effect of shrinkage on air-entry value of soils. *Soils and Foundations*, 55(1):166–180.

Wild, K. M. and Amann, F. (2018). Experimental study of the hydro-mechanical response of Opalinus Clay – Part 1: Pore pressure response and effective geomechanical properties under consideration of confinement and anisotropy. *Engineering Geology*, 237(4):32–41.

Wild, K. M., Walter, P., and Amann, F. (2017). The response of Opalinus Clay when exposed to cyclic relative humidity variations. *Solid Earth*, 8(2):351–360.

Wileveau, Y. and Rothfuchs, T. (2007). THM behaviour of host rock (HE-D) Experiment: Study of Thermal effects on Opalinus Clay: Mont Terri Project, Technical Report 2006-01.

Wilson, P. (2020). *A-Z of tree terms: A companion to British arboriculture.* Ethelburga House, Lyminge, Kent, third edition.

Wittke, M. (2003). Begrenzung der Quelldrücke durch Selbstabdichtung beim Tunnelbau in anhydritführenden Gebirge. *Geotechnik in Forschung und Praxis, WBI-PRINT 13*, Essen, Verlag Glückauf GmbH.

Wittke, W., Wittke, M., and Wahlen, R. (2004). Zum Quellgesetz für den anhydritführenden, unausgelaugten Gipskeuper. *geotechnik*, 27(2):112–117.

Ye, W. M., Zhu, C. M., Chen, Y. G., Chen, B., Cui, Y. J., and Wang, J. (2015). Influence of salt solutions on the swelling behavior of the compacted GMZ01 bentonite. *Environmental Earth Sciences*, 74(1):793–802.

Yigzaw, Z. G., Cuisinier, O., Massat, L., and Masrouri, F. (2016). Role of different suction components on swelling behavior of compacted bentonites. *Applied Clay Science*, 120:81–90.

Yu, C., Matray, J.-M., Gonçalvès, J., Jaeggi, D., Gräsle, W., Wieczorek, K., Vogt, T., and Sykes, E. (2017). Comparative study of methods to estimate hydraulic parameters in the hydraulically undisturbed Opalinus Clay (Switzerland). *Swiss Journal of Geosciences*, 110(1):85–104.

Zambas, C. (2017). More light in the tunnel of Eupalinos. *Mitteilungen des Deutschen Archäologischen Instituts - Athenische Abteilung*, (131/132):99–145.

Zeng, Z., Cui, Y.-J., and Talandier, J. (2021). Compaction and sealing properties of bentonite/claystone mixture: Impacts of bentonite fraction, water content and dry density. *Engineering Geology*, 287:106122.

Zeng, Z., Cui, Y.-J., and Talandier, J. (2023). Evaluation of swelling pressure of bentonite/claystone mixtures from pore size distribution. *Acta Geotechnica*, 18(3):1671–1679.

Zhang, C.-L., Rothfuchs, T., Moog, H., Dittrich, J., and Müller, J. (2004). Thermo-hydromechanical and geochemical behaviour of the Callovo-oxfordian Argillite and the Opalinus clay: Technical Report, GRS - 202, Society for Plant and Reactor Safety (GRS), Germany.

Zhang, L. C., Wieczorek, and Xie, M. L. (2010). Swelling experiments on mudstones. *Journal of Rock Mechanics and Geotechnical Engineering*, 2(1):44–51.

Zhao, G., Peacor, D. R., and McDowell, S. D. (1999). "Retrograde Diagenesis" of Clay Minerals in the Precambrian Freda Sandstone, Wisconsin. *Clays and Clay Minerals*, 47(2):119–130.

Ziegler, M., Brixel, B., Lavasan, A. A., Christ, F., and Loew, S. (2022a). Investigations in the new TBM-excavated Belchen highway tunnel: Summary and conclusions: ENSI Research and Experience 2021. (ENSI-AN-11284):342–358.

Ziegler, M., Lavasan, A. A., Christ, F., Schoen, M., and Loew, S. (2020). Investigations in the new TBM-excavated Belchen highway tunnel - Status update (Part 4): ENSI Research and Experience 2019. (ENSI-AN-10919):331–336.

Ziegler, M., Lavasan, A. A., and Loew, S. (2022b). Stress evolution around a TBM tunnel in swelling clay shale over four years after excavation. *Tunnelling and Underground Space Technology*, 128(2):104649.

Ziegler, M. and Loew, S. (2017). Investigations in the new TBM-excavated Belchen highway tunnel - Program, design and installations (Part 1): ENSI Research and Experience 2016. (ENSI-AN-9961):281–288.

Ziegler, M. and Loew, S. (2018). Investigations in the new TBM-excavated Belchen highway tunnel - Final installations and first results (Part 2): ENSI Research and Experience 2017. (ENSI-AN-10294):317–324.

Ziegler, M., Lukovic, M., Lavasan, A. A., Christ, F., Schoen, M., and Loew, S. (2021). Investigations in the new TBM-excavated Belchen highway tunnel - Status update (Part 5): ENSI Research and Experience 2020. (ENSI-AN-11061):313–320.

Schriftenreihe des Instituts für Grundbau, Wasserwesen und Verkehrswesen der Ruhr-Universität Bochum

Herausgeber: H.L. Jessberger

15   (1991)   **Mahmud Thaher**
Tragverhalten von Pfahl-Platten-Gründungen im bindigen Baugrund,
Berechnungsmodelle und Zentrifugen-Modellversuche

Schriftenreihe des Instituts für Grundbau der Ruhr-Universität Bochum

Herausgeber: H.L. Jessberger

16   (1992)   **Rainer Scherbeck**
Geotechnisches Verhalten mineralischer Deponieabdichtungsschichten
bei ungleichförmiger Verformungswirkung

17   (1992)   **Martin M. Bizialiele**
Torsional Cyclic Loading Response of a Single Pile in Sand

18   (1993)   **Michael Kotthaus**
Zum Tragverhalten von horizontal belasteten Pfahlreihen aus langen Pfählen in Sand

19   (1993)   **Ulrich Mann**
Stofftransport durch mineralische Deponieabdichtungen:
Versuchsmethodik und Berechnungsverfahren

20   (1992)   **Festschrift anlässlich des 60. Geburtstages von
Prof. Dr.-Ing. H. L. Jessberger**
20 Jahre Grundbau und Bodenmechanik an der Ruhr-Universität Bochum

21   (1993)   **Stephan Demmert**
Analyse des Emissionsverhaltens einer Kombinationsabdichtung im Rahmen der
Risikobetrachtung von Abfalldeponien

22   (1994)   **Diethard König**
Beanspruchung von Tunnel- und Schachtausbauten in kohäsionslosem Lockergestein
unter Berücksichtigung der Verformung im Boden

23   (1995)   **Thomas Neteler**
Bewertungsmodell für die nutzungsbezogene Auswahl von Verfahren zur Altlastensanierung

24   (1995)   **Ralph Kockel**
Scherfestigkeit von Mischabfall im Hinblick auf die Standsicherheit von Deponien

25   (1996)   **Jan Laue**
Zur Setzung von Flachfundamenten auf Sand unter wiederholten Lastereignissen

26   (1996)   **Gunnar Heibrock**
Zur Rissbildung durch Austrocknung in mineralischen Abdichtungsschichten
an der Basis von Deponien

27   (1996)   **Thomas Siemer**
Zentrifugen-Modellversuche zur dynamischen Wechselwirkung zwischen Bauwerken
und Baugrund infolge stoßartiger Belastung

28   (1996)   **Viswanadham V. S. Bhamidipati**
Geosynthetic Reinforced Mineral Sealing Layers of Landfills

29 (1997) **Frank Trappmann**
Abschätzung von technischem Risiko und Energiebedarf bei Sanierungsmaßnahmen
für Altlasten

30 (1997) **André Schürmann**
Zum Erddruck auf unverankerte flexible Verbauwände

31 (1997) **Jessberger, H. L. (Herausgeber)**
Environment Geotechnics, Report of ISSMGE Technical Committee TC 5
on Environmental Geotechnics

Schriftenreihe des Instituts für Grundbau und Bodenmechanik der Ruhr-Universität Bochum

Herausgeber: Th. Triantafyllidis

32 (2000) **Triantafyllidis, Th. (Herausgeber)**
Boden unter fast zyklischer Belastung: Erfahrung und Forschungsergebnisse (Workshop)

33 (2002) **Christof Gehle**
Bruch- und Scherverhalten von Gesteinstrennflächen mit dazwischenliegenden Materialbrücken

34 (2003) **Andrzej Niemunis**
Extended hypoplastic models for soils

35 (2004) **Christiane Hof**
Über das Verpressankertragverhalten unter kalklösendem Kohlensäureangriff

36 (2004) **René Schäfer**
Einfluss der Herstellungsmethode auf das Verformungsverhalten von Schlitzwänden
in weichen bindigen Böden

37 (2005) **Henning Wolf**
Zur Scherfugenbänderung granularer Materialien unter Extensionsbeanspruchung

38 (2005) **Torsten Wichtmann**
Explicit accumulation model for non-cohesive soils under cyclic loading

39 (2008) **Christoph M. Loreck**
Die Entwicklung des Frischbetondruckes bei der Herstellung von Schlitzwänden

40 (2008) **Igor Arsic**
Über die Bettung von Rohrleitungen in Flüssigböden

41 (2009) **Anna Arwanitaki**
Über das Kontaktverhalten zwischen einer Zweiphasenschlitzwand und nichtbindigen Böden

Schriftenreihe des Lehrstuhls für Grundbau, Boden- und Felsmechanik der Ruhr-Universität Bochum

Herausgeber: T. Schanz

42 (2009) **Yvonne Lins**
Hydro-Mechanical Properties of Partially Saturated Sand

43 (2010) **Tom Schanz (Herausgeber)**
Geotechnische Herausforderungen beim Umbau des Emscher-Systems
Beiträge zum RuhrGeo Tag 2010

44 (2010) **Jamal Alabdullah**
Testing Unsaturated Soil for Plane Strain Conditions: A New Double-Wall Biaxial Device

45 (2011) **Lars Röchter**
Systeme paralleler Scherbänder unter Extension im ebenen Verformungszustand

46 (2011) **Yasir Al-Badran**
Volumetric Yielding Behavior of Unsaturated Fine-Grained Soils

47 (2011) **Usque ad finem**
Selected research papers

48 (2012) **Muhammad Ibrar Khan**
Hydraulic Conductivity of Moderate and Highly Dense Expansive Clays

49 (2014) **Long Nguyen-Tuan**
Coupled Thermo-Hydro-Mechanical Analysis: Experimental and Back Analysis

50 (2014) **Tom Schanz (Herausgeber)**
Ende des Steinkohlenbergbaus im Ruhrrevier: Realität und Perspektiven für die Geotechnik
Beiträge zum RuhrGeo Tag 2014

51 (2014) **Usque ad finem**
Selected research papers

52 (2014) **Houman Soleimani Fard**
Study on the Hydro-Mechanical Behavior of Fiber Reinforced Fine Grained Soils,
with Application to the Preservation of Historical Monuments

53 (2014) **Wiebke Baille**
Hydro-Mechanical Behaviour of Clays - Significance of Mineralogy

54 (2014) **Qasim Abdulkarem Jassim Al-Obaidi**
Hydro-Mechanical Behavior of Collapsible Soils

55 (2015) **Veselin Zarev**
Model Identification for the Adaption of Numerical Simulation Models -
Application to Mechanized Shield Tunneling

56 (2015) **Meisam Goudarzy**
Micro and Macro Mechanical Assessment of Small and Intermediate Strain
Properties of Granular Material

Schriftenreihe des Lehrstuhls für Bodenmechanik, Grundbau und Umweltgeotechnik der Ruhr-Universität Bochum

Herausgeber: T. Wichtmann

70 (2019) **Mahmoud Qarmout**
Tunnel face stability using Kinematical Element Method (KEM)

71 (2021) **Raoul Hölter**
Optimal Experimental Design in Geotechnical Engineering

72 (2022) **Wolfgang Lieske**
Impact of polymer constitution on the hydro-mechanical behaviour of modified bentonite for the application in geotechnical and geoenvironmental engineering

73 (2022) **Patrick Staubach**
Contributions to the numerical modelling of pile installation processes and high-cyclic loading of soils

74 (2022) **Lingyun Li**
On the hydromechanical behaviour of loess and its effect on slope stability under rainfall infiltration

75 (2022) **Debdeep Sarkar**
Influence of particle characteristics on the behaviour of granular materials under static, cyclic and dynamic loading

76 (2023) **Torsten Wichtmann (Herausgeber)**
Umbau des Emscher-Systems – Geotechnische Erfahrungen
Beiträge zum RuhrGeo Tag 2023

77 (2023) **Abbas Farhat**
Fluidization and erosion of cemented granular materials. Experimental characterization and micromechanical simulation

78 (2023) **Andrea Geppetti**
Experimental and numerical investigations on the behaviour of tailing storage facilities under seismic loading

79 (2023) **Mohammad Hassan Sanayei**
Micromechanical modelling for the analysis of piping erosion in cemented soils for suction-assisted offshore foundations

80 (2024) **Christoph Schmüdderich**
Contributions to the stability assessment of slopes subjected to seismic loading

81 (2024) **Thomas Barciaga**
Constitutive modeling of natural clay with application to mechanized tunneling

82 (2024) **Cristian Rodriguez**
Contributions to the modelling of large deformations of soils: A particle-based approach